Analysis and Design of A New Class of Miniaturized Circular Waveguides Containing Anisotropic Metamaterial Liners

by

Justin G. Pollock

A thesis submitted in partial fulfillment of the requirements for the degree of

Doctor of Philosophy

in

Electromagnetics & Microwaves

Department of Electrical and Computer Engineering
University of Alberta

Abstract

This work presents the analysis and design of a new class of miniaturized circular waveguides containing anisotropic metamaterial liners, and reveals in detail intriguing and potentially useful propagation and radiation phenomena. An analytical construction of the liner as a homogeneous, anisotropic medium is used to develop a theoretical formulation that predicts the general dispersion features, cutoff frequencies, and field configurations of a metamaterial-lined circular waveguide. It is shown that a circular waveguide whose interior surface is coated with a thin uniaxial metamaterial liner possessing an epsilon-negative and near-zero (ENNZ) permittivity can permit propagation well below the unlined waveguide's fundamental-mode cutoff frequency, which is tantamount to extreme miniaturization. These liners are realized using a simple, printed-circuit implementation based on inductively loaded wires, which yields dispersion and miniaturization properties that are consistent with those observed for homogeneous, anisotropic metamaterial liners. A homogenization scheme is developed to characterize the liner's anisotropic effective-medium parameters, which is shown to accurately describe a set of frequency-reduced cutoffs. This work numerically and experimentally demonstrates that the inclusion of the thin liner substantially improves the transmission between two embedded shielded-loop sources while maintaining access to the waveguide's interior, thereby offering the potential for miniaturized waveguide components suitable for applications in which the waveguide volume must remain largely empty. Below-cutoff transmission through metamaterial-lined circular waveguides is shown to provide analogous benefits in equivalent metamaterial-lined open-ended waveguide (OEWG) probe antennas. Accordingly, this work presents the radiation performance of OEWG probe antennas that have been miniaturized by the introduction of thin ENNZ liners, which is shown to provide substantial gain improvements over a similarly sized (below-cutoff) waveguide probe. The far-field characteristics of a prototype metamaterial-lined waveguide excited by a shielded loop is investigated using full-wave simulations and near-field antenna measurements. Several emerging applications that may be enabled by these metamaterial-lined circular waveguides and OEWG probe antennas are explored, including travelling-wave imaging in MRI scanner bores at low static magnetic-field strengths, characterization of the properties of small quantities of fluids, and sampling electromagnetic field profiles over sub-wavelength spatial intervals. This work also investigates the application of the theoretical formulation, which describes a general class of anisotropic circular waveguides, towards the design of a metamaterial-coated PEC rod and metamaterial shell. It is shown that the introduction of anisotropic metamaterials provide new insights into controlling the dispersion of modes, cutoff frequencies, and field patterns. Relying on this theory, a transmission-line type metamaterial formed into a circular shell is shown to significantly enhance the radiation efficiency of a nearby antenna.

Preface

A portion of the research conducted for this thesis involved interactions with a few other research groups. Professor Nicola De Zanche at the University of Alberta provided the problem and background for the biomedical imaging application in Section 5.3. Initial investigations of a general class of anisotropic cylindrical waveguides in Chapter 7 were performed in part with the research group led by Professor S. Anantha Ramakrishna at the Indian Institute of Technology (Kanpur). However, the developed analysis for the specific classes of anisotropic cylindrical waveguides is my original work.

A portion of Chapter 3 has been published as J. G. Pollock and A. K. Iyer, "Below-Cutoff Propagation in Metamaterial-Lined Circular Waveguides", *IEEE Trans. Microw. Theory Techn.*, vol. 61, no. 9, pp. 3169–3178, 2013; Chapter 4 and Chapter 5 have been published as J. G. Pollock and A. K. Iyer, "Experimental Verification of Below-Cutoff Propagation in Miniaturized Circular Waveguides Using Anisotropic ENNZ Metamaterial Liners", *IEEE Trans. Microw. Theory Techn.*, vol. 64 , no. 4, pp. 1297-1305, 2016; Chapter 6 has been published as J. G. Pollock and A. K. Iyer, "Miniaturized Circular-Waveguide Probe Antennas Using Metamaterial Liners", *IEEE Trans. Antennas Propag.*, vol. 63, no. 1, pp.428-433, 2015. Prof. Iyer played a strong supervisory role in providing the initial ideas, concepts, and in editing and guiding the research, while I developed the ideas further and obtained and compiled the research material. A portion of Section 5.3 has been published as J. G. Pollock, N. DeZanche, and A. K. Iyer, "Travelling-Wave MRI at Lower B_0 Field Strength Using Metamaterial Liners", *International Society for Magnetic Resonance in Medicine Annual Meeting ISMRM 2012*, Melbourne, Australia, 2012. I performed the analysis and simulation and Prof. De Zanche and Prof. Iyer provided the background on imaging and metamaterials and assisted in manuscript organization and preparation. A portion of Chapter 7 has been published as D. Pratap, S.A. Ramakrishna, J. G. Pollock, and A. K. Iyer, "A class of circular waveguiding structures containing cylindrically anisotropic metamaterials: Applications from radio frequency/microwave to optical frequencies", *Opt. Express*, vol. 119, no. 8, pp. 83103-83113, 2016 and J. G. Pollock and A. K. Iyer, "Effective-Medium Properties of Cylindrical Transmission-Line Metamaterials", *IEEE Antennas Wireless Propag. Lett.*, vol. 10, pp. 1491–1494, 2011. I developed the theory and performed the data analysis, Prof. Ramakrishna and D. Pratap assisted in verifying the theory, and Prof. Iyer assisted in manuscript organization and preparation.

Acknowledgements

First, I would like to extend my warm gratitude to my advisor Prof. Ashwin K. Iyer for his continuous support of my Ph.D study and related research, for his mentorship, motivation, valuable insight, and immense knowledge. I did not even consider graduate studies until Prof. Iyer inspired me through his charismatic and demanding undergraduate lectures. I am extremely grateful for the opportunity to have met and studied under Prof. Iyer - I will be eternally in debt to you my dear friend. I could not have imagined having a better advisor and mentor for my Ph.D study.

Second, (although arguably more important) I wouldn't have been able to pursue my studies without the love and support of my wife Jessica, who put up with an often intrusive and stressful work schedule - I thank you for providing care when I couldn't for our wonderful daughter Vera. To my Dad and Mom, thank you for being world-class parents and for your continued emotional, tangible, and intangible support. I would like to thank all my family and friends, without whose precious support it would not have been possible to conduct this research.

Special thanks to my colleagues – Linh, Stuart, Elham, Sanghamitro, Will, Mitchell, and Braden – for their insightful conversations and valuable assistance in writing, simulations, and experiments. I couldn't have completed my Ph.D in a timely manner without you. I would like to thank Herb and Reiner for their assistance in fabricating my prototypes quickly and without undue expenses. I would like to express my gratitude to Prof. Nicola De Zanche who came to us with a problem that needed to be solved, which helped inspire a large portion of this work.

I would also like to acknowledge the financial support provided by the Natural Sciences and Engineering Research Council (NSERC) of Canada, University of Alberta, Alberta Innovates, IEEE Antennas and Propagation Society, IEEE Microwave Theory and Techniques

Society, and the generosity of Rogers Corporation for their donation of substrate materials.

Last, I would like to dedicate this thesis to my brother Bradlea and grandmother Joanne who recently passed on - I miss you both terribly.

Contents

List of Symbols

t	Time
∇	Vector Differential (Dell) operator
γ	Complex Axial Propagation Constant
α	Axial Attenuation Constant
β	Axial Propagation Constant
γ_ϵ^μ	*EH* Radial Propagation Constant
γ_ρ^μ	*HE* Radial Propagation Constant
ρ	Cylindrical Coordinate System's Radial Distance
ϕ	Cylindrical Coordinate System's Azimuthal Angle
z	Cylindrical Coordinate System's Axial Distance
$\hat{\rho}$	Cylindrical Coordinate System's Radial Unit Vector
$\hat{\phi}$	Cylindrical Coordinate System's Azimuthal Unit Vector
$\hat{z}$	Cylindrical Coordinate System's Axial Unit Vector
k_0	Free-space Propagation Constant
ϵ_0	Free-space Permittivity
ϵ	Permittivity
μ_0	Free-space Permeability
μ	Permeability
L	Inductance
C	Capacitance
Q	Quality Factor
R	Resistance
ω	Angular Frequency
ω_{ep}	Plasma Frequency
f	Frequency
f_c	Cutoff Frequency
$\mathbf{B}$	Magnetic Flux Density Vector
$\mathbf{D}$	Electric Flux Density Vector
$\mathbf{E}$	Electric Field Intensity Vector
$\mathbf{H}$	Magnetic Field Intensity Vector

List of Acronyms

1-D	One-dimensional
2-D	Two-dimensional
3-D	Three-dimensional
EH	Hybrid Magnetic
ENG	Epsilon-negative
ENNZ	Epsilon-negative-near-zero
ENZ	Epsilon-near-zero
EPS	Epsilon-positive
EPNZ	Epsilon-positive-near-zero
FEM	Finite-Element Method
HE	Hybrid Electric
GHz	Gigahertz (10^9 Hz)
MHz	Megahertz (10^6 Hz)
MNG	Mu-negative
MNZ	Mu-near-zero
MPS	Mu-positive
NRI	Negative Refractive Index
OEWG	Open-ended waveguide
PCB	Printed-Circuit Board
SRR	Split-Ring Resonator
TE	Transverse Electric
TEM	Transverse Electric and Magnetic
THz	Terahertz (10^{12} Hz)
TL	Transmission Line
TM	Transverse Magnetic

List of Figures

List of Tables

Chapter 1

Introduction

1.1 Motivation

As society enters the 21st century, miniaturization has become one of the foremost objectives in engineering, a development that is driven by the need to increase the compactness of devices and to reduce material costs. In telecommunications, the performance of several components, such as waveguiding and radiating structures, is typically wavelength-dependent, which places restrictions on the degree of miniaturization for the so-called "electrical length" of these devices (i.e. physical length with respect to wavelength). Many of today's emerging wireless technology requirements would be fulfilled if electromagnetic devices that are electrically small could retain a high efficiency and significant bandwidth.

Although planar electromagnetic structures have gained much traction in applications requiring miniaturization, they suffer from dielectric losses, cross-talk, and substrate breakdown at high driving powers. On the other hand, volumetric hollow metallic waveguides are widely used in applications requiring low propagation loss, moderate bandwidths, shielding properties, high power-handling capability and simple integration with radiating devices, such as horn antennas. As such, they are ideally suited to microwave radio links, radar, and satellite communications and in the characterization of materials and antennas. One manifestation is the circular perfect-electric-conductor (PEC) waveguide which only operates efficiently for frequencies above its fundamental TE_{11}-mode cutoff frequency (f_c). This cutoff frequency is inversely proportional to the waveguide's radius, and therefore increases as the waveguide gets smaller. Inhomogeneously filling the circular waveguide's cross-section with dielectric regions relaxes this condition while retaining access to the waveguide's interior, and can introduce new propagation phenomena, such as frequency-reduced propagating bands with forward-wave or backward-wave behaviour [1]. For instance, a circular waveguide whose interior surface is corrugated will support a hybrid-electric HE_{11} mode that is akin to the TE_{11} mode in a homogeneously filled waveguide but with a comparably lower attenuation loss that is useful in antenna applications [2, 3]. These structures belong to a general class of circular waveguides whose interior surface is said to be 'lined' or 'coated' with either a dielectric or artificial material.

Metamaterial loading of waveguides is a new avenue of research in which the propagation characteristics of an unloaded waveguide are altered through the inclusion of metamaterials, whose characteristics may be engineered to achieve intriguing propagation phenomena. It has been shown that propagation can be restored in below-cutoff waveguides by loading their interior with chains of magnetic and/or electric scatterers, such as the split-ring resonator (SRR), complimentary split-ring-resonator (CSRR), or wire-lines [4,5]. Metamaterial-loaded waveguides, although strictly inhomogeneously filled, are often treated as homogeneously filled by a metamaterial possessing an effective permittivity (ϵ) and permeability (μ) in which backward-, forward-, and slow-wave propagating bands are introduced where the metamaterial exhibits exotic material parameters [6–11]. The unique propagation characteristics afforded by metamaterials have also led to beneficial radiation characteristics for waveguide-type antennas. For instance, rectangular thin-wire grids exhibiting negative permittivity provide an improvement in the bandwidth and/or gain of rectangular and conical horn antennas [12, 13]. Similarly, small antennas placed next to isotropic and homogeneous cylindrical structures possessing negative permeability exhibit dramatically enhanced radiated power [14].

Whereas homogeneously filled models may explain certain elementary dispersion features, certain applications and practical metamaterial implementations may necessitate an inhomogeneous model for a complete description of the propagation phenomena, such as the distribution of power in the transverse cross-section, and the possibility of backward coupling of power, all of which have been observed in inhomogeneously filled structures. For instance, theoretical investigations of reverse-Cherenkov radiation in metamaterial-loaded waveguides consider the circular waveguides homogenously filled by a metamaterial possessing both negative permeability and permittivity [15]. However, an inner vacuum region is required in experimental verification to allow for the free passage of relativistic particles, rendering the resulting dielectric-lined waveguide inhomogeneous [16]. Although the standard analysis of the dielectric-lined circular waveguide has been applied to the case of metamaterial liners [17–20], these works have either omitted the necessary frequency dispersion, concerned themselves with a particular case of material parameters, limited their study to obtaining the field expressions and dispersion relations of simplified isotropic media and azimuthally symmetric modes, or only briefly investigated potentially intriguing propagation phenomena. Furthermore, these works lack an insightful and in-depth analysis of the dispersion and cutoffs of supported modes and their dependency on a metamaterial liner's dispersive permittivity and permeability.

Current practical realizations of metamaterials are inherently anisotropic [21–23], which is particularly true in manifestations employing cylindrical symmetry. For example, cylindrical arrangements of metamaterials can be characterized by cylindrically anisotropic permittivity and permeability tensors ($\bar{\bar{\epsilon}}$, $\bar{\bar{\mu}}$). Although these tensors can be simplified under certain conditions, such as by restricting the incident field polarization so that they may be approximated as isotropic, a biaxial description is more rigorous and can account for arbitrary field polarizations. Nevertheless, the axial invariance of a partially filled circular waveguide's cross-section suggests that some practical metamaterial loadings could be approximated by a uniaxial description [4]. While it is a challenge to design metamaterials with both negative permittivity and permeability [22, 24, 25], interesting propagation phenomena are also associated with much simpler metamaterials, such as those in which only one of two parameters is negative. For example, complete transmission occurs in thin rectangular and parallel-plate waveguides considered homogeneously filled with a metamaterial exhibiting near-zero permittivity [26]. It is worth questioning if a waveguide partially loaded with a near-zero permittivity displays similar tunneling. The interface between thin positive- and negative-permittivity layers support tightly bound surface modes with high field intensity and subwavelength spatial confinement. When arranged into annular layers in a circular waveguide, these surface modes would couple with the waveguide environment, potentially introducing novel propagation phenomena.

The early part of this work investigates the intriguing effects and implications of partially filling PEC circular waveguides with metamaterial liners possessing anisotropic, dispersive, and negative permittivity. For instance, using thin metamaterial liners to introduce an HE_{11} mode well below the natural cutoff would enable the miniaturization of circular waveguides while maintaining access to their interiors. This could prove useful in fluid-density measurements in the oil/gas industry [27], microwave heating of fluids [28], the observation of exotic radiation in particle physics [29], and enabling traveling-wave imaging at low static field strengths inside magnetic-resonance scanners [30]. Similarly, the miniaturization of circular waveguide probe antennas would enable subwavelength spatial sampling of an antenna-under-test's electromagnetic field profiles or a material's electromagnetic properties. Here, miniaturization of waveguides or antennas refers to operating at a frequency anywhere below their natural resonances, at which they are typically a significant fraction of a wavelength in size. The latter part of this investigation demonstrates below-cutoff propagation in enclosed and open metamaterial-lined PEC circular waveguides analytically using an effective-medium description, which is later verified numerically and experimentally with a prototyped printed-circuit realization of the liner.

Although the metamaterial-lined PEC circular waveguide is the focus of this work, the theoretical dispersion and field analysis relies upon a general class of solutions that is valid for many other types of electromagnetic structures exhibiting cylindrical symmetry. These structure simply differ by one or more boundary conditions and/or the introduction of an external source, and, as a result, their theoretical dispersion and field relations tend to have similar form. This work concludes by investigating a general class of inhomogeneous, anisotropic circular waveguides (the term 'waveguide' here can refer to structures that can either guide or radiate electromagnetic energy, depending on how they are operated) in which the introduction of anisotropy is shown to provide substantial control of the dispersion and field distributions of several supported modes. For exotic material parameters such as permittivity and permeability that are typically associated with metamaterials, intriguing propagation phenomena such as monomodal propagation, field confinement, and miniaturization are observed, provide enabling functionalities for a wide range of RF/microwave and optical applications.

1.2 Objectives

The objectives of this work can be summarized as follows: (1) develop the complete theoretical analysis for the dispersion and full electromagnetic field profiles of circular waveguides lined using metamaterials exhibiting cylindrically anisotropic material parameters; (2) investigate the relationships between certain anisotropic material parameters and novel phenomena, including miniaturization, backward-wave dispersion, and the introduction of frequency-reduced modes; (3) design a novel realization of anisotropic cylindrical metamaterials exhibiting negative permittivities at RF frequencies and develop techniques to homogenize their effective material parameters; (4) employ the metamaterial-lined waveguide for transmission and radiation applications and validate the expected phenomena numerically and experimentally; and (5) extend the theory to a general class of anisotropic cylindrical waveguide and antenna structures, and investigate their potentially useful propagation and radiation characteristics.

1.3 Outline

Chapter 2 provides a comprehensive background on waveguides either fully or partially filled by vacuum, natural dielectrics, or metamaterials. It begins with an introductory review of metamaterials and concludes with a discussion of several emerging applications of metamaterial-loaded waveguides. Chapter 3 explores the dispersion of several new modes supported by circular waveguides whose inner surface is lined by a thin anisotropic metamaterial region. We present a rigorous hybrid-mode analysis to determine the metamaterial-lined waveguide's general dispersion features, cutoff frequencies, and field configurations, which is used to develop relationships between individual material parameters and the cutoff frequencies of modes of interest. Several novel phenomena are established, including below-cutoff propagation, backward-wave dispersion, field collimation, and the possibility of waveguide miniaturization. This is followed by the analysis of a representative metamaterial-lined waveguide's dispersion features, in which design guidelines are offered for engineering the frequency response of a suite of frequency-reduced modes. Chapter 4 develops a printed-circuit implementation of the metamaterial liner and introduces a novel homogenization approach that gives insight into the metamaterial's effective-medium parameters based on the dispersions of frequency-reduced modes supported by the liner and their similarity to the transmission-line (TL) modes of TL metamaterials. An experimental prototype is developed, and parametric studies are performed to gauge the impact of fabrication tolerances on the dispersion of frequency-reduced modes. Chapter 5 numerically and experimentally investigates below-cutoff transmission in a metamaterial-lined waveguide possessing a dispersive anisotropic permittivity. Full-wave electromagnetic simulations are first employed to study the resonant transmission features of a metamaterial-lined waveguide placed between two larger excitation waveguides. A novel feeding arrangement employing a shielded-loop source embedded inside a miniaturized waveguide is investigated for the fabricated liners in both simulations and experiments. The advantages of miniaturized waveguides are explored for applications in medical imaging. Chapter 6 presents the radiation performance of open-ended circular-waveguide probe antennas that have been miniaturized by the introduction of thin metamaterial liners. The far-field characteristics of a designed frequency-reduced mode are compared to those of the modes of a conventional-sized OEWG using aperture theory and full-wave simulations. Numerical and experimental investigations of a prototype metamaterial-lined waveguide excited by a shielded loop are presented. Chapter 7 investigates other classes of anisotropic cylindrical waveguides that share a similar theoretical analysis, and focuses additionally on the novel dispersion features of an anisotropic metamaterial-coated rod waveguide and the radiation performance of an electric line source exciting an anisotropic metamaterial shell constructed from existing metamaterials. To conclude, Chapter 8 proposes a number of potential future directions of research, including novel applications of anisotropic metamaterials in circular waveguides and the benefits afforded when they are loaded by a fully biaxial metamaterial.

Chapter 2

Background

2.1 Homogeneously-Filled Waveguides

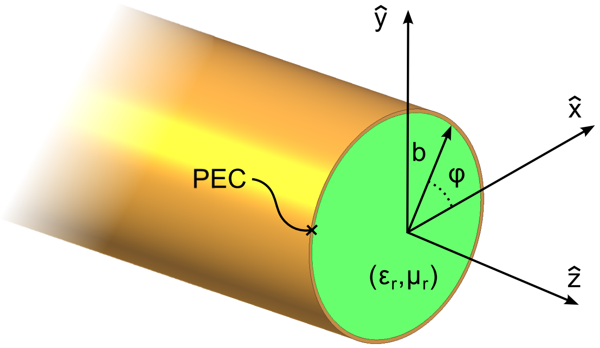

Figure 2.1: A circular waveguide of radius b homogeneously filled by a material possessing a relative permittivity (ϵ_r) and permeability (μ_r).

Hollow waveguides are widely used in applications requiring high power-handling capability and simple integration with radiating devices such as horn antennas. As such, they are ideally suited to microwave radio links, radar, and satellite communications. It is well known that air-filled waveguides enclosed by perfect-electric-conducting (PEC) boundaries support a discrete spectrum of modes, each possessing a cutoff frequency, f_c, above which they are capable of propagating power. One example is shown in Figure 2.1, which presents a circular waveguide of radius b whose waveguide axis coincides with the z-axis of the cylindrical coor-

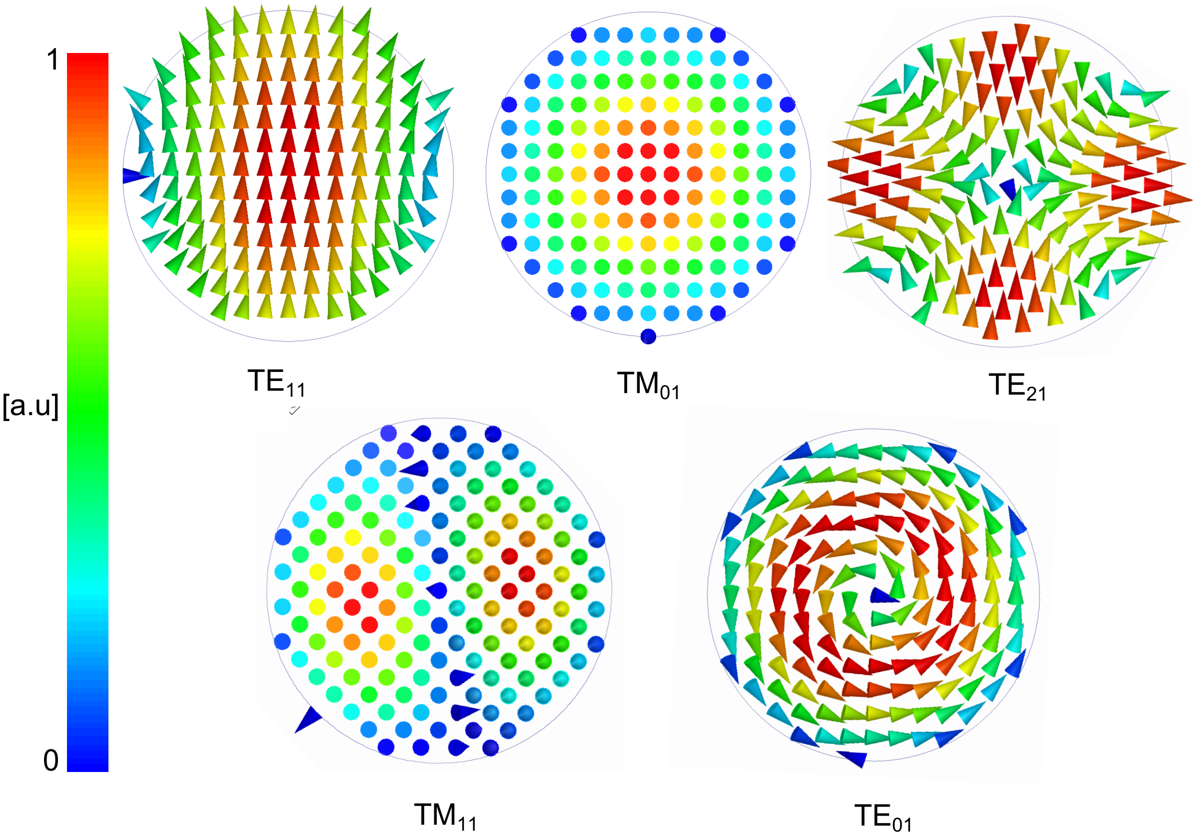

Figure 2.2: The electric-field vectors of the five lowest-order modes of a homogeneously-filled circular waveguide. The vector's colour represent the electric-field magnitude.

dinate system. Whereas Lord Rayleigh is now credited for the first theoretical analysis of an electromagnetic wave in a PEC circular waveguide [31], they were rediscovered independently by a number of research groups [32] and did not see wide use for almost 40 years until the development of high frequency radar in World War II [33]. To this day, circular waveguides are widely used as rotary joints which provide a continuous microwave transmission path between rotating and stationary sections of a mechanically scanned antenna system.

In general, homogeneous PEC waveguides support transverse electric (TE) and transverse magnetic (TM) modes in which the longitudinal (z-) electric- and magnetic-field components, respectively, are zero. The modes of a circular waveguide are described by the solutions of Bessel's differential equation which are termed Bessel functions. For a circular waveguide homogeneously filled by a material with permittivity ($\epsilon = \epsilon_r\epsilon_0$) and permeability ($\mu =$

$\mu_r\mu_0$), the TE and TM modes' cutoffs are determined from $f_{c,nm}^{TE} = p'_{nm}/(2\pi b\sqrt{\epsilon\mu})$ and $f_{c,nm}^{TM} = p_{nm}/(2\pi b\sqrt{\epsilon\mu})$, in which p_{nm} and p'_{nm} are the roots (or zeros) of a Bessel function of the first kind (J_n) and its derivative (J'_n), respectively, where n and m are the azimuthal and radial orders of the mode, respectively. The TE_{11} is the fundamental mode with the lowest cutoff frequency followed in increasing frequency by the TM_{01}, TE_{21}, TM_{11}, and TE_{01} modes' cutoffs, where the latter two are degenerate. The electric-field vectors of these modes are shown in Fig. 2.2. Due to the forward-wave (i.e., co-directional group and phase velocity) dispersion of the modes' propagating bands above their cutoffs, in general multiple modes can co-propagate. Only the TE_{11} mode has a monomodal propagating band up to the cutoff of the TM_{01} cutoff frequency where all other modes are evanescent. Designing sources for multimode waveguides requires special measures to excite a single desired mode while suppressing others. Homogeneously filling the vacuum region of the waveguide with an isotropic dielectric material serves to reduce these cutoff frequencies, without modifying the corresponding transverse modal field distributions. This is especially useful, for example, in tailoring the operational bandwidth and aperture-field distribution of horn antennas [34].

2.2 Inhomogeneous Waveguides

In applications requiring uninhibited motion through the waveguide, such as the microwave heating and characterization of fluids [27, 35] and the acceleration of particles to relativistic speeds [36], it is desirable to have access to the enclosed region of a waveguide, making it convenient to partially fill the waveguiding structure with a dielectric to achieve similar results. These inhomogeneous structures have special impedance boundary conditions and support modal field distributions that can differ significantly from those of their conventional, homogeneously-filled counterparts. The dielectric-lined circular waveguide, whose geometry is shown in Fig. 2.3, is an example of a composite structure. An inner core region of permittivity $\epsilon_1 = \epsilon_{r1}\epsilon_0$ and permeability $\mu_1 = \mu_{r1}\mu_0$ is surrounded by a dielectric

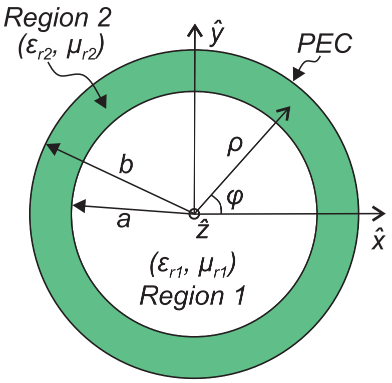

Figure 2.3: Transverse cross-section of the dielectric-lined cylindrical waveguide consisting of two concentric dielectric regions. An inner core region of radius a and a liner of thickness $b-a$ are filled with materials described by relative parameters $\{\epsilon_{r1},\ \mu_{r1}\}$ and $\{\epsilon_{r2},\ \mu_{r2}\}$, respectively.

material of thickness $t = b - a$ with permittivity $\epsilon_2 = \epsilon_{r2}\epsilon_0$ and permeability $\mu_2 = \mu_{r2}\mu_0$. It has been extensively investigated in the form of an otherwise hollow waveguide loaded with a dielectric rod [1, 37]. This structure supports hybrid electric (HE) and hybrid magnetic (EH) modes which are similar to the TE and TM modes in a conventional homogeneously-filled PEC circular waveguide. However, in hybrid modes the longitudinal (z-) electric-and magnetic-field components, in general, do not vanish. These hybrid modes have complex propagation constants of the form $\gamma = \alpha + j\beta$. Whereas nonzero α is attributed to dielectric or conductive loss in homogeneous waveguides, its existence in inhomogeneous waveguides is a direct result of the coupling of power between regions and can appear even in the absence of losses [1].

In low-loss structures, modes for which the value of α is substantially larger than β are termed evanescent. These modes attenuate rapidly in the longitudinal direction, and are limited in their ability to transport power along the waveguide, much like the evanescent modes of a homogeneously filled waveguide; as a result, they shall not be the focus of this study. On the other hand, modes with α much smaller than β can lead to the propagation of real power; we term these propagating modes. Modes with α comparable in magnitude to β can be considered neither purely propagating nor evanescent, and are therefore termed complex modes. These complex modes exist in complex conjugate pairs, and the two conjugate modes transport power in opposite directions so that net power is zero across any transverse plane of the waveguide [38]. Only if the conjugate modes are excited unequally can they transport real power [39]. A rigorous demonstration of the complex mode's power conservation property can be found in Ref. [39].

Due to the longitudinal symmetry in the structure, the analysis of the dielectric-lined cylindrical waveguide consists of finding the cutoff, or resonant, frequencies of the waveguide's cross section. Using these analysis techniques, it has been shown that it is possible to attain a bandwidth enhancement of the TE_{11} and TM_{01} modes through properly designing the dielectric liner [40]. The inhomogeneous nature of the waveguide introduces additional degrees of freedom in engineering its modal dispersion characteristics, such as the dielectric layer's permittivity, permeability, and thickness, providing benefits like bandwidth enhancement and introducing backward-wave propagation [1, 40].

Multilayered circular PEC waveguides are a generalization of the dielectric-lined waveguide, in which the material parameters of multiple dielectric layers are individually tailored to achieve useful propagation characteristics. They have received attention for their capability to significantly alter the dispersion and attenuation loss of propagating modes, which is useful in creating low-loss, slow-wave microwave accelerating structures that dampen non-EH_{01} modes [41], and, conversely in other instances, in significantly lowering the attenuation of the HE_{11} mode [42]. The ability to dampen or enhance select modes over others in multimode waveguides can be designed with a narrow and wide bandwidth, but the selectivity between modes is limited [42].

Periodically loading circular waveguides with metallic or dielectric inclusions offers additional flexibility in designing the mode's cutoffs, field profiles, and dispersion by engineering the physical and electrical properties of the inclusions. For instance, the gyrotron amplifier is a high-power microwave source that is constructed from a circular waveguide periodically loaded by either metallic discs or a helix, which act to slow the phase velocity of the waveguide's propagating modes to the velocity of an interacting electron beam [43]. Significant levels of amplification over broad bandwidths are achieved through proper choice of the disc's and helix's geometrical properties [44]. Instead of loading the vacuum interior with discs, corrugating the waveguide's walls with periodic air- or dielectric-filled grooves offers similar dispersion features with those of the disc-loaded waveguides. Corrugated waveguide horn antennas are now an industry standard for antenna applications requiring radiation patterns with low sidelobes and low cross polarization [45]. These corrugations are often analyzed using anisotropic surface impedance concepts, in which transverse and longitudinal corrugations are described as possessing a soft and hard boundary condition, respectively [46, 47]. Whereas introducing transverse corrugations in rectangular waveguides can enable propagation well below the natural cutoff frequency of a similarly sized unlined waveguide, these corrugations are typically resonant in length and either occupy a significant portion of the waveguide's interior and/or require high-permittivity dielectrics [48]. However, it may be possible to provide additional control over the mode's dispersion and enable similar below-cutoff propagation by introducing a thin metamaterial region possessing dispersive, anisotropic, and/or otherwise exotic material parameters.

2.3 Metamaterials

Electromagnetic-wave interaction with matter is often facilitated through macroscopic descriptors such as permittivity and permeability, which average (or homogenize) the influence an electric and magnetic field has on an ensemble of particles. In conventional materials, these homogenized effective-medium parameters rely upon the natural arrangement of individual atoms whose size and inter-atom spacing are far below the radiation's wavelength. Metamaterials are artificial dielectrics that employ a similar homogenized effective-medium description except the role of atoms is replaced by periodic inclusions, whose shape and arrangement can be precisely engineered using available technologies from RF to optical frequencies. Through proper design, metamaterials can take on a wide range of inhomogeneous (spatially variant) and anisotropic (polarization-dependent) electromagnetic material parameters, such as ϵ and μ, that can be used to control electromagnetic fields in space. Metamaterials can be designed to possess epsilon-positive (EPS), mu-positive (MPS), epsilon-negative (ENG), and/or mu-negative (MNG) responses. Simultaneous EPS and MPS is referred to as 'double-positive' (DPS), and simultaneous ENG and MNG is referred to as 'double-negative' (DNG). In DNG metamaterials, both $\epsilon < 0$ and $\mu < 0$ will cause the refractive index ($n = \sqrt{\epsilon\mu}$) to become negative, which enables some rather unique phenomena. A negative refractive index (NRI) causes light incident from a positive refractive index (PRI) to an NRI medium to refract beyond, rather than merely towards, the normal. Whereas a semi-infinite PRI material will generally support forward waves in which phase lags in the direction of power flow, an equivalent NRI material will support backward-wave propagation in which the phase advances as power flows.

Metamaterial studies now encompass a majority of the electromagnetic spectrum, with research in the radio frequency (RF), microwave, terahertz (THz), and optical regimes [49]. They have received much recent attention for such discoveries as the invisibility cloak [50] and the super-resolving lens [51]. Metamaterials have been used to alter the propagation in guiding structures; one such instance is the tunneling of electromagnetic waves through miniaturized waveguides [52]. Researchers have also used metamaterials to improve upon the design of antennas, in particular, providing new techniques in antenna miniaturization, beam forming, and gain and bandwidth improvement [53–55].

2.3.1 Realization and Modeling

Metamaterials take on a variety of forms, but are generally composed of an array of subwavelength electric and magnetic scatters. In this work, the periodic scatters are referred to as the metamaterial's unit cells. A metamaterial's effective-medium description is said to be valid when the phase incurred βd incurred by a wave possessing a wavenumber β across a unit cell of periodicity d satisfies the condition $\beta d \lesssim \pi/4$ [56, 57]. In metamaterials, relying on the unit cell's parasitic reactance alone, d is on the order of $\lambda/5$ [58]; however, strong, discrete reactive loading can significantly miniaturize the metamaterial's size; in fact, d on the order of $\lambda/75$ has been reported in the literature [59]. Several approaches to homogenize a metamaterial as an effective medium have been proposed in the literature such as those based on field-averaging [57, 60–63], curve-fitting [64], a dispersion relation [65], and an inversion of the scattering parameters [58, 66–68].

The bulk effective medium properties of (generally dispersive) metamaterials are frequency-dependent (i.e., $(\epsilon(\omega), \mu(\omega))$, in which ω is angular frequency) and can exhibit negative, near-zero, or positive complex values [69]. Several mathematical models have been proposed to model a dispersive metamaterial's material parameters; one being the Lorentz model, which describes electron motion in terms of a damped harmonic oscillator driven by an external force. In materials where the electrons are not bound to the nucleus, such as metals, the oscillator's restoring force is negligible, and the dispersion is described by a simpler Drude model. In fact, the Drude model can accurately model the electric response of most ENG metamaterials over a select frequency range around their plasma frequencies [70].

Whereas metals and plasmas are well-known conventional materials obeying a Drude response with isotropic negative permittivity at frequencies just below their plasma frequency, realizing these exotic values at microwave frequencies requires the use of structured materials. Some of the earliest envisioning of artificial microwave plasmas are the parallel-plate waveguides operating just below its TE_{01} mode cutoff and arrays of thin metallic wires, which exhibited plasma-like complex propagation without the need for a DC magnetic field [73]. An illustration of the thin metallic wires is shown in Fig. 2.4(a) and discussed in detail in Sec. 4.1. Over three decades later, thin-wire media saw a revival in the pursuit of an artificial medium possessing a NRI [21]. However, to achieve a NRI condition requires the creation of metamaterials with a magnetic response. To this end, Pendry et al. introduced the split-ring resonator (SRR) (shown in Fig. 2.4(b)) which consists of a capacitively-loaded metallic loop [71] that can be described by an effective permeability (μ_{eff}) that exhibits a

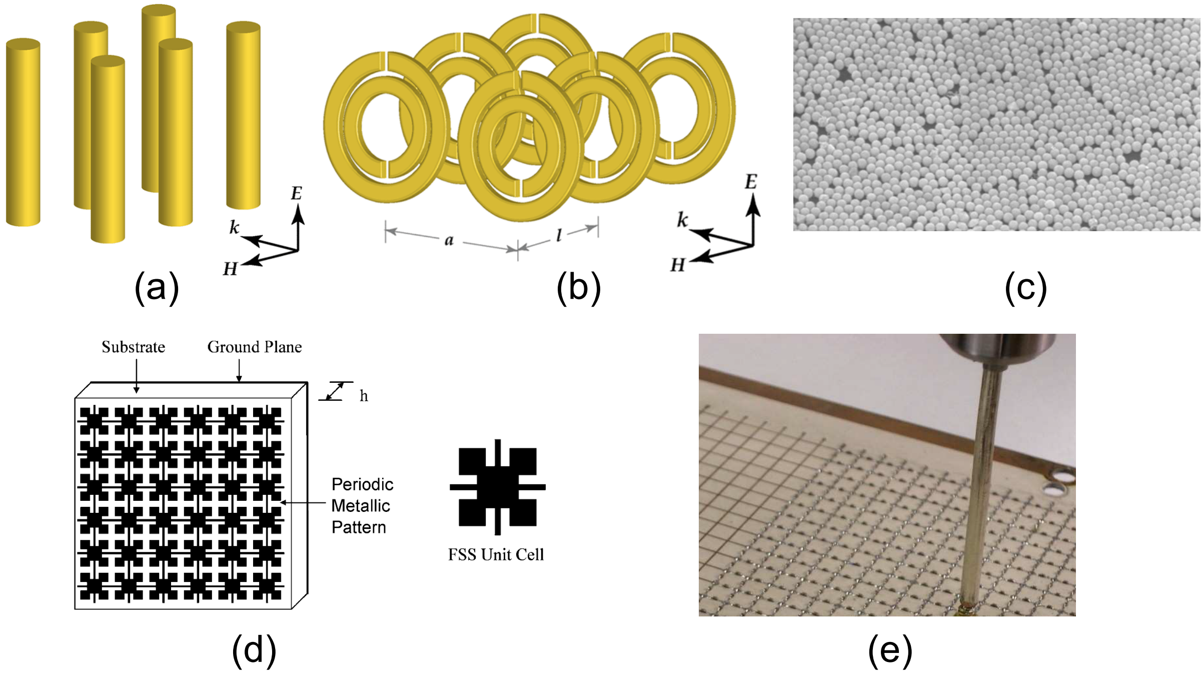

Figure 2.4: Various metamaterial realizations at RF, microwave, THz, and optical frequencies: (a) Thin-Wire Media [21], (b) Split-ring resonator [71], (c) Spherical silver nanoparticles [72] (d) Patterned Frequency-Selective Surfaces [56] (e) Periodically-loaded Transmission-Line [56].

Lorentz-type dispersion. At this stage it is useful to investigate in detail the Lorentz-type profile of μ_{eff}, which is applicable to many different types of metamaterial unit cells and can be represented using the following form:

$$\mu_{eff} = 1 + \frac{\omega_{mp}^2 - \omega_{mo}^2}{\omega_{mo}^2 - \omega^2 + j\omega\omega_{mt}}. \tag{2.1}$$

Here, ω_{mp} is the magnetic-plasma frequency, ω_{mo} is the magnetic-resonance frequency, and ω_{mt} is the magnetic damping factor. Figure 2.5 presents the dispersion of the real (solid-red curve) and imaginary (dashed-blue curve) components of $\mu_{eff} = \mu'_{eff} - j\mu''_{eff}$ obtained using Eq. 2.1 with $\omega_{mp} = 2\pi \times 4.5\text{GHz}$, $\omega_{mo} = 2\pi \times 5\text{GHz}$, and $\omega_{mt} = 2\pi \times 3\text{MHz}$.

Below ω_{mo}, μ_{eff} is positive and approaches its DC value. μ_{eff} exhibits negative permeability for frequencies just above ω_{mo}. In the case of the SRR, this frequency corresponds to a resonance formed between the capacitive gap and the metallic loop's inductive path [71].

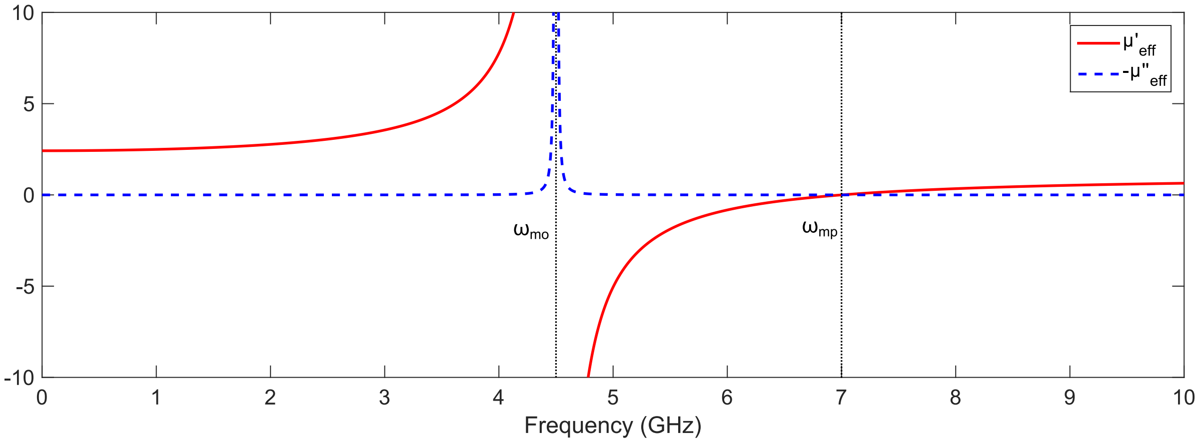

Figure 2.5: Lorentz dispersion of $\mu_{eff} = \mu'_{eff} - j\mu''_{eff}$ for a representative metamaterial with a magnetic response.

At higher frequencies, the negative permeability must pass through zero at ω_{mp} after which it assumes positive values that approach the permeability of free space (μ_0).

In addition to thin-wire and SRR metamaterials being scaled up to THz [74, 75] (and for the latter case, optical [76, 77]) frequencies, there exist countless other metamaterial implementations composed of linear, planar, or volumetric arrays of metallic and dielectric objects. This includes dielectric and metallic spheres [78, 79], patterned surfaces [80], or transmission-line topologies [56], which are respectively shown in Figs. 2.4(c)–2.4(e).

In initial theoretical studies, metamaterials are often modeled as homogeneous isotropic effective media. However, the design of isotropic 3-D metamaterials is a challenging endeavor because it requires its constituent unit cell's structural design to appear physically symmetric for an incident wave of arbitrary polarization [21–23]. This is eased in planar metamaterials, in which the symmetry requirement is relaxed by restricting propagation to 2-D. Furthermore, even physically asymmetric unit cells may appear isotropic by restricting the polarization of the incident wave [81]. Anisotropy becomes problematic again in manifestations employing cylindrical symmetry, in which the curvature, periodic nature, and axis-dependent boundary conditions must be considered.

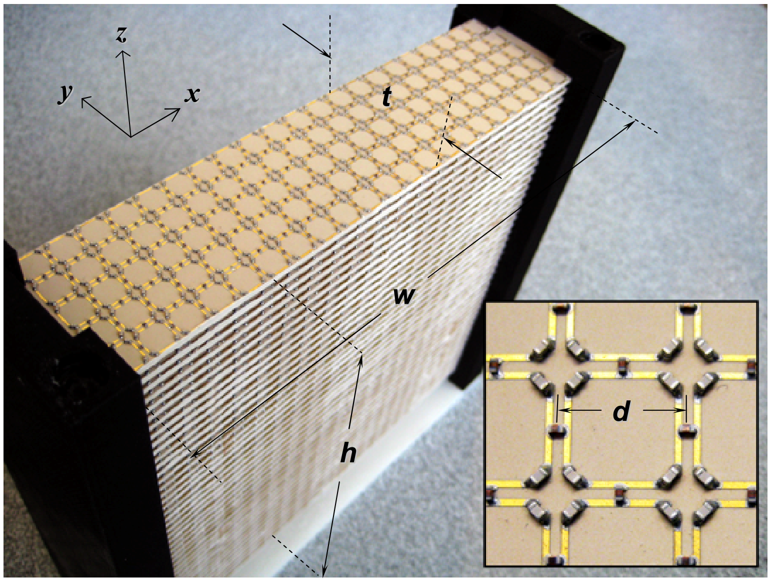

Figure 2.6: Photograph of fabricated NRI-TL superlens with inset showing lumped loading of the host CPS-TL using discrete surface-mount inductors and capacitors [51].

2.3.2 Negative Refractive Index Transmission-Line Metamaterials

One important subclass of metamaterials, which is a good candidate for cylindrical orientations, is the negative-refractive-index transmission-line (NRI-TL). In one form, the NRI-TL consists of a capacitively loaded host coplanar-strip (CPS) transmission line shaped into rings that are connected inductively [81]. The benefits of using the CPS technology is its balanced quasi-transverse electric and magnetic (TEM) mode, high bandwidth, and fully planar design that allows for ease of fabrication. Through the use of discrete loading components and the resulting miniaturization of the unit cells, there is tight coupling between resonators leading to larger NRI bandwidths and low propagation losses. These metamaterials have been realized in planar and volumetric form, and have been designed and experimentally verified to exhibit properties associated with left-handed-media such as the support of backward waves in leaky-wave-antennas and sub-diffraction focusing with a so-called 'Veselago-Pendry superlens' [51]. The first experimental verification of sub-diffraction focusing using a 'Veselago-Pendry superlens' in a free space environment was achieved by Iyer et al., and employs the NRI-TL metamaterial in a layered planar arrangement, as shown in Fig. 2.6. Strictly speaking, the stacked NRI-TL structure is uniaxially anisotropic, but appears isotropic under excitation by a vertical magnetic line source, which produces magnetic fields normal to the NRI-TL layers and limits propagation to the 2D isotropic layer planes. The NRI properties of the rectangular arrangement are derived from several parameters, including the $L - C$ loading, TL parameters, and the constant spacing between layers.

2.4 Metamaterial-Loaded Waveguides

Since their inception, metamaterials have been extensively investigated in waveguide environments in order to observe the intriguing propagation phenomena that arise from their exotic and dispersive material parameters. Waveguides are typically employed in experiments to verify the theoretical responses of metamaterials and to extract their effective-medium parameters [58]. For example, the theory of images enables propagation inside an infinite array of metamaterial inclusions to be described by placing a finite number of such inclusions inside a waveguide. Furthermore, the waveguide mode's fixed polarization can be employed to extract select components of a metamaterial's anisotropic material parameters.

Investigations of miniaturizing waveguides using metamaterials began with theoretical studies of a thin, subwavelength 1-D cavity resonator composed of slabs of PRI and NRI materials [82]. Since the backward-wave dispersion of the NRI slab introduces phase advance, it may compensate for the phase lag from the forward-wave dispersion in the PRI slab. Hence, the transverse resonance boundary condition can be satisfied for cavity lengths much shorter than approximately $\lambda/2$, which is the lowest resonance condition for a cavity homogeneously filled by a PRI medium. These theoretical studies were extended to the parallel-plate waveguide filled with PRI and NRI slabs, which support a backward-wave passband with an extremely small group velocity that could enable the reduction of the waveguide's transverse dimensions [83, 84]. In 2004, Alù et al. observed that the propagation of *TE* and *TM* modes can be made independent of the thickness of a parallel-plate

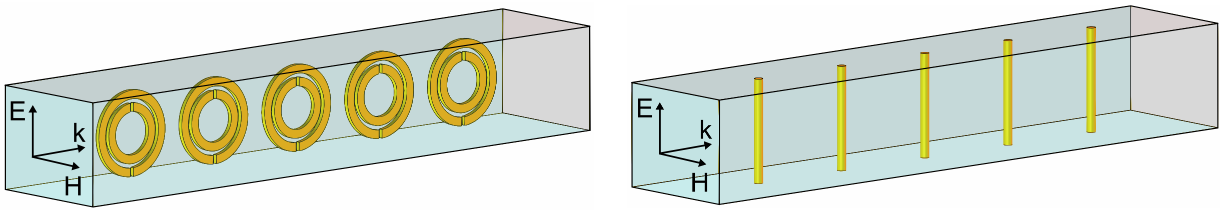

(a) (b)

Figure 2.7: A waveguide loaded by an array of (a) split-ring resonators (SRR) and (b) thin wires.

waveguide, provided that it is filled inhomogeneously with bilayers of the varieties DPS-DNG, DNG-ENG, DPS-MNG and ENG-MNG [85]. Furthermore, it was shown from the parallel-plate waveguide's dispersion relation that propagation of the TE modes is forbidden in thin waveguides for the bilayer combination DPS-ENG.

2.4.1 SRR and Thin-Wire-Loaded Waveguides

In 2005, Hrabar et al. experimentally demonstrated below-cutoff propagation in waveguides loaded by metamaterial inclusions, such as the SRR and thin wires shown in Figs. 2.7(a) and 2.7(b) [4]. This phenomenon was interpreted by considering the waveguide as homogeneously filled with a plasma with an effective permittivity ($\epsilon_{wg,eff}$) that follows a Drude profile. In this description, the cutoff frequency of the fundamental TE_{10} mode corresponds to the Drude plasma frequency, below which the waveguide has $\epsilon_{wg,eff} < 0$ [86]. Therefore, the waveguide's propagation constant $k = \omega\sqrt{\mu_0 \epsilon_{wg,eff}}$ is imaginary below the waveguide's cutoff frequency and propagation is forbidden. Loading the below-cutoff waveguide with an array of SRRs exhibiting $\mu_{eff} < 0$ results in $k = \omega\sqrt{\mu_{eff} \epsilon_{wg,eff}}$ being real and negative, and backward-wave propagation can occur. By mounting the SRR onto thin metallic rods that can rotate, the metamaterial's effective parameters can be mechanically tuned to introduce below-cutoff propagation with backward- or forward-wave dispersion [5].

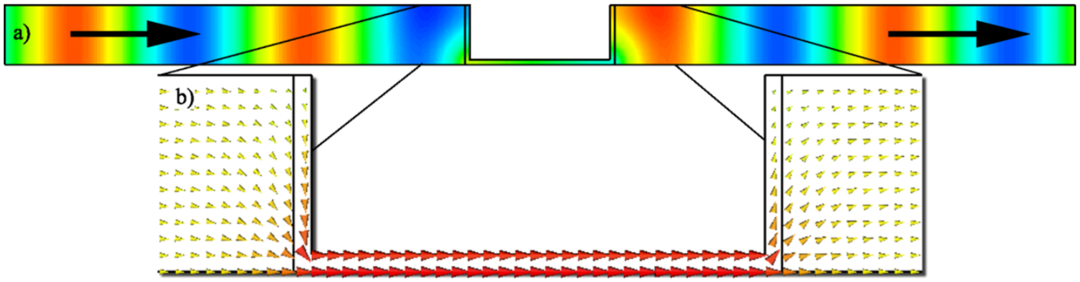

Figure 2.8: Simulated (a) magnetic-field magnitude (snapshot in time) and (b) Poynting vector distribution of the complete transmission through a subwavelength channel [87].

2.4.2 Epsilon-near-zero Waveguides

It was shown by Silveirinha and Engheta that complete transmission or 'supercoupling' could be achieved in discontinuous waveguides of arbitrarily small cross section, provided that they are homogeneously filled with SNG metamaterials possessing epsilon-near-zero (ENZ) values [88]. The physical insight behind this idea is that since the wavelength of radiation inside the ENZ material is extremely large, the wave must be able to propagate inside the ENZ material with no relevant reflection losses at abrupt bends or junctions. Since ENZ materials have a refractive index near zero, the phase variation inside such media is expected to be slow. In fact, this can be observed in Figs. 2.8(a) and 2.8(b) which present the simulated magnetic-field magnitude and Poynting vector of the complete transmission through an ultranarrow parallel-plate waveguide channel that is placed between two above-cutoff parallel-plate waveguides. In this figure, the ultranarrow waveguide channel naturally exhibits zero effective permittivity at its cutoff [89], which is made evident by the uniform phase variation in the channel. This tunneling is effectively a *zero-order* resonance. This terminology should not be confused with a conventional Fabry-Perot resonance because the frequency at which complete transmission occurs is strictly dependent on the $\epsilon = 0$ condition and not on the waveguide's length. Despite the huge impedance contrast between the feeding and channel waveguides, an incident wave will be able to tunnel through provided one of the physical transverse dimensions of the channel is electrically small [90].

Although initial studies considered waveguides filled with isotropic ENZ materials, in some scenarios complete transmission can also occur in anisotropic ENZ metamaterials. This eases the design of practical anisotropic metamaterial implementations to achieve supercoupling in bends of arbitrary geometry. For instance, arrays of thin-wires exhibiting an anisotropic ENZ response can be easily formed to fill complex waveguide-bend geometries to enable complete transmission, one example being a parallel-plate waveguide with a 180° bend [85]. Furthermore, tunneling in anisotropic ENZ metamaterials has enabled experimental validations of supercoupling in a waveguide containing an embedded anisotropic metamaterial with zero permittivity, such as the complimentary SRR at microwave frequencies [91] and silver and silicon nitride nanolamellae at optical frequencies [92]. This body of work has inspired novel dielectric-sensing waveguides [93, 94], in which the highly-selective transmission through ultranarrow channels can enable the detection of minute amounts of a dielectric material.

2.5 Antennas

Miniaturization is a driving force in many areas of electrical engineering and antenna design is no exception. However, common to many electromagnetic systems, there exist fundamental performance limits with respect to how small antenna elements can be made. Resonant antennas, such as the electric dipole, microstrip-patch, and open-ended waveguide, rely on a minimum wavelength condition being supported in one of their physical dimensions in order to maximize radiation efficiency. In 1947, Wheeler [95] modeled electrically small electric and magnetic dipoles as capacitive and inductive circuit elements, which he used to derive simple formulas that describe their maximum radiated power. These limits were generalized to all antennas by Chu [96] and Harrington [97]. In Chu's analysis, the whole antenna system, including any feed network to aid in reactive matching, is enclosed within a sphere of radius (r) and the antenna's radiated fields are expressed as a summation over orthogonal spherical-wave functions representing the full-spectrum of excited modes. The antenna's quality factor, which is a measure of antenna efficiency and bandwidth and is engineered to have low values in antennas, was calculated through relating the modes that propagate to real radiated power and the modes that decay evanescently to imaginary reactive power. For electrically-small-antennas (i.e., $k_0 r \ll 1$ where k_0 is the free-space wave vector), their quality factor takes the form:

$$Q \simeq \frac{1}{(k_0 r)^3}. \tag{2.2}$$

Therefore, as an antenna shrinks in size the quality factor inherently increases. While this limit can never be exceeded, researchers have been able to approach it even closer than before through the use of metamaterials [14].

2.6 Waveguide-Type Antennas

Although waveguides are typically used to guide waves within their confines, by simply opening up one end of the waveguide the resulting exposed aperture will radiate into free space. Open-ended waveguide (OEWG) probe antennas are popular for their well known near- and far-field patterns, ease of integration with standardized waveguides, and established calibration techniques. In the microwave and millimeter-wave regimes, waveguides are recognized for their applications in non-destructive dielectric sensing [98], surface crack detection [99], thermography [100], and near-field antenna and material characterization [101]. In fact, our recently acquired near-field measurement facilities at the University of Alberta utilize OEWG probes to accurately measure the fields of an antenna under test (AUT).

In antenna and material characterization, an OEWG probe is used to sample the spatial electromagnetic field profiles, where the measured signal is related to an analog integration of the fields across the aperture. However, like waveguides, these probes only operate efficiently for frequencies above a f_c which can lead to a few inherent drawbacks [102]. For instance, conventional above-cutoff waveguides are large and unable to sample the fields to even moderately sub-wavelength resolutions; moreover, they can unnecessarily load the antenna or material under test, potentially introducing errors into the measurements. Decreasing the aperture size of an OEWG probe would present several benefits, provided its efficiency could be maintained. One of these is the mitigation of errors introduced by approximations in near-field probe corrections [103].

Whereas OEWG probes may be miniaturized by operating in their evanescent region (i.e., below their fundamental cutoff frequency), such evanescent waveguide antennas require additional design, such as the inclusion of dielectric regions or complex matching networks, to compensate for their naturally reactive guided-wave impedance. For instance, the evanescent rectangular waveguide antenna reported in Ref. [104] requires multiple capacitive posts to achieve a -10dB bandwidth of 15% with a gain less than 4.7dB. Furthermore, this band resides immediately below its fundamental cutoff, implying only moderate or no miniaturization. Operating more deeply into cutoff to achieve larger degrees of miniaturization would result in severe decreases in gain and bandwidth. Another approach is to homogeneously fill the waveguide with a high-permittivity dielectric to reduce its cutoff frequency; however, at low frequencies, the dielectric filling leads to further increases in weight and manufacturing cost. Furthermore, this approach is unsuitable for applications requiring access to the interior of the waveguide. For example, uninhibited motion of particles through waveguides is required in both microwave heating of fluids [28] and in cyclotron masers for electron beams [29]. In these cases, it may be more prudent to partially fill, or line, the waveguide with a dielectric [105].

2.7 Metamaterial-Loaded Antennas

The metamaterial loading of antennas has resulted in the development of novel radiating systems and new techniques to improve the radiation characteristics of electrically small antennas. Some examples include leaky-wave antennas exhibiting entirely new phenomena, such as frequency scanning from backfire to endfire through broadside [106, 107]; compact horn antennas with up to octave bandwidths and improved gain [108–110]; and super-directive antenna arrays whose elements exhibit minimal mutual coupling despite their dense arrangement [111]. These properties are achieved through engineering the metamaterial's electromagnetic effective-medium parameters, which includes designing their spatial variation, as well as their dispersive response. Metamaterials have enabled dramatic size reductions of the monopole wire [112, 113], microstrip patch [114], and OEWG probe [115, 116].

Naturally, below-cutoff transmission in waveguides homogeneously-filled by metamaterials also enables the miniaturization of OEWG probe antennas. It was found that rectangular OEWG probes filled by SRRs suffer from highly resonant narrowband operation and low radiation efficiency, but offer a high degree of miniaturization of the waveguide's fundamental TE_{01} mode whose radiation pattern is similar to that of a vacuum-filled OEWG probe antenna but with a broader beamwidth and decreased directivity [115]. On the other hand, thin-wire ENG fillings provide only marginal degrees of miniaturization of the waveguide's TM_{11} mode, but with low losses. Whereas inductively loading the wires offers higher degrees of miniaturization, this comes at the expense of lower radiation efficiency.

In some instances, it may be prudent to consider these OEWG probe antennas as inhomogeneously loaded by metamaterials in order to properly characterize their radiation. This is particularly true in circular OEWG probe antennas, whose rotational symmetry requires cylindrical arrangements of metamaterial inclusions that prohibits the application of homogenization techniques developed for rectangular orientations. To enable access to the waveguide's interior, the metamaterial can line the interior surface of the circular OEWG probe antenna. Therefore, it would be useful to develop a complete analytical theory that accurately describes a circular waveguide whose interior contains two concentric layers possessing generally anisotropic and dispersive ϵ and μ.

Chapter 3

Theoretical Analysis of an Anisotropic Metamaterial-Lined PEC Circular Waveguide

3.1 Theory

This section presents, in detail, the approach used in this work to theoretically determine the dispersion and field relations of a generally inhomogeneous and anisotropic circular waveguide. The lined circular-waveguide cross section presented in Fig. 3.1 consists of an inner core region (Region I) that is surrounded by an anisotropic liner region (Region II), of radius a and b, respectively, which is embedded in a PEC background medium. In general, each region possesses anisotropic material parameters that are described by tensors diagonalized in a cylindrical coordinate system. Taking the coordinate axis to coincide with the waveguide axis, these take the form $\bar{\bar{\epsilon}} = \bar{\bar{I}}(\epsilon_\rho, \epsilon_\phi, \epsilon_z)\epsilon_0$ and $\bar{\bar{\mu}} = \bar{\bar{I}}(\mu_\rho, \mu_\phi, \mu_z)\mu_0$, in which $\bar{\bar{I}}$ is the identity

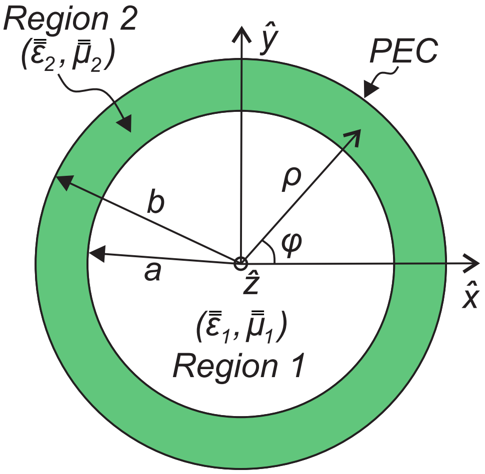

Figure 3.1: Transverse cross-section of the anisotropic metamaterial-lined circular waveguide.

dyadic defined as:

$$\bar{\bar{I}} = \begin{bmatrix} 1 & 0 & 0 \\ 0 & 1 & 0 \\ 0 & 0 & 1 \end{bmatrix} \tag{3.1}$$

In the following analysis, these material parameters can assume negative, near zero, positive, and other extreme values that are typically associated with dispersive metamaterials.

3.1.1 Field Analysis

The generally inhomogeneous nature suggests the waveguide supports hybrid electric HE_{nm} and hybrid magnetic EH_{nm} modes in which both the longitudinal (z-directed) electric and magnetic fields generally exist. Here, the indices n and m refer to the order of the mode's ϕ and ρ variation, respectively, and take on integer values. Let $\overline{E}(\rho, \phi, z) = \overline{E}(\rho, \phi)e^{-\gamma z}$ and $\overline{H}(\rho, \phi, z) = \overline{H}(\rho, \phi)e^{-\gamma z}$, in which $\gamma = \alpha + j\beta$ is the longitudinal (z) complex propagation constant. A time-harmonic behavior $e^{+j\omega t}$ is assumed and suppressed throughout. To solve for the fields and full dispersion of hybrid modes, a transverse decomposition of Maxwell's equations in a cylindrical coordinate system is employed. The general solution for the longitudinal (z) components of the electric and magnetic fields in any region is obtained from the cylindrical wave equation in an unbounded cylindrically anisotropic medium and derived in detail in Appendix A, and their final form is given by Eqs. A.24b and A.25. To avoid a singularity at $\rho = 0$ in Region 1, $b_4 = a_4 = 0$ in Eqs. A.24b and A.25, and they reduce to the form:

$$E_{z1} = C_1 J_{\nu_1}(\gamma^{\epsilon}_{\rho 1}\rho) cos(n\phi) e^{-\gamma z}, \tag{3.2a}$$

$$H_{z1} = C_2 J_{\tau_1}(\gamma^{\mu}_{\rho 1}\rho) sin(n\phi) e^{-\gamma z}, \tag{3.2b}$$

in which,

$$\gamma^{\epsilon}_{\rho 1} = \sqrt{\frac{\epsilon_{z1}}{\epsilon_{\rho 1}}}\sqrt{\gamma^2 + {k_0}^2 \epsilon_{\rho 1}\mu_{\phi 1}}, \quad \gamma^{\mu}_{\rho 1} = \sqrt{\frac{\mu_{z1}}{\mu_{\rho 1}}}\sqrt{\gamma^2 + {k_0}^2 \epsilon_{\phi 1}\mu_{\rho 1}}, \tag{3.3a}$$

$$\nu_1 = \sqrt{\frac{\epsilon_{\phi 1}\mu_{z1}}{\epsilon_{z1}\mu_{\rho 1}}}\frac{\gamma^{\epsilon}_{\rho 1}}{\gamma^{\mu}_{\rho 1}} n, \quad \tau_1 = \sqrt{\frac{\mu_{\phi 1}\epsilon_{z1}}{\mu_{z1}\epsilon_{\rho 1}}}\frac{\gamma^{\mu}_{\rho 1}}{\gamma^{\epsilon}_{\rho 1}} n. \tag{3.3b}$$

Here, $\gamma^{\mu}_{\rho 1}$ and $\gamma^{\epsilon}_{\rho 1}$ are the ρ-directed components of the propagation vectors, $k_0 = \omega/c$ is the free-space propagation constant, ν_1 and τ_1 are the generally complex orders of the Bessel (J) and Neumann (Y) functions, n is the azimuthal mode index, and C_1 and C_2 are the region-dependent constants that are derived from applying the appropriate boundary conditions.

In Region 2, the longitudinal fields can be expressed as:

$$E_{z2} = (C'_1 J_{\nu_2}(\gamma^{\epsilon}_{\rho 2}\rho) + C'_2 Y_{\nu_2}(\gamma^{\epsilon}_{\rho 2}\rho)) cos(n\phi) e^{-\gamma z}, \tag{3.4a}$$

$$H_{z2} = (C'_3 J_{\tau_2}(\gamma^{\mu}_{\rho 2}\rho) + C'_4 Y_{\tau_2}(\gamma^{\mu}_{\rho 2}\rho)) sin(n\phi) e^{-\gamma z}, \tag{3.4b}$$

in which,

$$\gamma^{\epsilon}_{\rho 2} = \sqrt{\frac{\epsilon_{z2}}{\epsilon_{\rho 2}}}\sqrt{\gamma^2 + {k_0}^2 \epsilon_{\rho 2}\mu_{\phi 2}}, \quad \gamma^{\mu}_{\rho 2} = \sqrt{\frac{\mu_{z2}}{\mu_{\rho 2}}}\sqrt{\gamma^2 + {k_0}^2 \epsilon_{\phi 2}\mu_{\rho 2}}, \tag{3.5a}$$

$$\nu_2 = \sqrt{\frac{\epsilon_{\phi 2}\mu_{z2}}{\epsilon_{z2}\mu_{\rho 2}}}\frac{\gamma^{\epsilon}_{\rho 2}}{\gamma^{\mu}_{\rho 2}} n, \quad \tau_2 = \sqrt{\frac{\mu_{\phi 2}\epsilon_{z2}}{\mu_{z2}\epsilon_{\rho 2}}}\frac{\gamma^{\mu}_{\rho 2}}{\gamma^{\epsilon}_{\rho 2}} n. \tag{3.5b}$$

We can simplify the expressions in Region 2 by applying the PEC boundary condition at

$\rho = b$ on E_{z2} and $E_{\phi 2}$. After manipulation, Eqs. 3.4a and 3.4b can be expressed as:

$$E_{z2} = C_3 F_{\nu_2}(\gamma^{\epsilon}_{\rho 2}\rho) cos(n\phi) e^{-\gamma z}, \tag{3.6a}$$

$$H_{z2} = C_4 G_{\tau_2}(\gamma^{\mu}_{\rho 2}\rho) sin(n\phi) e^{-\gamma z}, \tag{3.6b}$$

in which,

$$F_{\nu_2}(\gamma^{\epsilon}_{\rho 2}\rho) = Y_{\nu_2}(\gamma^{\epsilon}_{\rho 2}b) J_{\nu_2}(\gamma^{\epsilon}_{\rho 2}\rho) - J_{\nu_2}(\gamma^{\epsilon}_{\rho 2}b) Y_{\nu_2}(\gamma^{\epsilon}_{\rho 2}\rho), \tag{3.7a}$$

$$G_{\tau_2}(\gamma^{\mu}_{\rho 2}\rho) = Y'_{\tau_2}(\gamma^{\mu}_{\rho 2}b) J_{\tau_2}(\gamma^{\mu}_{\rho 2}\rho) - J'_{\tau_2}(\gamma^{\mu}_{\rho 2}b) Y_{\tau_2}(\gamma^{\mu}_{\rho 2}\rho). \tag{3.7b}$$

The transverse field components in each region are determined from the longitudinal components using Eqs. A.9 in Appendix A and take the form:

$$E_{\rho 1} = \left(\frac{-\gamma \epsilon_{z1}}{\epsilon_{\rho 1}\gamma^{\epsilon}_{\rho 1}} C_1 J'_{\nu_1}(\gamma^{\epsilon}_{\rho 1}\rho) - \frac{j\omega n \mu_{\phi 1}\epsilon_{z1}}{\epsilon_{\rho 1}{\gamma^{\epsilon}_{\rho 1}}^2 \rho} C_2 J_{\tau_1}(\gamma^{\mu}_{\rho 1}\rho) \right) \cos(n\phi) e^{-\gamma z}, \tag{3.8a}$$

$$E_{\phi 1} = \left(\frac{\gamma n \mu_{z1}}{\mu_{\rho 1}{\gamma^{\mu}_{\rho 1}}^2 \rho} C_1 J_{\nu_1}(\gamma^{\epsilon}_{\rho 1}\rho) + \frac{j\omega \mu_{z1}}{\gamma^{\mu}_{\rho,1}} C_2 J'_{\tau_1}(\gamma^{\mu}_{\rho 1}\rho) \right) \sin(n\phi) e^{-\gamma z}, \tag{3.8b}$$

$$E_{\rho 2} = \left(\frac{-\gamma \epsilon_{z2}}{\epsilon_{\rho 2}\gamma^{\epsilon}_{\rho 2}} C_3 F'_{\nu_2}(\gamma^{\epsilon}_{\rho 2}\rho) - \frac{j\omega n \mu_{\phi 2}\epsilon_{z2}}{\epsilon_{\rho 2}{\gamma^{\epsilon}_{\rho 2}}^2 \rho} C_4 G_{\tau_2}(\gamma^{\mu}_{\rho 2}\rho) \right) \cos(n\phi) e^{-\gamma z}, \tag{3.8c}$$

$$E_{\phi 2} = \left(\frac{\gamma n \mu_{z2}}{\mu_{\rho 2}{\gamma^{\mu}_{\rho 2}}^2 \rho} C_3 F_{\nu_2}(\gamma^{\epsilon}_{\rho 2}\rho) + \frac{j\omega \mu_{z2}}{\gamma^{\mu}_{\rho 2}} C_4 G'_{\tau_2}(\gamma^{\mu}_{\rho 2}\rho) \right) \sin(n\phi) e^{-\gamma z}, \tag{3.8d}$$

$$H_{\rho 1} = \left(\frac{-\gamma \mu_{z1}}{\gamma^{\mu}_{\rho 1}} C_2 J'_{\tau_1}(\gamma^{\mu}_{\rho 1}\rho) - \frac{j\omega n \epsilon_{\phi 1}\mu_{z1}}{\mu_{\rho 1}{\gamma^{\mu}_{\rho 1}}^2 \rho} C_1 J_{\nu_1}(\gamma^{\epsilon}_{\rho 1}\rho) \right) \sin(n\phi) e^{-\gamma z}, \tag{3.8e}$$

$$H_{\phi 1} = \left(\frac{\gamma n}{{\gamma^{\epsilon}_{\rho 1}}^2 \rho} C_2 J_{\tau_1}(\gamma^{\mu}_{\rho 1}\rho) - \frac{j\omega \epsilon_{z1}}{\gamma^{\epsilon}_{\rho 1}} C_1 J'_{\nu_1}(\gamma^{\epsilon}_{\rho 1}\rho) \right) \cos(n\phi) e^{-\gamma z}, \tag{3.8f}$$

$$H_{\rho 2} = \left(\frac{-\gamma \mu_{z2}}{\gamma^{\mu}_{\rho 2}} C_4 G'_{\tau_2}(\gamma^{\mu}_{\rho 2}\rho) - \frac{j\omega n \epsilon_{\phi 2}\mu_{z2}}{\mu_{\rho 2}{\gamma^{\mu}_{\rho 2}}^2 \rho} C_3 F_{\nu_2}(\gamma^{\epsilon}_{\rho 2}\rho) \right) \sin(n\phi) e^{-\gamma z}, \tag{3.8g}$$

$$H_{\phi 2} = \left(\frac{\gamma n}{{\gamma^{\epsilon}_{\rho 2}}^2 \rho} C_4 G_{\tau_2}(\gamma^{\mu}_{\rho 2}\rho) - \frac{j\omega \epsilon_{z2}}{\gamma^{\epsilon}_{\rho 2}} C_3 F'_{\nu_2}(\gamma^{\epsilon}_{\rho 2}\rho) \right) \cos(n\phi) e^{-\gamma z}. \tag{3.8h}$$

in which,

$$F'_{\nu_2}(\gamma^{\epsilon}_{\rho 2}\rho) = Y_{\nu_2}(\gamma^{\epsilon}_{\rho 2}b) J'_{\nu_2}(\gamma^{\epsilon}_{\rho 2}\rho) - J_{\nu_2}(\gamma^{\epsilon}_{\rho 2}b) Y'_{\nu_2}(\gamma^{\epsilon}_{\rho 2}\rho), \tag{3.9a}$$

$$G'_{\tau_2}(\gamma^{\mu}_{\rho 2}\rho) = Y'_{\tau_2}(\gamma^{\mu}_{\rho 2}b)J'_{\tau_2}(\gamma^{\mu}_{\rho 2}\rho) - J'_{\tau_2}(\gamma^{\mu}_{\rho 2}b)Y'_{\tau_2}(\gamma^{\mu}_{\rho 2}\rho). \tag{3.9b}$$

The continuity of the tangential electric- and magnetic-field components in Eqs. 3.8a–3.8h at $\rho = a$ relate the coefficients to one another as follows:

$$C_3 = C_1 \frac{J_{\nu_1}(\gamma^{\epsilon}_{\rho 1}a)}{F_{\nu_2}(\gamma^{\epsilon}_{\rho 2}a)}, \quad C_4 = C_2 \frac{J_{\tau_1}(\gamma^{\mu}_{\rho 1}a)}{G_{\tau_2}(\gamma^{\mu}_{\rho 2}a)} \tag{3.10a}$$

$$\frac{C_1}{C_2} = \frac{j\omega n}{\gamma a} \frac{J_{\tau_1}(\gamma^{\mu}_{\rho 1})}{J_{\nu_1}(\gamma^{\epsilon}_{\rho 1})} \left[\frac{\mu_{\phi 2}\epsilon_{z2}}{{\gamma^{\epsilon}_{\rho 2}}^2} - \frac{\mu_{\phi 1}\epsilon_{z1}}{{\gamma^{\epsilon}_{\rho 1}}^2} \right] \left[\frac{\epsilon_{z1}}{\gamma^{\epsilon}_{\rho 1}} \frac{J'_{\nu_1}(\gamma^{\epsilon}_{\rho 1}a)}{J_{\tau_1}(\gamma^{\epsilon}_{\rho 1}a)} - \frac{\epsilon_{z2}}{\gamma^{\epsilon}_{\rho 2}} \frac{F'_{\nu_2}(\gamma^{\epsilon}_{\rho 2}a)}{F_{\nu_2}(\gamma^{\epsilon}_{\rho 2}a)} \right]^{-1} \tag{3.10b}$$

$$\frac{C_2}{C_1} = \frac{j\omega n}{\gamma a} \frac{J_{\nu_1}(\gamma^{\epsilon}_{\rho 1})}{J_{\tau 1}(\gamma^{\mu}_{\rho 1})} \left[\frac{\mu_{z2}\epsilon_{\phi 2}}{{\gamma^{\mu}_{\rho 2}}^2} - \frac{\mu_{z1}\epsilon_{\phi 1}}{{\gamma^{\mu}_{\rho 1}}^2} \right] \left[\frac{\mu_{z1}}{\gamma^{\mu}_{\rho 1}} \frac{J'_{\tau_1}(\gamma^{\mu}_{\rho 1}a)}{J_{\tau_1}(\gamma^{\mu}_{\rho 1}a)} - \frac{\mu_{z2}}{\gamma^{\mu}_{\rho 2}} \frac{G'_{\tau_2}(\gamma^{\mu}_{\rho 2}a)}{G_{\tau_2}(\gamma^{\mu}_{\rho 2}a)} \right]^{-1} \tag{3.10c}$$

where Eq. 3.10b and Eq. 3.10c are implicated in the computation of the EH and HE modes, respectively, which will be discussed shortly.

3.1.2 Dispersion Relation

Before Eqs. 3.2–3.10 can be applied to calculate the total electric and magnetic fields of a given mode at a certain frequency, we need to know the relationship between the mode's axial propagation constant γ and said frequency (i.e., the dispersion relation). The coefficients C_1 and C_2 are eliminated in Eqs. 3.10b and 3.10c to obtain the following dispersion relation:

$$AB = \frac{-{k_0}^2 n^2}{\gamma^2 a^2} \left[\frac{\mu_{\phi 2}\epsilon_{z2}}{{\gamma^{\epsilon}_{\rho 2}}^2} - \frac{\mu_{\phi 1}\epsilon_{z1}}{{\gamma^{\epsilon}_{\rho 1}}^2} \right] \left[\frac{\mu_{z2}\epsilon_{\phi 2}}{{\gamma^{\mu}_{\rho 2}}^2} - \frac{\mu_{z1}\epsilon_{\phi 1}}{{\gamma^{\mu}_{\rho 1}}^2} \right] \tag{3.11a}$$

$$A = \left[\frac{\mu_{z1}}{\gamma^{\mu}_{\rho 1}} \frac{J'_{\tau_1}(\gamma^{\mu}_{\rho 1}a)}{J_{\tau_1}(\gamma^{\mu}_{\rho 1}a)} - \frac{\mu_{z2}}{\gamma^{\mu}_{\rho 2}} \frac{G'_{\tau_2}(\gamma^{\mu}_{\rho 2}a)}{G_{\tau_2}(\gamma^{\mu}_{\rho 2}a)} \right] \tag{3.11b}$$

$$B = \left[\frac{\epsilon_{z1}}{\gamma^{\epsilon}_{\rho 1}} \frac{J'_{\nu_1}(\gamma^{\epsilon}_{\rho 1}a)}{J_{\tau_1}(\gamma^{\epsilon}_{\rho 1}a)} - \frac{\epsilon_{z2}}{\gamma^{\epsilon}_{\rho 2}} \frac{F'_{\nu_2}(\gamma^{\epsilon}_{\rho 2}a)}{F_{\nu_2}(\gamma^{\epsilon}_{\rho 2}a)} \right] \tag{3.11c}$$

Muller's method is used to determine the roots of Eqs. 3.11 in the complex-γ plane and numerically arrive at a set of continuous dispersion curves. Muller's approach is an extension of the secant method in which the complex roots may be found using a quadratic interpolation as opposed to a simpler linear interpolation. Numerical implementation of Muller's method is performed in MATLAB using an iterative approach to find a final complex root γ_i at each evaluated frequency f, where i refers to the index of the iteration. To ensure the method's accuracy, we define the function g as the difference in the left-hand side (LHS) and right-hand side (RHS) of Eq. 3.11a when evaluated at (γ_i, f). In this work, the method is said to be converged when $|g(\gamma_i)| < \sigma$ and $|\gamma_i - \gamma_{i-1}| < \sigma$, where $\sigma = 10^{-8}$. To begin the root-finding algorithm, we supply an initial guess – typically a known cutoff frequency where $\gamma = 0$ – after which the roots are slowly tracked in the complex-γ plane to obtain the full dispersion curve. In instances where there are multiple branches (i.e., solutions), both branches are tracked but only the most relevant curves are shown. To ensure the accuracy of the root solver, a subset of the dispersion curves were verified using COMSOL's eigenmode module.

It should be noted that there exist certain limiting cases in which the modal fields revert to the equivalent transverse modes of the homogeneous case. For $\gamma = 0$ (i.e., at cutoff) and $n = 0$, the RHS of the dispersion relation (Eq. 3.11a) becomes zero and the *HE* and *EH* modes are decoupled and are said revert to *TE* and *TM* modes, respectively. This work maintains a hybrid mode notation even in such instances. In general, this results in the roots of (Eq. 3.11b) and (Eq. 3.11c) determining, respectively, the cutoff frequencies of the *HE* and *EH* modes, and the full dispersion of γ of any azimuthally symmetric ($n = 0$) modes.

It is interesting to note that the Bessel and Neumann functions in Eqs. 3.11b and 3.11c share similar arguments and orders. For instance, the dispersion of *HE* and *EH* modes are strongly impacted by (γ_ρ^μ, ν) and (γ_ρ^ϵ, τ), respectively. At cutoff (i.e., $\gamma = 0$), these expressions reduce to ($\gamma_\rho^\mu = \omega\sqrt{\mu_z \epsilon_\phi}$, $\nu = n\sqrt{\epsilon_\phi/\epsilon_\rho}$) and ($\gamma_\rho^\epsilon = \omega\sqrt{\epsilon_z \mu_\phi}$), $\tau = n\sqrt{\mu_\phi/\mu_\rho}$). Therefore, only a subset of the tensor elements will dictate the cutoffs for each mode, which as will be shown, are closely related to the field polarization of that mode.

For metamaterials with negative permittivity and/or permeability tensor elements, these arguments and orders can assume either extremely large or small complex values that can introduce novel propagation phenomena not usually observed in isotropic dielectric-lined waveguides. In the case of an anisotropic medium with biaxial permittivity and/or permeability (i.e., $\epsilon_{\rho i} \neq \epsilon_{\phi i}$, $\mu_{\rho i} \neq \mu_{\phi i}$), ν_i and τ_i generally assumes complex values. This requires evaluation of Bessel and Neumann functions of complex orders using a series representation based on complex Gamma functions that can be highly inaccurate for extremely complex orders if evaluated using MATLAB, due to its limited precision. Instead, this work employs Mathematica which is capable of accurately obtaining Bessel and Neumann functions for complex orders. The values are then passed to MATLAB with double-point precision.

3.2 Numerical Investigations

In this study, we look at the dispersion of a circular waveguide whose interior surface is coated with a thin anisotropic metamaterial liner. Although Eqs. 3.11 accurately model the dispersion of a generally anisotropic metamaterial-lined circular PEC waveguide, at this stage it is useful to make the following simplifications. The inner core region is rendered as vacuum (i.e., $\bar{\bar{\epsilon}}_1 = \bar{\bar{I}}(1,1,1)\epsilon_0$ and $\bar{\bar{\mu}}_1 = \bar{\bar{I}}(1,1,1)\mu_0$) so as to accommodate applications requiring access to the waveguide's interior. The liner is assigned a uniaxial permittivity $\bar{\bar{\epsilon}}_2 = \bar{\bar{I}}(\epsilon_{t2}, \epsilon_{t2}, \epsilon_{z2})$ with $\epsilon_{z2} = 1$ and a non-magnetic response (i.e, $\bar{\bar{\mu}}_2 = \bar{\bar{I}}(1,1,1)\mu_0$). Recall from the previous discussion that the *EH* mode's cutoffs are a function ϵ_{z2} and the *HE* mode's cutoffs are a function $(\epsilon_{\rho 2}, \epsilon_{\phi 2})$. Therefore, by maintaining that $\epsilon_{\rho 2} = \epsilon_{\phi 2} = \epsilon_{t2} \neq \epsilon_{z2}$, in which ϵ_{t2} shall hereafter be referred to as the transverse permittivity, we retain independent control over the *EH* and *HE* modes' cutoffs, but, as previously noted, significantly ease the theoretical analysis. As will be shown in Chapter 4, practical implementations of metamaterial liners can be successfully modeled using such uniaxial approximations, provided the liner is thin. In these structures, ϵ_{t2} can take on values that are typically associated with dispersive metamaterials (i.e., EPS, ENG, or ENZ). The fully biaxial case (i.e., $\epsilon_{\rho 2} \neq \epsilon_{\phi 2} \neq \epsilon_{z2}$) will be revisited in Sec. 3.2.5 and Chapter 7.

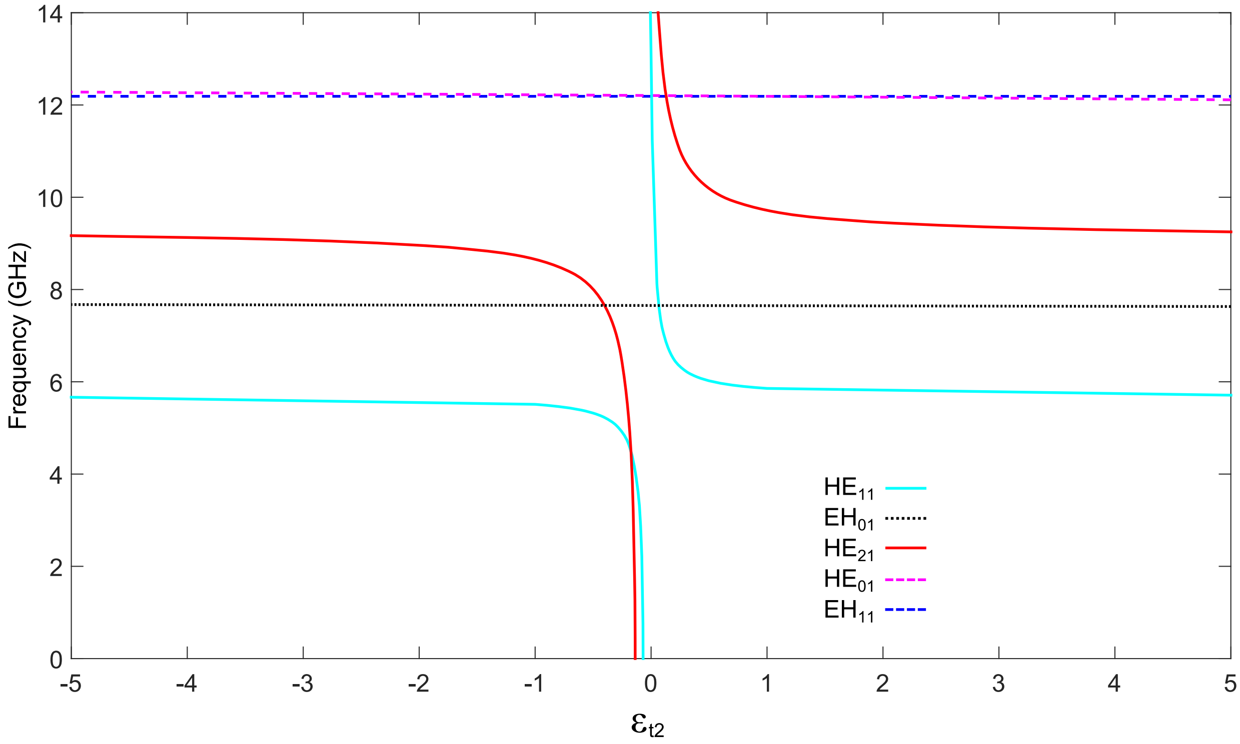

Figure 3.2: Cutoff frequency of the EH_{01}, HE_{01}, EH_{11}, HE_{11} and HE_{21} modes versus the relative permittivity, ϵ_{t2}, of the metamaterial-lined PEC circular waveguide possessing anisotropic permittivity $[\bar{\bar{\epsilon}}_2 = (\epsilon_{t2}, \epsilon_{t2}, 1)\epsilon_0]$.

3.2.1 Cutoff Frequency Dependence on Transverse Permittivity for Thin Uniaxial Liners

Consider a metamaterial-lined waveguide with dimensions $b = 15$mm and $t = 1$mm. The liner is termed 'thin' because it only occupies a small portion (in this case 12.89%) of the total cross-sectional area. Figure 3.2 presents the dependence of the metamaterial-lined circular waveguide's EH_{01}, HE_{01}, EH_{11}, HE_{11} and HE_{21} modes' cutoff frequencies on ϵ_{t2}, which is obtained using the analytically derived dispersion relation (Eqs. 3.11) through enforcing the cutoff condition, $\gamma = 0$. It should be noted that ϵ_{t2} is here an independent variable; i.e., each point on the curve is only concerned with ϵ_{t2} at a single frequency (specifically, cutoff). Figure 3.2 may be employed in choosing the value of permittivity required to achieve a desired cutoff frequency, after which a suitable dispersive permittivity function satisfying this condition may be selected. The case of a realistic, dispersive liner permittivity will be treated in a later discussion.

Under these simplifications, Eqs. 3.11a and 3.11b can be reduced to the following form:

$$A = \left[\frac{J_n'(k_0a)}{J_n(k_0a)} - \frac{1}{\sqrt{\epsilon_{t2}}}\frac{G_n'(k_0\sqrt{\epsilon_{t2}}a)}{G_n(k_0\sqrt{\epsilon_{t2}}a)}\right], \tag{3.12a}$$

$$B = \left[\frac{J_n'(k_0a)}{J_n(k_0a)} - \frac{F_n'(k_0a)}{F_n(k_0a)}\right], \tag{3.12b}$$

The solutions of Eqs. 3.12a and 3.12b when $A = B = 0$ determine the cutoff frequencies of the HE and EH modes, respectively. As previously noted, these equations suggest that ϵ_{t2} strongly affects the cutoff frequency of HE modes and not the EH modes, which can be verified by Fig. 3.2. The EH_{01} and EH_{11}-modes' cutoff frequency remain fixed, and, in general, HE modes vary significantly. The HE_{01}-mode cutoff is degenerate with the EH_{11} mode in a homogenous waveguide, and although not readily apparent, its cutoff marginally varies with ϵ_{t2}. This is consistent with its dominant electric-field polarization whose purely azimuthal orientation (E_ϕ) and radially decaying profile (i.e., $E_\phi \to 0$ as $\rho \to b$) can only weakly interact with the thin liner. However, for $n > 0$ the generally ρ- and ϕ- directed electric fields of the HE_{n1} modes causes their cutoff frequencies to be strongly affected by ϵ_{t2}.

Positive-Permittivity Liner

A well known result of the homogeneously filled dielectric waveguide is that the cutoff frequencies of the TE_{n1} modes scale as the inverse square root of permittivity (see Sec. 2.1), when that permittivity is assumed positive and nondispersive. Even though the metamaterial liner only occupies a small portion of the total cross-section of the waveguide, it is to be expected that a thin EPS liner with permittivity larger than unity marginally lowers the natural cutoff frequency, and conversely, that an EPS liner with permittivity smaller than unity will increase the natural cutoff frequency. Indeed, Fig. 3.2 shows that the HE_{11} and HE_{21} cutoff frequencies are weakly dependent on large positive permittivity values. However, the cutoff frequencies increase dramatically for small positive ENZ values, suggesting that the waveguide is thrust more deeply into cutoff as $\epsilon_{t2} \to 0^+$. In this region, the liner permittivity is characterized by both EPS and ENZ, which we more compactly refer to as ‘epsilon positive and near zero’ (EPNZ).

Negative-Permittivity Liner

The cutoff frequency’s dependence on negative permittivity values is even less intuitive: large, negative liner permittivities in the range shown produce marginally decreased cutoff frequencies; however, as $\epsilon_{t2} \to 0^-$, the cutoff frequency of the HE_{11} and HE_{21} modes are dramatically *lowered*, suggesting that a waveguide lined with a metamaterial possessing such permittivity values may support propagation at very low frequencies, well below its natural cutoff. It is evident from Fig. 3.2 that this regime is characterized by both ENG and ENZ, which we term ‘epsilon negative and near zero’ (ENNZ). In fact for a particular ENNZ permittivity value, each mode’s cutoff frequency can, in theory, be reduced to dc. Of course, this is a pathological case, since it would require an ENZ material at dc and, in any event, could only result in the trivial electrostatic field solution.

Figure. 3.2 shows that, as the azimuthal order increases, the ϵ_{t2} required to reduce the mode’s cutoff frequency to dc tends to increasingly negative values. This results in a crossing of these curves in which, past this point, the HE_{21} mode has a lower cutoff frequency than the HE_{11} mode. This is counter-intuitive to the homogeneous case in which, as n increases, the cutoffs of the HE modes increase. To retain clarity, higher-azimuthal-order HE_{n1} (i.e., $n > 3$) modes are not shown; however, they too follow the same decreasing trend of f_c in the ENNZ range. It should be noted from Eq. 3.12a that all of the HE modes’ cutoff frequencies are independent of the value of ϵ_{z2}, and so these results are shared with the fully isotropic-liner case in which $\epsilon_{z2} = \epsilon_{t2}$. Although not shown, it has been determined that thinner liners require more extreme ENNZ values (i.e., closer to zero) to realize the same reduction in cutoff frequency.

3.2.2 Field-Profile Dependence on Transverse Permittivity for Thin Uniaxial Liners

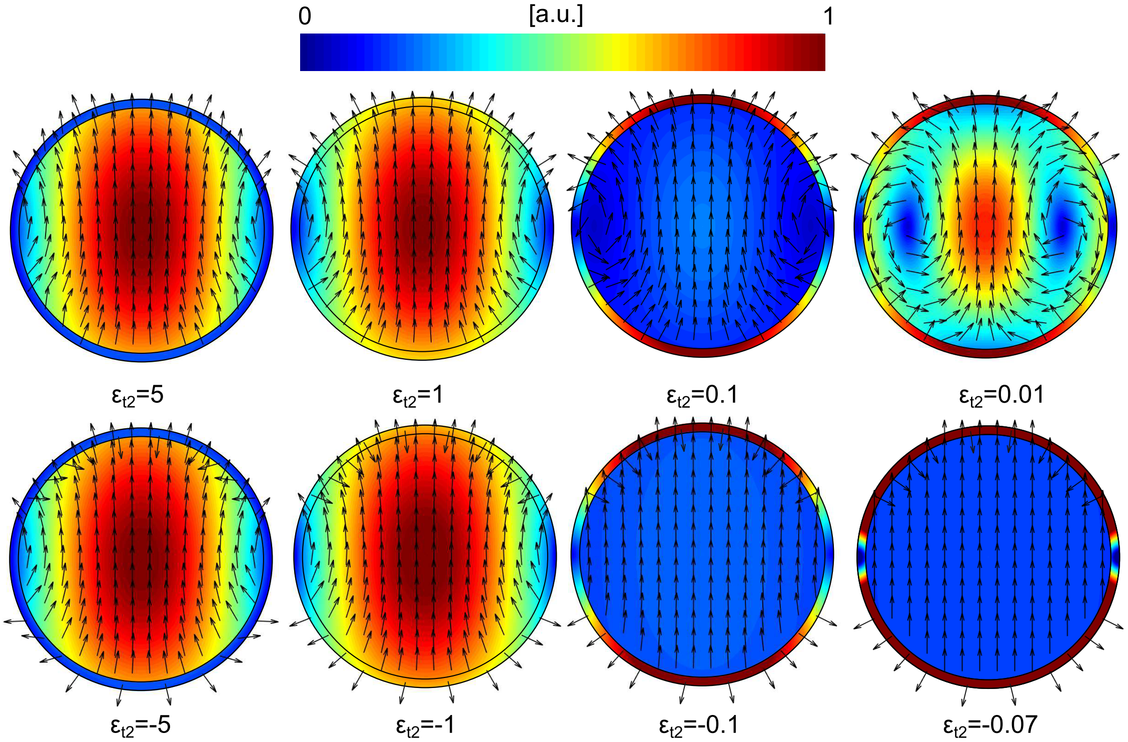

Figure 3.3: The HE_{11} mode's complex electric field magnitudes and vectors of a metamaterial-lined circular PEC waveguide as liner permittivity ϵ_{t2} varies.

Positive-Permittivity Liner

The evolution of the HE_{11} mode's complex electric-field magnitudes and vectors as the liner permittivity (ϵ_{t2}) varies from positive to negative values are shown in Figs. 3.3. The frequencies plotted track the HE_{11} curve in Fig. 3.2, and the fields were calculated from numerical implementation of the theory developed in Sec. 3.1. The expected continuity of the electric-flux density's normal component at the interface between the vacuum and liner region (i.e., $E_{\rho 1} = \epsilon_{t2} E_{\rho 2}$ at $\rho = a$) is readily observed. For $\epsilon_{t2} = 1$, the waveguide is rendered homogeneous and the electric fields revert to the well-known TE_{11} profiles. We note that there exists a significant ρ-directed electric field at the liner-vacuum interface, which suggests ϵ_{t2} (implicated in the continuity condition) will largely impact the HE_{11} fields in the case of radial inhomogeneity. Indeed, for $\epsilon_{t2} = 5$, the inner vacuum region's fields are of higher concentration than the liner region. However, the liner is so thin that a TE_{11}-like field polarization is still evident in the inner vacuum region. As $\epsilon_{t2} \to 0^+$, the fields become increasingly concentrated in the liner region. Recall that the HE_{11} cutoff increases for EPNZ liners, which leads to an increase to the vacuum region's radial phase variation ($\gamma_{\rho 1}^{\epsilon} = \gamma_{\rho 1}^{\mu} = \sqrt{k_0^2 + \gamma^2}$). This is made evident for $\epsilon_{t2} = 0.1$ and 0.01, in which the vectors display additional field-line curvature and the nulls in magnitude appear to push in towards the center.

Negative-Permittivity Liner

For $\epsilon_{t2} = -5$ we observe an electric-field profile that displays a similar degree of contrast between the liner and vacuum regions as the EPS liner of similar absolute magnitude. However, for ENZ liners the orientation of the electric field's normal component reverses across the interface. In the ENNZ regime, two major differences in the field profiles are observed: a decrease in the curvature of field lines in the inner vacuum region and a discontinuous higher concentration of fields in the metamaterial-liner region. The latter property can be explained using the normal electric-field boundary condition which requires that the normal component of the electric field in the liner must increase as $|\epsilon_{t2}| \to 0$. It should be stressed that the field strengths in the vacuum region, although small in comparison to those in the liner, are not negligible. Furthermore, the reduction in frequency suggests a larger operating wavelength inside the vacuum region and, therefore, less field variation. It is interesting to note that as $\epsilon_{t2} \to 0^-$ the electric-field vectors are collimated, resembling those inside a parallel-plate waveguide. Indeed, sharp negative refraction of the electric-field lines at the vacuum-ENNZ interface allows the observed collimation in the vacuum region while still ensuring that the liner fields at the outer PEC boundary are purely normal. It should be noted that the significant concentration of fields in the liner region suggests that the liner's material loss will play a pivotal role in the propagation and attenuation of these frequency-reduced modes.

Although the electric fields for other modes are not shown here, it is simple to deduce their expected profiles with the help of Figs. 3.2-3.3. Modes whose cutoffs do not vary significantly with ϵ_{t2}, such as the EH_{01}, HE_{01}, and EH_{11} modes, will have fields that are either exactly the same or only slightly deviate from the equivalent modal profile in an homogeneous waveguide. However, for HE_{n1} modes ($n > 0$) whose cutoff is a strong function of ϵ_{t2}, the fields will exhibit similar traits as those for the HE_{11} mode (i.e., discontinuous field strengths and increased or decreased field variation), but with additional azimuthal variation.

3.2.3 Asymptotic Analysis of Thin Uniaxial Liners

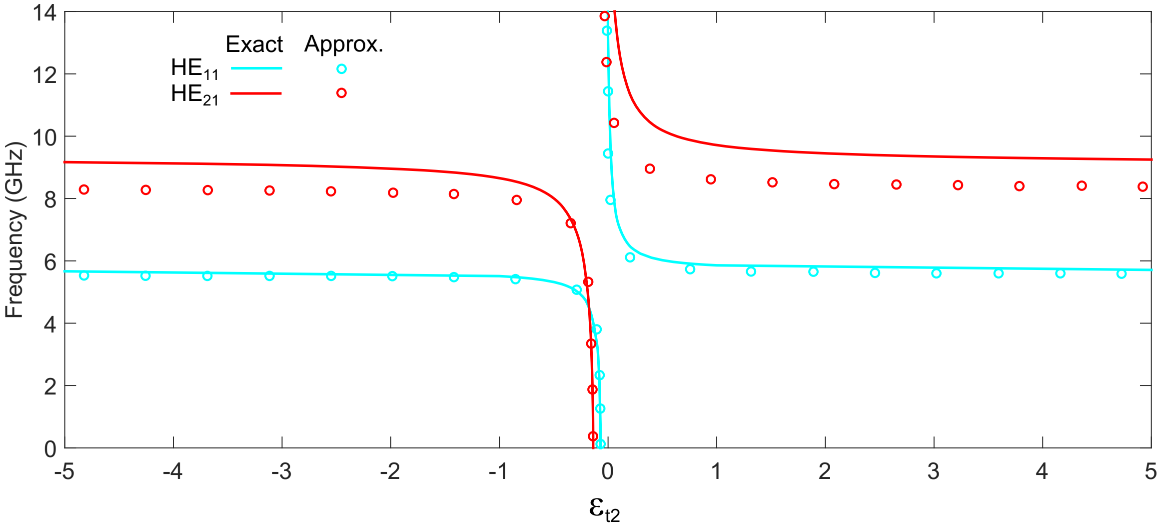

Figure 3.4: The HE_{11}- and HE_{21}-mode cutoff frequency versus liner permittivity ϵ_{t2}. The full and exact dispersion relation (3.11) is compared to the approximate expression (3.13).

Knowing that ENNZ liners reduce the cutoff frequency of the HE_{n1} modes, the decoupled simplified dispersion relation for the HE modes (3.12a) can be simplified further using small-argument approximations to reduce the Bessel and Neumann functions with the goal of obtaining a non-transcendental expression. The two conditions provided by the ENNZ liner, namely that $f_c \to 0$ and $\epsilon_{t2} \to 0^-$, validate the assumption $\{k_0\sqrt{\epsilon_{t2}}a,\ k_0 a\} \to 0$ in this frequency regime. Therefore, a first-order power-series approximation of the Bessel and Neumann functions can be applied to Eq. 3.12a, which yields the result that the cutoff frequency of the HE_{n1} mode is related to the permittivity, ϵ_{t2}, of the liner and thickness,

$t = b - a$, as follows:

$$f_{c,n} = \left(\frac{2c}{2\pi a}\right)\sqrt{\frac{(n^2+n)(1-K)}{n-(n+2)K}} \quad (n > 0), \tag{3.13a}$$

where

$$K = \epsilon_{t2}\left[\frac{1+\left(\frac{b}{a}\right)^{2n}}{1-\left(\frac{b}{a}\right)^{2n}}\right] \quad (n > 0). \tag{3.13b}$$

This simple relationship constitutes a design equation, since it specifies the ENNZ values of ϵ_{t2} necessary to produce a desired $f_{c,n}$, given waveguide dimensions a and b. The particular small-angle approximations that were used in deriving this expression are not valid for $n = 0$, but the cutoffs in such cases are most easily obtained numerically from Eqs. 3.12. In Fig. 3.4, the approximate expression (3.13a) is compared to the exact analytical expression (3.12) for the HE_{11} and HE_{21} modes. It is evident that Eq. 3.13a models the trend over all ϵ_{t2} values and is more accurate for the HE_{11} mode. The asymptotic approximations fail for the generally higher cutoff frequencies of the HE_{21} mode, which results in significant discrepancies. However, Eq. 3.13a is expectedly most accurate in the ENNZ region in which the asymptotic limits are valid and the cutoff frequency is strongly reduced. The margin of error in this expression can be evaluated for the HE_{11} mode by applying the two cases describing an unloaded waveguide: one in which $\epsilon_{t2} \to 1$ and simultaneously $a \to 0$, and the other in which $a \to b$, and comparing the results to the well-known expression for the TE_{11}-mode cutoff frequency of a homogeneously vacuum-filled circular waveguide ($f_{c,unlined} = 1.841c/(2\pi a)$). It is easily shown that the former case produces $f_{c,1} = 2c/(2\pi a)$, whereas the latter case yields $f_{c,1} = 1.633c/(2\pi a)$; the geometric average of these limiting cases is within 2% of $f_{c,unlined}$.

Cutoff Frequency at dc

By setting $K = 1$, Eq. 3.13a captures the behaviour of the cutoff frequency tending to zero in Fig. 3.2, which if applied to Eq. 3.13b yields

$$\epsilon_{t2,max,n} = \frac{1-(b/a)^{2n}}{1+(b/a)^{2n}}. \tag{3.14}$$

In this expression, $\epsilon_{t2,max,n}$ specifies the maximum ENNZ value required of the anisotropic liner to arbitrarily lower the cutoff frequency, which is strictly dependent on the waveguide's and liner's dimensions. Equation 3.14 explicitly captures the action of the ENNZ liners, in that as $a \to b$ (i.e., the liner is of infinitesimal thickness), $\epsilon_{t2,max,n}$, and therefore ϵ_{t2}, must more closely approach zero to restore propagation. It should be noted that Eq. 3.13a become increasingly accurate as $\epsilon_{t2} \to \epsilon_{t2,max,n}$ (hence, $f_c \to 0$). Furthermore, Eq. 3.14 highlights the shift of $\epsilon_{t2,max,n}$ to more negative values as n increases and in the limit $n \to \infty$, $\epsilon_{t2,max,n} \to -1$. This suggests a crowding of higher-azimuthal-order HE_{n1} modes at $\epsilon_{t2} = -1$.

3.2.4 Dispersion Analysis of Thin Uniaxial Liners

HE_{n1} Cutoff Frequencies

In Fig. 3.2, it was implicitly assumed that the liner permittivity required to produce a desired cutoff frequency could actually be achieved at that frequency. However, designing for a particular HE_{n1}-mode cutoff requires the dispersive nature of ϵ_{t2} to be taken into account. Hence, the liner permittivity's dispersion is now described by a Drude model with $\epsilon_{t2}(\omega) = 1 - \omega_{ep}^2/\omega(\omega - j\omega_t)$, in which ω_{ep} is the plasma frequency and ω_t is the damping frequency establishing the liner's loss. This model accurately approximates the complex, dispersive nature of the liner's permittivity over a select frequency range near the plasma frequency. This type of dispersion can be realized by any number of existing metamaterial technologies including wire-grid media [117] or radially arranged transmission-line metamaterials [118], and therefore lends itself readily to practical implementation. To

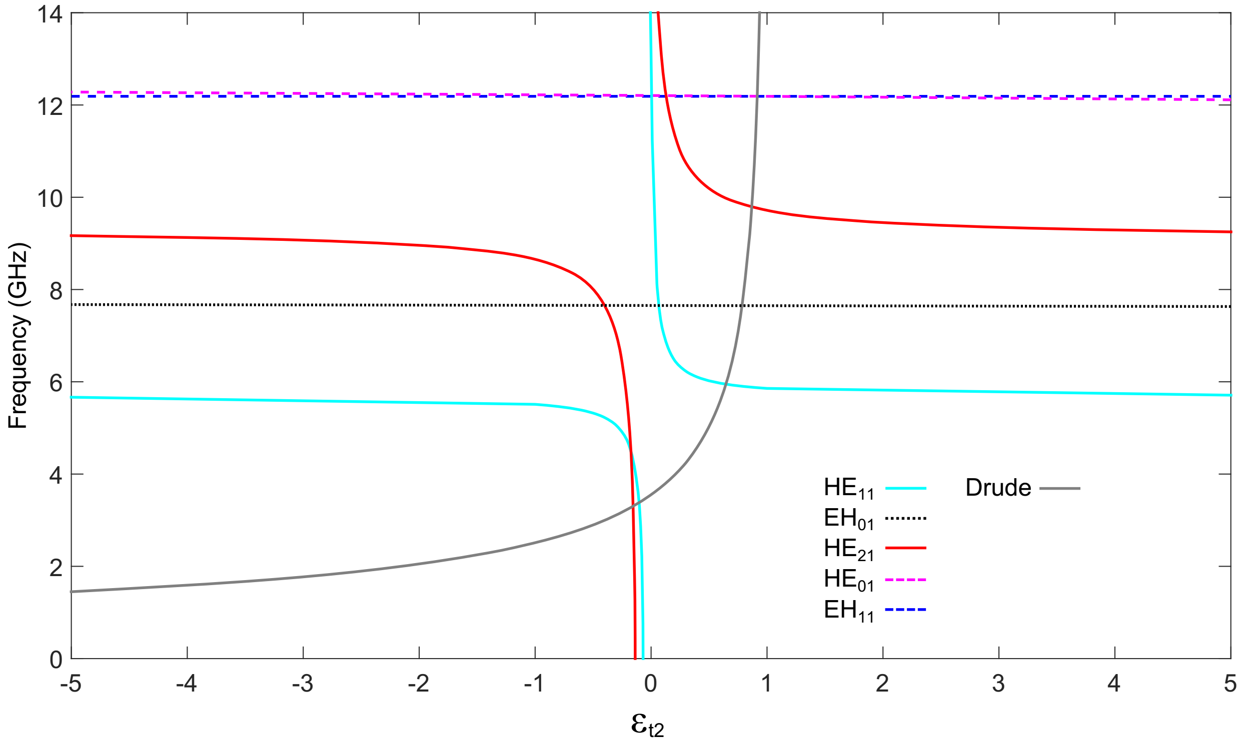

Figure 3.5: Cutoff frequency of the EH_{01}, HE_{01}, EH_{11}, HE_{11} and HE_{21} modes versus the relative permittivity, ϵ_{t2}, of the metamaterial-lined PEC circular waveguide possessing anisotropic permittivity $[\bar{\bar{\epsilon}}_2 = (\epsilon_{t2}, \epsilon_{t2}, 1)\epsilon_0]$. A Drude dispersion profile of $\epsilon_{t2}(\omega)$ which is defined in Sec. 3.2.4 is also shown.

design the metamaterial-lined circular waveguide for a specific HE_{11} cutoff frequency $f_{c,1}$, the waveguide dimensions (outer radius b, inner radius a) are chosen and the corresponding required ϵ_{t2} may be determined from Eq. 3.13a. Thereafter, it remains only to choose an appropriate dispersion model for the liner permittivity such that ϵ_{t2} assumes the needed value at the desired cutoff frequency. Conversely, the dimensions of the waveguide can be determined if given an $\epsilon_{t2}(\omega)$ based on a known metamaterial frequency response.

At this stage, we will focus on the HE_{11} mode and later will generalize the results to higher-order HE_{n1} modes. To aid in the discussion, the EH_{01}, HE_{01}, EH_{11}, HE_{11} and HE_{21} modes cutoff frequency curves are reproduced in Fig. 3.5 with the addition of a Drude-profile curve that will explained shortly. For the chosen waveguide dimensions ($b = 15$mm and $a = 14$mm), it can be observed from Fig. 3.5 that a liner permittivity of $\epsilon_{t2} = -0.09$ will result in a reduced HE_{11} cutoff frequency of $f_{c,1} = 3.381$GHz. To achieve this goal, the

Drude model parameters for the liner are set to $\omega_{ep} = 2\pi \times 3.550\text{GHz}$ and $\omega_t = 2\pi \times 3\text{MHz}$. Superposing the metamaterial's dispersive permittivity (grey curve) on the cutoff-frequency curve, as also shown in Fig. 3.5, two intersections are observed for the HE_{11} mode: the lower-frequency intersection corresponds to the designed HE_{11}-mode cutoff, which, for $\epsilon_{t2} = -0.09$, indeed produces $f_{c,1} = 3.381\text{GHz}$; the higher-frequency intersection occurs at $\epsilon_{t2} = 0.6438$, which results in $f_{c,1} = 5.958\text{GHz}$ – a slight increase as compared to the cutoff frequency of the homogeneously vacuum-filled waveguide. Since each of these intersections corresponds to a cutoff frequency of the HE_{11} mode, it is evident that the lined waveguide supports dual-band operation. These cutoff frequencies may be adjusted simply by modifying the liner's permittivity profile and/or the waveguide's dimensions using Eq. 3.13a and/or a figure equivalent to Fig. 3.5. However, owing to the Drude-like permittivity dispersion, which varies slowly at low frequencies, the lower-frequency cutoff is less sensitive to such modifications than the higher-frequency cutoff; conversely, this also implies that the lower-frequency cutoff is more resistant to tolerances in modeling and/or fabrication.

For the higher order HE_{21} mode, two intersections also occur that correspond to a lower and higher frequency cutoff. As expected, the higher frequency cutoffs in the EPS regime tend to increase as the azimuthal order increases (i.e., $HE_{11} < HE_{21} < HE_{31}...$). However, this does not hold in the ENNZ regime of this particular Drude profile. The frequency-reduced HE_{21} intersection at $\epsilon_{t2} = -0.16$ and $f_c = 3.300\text{GHz}$ is actually lower than that of the HE_{11} mode. In fact, although not shown, the intersections generally tend to decrease as the azimuthal order increases for HE_{n1} modes. In the previous asymptotic study, it was suggested a crowding of higher-azimuthal-order HE_{n1} modes occurs at $\epsilon_{t2} = -1$. Expanding on this, an intersection and corresponding cutoff frequency will then occur for all higher-azimuthal-order HE_{n1} modes. Therefore, there exists the possibility to propagate all HE_{n1} modes in the range $-1 < \epsilon_{t2} < \epsilon_{t2,max,1}$. However, as will be shown in Chapter 5, multimode propagation in this regime can be mitigated through proper design of a practical liner implementation and realistic excitation source.

Full Dispersion of the HE_{11} Mode

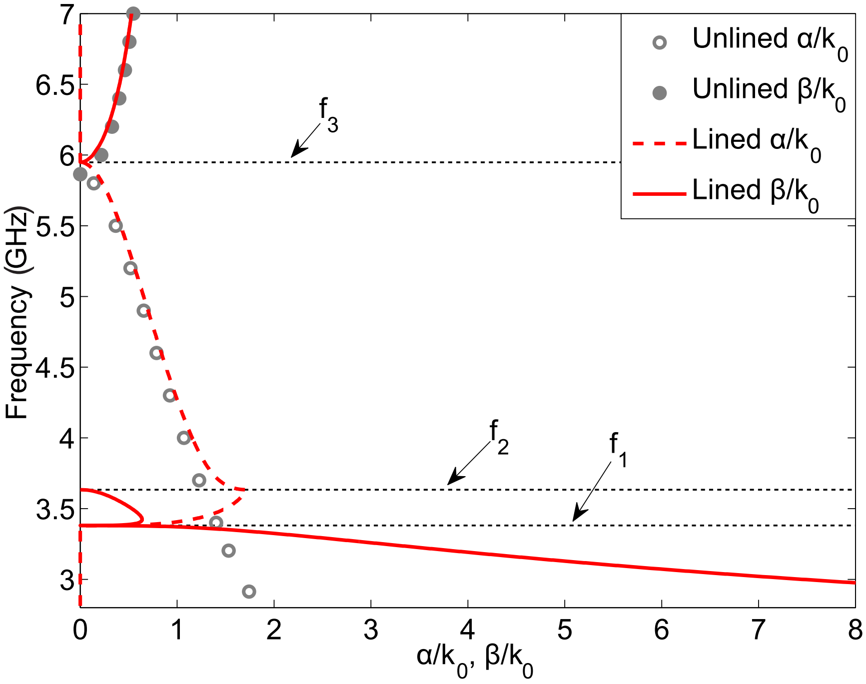

Figure 3.6: Dispersion of α/k_0 and β/k_0 for the metamaterial-lined waveguide's HE_{11} mode as compared to the dispersion of the TE_{11} mode of an unlined waveguide of the same outer radius.

Figure 3.6 presents the HE_{11}-mode dispersion of the lossy metamaterial-lined waveguide as obtained from Eqs. 3.12. Here, the solid and dashed curves, respectively, indicate the normalized propagation constant (β/k_0) and normalized attenuation constant (α/k_0), in which $\gamma = \alpha + j\beta$. For clarity, the dispersion of non-HE_{11} modes have been omitted. Also shown for comparison is the TE_{11}-mode dispersion of a homogeneously vacuum-filled (unlined) waveguide of the same outer dimension, where β/k_0 and α/k_0 are represented using grey solid and open circles, respectively. As suggested from the two intersections in Fig. 3.2, the metamaterial-lined waveguide supports two HE_{11}-mode propagating bands: a forward-wave band near the cutoff of the unlined waveguide, and a new frequency-reduced band well below this cutoff frequency. The frequency-reduced band has two regions of interest: a propagating backward-wave band for $f \leq f_1 = 3.381$GHz and a complex-propagation band for $f_1 < f < f_2 = 3.644$GHz. Backward-wave propagation has previously been observed in inhomogeneous waveguides, albeit with conventional positive-valued dielectrics, and resulted in only a marginal reduction in cutoff frequency [119]. The use of ENNZ materials in the present work suggests that backward-wave propagation can be achieved at dramatically reduced frequencies. As will be shown in the next chapter, the complex-propagation band does not allow for propagation of real power, a fact that may be attributed to the simultaneous existence of it's complex conjugate, which is excited equally in this region [38]. The stopband in the region $f_2 \leq f \leq f_3 = 5.958\text{GHz}$ is explained by the fact that the metamaterial liner exhibits positive permittivities approaching unity as frequency is increased; as a result, propagation in the lined waveguide at these frequencies strongly resembles that in the unlined waveguide under its natural TE_{11} cutoff. Accordingly, the forward-wave band in the region $f \geq f_3$ is also very similar in curvature and shape to that of the unlined waveguide. These results affirm that the metamaterial liner only significantly alters the propagation characteristics of the waveguide in the ENNZ frequency region.

Non-$\boldsymbol{HE}_{n1}$ Cutoff Frequencies and Dispersion

Figure 3.5 also indicates equivalent cutoff frequency intersections for the EH_{01}, EH_{11}, and HE_{01} modes. Due to the weak dependence of these modes' cutoffs on ϵ_{t2}, Fig. 3.5 suggests each mode has only a single higher-frequency intersection which slightly deviates from the natural cutoffs of a homogeneous vacuum-filled waveguide. However, for the EH_{01} mode, $\epsilon_{t2}(f_{ep}) = 0$ satisfies Eq. 3.12b; this corresponds to the intersection of the vertical axis with $\epsilon_{t2}(f)$ in Fig. 3.5. The resulting important implication is the cutoff of this frequency-reduced EH_{01} mode occurs precisely at the Drude plasma frequency of ϵ_{t2}. Strictly speaking, only $\epsilon_{\rho 2} = 0$ is required to introduce a EH_{01} cutoff; which results in $\epsilon_{t2} = 0$ for the uniaxial assumption. This condition is independent of the dimensions and remaining material parameters, and occurs in addition to its high-frequency natural cutoff.

To gain insight into the reason the $\epsilon_{t2} = 0$ solution is not shown in Fig. 3.5 recall that those cutoff frequency curves were calculated from Eqs. 3.12, which were obtained under the

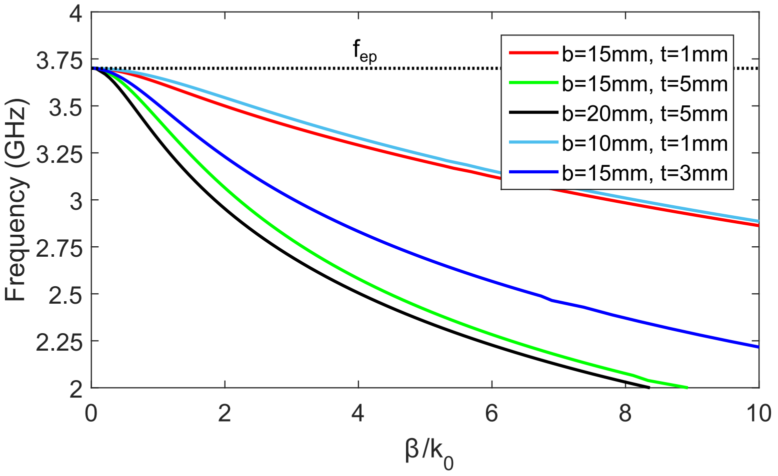

Figure 3.7: Dispersion of the frequency-reduced EH_{01} mode for a metamaterial-lined PEC circular waveguide possessing anisotropic permittivity $[\bar{\bar{\epsilon}}_2 = (\epsilon_{t2}, \epsilon_{t2}, 1)\epsilon_0]$ with a fixed Drude dispersion profile.

assumption $\gamma = 0$. If we relax this condition and let $\gamma \neq 0$ and $n = 0$, Eq. 3.11c reduces to

$$\frac{1}{\sqrt{\gamma^2 + k_0^2}} \frac{J_0'(\sqrt{\gamma^2 + k_0^2}a)}{J_0(\sqrt{\gamma^2 + k_0^2}a)} - \frac{1}{\sqrt{\gamma^2/\epsilon_{t2} + k_0^2}} \frac{F_0'(\sqrt{\gamma^2/\epsilon_{t2} + k_0^2}a)}{F_0(\sqrt{\gamma^2/\epsilon_{t2} + k_0^2}a)} = 0. \tag{3.15}$$

Whereas ϵ_{t2} is not implicated in Eq. 3.12b to determine the EH mode's cutoffs, by allowing $\gamma \neq 0$ here we observe multiple instances of the ratio γ/ϵ_{t2} in Eq. 3.15. There exist two cases for this ratio; a) $\{\gamma \to 0,\ \epsilon_{t2} \neq 0\}$ which implies $\gamma/\epsilon_{t2} = 0$ and Eq. 3.15 reduces back to Eq. 3.12b and b) $\{\gamma \to 0,\ \epsilon_{t2} \to 0\}$ which implies $\gamma/\epsilon_{t2} \neq 0$. For the latter case, evaluation of this limit is no simple task and is best determined numerically. Numerical studies revealed the γ/ϵ_{t2} generally tends to large values such that the solution $f = f_{ep}$ and $\epsilon_{t2} = 0$ always satisfies Eq. 3.15 irrespective of the value b, a, and the remaining material parameters.

To further validate this, Fig. 3.7 presents the dispersion curves for the EH_{01} mode for metamaterial-lined waveguides of different dimensions but sharing the same uniaxial liner permittivity $\bar{\bar{\epsilon}}_2 = \bar{\bar{I}}(\epsilon_{t2}, \epsilon_{t2}, 1)\epsilon_0$ in which ϵ_{t2} obeys a fixed Lorentz profile with $f_{ep} = 3.7$GHz and $f_t = 3$MHz. As is evident, each waveguide exhibits the same EH_{01} cutoff frequency at f_{ep}, below which it exhibits a backward-wave propagating band that generally varies between each case.

Although this study suggests that all higher-order EH modes will require evaluation of

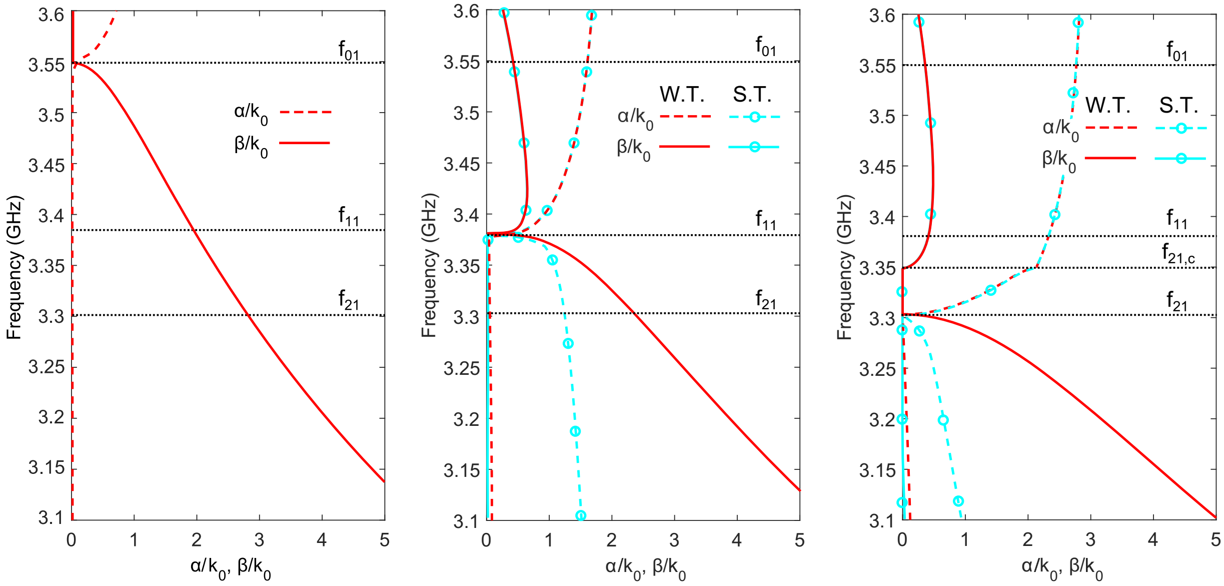

(a) (b) (c)

Figure 3.8: Dispersion of α/k_0 and β/k_0 for the following modes of the metamaterial-lined waveguide: (a) EH_{01}, (b) HE_{11} and (c) HE_{21} waveguide-type (W.T.) and surface-type (S.T.).

the special case $\gamma/\epsilon_{t2} \neq 0$, this is not the case for $n \neq 0$, in which the modes are hybrid. Their coupled full dispersion relation (Eqs. 3.11) must now be considered and the special functions F'_{τ_2} and F_{τ_2} take a vastly different form for $\tau_2 \neq 0$.

Dispersion of Frequency-Reduced Modes

We now focus on the dispersion of frequency-reduced EH_{01}, HE_{11}, and HE_{21} modes in Figs. 3.8(a), 3.8(b), and 3.8(c), respectively. The frequency-reduced EH_{01} mode is described by a backward-wave band and, as mentioned earlier, a cutoff frequency $f_{01} = f_{ep}$. The metamaterial-lined waveguide supports multiple highly dispersive frequency-reduced HE_{n1} propagating bands for $n > 0$. In addition to the waveguide-type (W.T.) HE_{n1} modes, there also exist corresponding surface-type (S.T.) modes that are bound to the metamaterial-vacuum interface [120]. These may be differentiated by their radial wavenumbers, $\gamma_{\rho 1}$. The waveguide-type modes exhibit a standing-wave distribution in the transverse plane due to an imaginary (i.e., propagating) $\gamma_{\rho 1}$. The surface-type modes, on the other hand, decay evanescently into vacuum from the interface, and are characterized by real (i.e., attenuating) values of $\gamma_{\rho 1}$. In the observed range, the dispersion relation (3.12) reveals the HE_{11} mode's waveguide-type (red curves) and surface-type (teal circle curves) solutions, each exhibiting complex-mode regions for $f > f_{11} = 3.381\text{GHz}$. Near f_{11} both solutions have comparable α and β values. This creates the potential for the backward-wave and complex bands to couple, and allows for regions of forward-wave propagation near cutoff. It is found that this effect may be mitigated by reducing the liner's thickness, increasing the degree of miniaturization, and choosing a lower-loss metamaterial. For this particular thin liner, the coupling of the surface-type and waveguide-type modes manifests as a region of nearly flat dispersion near f_{11}. Below f_{11}, the two solutions rapidly become distinct, such that one can be classified as an evanescent band and another as a backward-wave propagating band. The HE_{21} mode also exhibits waveguide-type and surface-type modes which diverge below f_{21}. However, there is an evanescent region for $f_{21} < f < f_{21,c}$ that separates the complex and backward-wave regions and prevents their coupling. It is interesting to note that despite the concentration of fields in the liner region, $\alpha << \beta$ in each frequency-reduced mode's backward-wave regime.

Comparison of Figs. 3.8(a)–3.8(c) reveal multiple regions of multimode propagation. For $f_{01} < f < f_{11}$, the EH_{01} mode propagates and the HE_{11} and HE_{21} modes are cutoff. This range of frequencies is termed the monomodal EH_{01} bandwidth, as there exist no other modes that can copropagate. This is a unique feature of ENNZ liners as the TM_{01} mode always copropagates with the TE_{11} mode in waveguides homogeneously filled with a positive permittivity and isotropic dielectric material. The monomodal EH_{01} bandwidth may be controlled through careful engineering of the waveguide's physical dimensions and anisotropic material parameters. For $f_{11} < f < f_{21}$, both the EH_{01} and HE_{11} modes propagate and the HE_{21} mode is cutoff. Due to the dominant backward-wave dispersion of these frequency-reduced modes, we can generalize this observation for all frequency reduced HE_{n1} modes: above f_{n1} the EH_{01}, $HE_{n-1,1}$, $HE_{n-2,1}$, $HE_{n-3,1}$... modes propagate and the HE_{n1} is cutoff. The overlapping dispersion of these modes signifies that using practical excitation sources

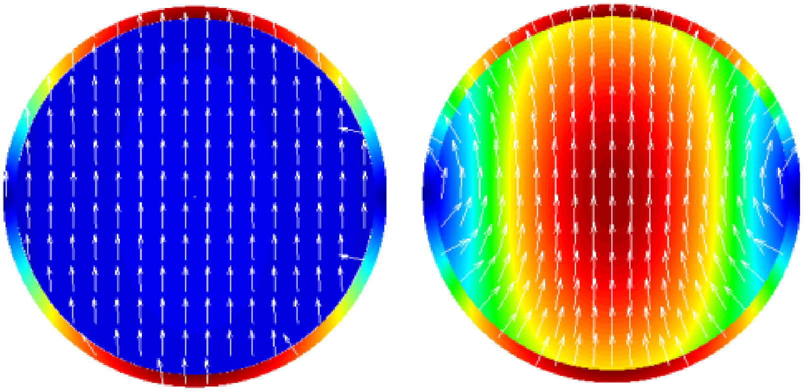

(a) (b)

Figure 3.9: The normalized complex electric-field magnitude and vectors in the transverse plane obtained from the theory for the lined waveguide at (a) $f_3 = 5.958\text{GHz}$ and (b) $f_1 = 3.381\text{GHz}$, corresponding to the respective cutoff frequencies of the forward-wave and backward-wave bands.

requires that all reduced modes be considered in the design process.

The Dispersive Liner's HE_{11}-Mode Field Profiles

The complex electric-field magnitudes, obtained using numerical implementation of the theory developed in Sec. 3.1, are shown for both the lined waveguide's forward-wave band (Fig. 3.9(a)) and its backward-wave band (Fig. 3.9(b)), at their respective cutoff frequencies. As expected, the forward-wave HE_{11}-mode cutoff exhibits fields very similar to those at the TE_{11}-mode cutoff of an unlined waveguide. However, in the ENNZ regime, two major differences in the field profiles are observed: a decrease in the curvature of field lines in the inner vacuum region and a discontinuous higher concentration of fields in the metamaterial-liner region. The latter property can be explained using the normal electric-field boundary condition which requires that the normal component in the liner must increase as $|\epsilon_{r2}| \rightarrow 0$. It should be stressed that the field strengths in the vacuum region, although small in comparison to those in the liner, are not negligible. Furthermore, the reduction in frequency suggests a larger operating wavelength inside the vacuum region and, therefore, less field variation. It is interesting to note that as $\epsilon_{r2} \rightarrow 0^-$ the electric-field vectors are collimated, resembling those inside a parallel-plate waveguide. Indeed, sharp negative refraction of the electric-field lines at the vacuum-ENNZ interface allows the observed collimation in the vacuum region while still ensuring that the liner fields at the outer PEC boundary are purely normal.

Coupling of Waveguide-Type and Surface-Type Modes

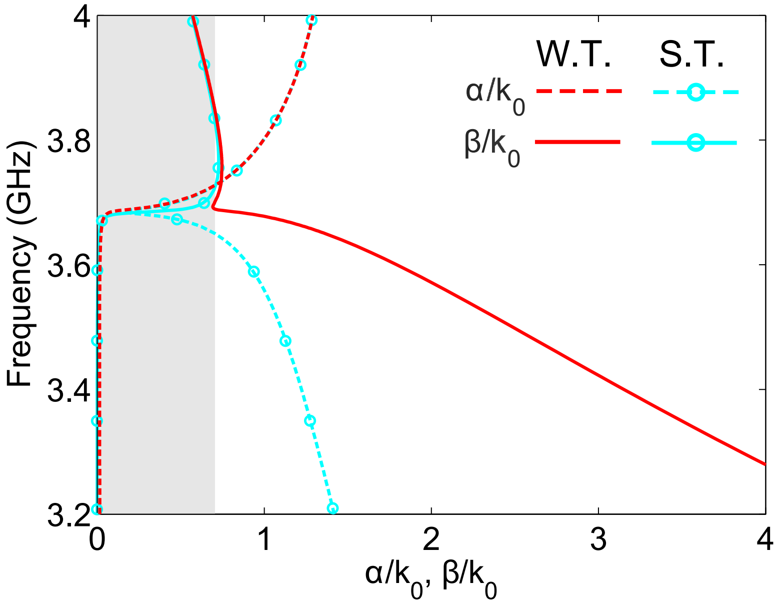

Figure 3.10: Dispersion of α/k_0 and β/k_0 for a metamaterial-lined waveguide's [$b = 15$mm, $b - a = 2.3$mm, $\bar{\bar{\epsilon}}_2 = (\epsilon_{t2}(f), \epsilon_{t2}(f), 1))$, $f_{ep} = 3.7$GHz] HE_{11} waveguide-type (W.T.) and surface-type (S.T.) modes.

To better illustrate the coupling of the HE_{11} mode's backward-wave and complex bands, we increase the liner thickness to $b - a = 2.3$mm and increase ϵ_{t2}'s plasma frequency to $f_{ep} = 3.7$GHz. All other material parameters are maintained from the previous study. Fig. 3.10 presents the dispersion of the frequency-reduced HE_{11} mode, in which all other frequency-reduced modes are not shown. There now exists an observable region of forward-wave propagation in the grey-shaded region, but the band is predominantly backward-wave outside it.

3.2.5 Dispersion of Anisotropic Versus Isotropic Thin Metamaterial Liners

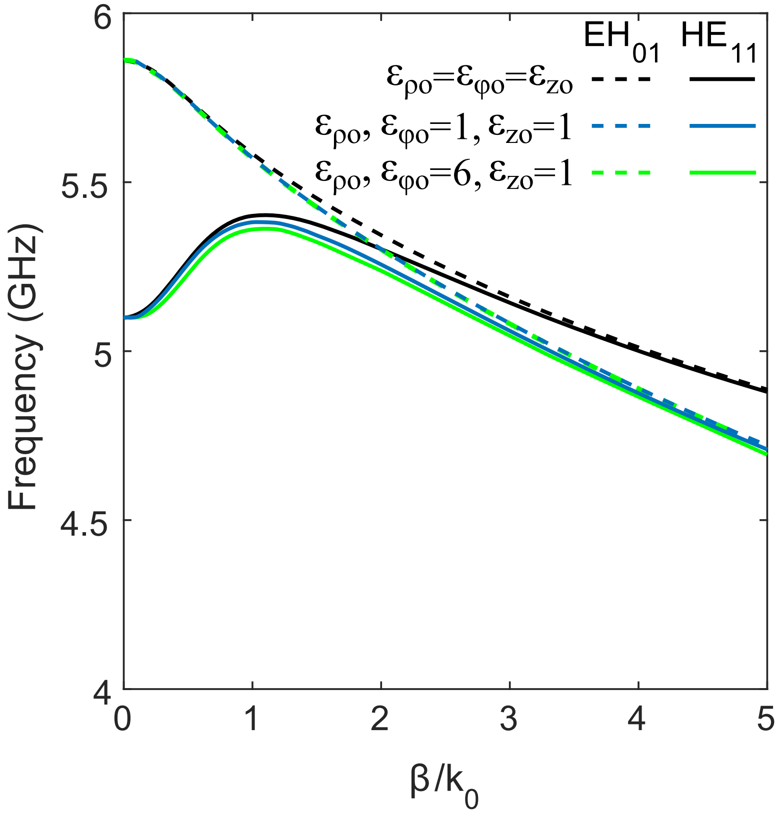

Figure 3.11: Dispersion of the frequency-reduced EH_{01} and HE_{11} modes for a thin liner ($b = 15$mm, $b - a = 1$mm) possessing particular isotropic ($\epsilon_{\rho 2} = \epsilon_{\phi 2} = \epsilon_{z2}$) and anisotropic ($\epsilon_{\rho 2} \neq \epsilon_{\phi 2}$, $\epsilon_{z2} = 1$) permittivities and an inner vacuum region ($\bar{\bar{\epsilon}}_1 = 1, 1, 1\epsilon_0$).

It has been shown that a liner with anisotropic permittivity whose transverse components (i.e., ϵ_ρ and ϵ_ϕ) take on ENNZ values is sufficient to effect these frequency-reduced cutoffs. In fact, provided the liner is sufficiently thin, numerical evaluation of Eq. (3.11b) reveals that only the ρ-component is required to be ENNZ. To illustrate this, Fig. 3.11 investigates the dispersion of the frequency-reduced EH_{01} and HE_{11} modes for a representative metamaterial-lined circular waveguide of radius $b = 15$mm with a thin liner region of thickness $b - a = 1$mm and an inner vacuum region ($\bar{\bar{\epsilon}}_1 = (1, 1, 1)\epsilon_0$). Three cases of permittivity tensors are examined: an isotropic permittivity with $\bar{\bar{\epsilon}}_2 = \bar{\bar{I}}(\epsilon_{\rho 2}, \epsilon_{\rho 2}, \epsilon_{\rho 2})\epsilon_0$, and two anisotropic permittivities with $\bar{\bar{\epsilon}}_2 = \bar{\bar{I}}(\epsilon_{\rho 2}, 1, 1)\epsilon_0$ and $\bar{\bar{\epsilon}}_2 = \bar{\bar{I}}(\epsilon_{\rho 2}, 6, 1)\epsilon_0$. In all cases, $\epsilon_{\rho o}$ follows a Drude

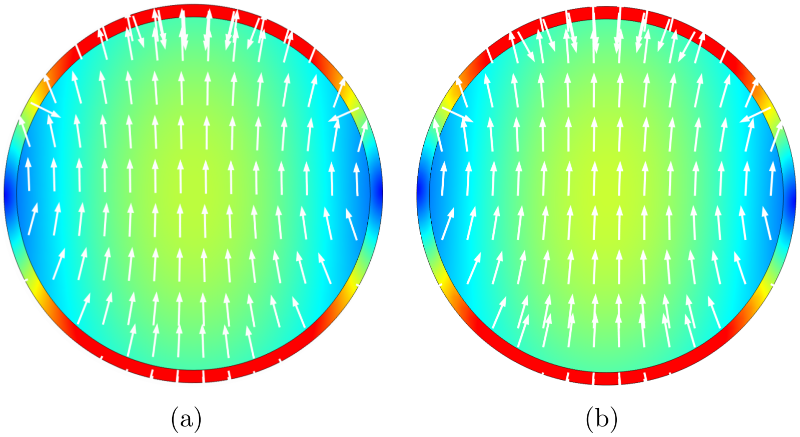
(a) (b)

Figure 3.12: The frequency-reduced HE_{11} mode's electric-field magnitude and vectors for an effective-medium liner with an (a) isotropic and (b) anisotropic (with $\epsilon_{\phi 2} = 1$) permittivity.

profile defined by $\epsilon_{\rho 2} = 1 - \omega_{ep}^2/[\omega(\omega - j\omega_t)]$ with a plasma frequency $\omega_{ep} = 2\pi \times 5.86$GHz and damping frequency $\omega_t = 2\pi \times 3$MHz. $\epsilon_{\phi 2}$ differs between the biaxial cases, but ϵ_{z2} is made to be unity.

For all of the examined permittivity tensors, the EH_{01} mode's cutoff frequency occurs at the liner's plasma frequency ($f = 5.86$GHz) [121]. On the other hand, the near-coincidence of the HE_{11} cutoffs at 5.10GHz for the various tensor cases is not a general result for liners of arbitrary thickness, and instead stems from the use of a thin liner in this example. Importantly, these unchanging cutoffs demonstrates (at last) that an ENNZ $\epsilon_{\rho 2}$ is sufficient to produce these frequency-reduced modes. Observation of the HE_{11} mode's electric-field magnitudes and vectors for the isotropic and anisotropic liners (the latter shown for $\epsilon_{\phi 2} = 1$, although the results are identical for $\epsilon_{\phi 2} = 6$) in Figs. 3.12(a)-3.12(a) reveal very similar distributions with a weak concentration in the inner vacuum region and a discontinuously strong concentration in the liner region. This insensitivity of the fields and miniaturization to the values of $\epsilon_{\phi 2}$ and ϵ_{z2} when the liners are thin greatly eases their design and practical implementation, which will be shortly demonstrated in the next chapter for the printed-circuit implementation of ENNZ liners.

Chapter 4

The Realization of Anisotropic Metamaterial Liners

The numerical investigation of anisotropic metamaterial-lined waveguides in Ch. 3 revealed that the frequency-reduced HE_{11} mode's passband occurs when ϵ_{t2} achieves ENNZ values. The goal of this chapter is to realize this ENNZ condition using practical metamaterial technologies that can be easily fabricated and placed into miniaturized circular waveguides. This work realizes this ENNZ condition through the plasmonic-like interaction of arrays of thin wires [21].

4.1 Thin-Wire Media

4.1.1 Linear Arrangements

Metallic thin-wire media present a Drude-like permittivity dispersion for electric fields aligned parallel to the thin-wire axes [21], and are a cost-effective realization of low-frequency negative-permittivity artificial dielectrics. They may also be easily fabricated using traditional printed-circuit techniques. For an array of thin wires whose axes coincide with the z direction, the anisotropic permittivity may be given by $\bar{\bar{\epsilon}} = \bar{\bar{I}}(1, 1, \epsilon_z)\epsilon_0$, where ϵ_z's dispersive profile can be approximated (to first order) as:

$$\epsilon_z = 1 - \omega_{ep}^2/\omega^2, \tag{4.1a}$$

where,

$$\omega_{ep}^2 = \frac{2\pi c_0^2}{a^2 ln(a/r)} \tag{4.1b}$$

is the plasma frequency of the corresponding effective medium, a is the spacing (or periodicity) between wires, c_0 is the speed of light in vacuum, and r is the wire's radius [21].

Due to the inherently weak loading from the thin wire's parasitic inductance, the unit-cell periodicity is typically $\lambda/5$ to $\lambda/8$ in the usable negative-permittivity range. This puts thin wires at a disadvantage in applications requiring even moderate levels of miniaturization, in which the full thin-wire array must be a small fraction of a wavelength. For instance, the metamaterial liner described in the previous sections has a thickness of approximately $\lambda_0/90$, where λ_0 is the wavelength in free space. Nevertheless, through loading the wires with discrete inductors, it is possible to lower their plasma frequency, enabling deeply subwavelength operation [122].

4.1.2 Cylindrical Arrangements

To realize a negative transverse permittivity using thin-wire media requires two orthogonal linear arrays of wires to be aligned with the waveguide's transverse electric-field components. While rectangular thin-wire grids have been used to improve the bandwidth and/or gain of rectangular and conical horn antennas [12, 13], the circular waveguide suggests the use of a cylindrical arrangement. Figure 4.1(a) presents a depiction of a vacuum-filled circular waveguide lined by a thin-wire medium. To interact with the ρ- and ϕ-directed fields of the circular waveguide, this work employs a connected orthogonal grid of azimuthally and radially directed PEC thin wires. No z-directed wires are employed, so as to avoid the propagation

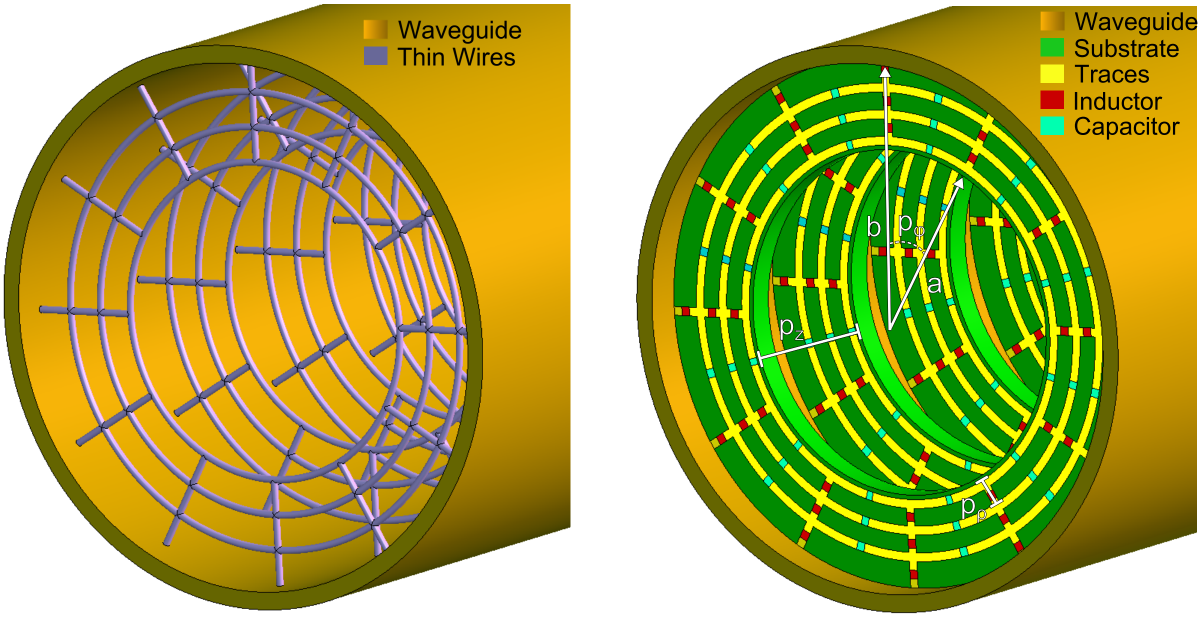

(a) (b)

Figure 4.1: A depiction of a circular waveguide loaded by multiple layers of a cylindrical arrangement of (a) thin wires and (b) reactively loaded copper traces printed on a substrate.

of TEM modes supported between non-connected longitudinally directed conductors [123].

As an instructive starting point, the cylindrically arranged thin-wire liner in Fig. 4.1(a) is modeled as a linear thin-wire array. Of course, this model removes any angular and radial variation in the spacing between wires for their cylindrical arrangement and assumes that fields polarized perpendicular to the wire do not influence that wire's contribution to the permittivity. This allows for a first-order approximation of the cylindrical thin-wire array's ϵ_{t2} using Eq. 4.1.

It was established in Ch. 3 that a metamaterial-lined circular waveguide of radius $b = 15\text{mm}$ and liner thickness $t = 1\text{mm}$, possessing an ϵ_{t2} Drude profile with a plasma frequency of $\omega_{ep} = 2\pi \times 3.550\text{GHz}$, will introduce a suite of frequency-reduced modes. Equation 4.1 suggests that to achieve this plasma frequency with the thin-wire grid of wire radius $r = 100\mu\text{m}$ would require a unit-cell spacing $a = 15.06\text{mm}$. Therefore, in the circular waveguide of radius $b = 15\text{mm}$, only two unit cells would fit in its radial direction and the liner would effectively fill the entire waveguide environment. Although this is a highly simplified argument, it serves the purpose of highlighting that wires alone cannot strongly load the waveguide environment, and do not exhibit the strong metamaterial response needed for miniaturization. This can also be attributed to their finite length in ρ and ϕ, along with the additional boundary conditions imposed at the PEC and vacuum boundary [124]. In order to restore their negative-permittivity response at low frequencies, the wires must be loaded by discrete inductive elements. This will allow for the liner to remain thin while still offering useful miniaturization of the circular waveguide.

Whereas previous works employ thin-wire grids suspended in a vacuum environment [12, 13], a thin copper trace printed on a low-loss substrate presents itself as a much simpler implementation to fabricate. By choosing a substrate with a low bulk permittivity, we can minimize the impact the substrate has on the dispersion of the liner. Figure 4.1(b) presents a printed-circuit-board (PCB) implementation of a single layer of the thin-wire metamaterial liner, which consists of an orthogonal grid of azimuthally and radially directed thin copper traces. The metamaterial unit cell has thickness p_ρ in the ρ direction and period p_ϕ in the ϕ directions. Each layer is stacked axially with a periodicity p_z. Inductors of value L_0 load the ρ-directed traces to engineer ϵ_{t2} to achieve the negative-permittivity frequency response needed to effect miniaturization. Capacitive gaps modeled by a discrete capacitance C_0 are placed symmetrically between each ρ-directed inductor in the ϕ-directed traces, the purpose of which will be discussed in further detail shortly.

4.2 General Dispersion Analysis

Before an in-depth analysis of the ENNZ liner's PCB implementation is presented, it is instructive to investigate the dispersion of modes for a representative design. Dispersion curves are obtained using the full-wave simulation software HFSS, whose eigenmode module is a popular tool in the characterization of RF metamaterials [56]. To model the PCB implementation shown in Fig. 4.1(b), a single layer is placed within a vacuum-filled cylindrical

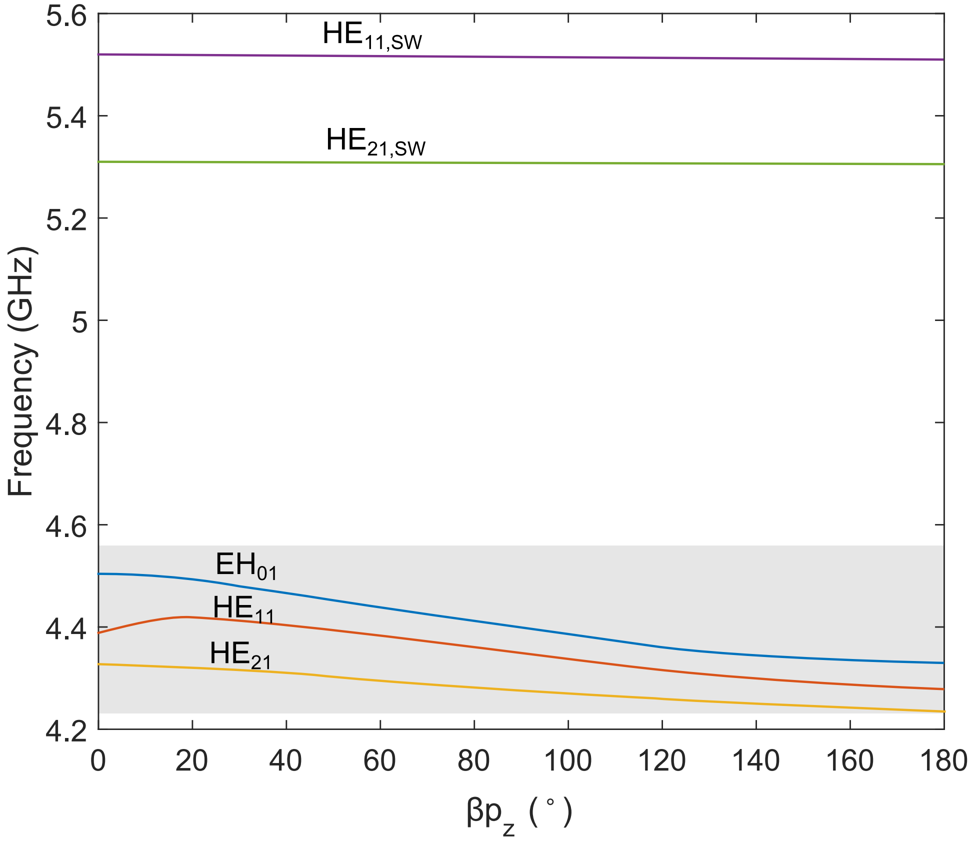

Figure 4.2: Dispersion of the frequency-reduced EH_{01}, HE_{11} and HE_{21} modes in a circular waveguide lined by the printed-circuit realization of an metamaterial liner shown in Fig. 4.1(b). The standing-wave (SW) $HE_{11,SW}$ and $HE_{21,SW}$ modes arise from unwanted azimuthal resonances whereas the modes located in the grey shaded area are due to the liner's ENNZ response.

simulation domain of radius b and length p_z that is assigned a PEC boundary condition on its circumferential surface. The single layer is rendered infinite in the eigenmode module by assigning periodic boundary conditions on the front and rear circular surfaces of the simulation domain. Due to an inherent limitation in the eigenmode solution process, only propagating modes (i.e. $\gamma \approx j\beta$) may be found; therefore, only the backward-wave and forward-wave (and not the complex) modes can be determined using this method.

Figures 4.2 present the dispersion of the modes for a representative design with 0.3mm-wide copper traces printed on a substrate with height 1.5mm and bulk permittivity $\epsilon = 2$, and with geometric parameters: $b = 15.0$mm, $a = 11.4$mm, $L_0 = 4.0$nH, $C_0 = 0.05$pF, $p_\phi = 45°$, $p_z = 4$mm, and 3 periods in ρ with $p_\rho = 1.2$mm. This discussion will focus on the dispersion

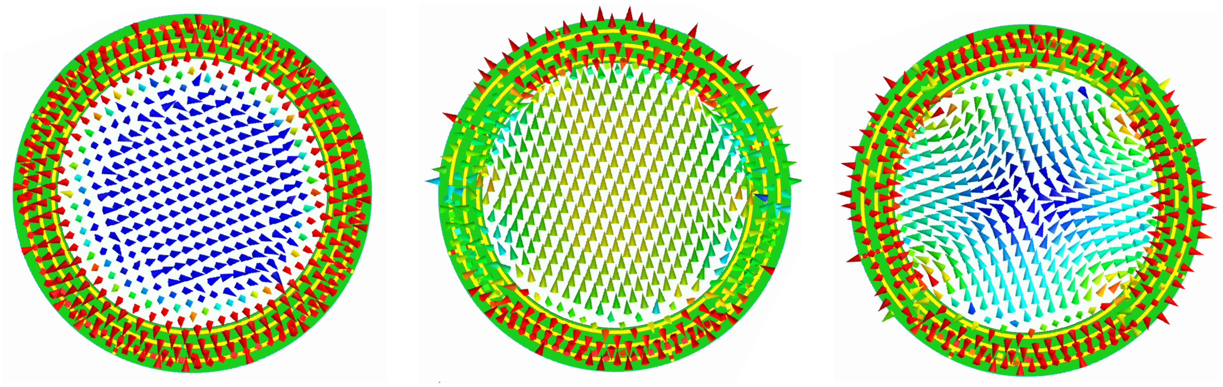

(a) (b) (c)

Figure 4.3: Electric-field vectors of the frequency-reduced (a) EH_{01}, (b) HE_{11} and (c) HE_{21} modes in a circular waveguide lined by the printed-circuit implementation.

of the EH_{01}, HE_{11}, and HE_{21} modes at frequencies below the fundamental TE_{11} mode cutoff (5.86GHz) in a equivalently sized vacuum-filled circular waveguide. As desired, a number of frequency-reduced modes are supported. In the highlighted region, the EH_{01}, HE_{11} and HE_{21} modes each exhibit a backward-wave propagating band with cutoff frequencies of 4.51GHz, 4.39GHz, and 4.30GHz, respectively. The electric-field vectors for these modes are shown in Figs. 4.3(a)–4.3(c). Despite the PCB liner being considerably thicker, the field profiles of the frequency-reduced modes in the printed-circuit realization are very similar to those of the effective-medium ENNZ liner. This is quite clear in comparisons to the field profile shown in Fig. 3.9(b) for the effective-medium model's frequency-reduced HE_{11} mode. This includes an electric field that is discontinuously and more highly concentrated in the liner region and strongly collimated field lines in the vacuum region. Furthermore, the backward-wave dispersion, field profiles, and cutoff frequency order of these frequency-reduced modes is reminiscent of the effective-medium liners in the previous chapter. This suggests that the PCB implementation is in fact an effective realization of the uniaxial ENNZ permittivity.

Although not shown, the PCB liner also supports higher order frequency-reduced HE_{n1} modes whose cutoffs occur at lower frequencies. However, as the order (n) increases, the field profile of these higher-order modes begins to deviate from those observed for the effective-medium ENNZ liner. This is to be expected since each metamaterial layer essentially consists of a linear array of N sub-wavelength resonators that are arranged along the inner wall of the circular waveguide. By increasing n, the spatial variation of the fields increases across each unit-cell ($\phi' = n\pi/N$), such that it no longer behaves as a homogeneous effective-medium. In fact, because this particular design has 8 radial traces, it only supports up to the HE_{41} mode, which suggests that the effective-medium limit completely breaks down when $\phi' > \pi/2$ and $n > N/2$.

Whereas the effective-medium ENNZ liners introduce a single backward-wave propagating band for each frequency-reduced mode, this particular PCB implementation introduces an additional highly-dispersive backward-wave propagating band for the HE_{11} and HE_{21} modes. These appear as nearly horizontal lines in Fig. 4.2 that are marked as $HE_{11,SW}$ and $HE_{21,SW}$, and they are a result of a standing-wave (SW) resonance being formed on the azimuthal traces. To isolate the frequency-reduced modes that are associated with the liner's ENNZ response, the azimuthal capacitance C_0 is carefully chosen to place these standing-wave resonances at sufficiently high frequencies that they do not obscure the interpretation of the desired frequency-reduced modes..

4.3 Parametric Studies

This section will present a number of parametric studies which reveal the effect that geometric and loading parameters have on the dispersion of frequency-reduced modes. Although the dispersion will vary for the complete suite of frequency-reduced modes, the purpose of this study is to gain a deeper intuition into the operation of the the printed-circuit implementation. Therefore, this analysis will focus on the HE_{11} mode of a circular waveguide of radius $b = 15$mm lined by the printed-circuit implementation shown in Fig. 4.1(b) with 0.15mm-wide traces printed on a substrate of height 1.5mm with bulk relative permittivity $\epsilon = 2$. It is important to note that, in addition to the outer radius, the inner radius of $a = 12.5$mm is maintained; as a result, the number of unit cells in the radial direction, and therefore their

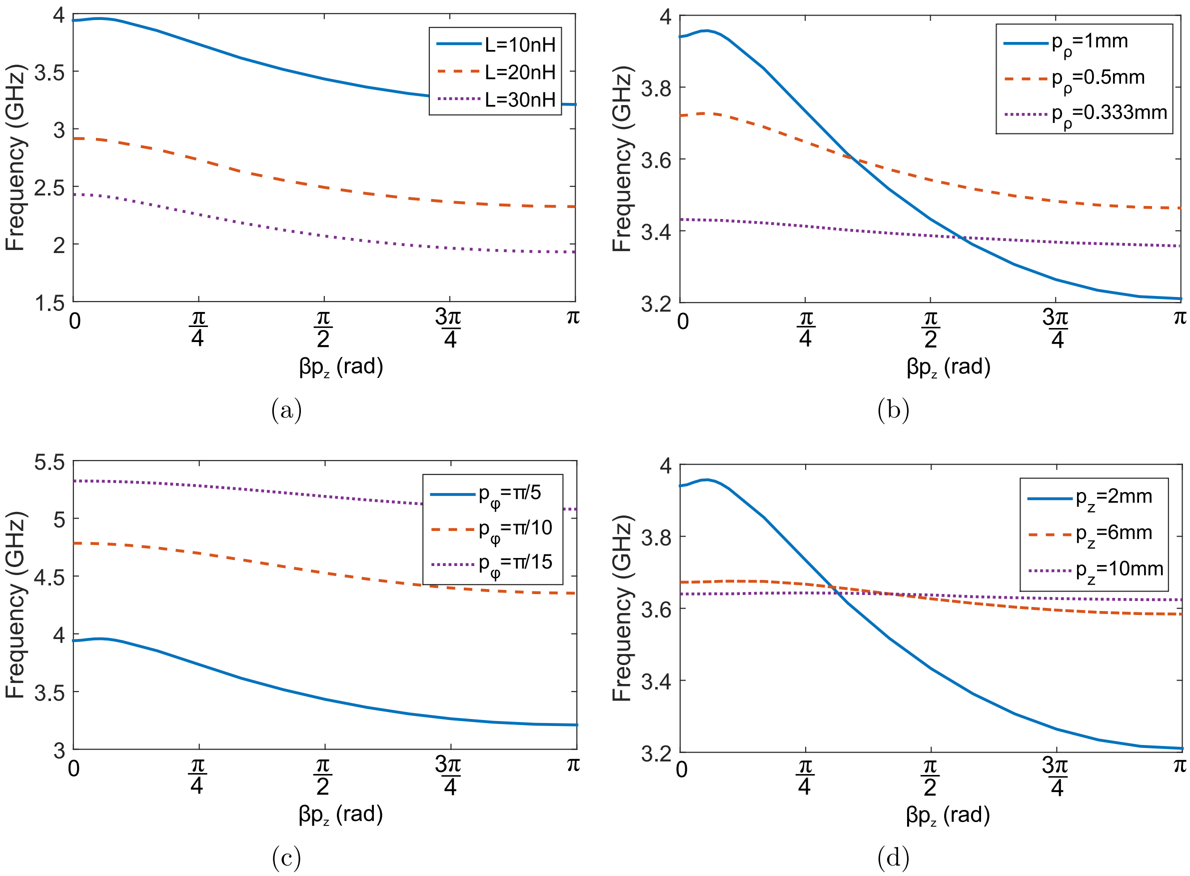

(a)

(b)

(c)

(d)

Figure 4.4: A comparison of the normalized dispersion curves for the thin-wire lined circular waveguide's HE_{11} mode's backward-wave band, for variations in (a) L_0 , (b) p_ρ, (c) p_ϕ, and (d) p_z.

period p_ρ, varies and is determined from the relation $(b-a)/p_\rho$. Figures 4.4(a)–4.4(d) present the dispersion curves for varying loading inductance L_0 and periodicity in ρ, ϕ, and z. Each figure shares a base case (solid blue curve) with the following periodicity and inductance parameters: $p_\rho = 2.5$mm, $p_\phi = 36°$, $p_z = 2$mm, $C_0 = 0.01$pF, and $L_0 = 20$nH. The circular waveguide lined with the proposed base-case PCB structure supports a backward-wave HE_{11} propagating band with a cutoff frequency of $f_c = 3.369$GHz.

In Fig. 4.4(d) the dispersion curves are shown for variations in L_0. As L_0 increases the backward-wave cutoff frequency and bandwidth decrease. Similarly, in Fig. 4.4(b) which shows the dispersion curves as p_ρ is varied, a decrease in p_ρ causes the backward wave band's cutoff frequency and the bandwidth to decrease. By decreasing p_ρ and increasing L_0 the effective total inductance in the radial traces is being increased; therefore, as in Fig. 3.5, this reduces the thin wire's plasma frequency and causes a reduction in the band's cutoff. However, decreasing p_ρ serves to increase the thin copper trace's plasma frequency (captured to first order by Eq. 4.1), which overall causes only a marginal reduction in cutoff frequency. It is interesting that a single radial inductor with $L_0 = 30$nH and $p_\rho = 2.5$mm decreased the cutoff frequency even more than three 30nH radial inductors and $p_\rho = 0.833$mm. This suggests it is possible to design extremely thin metamaterial liners consisting of only a single azimuthal trace that still achieve large degrees of miniaturization.

Consider Fig. 4.4(c), which shows the dispersion curves as p_ϕ is varied. As p_ϕ decreases, the number of inductors in the radial direction increases. This results in more inductors being in parallel to one another, and the total effective inductance decreases, which causes the backward wave's cutoff frequency to increase. In Fig. 4.4(d), the dispersion curves are shown for when p_z is varied. As p_z increases the backward-wave's cutoff and the bandwidth decreases, suggesting that coupling between traces in the z-direction plays a significant role in deciding the ENG bandwidth. It is interesting to note that the backward-wave band's bandwidth decreases as the thin copper traces become more densely packed in the ρ and ϕ directions, but the bandwidth increases if each layer is stacked closer together along the waveguide's (z) axis. In the limit in which $p_z \rightarrow \infty$, the unit cells cannot couple to one another and the backward-wave band disappears.

4.4 Homogenization

This section will investigate how to homogenize the printed-circuit implementation shown in Figure 4.5. In general, this arrangement of thin copper traces can be modeled by a biaxial permittivity tensor whose transverse components ($\epsilon_{\rho 2}$ and $\epsilon_{\phi 2}$) are dispersive [125]. To model the impact of the transversely oriented current-carrying traces on the HE_{11} mode's longitudinal magnetic field, μ_{z2} must also be determined. Due to the absence of longitudinal

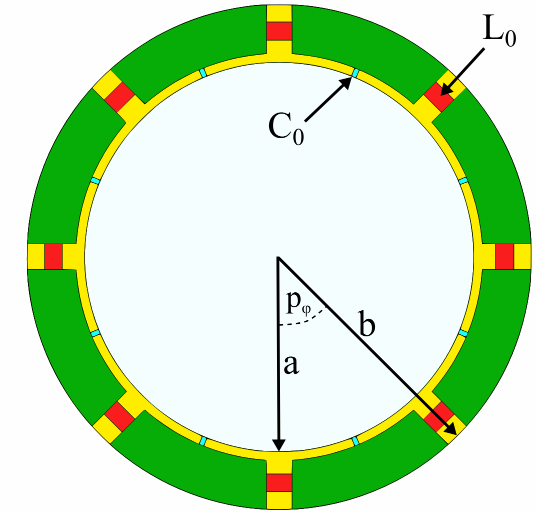

Figure 4.5: A representative printed-circuit implementation of an ENNZ metamaterial liner of thickness $t = b - a$.

traces and the small effect ϵ_{z2} has on the HE_{11} mode's dispersion, we assign $\epsilon_{z2} = 1$. Since it has further been established that $\epsilon_{\phi 2}$ has a minimal impact on the cutoffs of HE modes, we retain the uniaxial assumption employed in Sec. 3.2 (i.e., $\epsilon_{t2} = \epsilon_{\rho 2} = \epsilon_{\phi 2}$) to aid in the homogenization. The PCB implementation is also assumed to have a nonmagnetic transverse response (i.e., $\mu_{\rho 2} = \mu_{\phi 2} = 1$). We now describe a first-order homogenization procedure that may be used to determine the nature of ϵ_{t2} and μ_{z2}, following which the theoretical dispersion relation (Eqs. 3.11) may be used to predict the modes' cutoffs.

It was shown in Sec. 3.2.4 that a frequency-reduced EH_{01} mode cutoff frequency is introduced when $\epsilon_{t2} = 0$. A comparison of the EH_{01} mode's electric and magnetic field components in the effective-medium and practical metamaterial-lined waveguides' is performed in Appendix B. Observation of the fields of the practical metamaterial-lined waveguide reveals that, although they are predominantly EH_{01}-like in the vacuum region, the use of discrete inductive loading to realize a strongly near-zero permittivity and the introduction of azimuthally directed current-carrying copper traces results in a strong radial electric field and axial magnetic field in the liner region. These can be described as those of an azimuthally oriented TL mode supported between the copper trace and the waveguide wall. Here, this fact will be used to develop an equivalent-circuit model for the metamaterial liner based

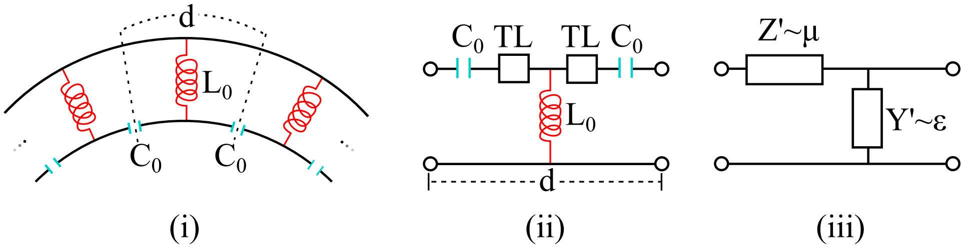

Figure 4.6: Evolution of a TL description of the printed-circuit implementation.

on TL metamaterial theory, from which its effective permittivity and permeability shall be extracted. The field polarizations of the TL mode suggest that these extracted parameters are intrinsically related to ϵ_{t2} and μ_{z2} of the liner.

Figure 4.6(i) shows a curved circuit description of multiple TL unit cells, in which $d = p_\phi(a+b)/2$ may be taken as an effective azimuthal periodicity. This is described by the equivalent-circuit model in Fig. 4.6(ii), which consists of a shunt inductor and series capacitor loading a host TL of periodicity d. In the effective-medium regime, the per-unit-length series impedance (Z') and shunt admittance (Y') of Fig. 4.6(iii) represent, respectively, the distributed inductance and capacitance of an effective TL describing the azimuthal TL mode. Here, Y' may be related to the liner's effective ϵ_{t2} (assumed real), whose frequency response is Drude-like in the vicinity of its plasma frequency f_{ep}, where ϵ_{t2} achieves a zero value [126]:

$$\epsilon_{t2} = \epsilon_p(1 - \frac{{f_{ep}}^2}{f^2}), \quad \text{where} \quad f_{ep} = \frac{1}{2\pi}\sqrt{\frac{g}{\epsilon_p L_0 d}}. \tag{4.2}$$

In this expression, ϵ_p is the intrinsic permittivity of the host TL segments and g is a geometrical parameter relating the TL mode's characteristic impedance to the wave impedance of the intrinsic medium. Similarly, Z' yields a response for μ_{z2} that is Drude-like in the vicinity of its own magnetic plasma frequency, f_{mp}. However, the typically narrowband magnetic response of metamaterials is often better approximated by a single- or multi-pole Lorentz dispersion, as in the split-ring resonator [71, 127], particularly at frequencies well below f_{mp}. In fact, although the proposed first-order homogenization scheme considered a single metamaterial layer in isolation, such additional resonances in μ_{z2} may result from the magnetic coupling between adjacent metamaterial layers. A more sophisticated equivalent-circuit model may look to multiconductor-TL (MTL) theory to include this mutual coupling to produce a more accurate dispersion profile for μ_{z2}. In the interest of conciseness, this shall be left for a future work. In the present model, the use of a gap capacitance C_0 that is diminutive in comparison to the strong inductive loading L_0 ensures that $f_{ep} << f_{mp}$; the assumption of a Lorentz-like dispersion therefore implies that μ_{z2} at f_{ep} is near its dc value of unity. It should be recalled that the frequency-reduced mode's cutoffs are dominated by $\epsilon_{\rho 2}$'s ENNZ response for thin liners, and are therefore not strongly affected by moderate deviations in μ_{z2} from this assumption.

To validate the proposed homogenization procedure, the representative design in Fig. 4.5 with 0.3 mm- and 0.6 mm-wide radial and azimuthal copper traces, respectively, printed on a Rogers/Duroid 5880 substrate, is assigned the following parameters: $b = 15.0$ mm, $a = 12.7$ mm, $L_0 = 8.4$ nH, $C_0 = 0.01$ pF, $p_\phi = 45°$, and $p_z = 2.66$ mm. To determine the parameters of the host TL, a flattened, unloaded, and similarly oriented copper trace of the same geometrical dimensions was simulated, revealing that $\epsilon_p = 1.438$ and $g = 0.7156$, and that both parameters vary weakly with frequency. For the specified loading values, ϵ_{t2} exhibits $f_{ep} = 3.963$ GHz.

The homogenized liner and waveguide share the same physical dimensions as the PCB implementation ($b = 15$ mm and $a = 12.7$ mm). Using these values, the above homogenization procedure predicts frequency-reduced EH_{01}, HE_{11}, HE_{21}, and HE_{31} modes with cutoff frequencies of $f_{01} = 3.963$ GHz, $f_{11} = 3.512$ GHz, $f_{21} = 3.380$ GHz, and $f_{31} = 3.238$ GHz, respectively. That $f_{01} = f_{ep}$ (i.e., where $\epsilon_{t2} = 0$) makes physical sense from a TL perspective, since this implies an infinite wavelength condition in the TL mode, which is only satisfied for no azimuthal variation (i.e., $n = 0$).

Figure 4.7 presents the dispersion of the axial phase incurred per unit cell (βp_z) obtained from HFSS's eigenmode simulator for the frequency-reduced EH_{01} (black dashed curve), HE_{11} (black solid curve), HE_{21} (dark grey solid curve), and HE_{31} (light grey solid curve) modes.

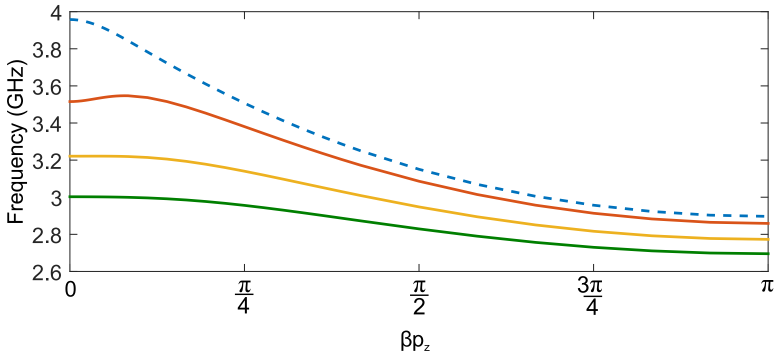

Figure 4.7: The dispersion of frequency-reduced modes for a representative printed-circuit implementation of an ENNZ metamaterial liner.

The eigenmode simulations are unable to capture the real component of the propagation constant (α), and only the propagating bands with $\beta >> \alpha$ are obtained accurately. The cutoff frequencies of the EH_{01}, HE_{11}, HE_{21}, and HE_{31} modes are $f_{01} = 3.958$GHz, $f_{11} = 3.515$GHz, $f_{21} = 3.221$GHz, and $f_{31} = 3.003$GHz, respectively, which are found to be within 1.2%, 0.08%, 4.8%, and 7.8%, respectively, of those predicted by the homogenization method. Interestingly, there remains a good agreement between the HFSS and homogenization results for the higher-azimuthal-order cutoffs, even though their associated large azimuthal phase variation significantly perturbs the assumption of homogeneity. The accuracy of the homogenization can be partially attributed to the dominant response of the inductance L_0 which dominates the TL mode's response [125]. It is believed the ENZ property of the TL further contributes to the homogenization's accuracy, in which the infinite-wavelength condition allows us to neglect the effect of curvature.

Although not shown, the homogenization results exhibit the same salient features as the HFSS data away from cutoff (backward-wave trends, cutoff frequencies decreasing with increasing azimuthal order, forward-backward coupling of the HE_{11} mode). However, the latter appear less dispersive than the former. Here, it should be noted that the above homogenization approach only seeks to match the cutoff frequencies of the EH_{01} and HE_{11} modes, and not the full dispersion profile away from cutoff, for several reasons. Most significantly, the effective-medium approximation disregards the perturbations introduced by

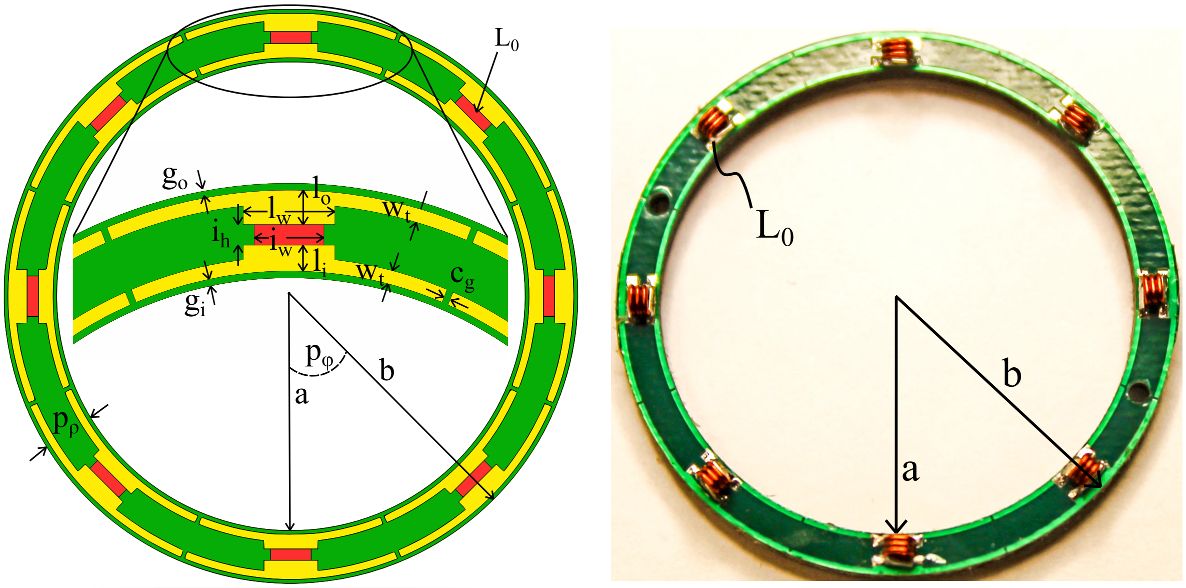

(a) (b)

Figure 4.8: (a) Simulation model and (b) fabricated prototype of the designed printed-circuit metamaterial based on inductively and capacitively loaded copper traces on a dielectric substrate.

axial periodicity, which result in the coupling of forward and backward spatial harmonics at the band edges. Furthermore, the longitudinal electric fields become more pronounced away from cutoff, which deviates from the assumed TL-mode polarizations and also contributes to stronger spatial dispersion. Both effects break down the assumed Drude dispersion profile for ϵ_{t2} [125].

4.5 Fabricated Metamaterial Liner

Figure 4.8(a) presents a slightly modified version of the printed-circuit metamaterial that is amenable to standard PCB fabrication. A small radial gap of width g_0 and an outer ϕ-directed trace of width w_t are introduced. The outer trace replaces the waveguide wall's function in establishing a continuous azimuthal current path between adjacent ρ-directed inductors. This eases the fabrication challenge of soldering to the waveguide wall, which was required in the previous design, and enables the ENNZ liner to be modular. In this design,

(mm)	b	a	c_g	w_t	g_0	g_i
	15.0	12.59	0.10	0.30	0.10	0.15
(mm)	l_0	l_i	i_h	l_w	i_w	
	1.00	0.65	0.51	2.60	1.83	

Table 4.1: Fabricated Liner Dimensions

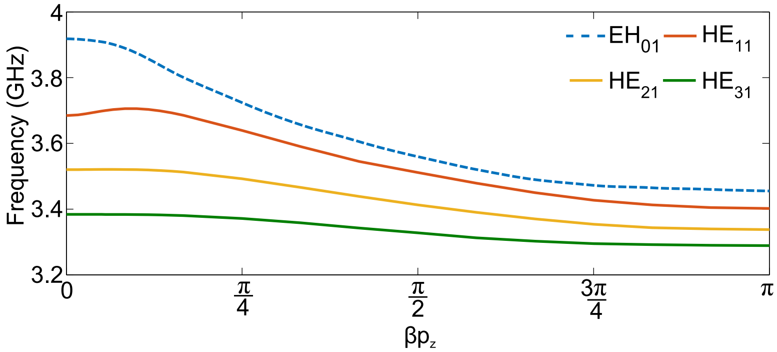

Figure 4.9: Dispersion of the frequency-reduced EH_{01}, HE_{11}, HE_{21}, and HE_{31} modes as obtained from full-wave eigenmode simulations.

Coilcraft ultra-high Q 0806SQ-6N0 inductors were chosen. Their inductance of $L_0 = 8.28$nH and quality factor $Q = 100$ at $f = 3.70$GHz were extrapolated outside the frequency range presented in their data sheets [128]. Due to the larger concentration of fields around each inductor, the value of Q is a pivotal factor in defining the HE_{11} mode's propagation loss. The traces are printed on a Rogers/Duroid 5880 substrate of 61-mil thickness which, with the chosen inductor's height, gives $p_z = 3.017$mm. The remaining design dimensions shown in Fig. 4.8(a) are listed in Table I, and were chosen to provide a reasonably close match to the cutoffs of the previous design shown in Fig. 3.8(a).

A photo of the fabricated PCB metamaterial is shown in Fig. 4.8(b). Full-wave eigenmode simulations of this structure reveal that it supports frequency-reduced EH_{01}, HE_{11}, HE_{21}, and HE_{31} modes, as shown in Fig. 4.9, with cutoff frequencies of $f_{01} = 3.918$GHz, $f_{11} = 3.685$GHz, $f_{21} = 3.520$GHz, and $f_{31} = 3.384$GHz, respectively. However, these simulated data do not include the impact of fabrication tolerances imposed through milling, etching, and component placement.

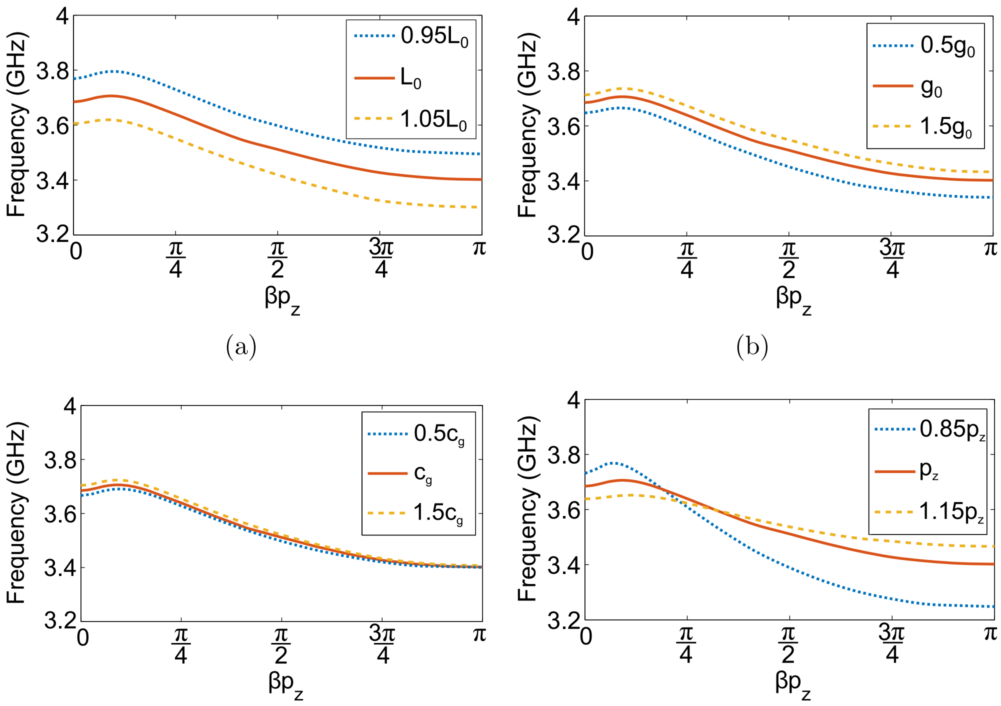

(a) (b)

(c) (d)

Figure 4.10: Variation of the dispersion of the frequency-reduced HE_{11} mode with (a) L_0, (b) g_0, (c) c_g, and (d) p_z.

4.5.1 Impact of Fabrication Tolerances on the Dispersion

Figures 4.10(a)-4.10(d) present the dispersion curves of the frequency-reduced HE_{11} mode for varying L_0, p_z, c_g, and g_0 values, respectively. Since the loading inductance, L_0, primarily controls the location of the frequency-reduced mode cutoffs, it is instructive to look at the impact of their listed tolerances of up to 5% (0.414nH). Furthermore, precise measurements of each of the fabricated layers' p_z reveal tolerances of up to 15% (0.45mm) per layer. Last, the metamaterial's extremely fine features push the limits of the milling and etching process and this leads to tolerances of up to 50% (50μm) in c_g and g_0. Each figure shares the nominal case (solid orange curve) whose dimensions were presented in Table I. While all the observed parameters shift the band up or down, L_0 commands the greatest change in the cutoff frequency. The cutoff is only moderately impacted by g_0 and p_z and only minutely by c_g. The latter is to be expected from the equivalent-circuit model, which predicts that small changes in the capacitance C_0 only impact μ_{z2} near its plasma frequency (i.e., for $f >> f_{ep}$). The dispersion profile's shape is dependent on p_z and is more dispersive when the unit cells are stacked closer together. It is worth noting that, despite the tolerance levels of each parameter, the HE_{11} mode's cutoff frequency always remains within 3% of its designed value of $f_{11} = 3.685$GHz.

Chapter 5

The Transmission Properties of Miniaturized Metamaterial-Lined Circular Waveguides

In Chapter 3, it was established that the cutoff frequency of the HE_{11} mode can be reduced well below the unlined waveguide's natural cutoff. This chapter aims to show that metamaterial-lined waveguides are also far more efficient at transporting power than their unlined counterparts. In the study of the metamaterial-lined waveguide whose liner is modeled as an effective-medium possessing a uniaxial permittivity, it was shown in Fig. 3.6 that the frequency-reduced HE_{11} mode's attenuation can be extremely low, and, in fact, significantly less than the reactive attenuation of the similarly sized below-cutoff unlined waveguide operating at the same frequency. This suggests the introduction of a metamaterial liner with a lossy permittivity profile can significantly improve the transmission in below-cutoff waveguides. Of course, the metamaterial-lined waveguide will need to be driven by some sort of 'electromagnetic source' that deposits power into the waveguide's interior.

Pins and loops driven by a coaxial waveguide are often employed in practice to couple electromagnetic energy into waveguides, and their orientation, size, and position determine which modes are strongly excited. Maximum energy transfer is accomplished by designing the feed so that its field pattern exactly matches that of the field configuration of the desired mode. However, this is impractical, since even a small amount of fringing fields will potentially couple to other modes, provided they are above cutoff. This is problematic for the metamaterial-lined waveguides, in which a suite of frequency-reduced modes copropagate over the liner's ENNZ frequency band. For instance, using a coaxial pin to excite the HE_{11} mode in a metamaterial-lined waveguide has the potential to excite the EH_{01} and HE_{21} mode (further details can be found in Appendix C), resulting in unexpected transmission characteristics.

This study considers both ideal and practical excitation sources to investigate the transmission characteristics of the HE_{11} mode in isolation. It begins with the waveguide-step transition, in which the TE_{11} mode in a larger vacuum-filled waveguide is used to couple to the HE_{11} mode in metamaterial-lined waveguide. Thereafter, a novel balanced shielded-loop source is shown to couple strongly to the HE_{11} mode while keeping the waveguide and feed compact. The transmission mechanisms in metamaterial-lined waveguides described using effective-medium models will shed insight into numerical and experimental investigations of a prototype metamaterial-lined waveguide employing the printed-circuit realization of the liner that was discussed in Chapter 4.

5.1 Numerical Investigations of ENNZ-Lined Circular Waveguides

5.1.1 Waveguide Step Transition

A waveguide step transition consists of changing the waveguide's cross-sectional dimensions discretely along the waveguide's axis. They have been successfully employed in investigations of ENZ-filled waveguides, in which complete transmission of the higher-order TE_{10} mode

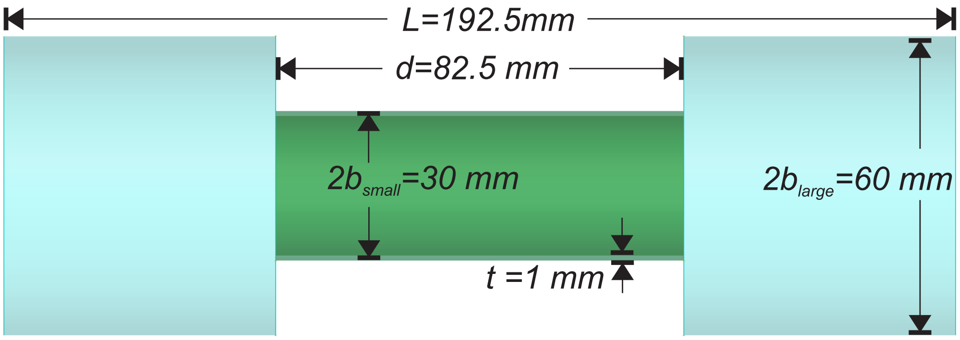

Figure 5.1: Full-wave simulation model employed in the transmission analysis. A smaller below-cutoff waveguide is placed between two larger above-cutoff waveguides and a metamaterial liner possessing the complex dispersive permittivity in Sec. 3.2.4 is introduced into the smaller waveguide.

was observed in an extremely thin parallel-plate waveguide fed by two larger parallel-plate waveguides (see Fig. 2.8) [89]. Despite the abrupt discontinuity exciting a spectrum of evanescent modes at the entrance to the metamaterial-filled waveguide, the symmetry of the waveguide's cross section in this particular step-transition ensures strong coupling to a single dominant propagating mode.

In an ideal feeding arrangement, the modal field pattern generated by the feed would have to exactly match the field pattern of the HE_{11} mode. The step transition shown in Fig. 5.1 presents an approximate solution, in which the field pattern of the hollow feeding waveguide's TE_{11} mode's is akin to the HE_{11} mode, and is only marginally disturbed by the transition. A transmission analysis is performed using the full-wave simulation software HFSS [129] on the simulation model shown in Fig. 5.1. In this representative setup, two larger vacuum-filled circular waveguides with a radius $b_{large} = 30$mm and a TE_{11} cutoff frequency of 2.928GHz are connected by a smaller vacuum-filled waveguide with a radius $b_{small} = 15$mm and a TE_{11} cutoff frequency of 5.857GHz. A waveport located at the end of one of the larger waveguide sections excites the TE_{11} mode at frequencies that lie in the propagating region of the larger waveguide, but which correspond to the natural evanescent region of the smaller waveguide. The dashed blue curve in Fig. 5.2(a) presents the insertion loss obtained for this setup and verifies that the intermediate waveguide under cutoff strongly attenuates the TE_{11} mode.

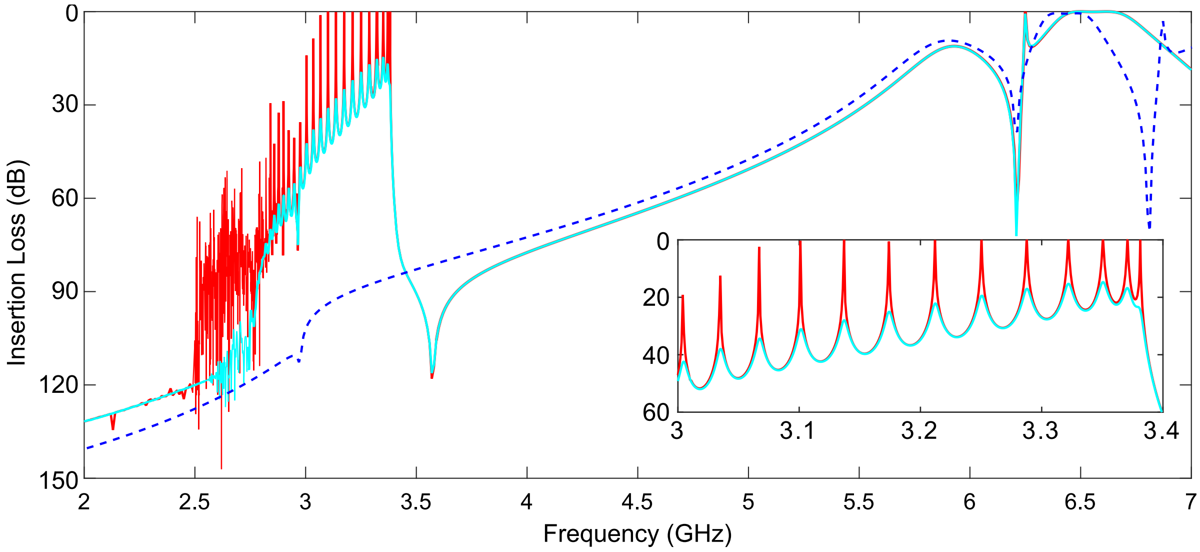

(a)

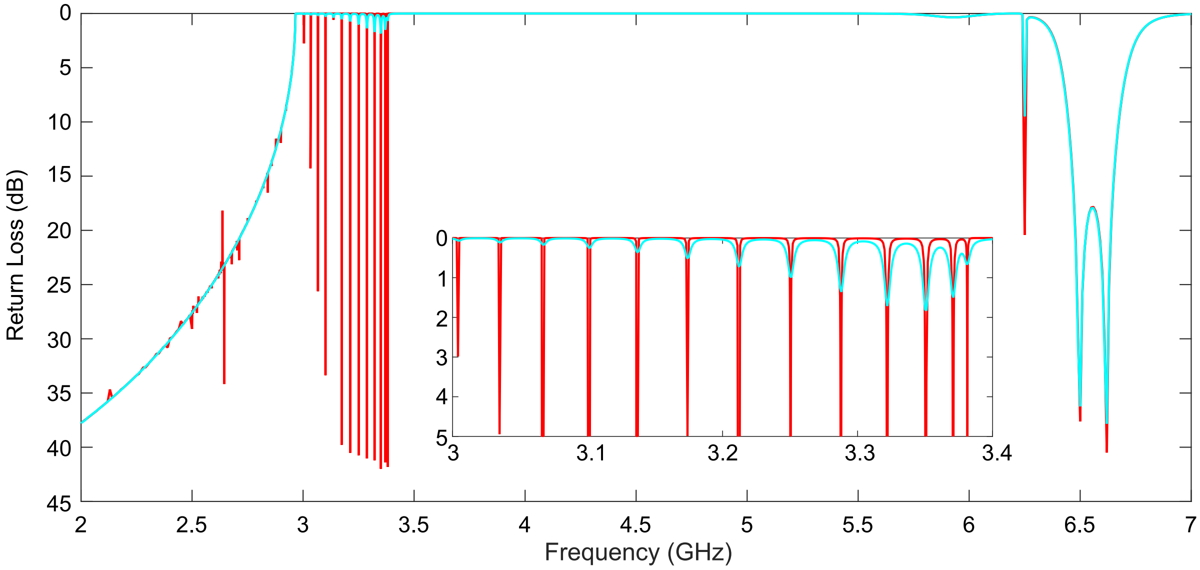

(b)

Figure 5.2: (a) Insertion loss and (b) return loss for the unlined case (dashed blue curve), the lined case with no loss (solid red curve) and the lined case with loss (solid teal curve). The inset shows in detail several resonances in the frequency-reduced backward-wave passband.

Although the return loss is not shown, it is close to 0dB below 5.0GHz.

Below-Cutoff Transmission

Now, a metamaterial liner of thickness $t = 1\text{mm}$ is introduced into the smaller waveguide and assigned the Drude dispersive permittivity, $\epsilon_{r2}(\omega)$, reported in Sec. 3.2.4 with $\omega_{ep} =$

$2\pi \times 3.55$GHz and $w_t = 2\pi \times 3$MHz. In this study the liner is modeled as isotropic due to HFSS's inability to simulate cylindrically anisotropic materials. The reader is reminded that the dispersion of the HE_{11} mode was shown in Sec. 3.2.5 to remain mostly unchanged between isotropic and uniaxial thin metamaterial liners; therefore, it is expected that an isotropic simplification only marginally impacts the transmission.

According to the theoretical results of the previous section, transmission should occur below 3.381GHz for the frequency-reduced backward-wave band and above 5.958GHz in the upper band. Inside the frequency-reduced band, the metamaterial liner would effectively enable a cross-sectional-area reduction of the unlined circular waveguide by a minimum of 75%. To understand the impact of losses in the metamaterial liner on the ability of the lined waveguide to transport power, both lossy ($\omega_t = 5$MHz) and lossless ($\omega_t = 0$) cases are compared. Figures 5.2(a) and 5.2(b) shows the insertion loss and return loss, respectively, in the lossless (solid red curve) and lossy (solid teal curve) cases.

As predicted by the theory, the metamaterial liner results in a new passband below $f = 3.381$GHz, corresponding to the backward-wave cutoff (f_1) in Fig. 3.6. An upper forward-wave band is also observed; however, its cutoff frequency is more difficult to infer from the insertion loss due to the excitation of high-order modes in the larger waveguide. By virtue of the particular geometrical parameters chosen in this arrangement (enabling the goal of a 75% cross-sectional-area reduction), the forward-propagating HE_{11} mode in the smaller waveguide couples to the TM_{11} mode in the larger output waveguide for frequencies above 6.09GHz. Another simulation with a smaller output waveguide of $b_{large} = 20$mm and associated TM_{11} mode cutoff frequency of 9.15GHz (not shown) exhibited the expected smooth high-pass response.

The inset of Fig. 5.2(a) and 5.2(b) presents the transmission and reflection features, respectively, of the backward-wave region in greater detail, and reveals multiple narrow transmission peaks. In both the lossless and lossy case, a very fine frequency resolution is required to sample the maximum of each peak. When the liner is lossless, these peaks appear to suggest total transmission of power, in which the insertion loss tends to 0dB and the return loss is generally greater than 30dB. Increasing the frequency resolution near the peaks and the numerical convergence of the simulation serves to further improve the return loss peaks. However, the transmission and reflection performance begins to degrade as the frequency approaches the larger feeding waveguide's cutoff at 2.928GHz, below which the transmission gets significantly worse.

Since the fields are concentrated strongly in the liner region, the introduction of loss in the liner degrades the transmission through the structure; nevertheless, the backward-wave band introduced by the liner exhibits a dramatic increase in transmission over the unlined case, at times showing enhancements of over 71dB. In fact, even in the lossy case, the transmission attains a peak value of - 14.7dB at $f = 3.351$GHz versus - 85.7dB at the same frequency in the unlined waveguide. It is important to note here that the poor matching of the lossy metamaterial-lined waveguide is attributed to this particular feeding arrangement. As will be shortly shown, the insertion loss can be further improved by using a better matched source. Also evident in Fig. 5.2(a) is a distinct antiresonance at $f = 3.58$GHz which is located near the plasma frequency of the liner and the edge of the stop band (i.e., f_2 in Fig. 3.6), which appears not to be affected by the losses in the liner.

Transmission Mechanism

The complex electric-field magnitude is plotted in the H-plane of the waveguide sections for the first six peaks in Figs. 5.3(a)–5.3(f). The E-planes (not shown) exhibit very similar field distributions, except that the liner fields are more pronounced. Each successive peak corresponds to a Fabry-Pérot-type resonance in which an integer number of half-wavelengths is supported by the lined waveguide section over its length. Moreover, that the order of the resonances increases as frequency decreases is characteristic of backward-wave propagation, and corroborates the dispersion data in Fig. 3.6. The uniformity of the complex field magnitudes at the input and output sides suggest traveling-wave behaviour, and observation of

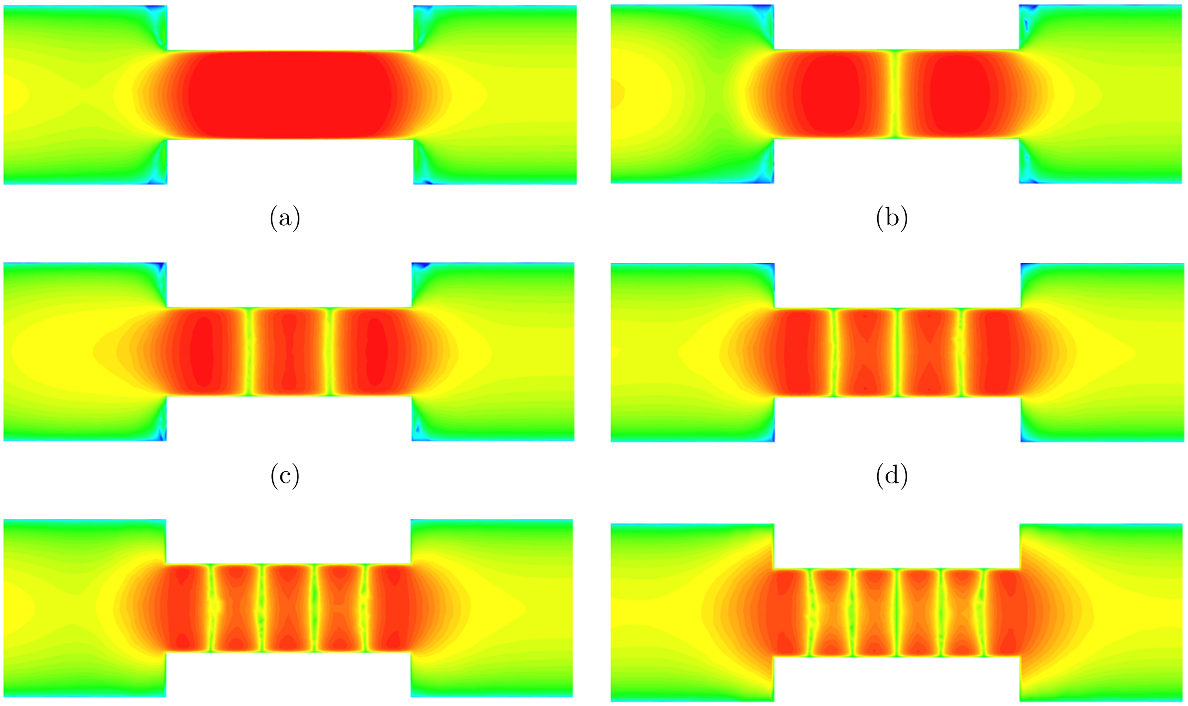

(a) (b)

(c) (d)

(e) (f)

Figure 5.3: Complex electric-field magnitudes in the waveguide's H-plane at the following transmission peaks in the frequency-reduced backward-wave passband: (a) $f = 3.381$GHz, (b) $f = 3.371$GHz, (c) $f = 3.351$GHz, (d) $f = 3.324$GHz, (e) $f = 3.291$GHz, and (f) $f = 3.256$GHz. Each frequency corresponds to a Fabry-Pérot-type resonant condition of an integer number of half-wavelengths supported by the lined waveguide section over its length.

the time evolution of the steady state fields in Fig. 5.4 at $f = 3.381$GHz also confirm that the incoming wavefronts are restored at the outgoing side of the lined waveguide. These results validate that hollow waveguides lined using thin, ENNZ metamaterial liners support unusual resonant tunneling phenomena akin to the supercoupling observed in homogeneously ENZ-metamaterial filled waveguides [88].

Comparison of Full-Wave Simulations and Theory

Figure 5.5(a) presents the transverse electric field vectors in the lined waveguide's cross section at the cutoff frequency of the upper forward-wave band (i.e., $f = f_3 = 5.958$GHz). Superposed on these are the complex electric-field magnitudes which reveals a TE_{11}-like field distribution that matches well with the theoretical results in Fig. 5.5(b). At the backward-

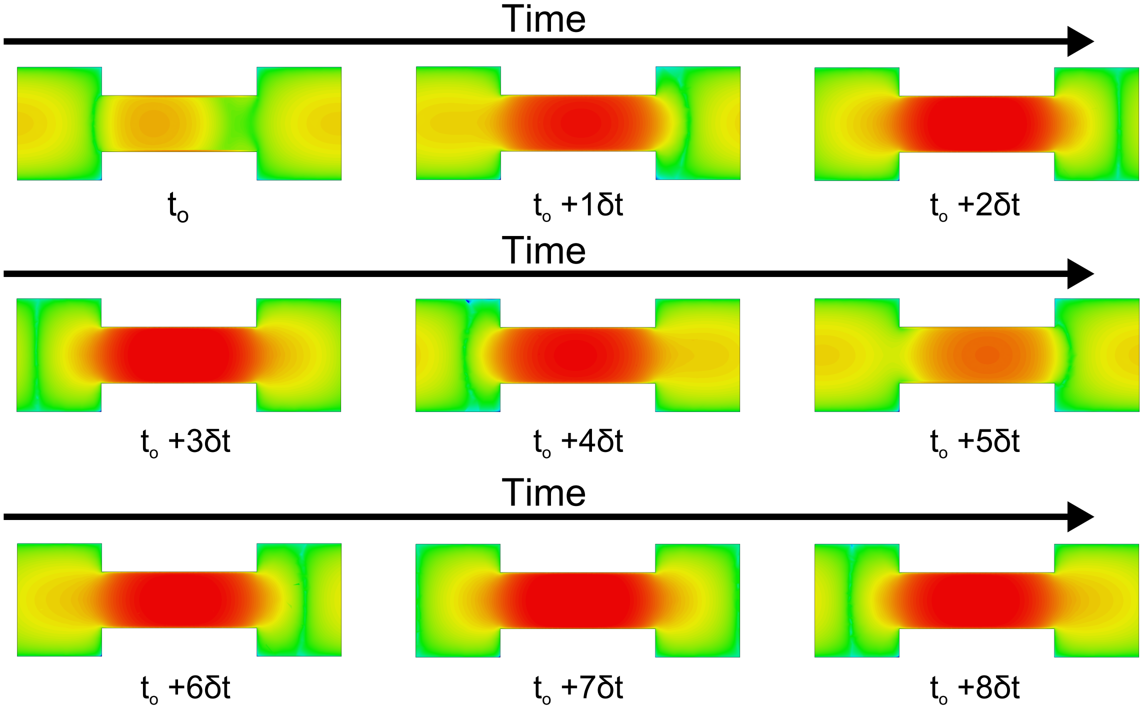

Figure 5.4: The time evolution of the complex electric-field in the metamaterial-lined waveguide at $f = 3.381\text{GHz}$. A time step of $\delta_t = (2\pi/9)/\omega$ is used.

wave band cutoff of $f = 3.381\text{GHz}$ where the first transmission peak is observed, Fig. 5.5(c) verifies the results obtained from the theory (Fig. 5.5(d)): that the transverse fields are strongly confined to the metamaterial liner and collimated in the vacuum region.

To further validate the dispersion of the backward-wave band, Fig. 5.6 compares the dispersion diagrams for the reduced HE_{11} mode obtained using three different methods. The first method is based on the theoretically derived dispersion relation (3.11) and is borrowed from Fig. 3.6 (solid red curve). The second method utilizes HFSS's eigenmode solver, but employs special techniques to overcome the following inherent limitations in the eigenmode solution process: first, only propagating modes (i.e. $\gamma \approx j\beta$) may be found; therefore, only the backward-wave and forward-wave (and not the complex) modes can be determined using this method. Second, the eigenmode solver determines the resonant frequencies of a particular geometry with known boundary conditions when the material properties at the solution frequency are known *a priori* (e.g., when the material properties are assumed constant with frequency). Consequently, in the case of dispersive materials, a conventional parametric

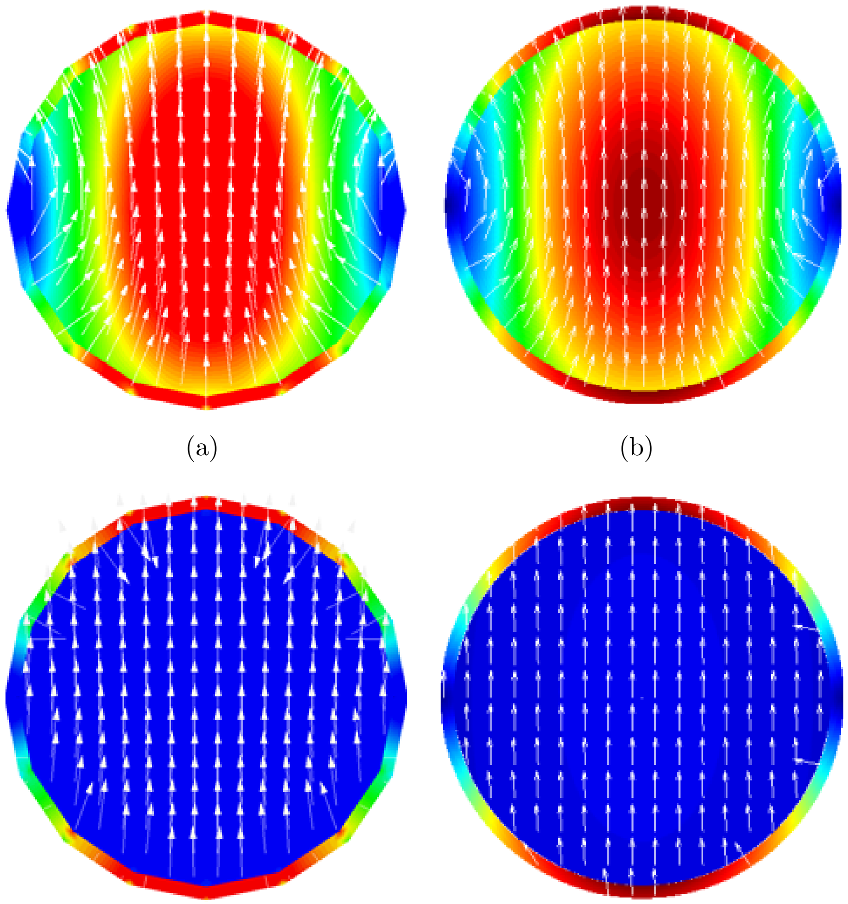

(a) (b)

(c) (d)

Figure 5.5: The simulated normalized electric-field vectors and complex electric-field magnitudes in the transverse cross-section at the center of the metamaterial-lined waveguide at (a) $f = 5.958$GHz and (c) $f = 3.381$GHz. The fields obtained from the theoretical analysis in Sec. 3.2.4 (Figs. 3.9(a) and 3.9(b)) are reproduced here in (b) and (d).

sweep of phase shifts across the structure to obtain the dispersion curve is not a valid approach. However, knowing the frequency at which the dispersive metamaterial liner achieves a particular permittivity (by way of its known dispersion), the parametric sweep may be carried out using this fixed permittivity with the knowledge that the obtained dispersion curve is valid only at the corresponding frequency. By repeating this process over a number of fixed permittivity values corresponding to different frequencies, it is possible to obtain the true dispersion curve for the metamaterial-lined waveguide from HFSS's eigenmode solver. This is indicated in Fig. 5.6 by the solid blue circles. The third method employs the full-wave

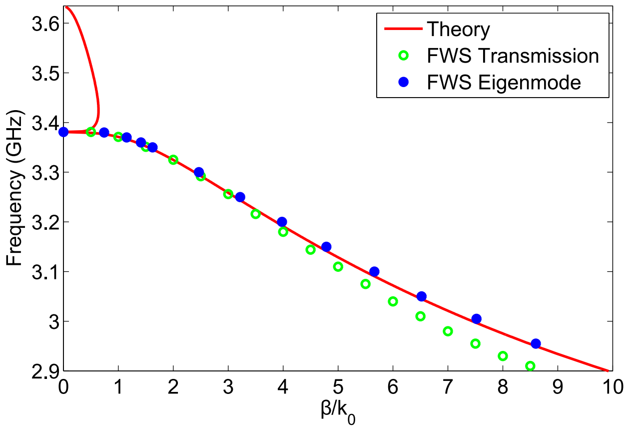

Figure 5.6: The dispersion curve of the frequency-reduced backward-wave passband obtained using three different methods: the full dispersion in equation (3.11) (solid red curve), full-wave eigenmode simulations (solid blue circles), and full-wave transmission simulations (empty green circles).

transmission simulation results by examining the phase shift through the lined waveguide section at each resonant frequency (empty green circles). This process has been employed by other research groups with experimental results and has demonstrated relatively high precision, since all the peaks correspond to integer numbers of half-wavelength phase shifts [130]. The dispersion curves obtained from full-wave eigenmode simulations and theoretical analysis correlate strongly with one another across the whole backward-wave band, while the data derived from the transmission results deviates at higher values of β/k_0. This is to be expected, since we are comparing the dispersion of a finite-length lined-waveguide section to that of an infinitely long lined waveguide.

Contradirectional Power Flow

It is well known that the direction of power flow can vary between different regions in inhomogeneous structures. For example, stacked DNG and DPS layers in a parallel-plate configuration can transport power forward in the DPS region that will, in turn, be coupled backward in the DNG region, resulting in zero net power being transported [85]. An imbalance of power in each region can lead to non-zero net power being directed either forward or backward, as in the case of the conventional dielectric-lined waveguides [37]. Figure 5.7

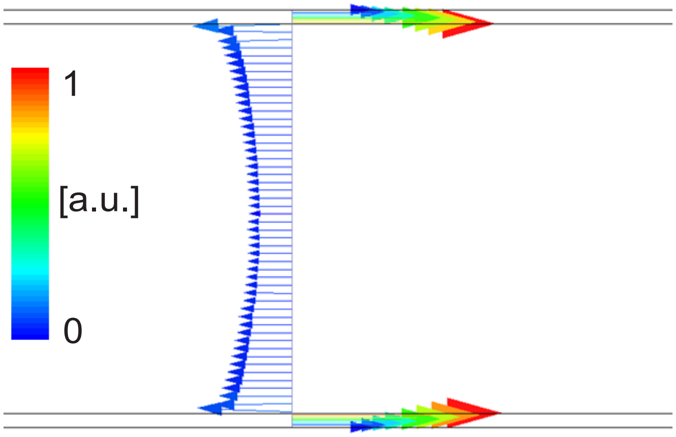

Figure 5.7: Transverse distribution of the Poynting-vector magnitude and direction at the center of the lined waveguide section at 3.381GHz.

presents the simulated Poynting vector directions and magnitudes at the first resonant peak, along a diameter located at the center of the metamaterial-lined waveguide. It is evident that power is being transported in the positive direction through the liner and in the negative direction in the vacuum region at this particular location and frequency, although the reverse is also possible and is highly dependent on the nature of the source [83]. It is also found (not shown) that the relative amounts of power in the liner and vacuum regions vary continuously both with frequency and along the length of the lined waveguide. However, it should be noted that a majority of the power tends to flow in the liner region over much of the backward-wave band. The total transmission of power at these resonant peaks, therefore, suggests a continuous resonant exchange of power between the liner and vacuum regions. It should be noted that this resonant transmission is achieved even though the liner occupies less than 13% of the transverse cross-sectional surface area. This allows for the waveguide to be miniaturized while still leaving the majority of its volume empty for applications that require access to its interior.

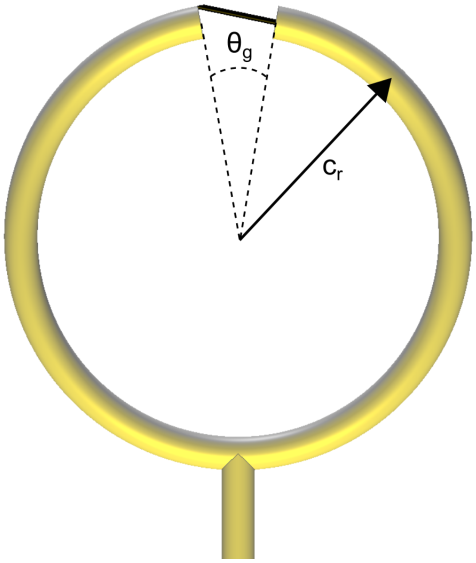

Figure 5.8: The coaxial implementation of the balanced shielded loop.

5.1.2 The Balanced Shielded-Loop Excitation

Whereas the waveguide-step transition is a useful numerical tool to excite the frequency-reduced HE_{11} mode, the larger feeding waveguide is impractical in applications requiring extreme levels of miniaturization of the whole waveguide ensemble. A more suitable approach is to embed the feed directly into the waveguide to maximize its compactness, as in the case of the coaxial pin/loop extending from the side/back [131]. However, this feed must also mitigate coupling to non-HE_{11} modes.

This spurred the investigation of the balanced shielded loop [132], which is discussed in detail in Appendix D. The coaxial implementation of the balanced shielded-loop antenna is shown in Fig. 5.8 and is composed of a teflon-filled 50Ω coaxial transmission line with inner- and outer-conductor radii of 0.29mm and 0.93mm, respectively, that is formed into a loop of radius c_r. The outer conductor and teflon are stripped over an angle θ_g, and the inner conductor is shorted to the outer conductor across this gap. When placed inside a circular waveguide, the balanced nature of the shield currents on the loop minimizes coupling to the longitudinal (z-directed) electric fields. Instead, it creates a longitudinal magnetic field that, in combination with the loop's size, ensures strong coupling to the HE_{11} mode and weak

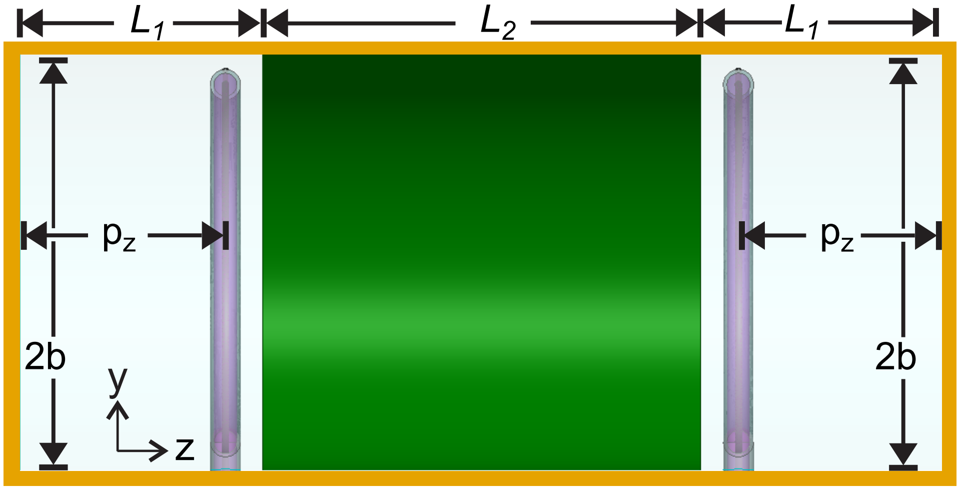

Figure 5.9: Full-wave simulation model employed in the transmission analysis, consisting of a metamaterial-lined waveguide possessing the complex dispersive permittivity in Sec. 3.2.4 that is placed between two balanced shielded-loop sources.

interaction with the EH_{01} and higher-order HE_{n1} modes.

The balanced shielded-loop antenna will now be employed to excite the metamaterial-lined waveguide, demonstrating a strong level coupling to the HE_{11} mode that is reminiscent of the waveguide-step transition, but showing drastically improved matching in the presence of liner loss. Figure 5.12 presents the full-wave-simulation setup, which consist of two vacuum-filled excitation waveguides of radius b = 15mm and a TE_{11} cutoff frequency of 5.857GHz that are smoothly connected to an intermediate metamaterial-lined waveguide of length $L_2 = 82.5$mm. The liner is assigned the isotropic Drude dispersive permittivity, $\epsilon_{r2}(\omega)$, reported in Sec. 3.2.4 with $\omega_{ep} = 2\pi \times 3.55$GHz and $\omega_t = 2\pi \times 3$MHz. As a result, the dispersion of the waveguide's HE_{11} mode is kept the same as in the previous waveguide-step transition study. Two balanced shielded loops ($c_r = 12.8$mm and $\theta_g = 20°$) are embedded within the closed evanescent waveguide sections of length $L_1 = 17.8$mm at a distance $p_z = 15.0$mm from a PEC back wall. Each shielded loop is connected to a small length of coaxial cable that extend to the exterior of the waveguide and whose TEM mode is excited using a waveport.

The red and blue curves in Fig. 5.10 present the insertion loss and return loss, respectively,

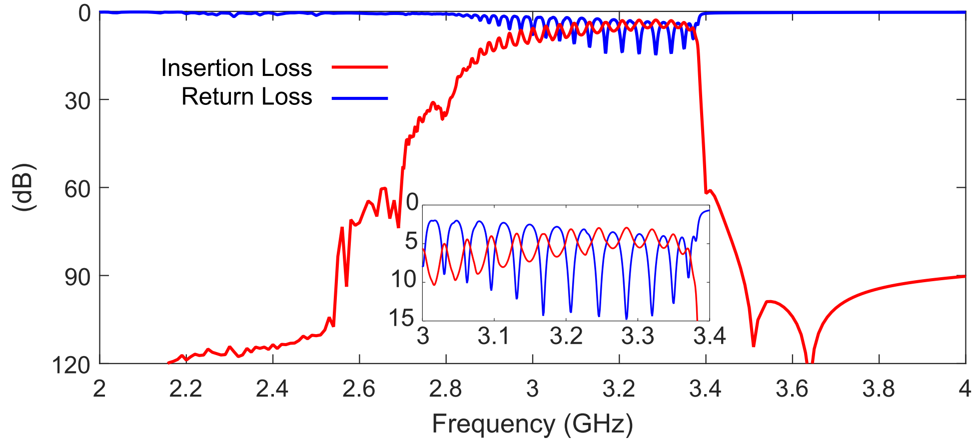

Figure 5.10: Simulated insertion (red curve) and return loss (blue curve) of the shielded-loop excited metamaterial-lined waveguide.

for the transmission setup. Here, the frequency range is limited to clearly observe the HE_{11} mode's backward-wave passband. It is evident that the shielded-loop-excited metamaterial-lined waveguide shares a number of transmission features with the previous waveguide-step transition, a passband below the HE_{11} cutoff ($f = 3.381$GHz) consisting of multiple resonant transmission peaks that is followed by a distinct antiresonance. Whereas the antiresonance frequency is not easy to infer, the transmission peak frequencies shown in the inset of Fig. 5.10 coincide with those observed in the waveguide-step transition. In fact, the only major difference is a relatively higher transmission in the shielded-loop excitation, in which improvements of up 10dB are observed. The reader is reminded that the degree of liner loss was kept fixed between the larger-waveguide and shielded-loop excitations. Therefore, this improvement in insertion loss can only be attributed to the better matched shielded-loop source. For instance, at $f = 3.351$GHz the waveguide-step excitation exhibits return and insertion losses of 1.8dB and 14.8dB, respectively; on the other hand, the shielded-loop excitation exhibits return and insertion losses of 12.2dB and 3.7dB, respectively, at the same frequency. The generally improved transmission allows us to define a 10dB insertion loss bandwidth from 3.018GHz to 3.379GHz, representing an appreciable fractional bandwidth of 11.3%. Below this band, the insertion loss drops off rapidly.

Although not shown, simulation of a lossless liner revealed highly resonant transmission

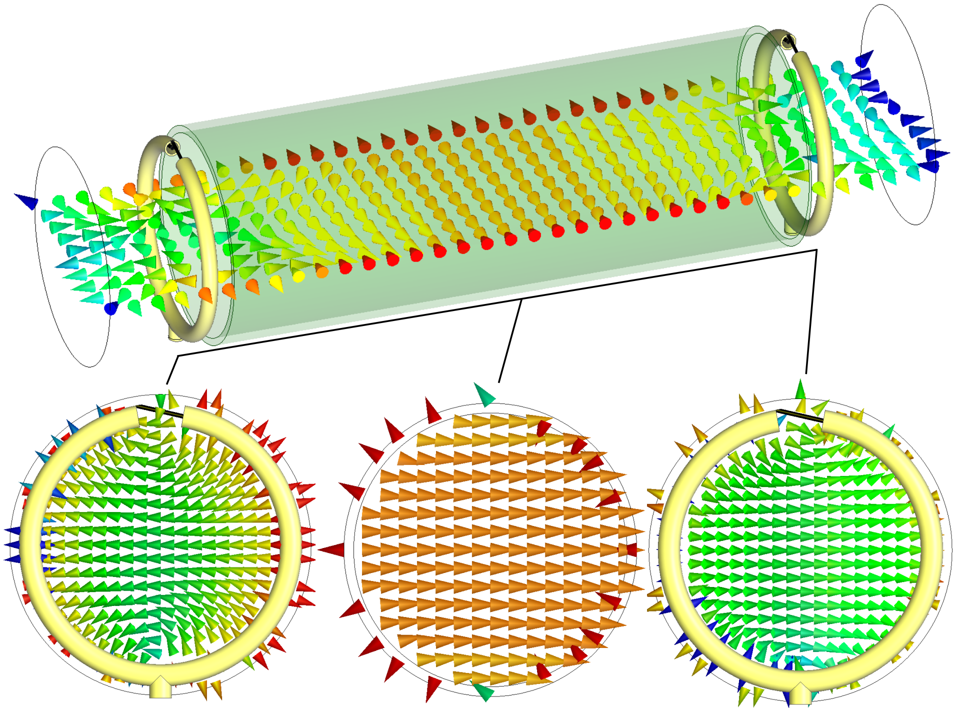

Figure 5.11: The shielded-loop-excited metamaterial-lined waveguide's electric-field vectors shown in the E-plane along the waveguide's axis, and in the planes of the excitation loop, center of the waveguide, and terminating loop at $f = 3.381\text{GHz}$. The vectors' colours indicates the magnitude.

peaks (akin to those observed in the waveguide-step transition) at which the insertion loss reached values as low as 0.3dB. It is expected the even lower insertion loss in the lossless metamaterial-lined waveguide can be achieved by significantly increasing the computational intensity of the simulation in order to more accurately capture the transmission of power. However, this is not further investigated due to the fact that the lossless assumption is unrealistic for most metamaterials.

The reader should recall that the EH_{01} mode co-propagates with the HE_{11} mode below their respective cutoffs of $f = 3.550\text{GHz}$ and $f = 3.330\text{GHz}$. Observations of the fields over the entire 10dB insertion-loss bandwidth (not shown) revealed an HE_{11} field profile, verifying that the shielded-loop antenna mitigates coupling to non-HE_{11} modes. This is illustrated in Fig. 5.11 by the electric-field vectors in the E-plane along the waveguide's axis, and in the planes of the excitation loop, center of the waveguide, and terminating

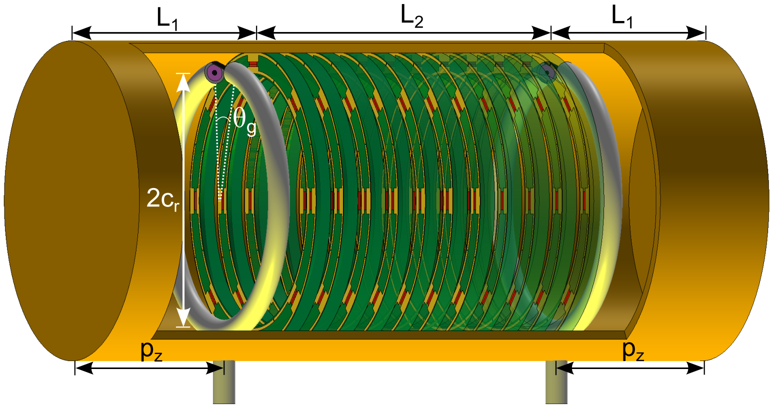

Figure 5.12: Full-wave simulation model of the metamaterial-lined waveguide realized using the printed-circuit implementation placed between two shielded-loop-antenna sources.

loop at $f = 3.381$GHz. These field profiles suggest that the shielded-loop antenna can be confidently used as a source in future practical studies to excite the HE_{11} mode in a miniaturized metamaterial-lined waveguide.

5.2 Experimental Demonstration of Below-Cutoff Transmission Using the Printed-Circuit Metamaterial Liner

This study investigates the transmission characteristics of a prototype metamaterial-lined waveguide whose liner is realized using the practical PCB metamaterial liner presented in Sec. 4.5. Figure 5.12 presents the full-wave-simulation setup, which consists of the same shielded-loop transmission setup shown in Fig. 5.9. However, now the PCB metamaterial presented in Figs. 4.8(a) is arranged into a stack of 11 layers along the intermediate waveguide's length $L_2 = 32$mm. Here, $b = 15$mm, $L_1 = 17.75$mm, $p_z = 15.0$mm, $c_r = 13.5$mm, and $\theta_g = 20°$.

The prototype metamaterial-lined waveguide's transmission setup was simulated on a Dell Precision T7610 Workstation. To achieve convergence of the simulation to within a change of 0.07 in the scattering-parameter magnitudes required 4.3 million tetrahedra and

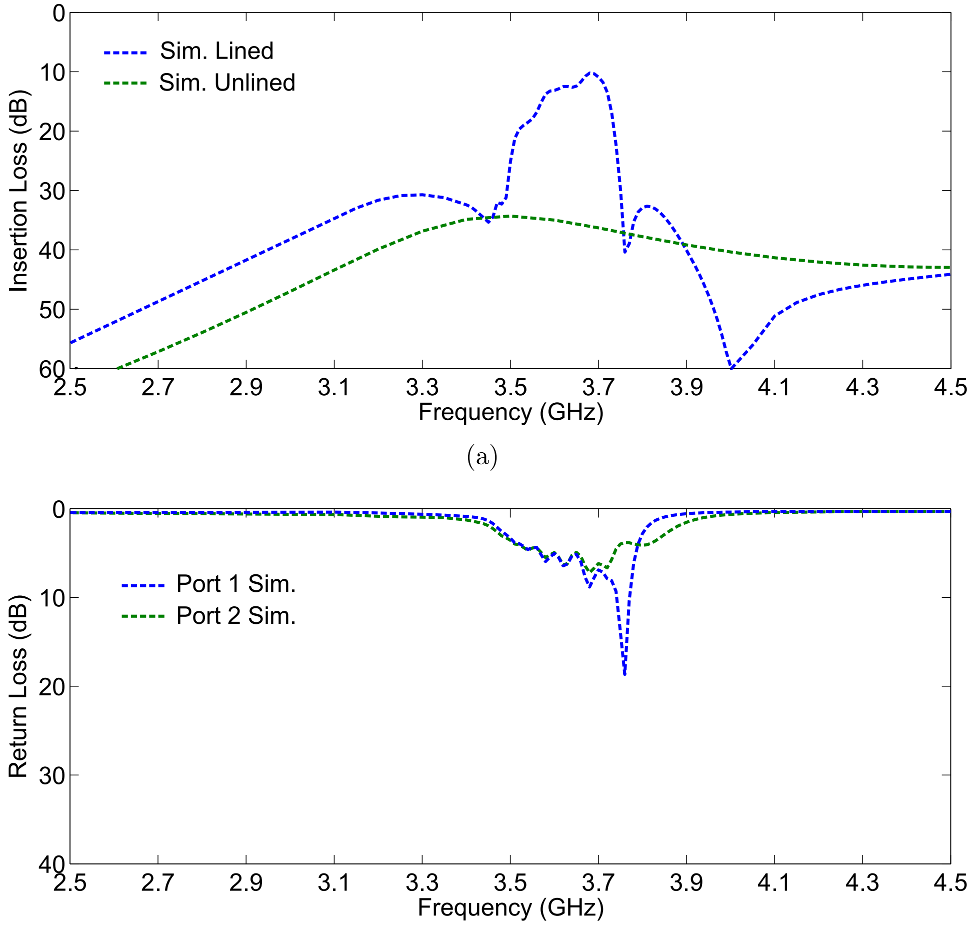

(a)

(b)

Figure 5.13: (a) Insertion loss and (b) return loss as obtained from simulation for the transmission setup depicted in Figs. 5.12.

127GB of RAM, which took 69 minutes per frequency point. Using HFSS's seed mesh, the meshing density is set to be higher in the liner region by setting the permissible maximum length of the tetrahedra. This is performed in regions of high field strength such as the host substrate, the gap (c_g) between the waveguide's inner wall, and the copper traces, radial inductors, and azimuthal gaps.

5.2.1 Transmission Simulations

Without the metamaterial liner, the unloaded vacuum-filled intermediate waveguide is within its natural evanescent region for frequencies below $f = 5.857$GHz. The dashed green curve

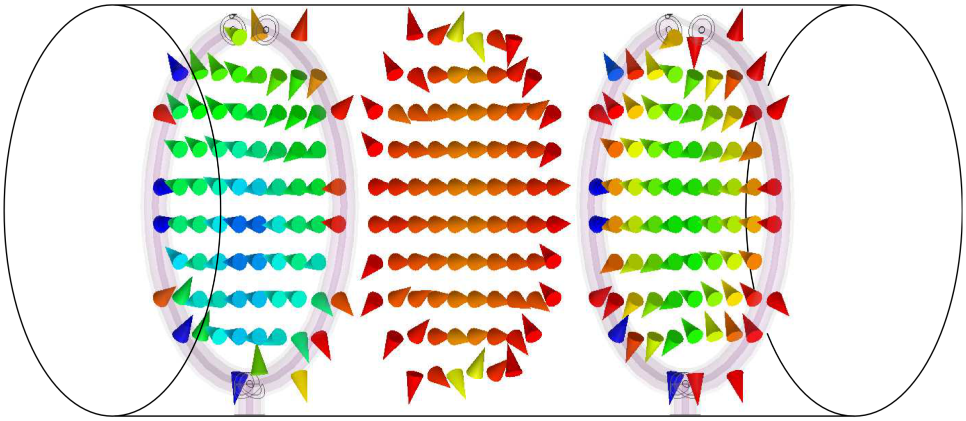

Figure 5.14: Simulated complex electric-field vectors at different planes at $f = 3.720$GHz showing excitation and detection of TE_{11} modes coupled through an HE_{11} mode supported by the metamaterial-lined waveguide.

in Fig. 5.13(a) presents the insertion loss obtained from simulations for this case, and verifies that the intermediate waveguide under cutoff strongly attenuates the TE_{11} mode. The insertion loss achieves a minimum of 34dB at $f = 3.500$GHz. Now, according to the dispersion of frequency-reduced modes in Fig. 4.9, introducing the PCB metamaterial layers should enable HE_{11} propagation below $f_{11} = 3.685$GHz by way of a frequency-reduced backward-wave band. HFSS full-wave simulations show that the insertion loss in this case (blue dashed curve in Fig. 5.13(a)) has a passband whose upper-band edge is roughly situated near f_{11} and which demonstrates improvements in the transmission by up to 25.4dB (at $f = 3.680$GHz). The dashed curves in Fig. 5.13(b) show the return loss of the simulated metamaterial-lined waveguide. It should be noted that the metamaterial layers are not symmetrical, since the shielded loops at ports 1 and 2 respectively face the inductor and the substrate dielectric. This asymmetry translates to unequal return loss profiles at Port 1 (blue dashed curves) and Port 2 (green dashed curves). Nevertheless, the return loss of both ports is described by several resonant peaks, and achieves maximum values of 18.7dB at $f = 3.760$GHz (Port 1) and 7.2dB at $f = 3.680$GHz (Port 2).

Figure 5.14 shows the simulated electric-field vectors at $f = 3.720$GHz located at the following cross sections: the transmitting shielded loop, the center of the metamaterial-lined region, and the receiving shielded loop. The field patterns reveal the characteristic

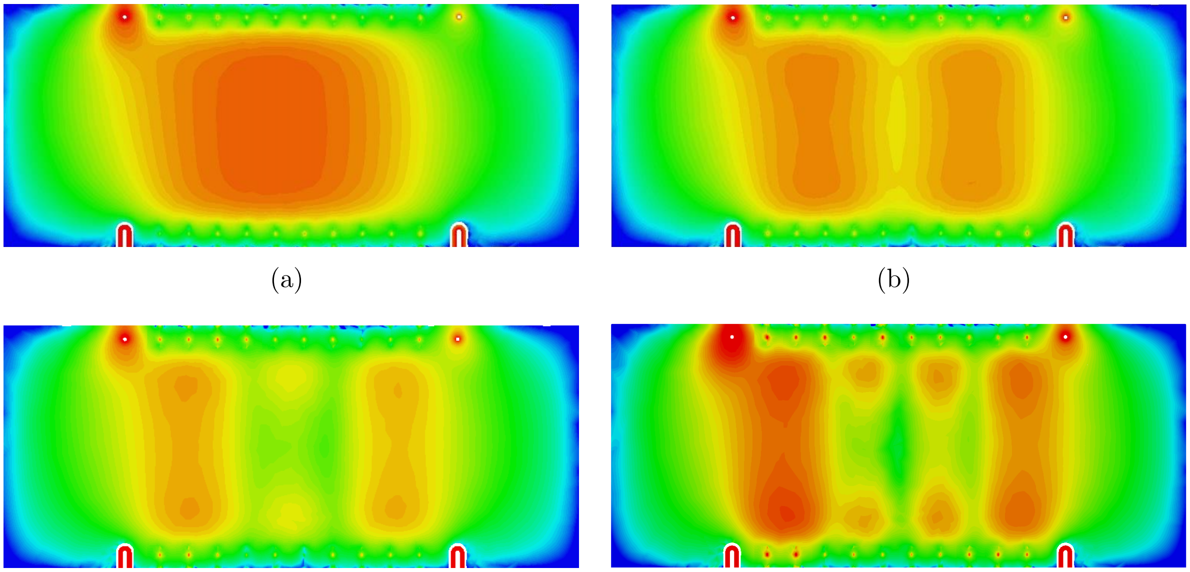

(a) (b) (c) (d)

Figure 5.15: Simulated complex electric-field magnitudes shown in the metamaterial-lined waveguide at the following transmission peaks in the frequency-reduced backward-wave passband: (a) $f = 3.720\text{GHz}$, (b) $f = 3.680\text{GHz}$, (c) $f = 3.620\text{GHz}$, and (d) $f = 3.580\text{GHz}$.

distributions and polarizations shown for the similarly excited effective-medium liners in Fig. 5.11 and confirm that the shielded loop strongly excites and receives the TE_{11} mode, which is coupled from the input to output waveguide sections through the HE_{11} mode in the metamaterial-lined waveguide.

Figures 5.15(a)–5.15(d) present the simulated complex electric-field magnitudes for the transmission setup of Fig. 5.12 in the metamaterial-lined waveguide's H-plane at the first four transmission peaks located at $f = 3.720\text{GHz}$, $f = 3.680\text{GHz}$, $f = 3.620\text{GHz}$, and $f = 3.580\text{GHz}$, respectively. It is instructive to compare these field data to those presented in Figs. 5.3(a)–5.3(f) for the isotropic, homogeneous ENNZ liner. They are similar in that each successive peak corresponds to a Fabry-Pérot-type resonance of the HE_{11} mode in which an integer number of half-wavelengths is supported by the lined waveguide section over its length. Indeed, the resonant nature of the transmission is readily observed in Figs. 5.15(a)–5.15(d). However, they differ in that the PCB metamaterial exhibits an electric field that is more evenly distributed across the waveguide's cross section and an overall reduced bandwidth of the passband. These differences are attributed to the periodic nature of the PCB implementation, which relaxes the strict boundary conditions enforced on the electric fields at the interfaces between vacuum and a homogeneous ENNZ metamaterial. Furthermore, as noted in Sec. 4.5, the finite periodicity results in a flattening of the HE_{11} dispersion, which therefore limits the lower edge of the propagating band. Nevertheless, across the PCB metamaterial liner's backward-wave band, the level of transmission is generally better than that of the homogeneous ENNZ liners. This improvement can be attributed to the decreased insertion loss over the shorter waveguide length and an improvement in matching owed to the use of the shielded-loop excitation.

5.2.2 Transmission Measurements

A Keysight PNA-X N5244A Network Analyzer was used to measure the response of the experimental prototype, as shown in Figs. 5.16(a)–5.16(b). For the unloaded vacuum-filled waveguide, the measured insertion loss (solid green curve in Fig. 5.17(a)) shows a general agreement with simulations, with a minimum of 32dB at $f = 3.676$GHz. This 4.8% upshift in its optimal transmission frequency with respect to simulations is attributed to the fabricated shielded loop's slightly smaller radius (c_r) and tolerances in realizing the gap (θ_g) by hand. The modular nature of the multi-layered PCB metamaterial allows it to now be easily inserted into the intermediate waveguide. Pins are used to ensure the position and alignment is kept consistent with the simulation model, and are removed before measurements. The measured insertion loss (solid blue curve in Fig. 5.16(a)) shows a very good agreement with simulations, in that both data exhibit the same salient features. These include an anti-resonance at frequencies above an appreciable passband, below which there is a moderate roll-off in the insertion loss. This passband achieves an insertion loss as low as 15.0dB at $f = 3.710$GHz, which is only a 4.8dB decrease and 0.8% frequency upshift with respect to the optimal transmission in simulations. This represents a 19dB enhancement in transmission over the unloaded waveguide. It should be noted that, at this frequency, the metamaterial-

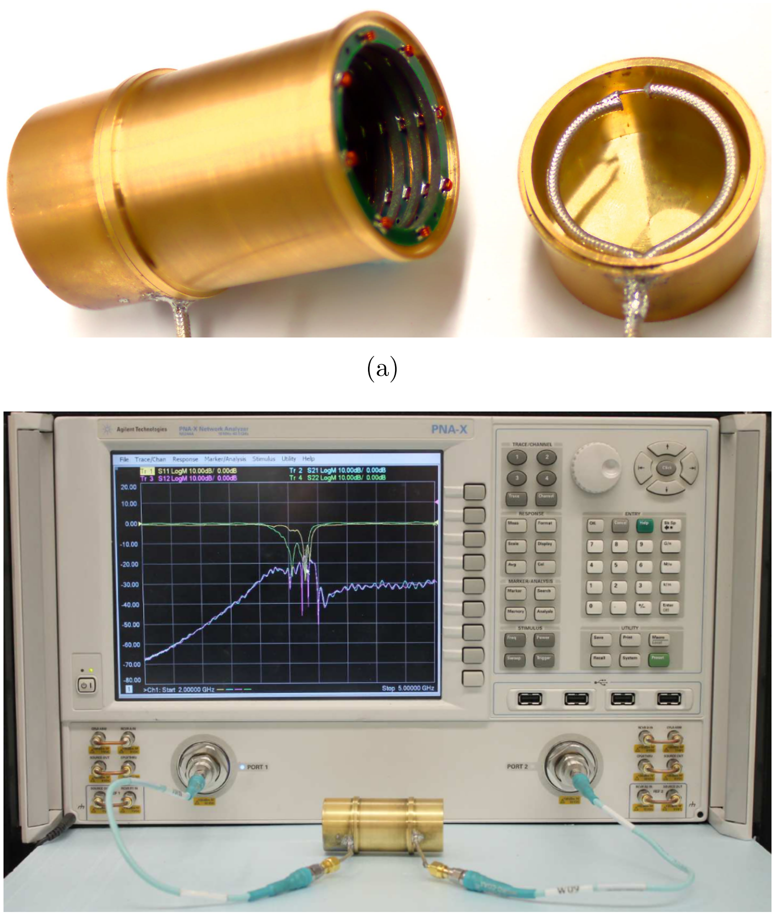

(a)

(b)

Figure 5.16: (a) Fabricated experimental prototype and (b) the experimental transmission setup of the metamaterial-lined waveguide showing one of two shielded-loop-antenna sources.

lined waveguide's cross-sectional area is 60% smaller than that of a vacuum-filled circular waveguide operating at cutoff. This is a representative example of the high levels of useful miniaturization that may be achieved with ENNZ metamaterial liners. The measured return loss in Fig. 5.17(b) for Port 1 (solid blue curve) and Port 2 (solid green curve) generally agree with those from simulations in the passband, but achieve better performance. Port 1 and Port 2 achieve a maximum return loss of 43.5dB at $f = 3.566$GHz and 26.0dB at $f = 3.675$GHz, respectively, and 10dB bandwidths of 3.3% and 7.0%, respectively.

The general agreement of the passband region between simulations and measurements occurs despite the fabrication tolerances imposed on the shielded loop and PCB metamaterial.

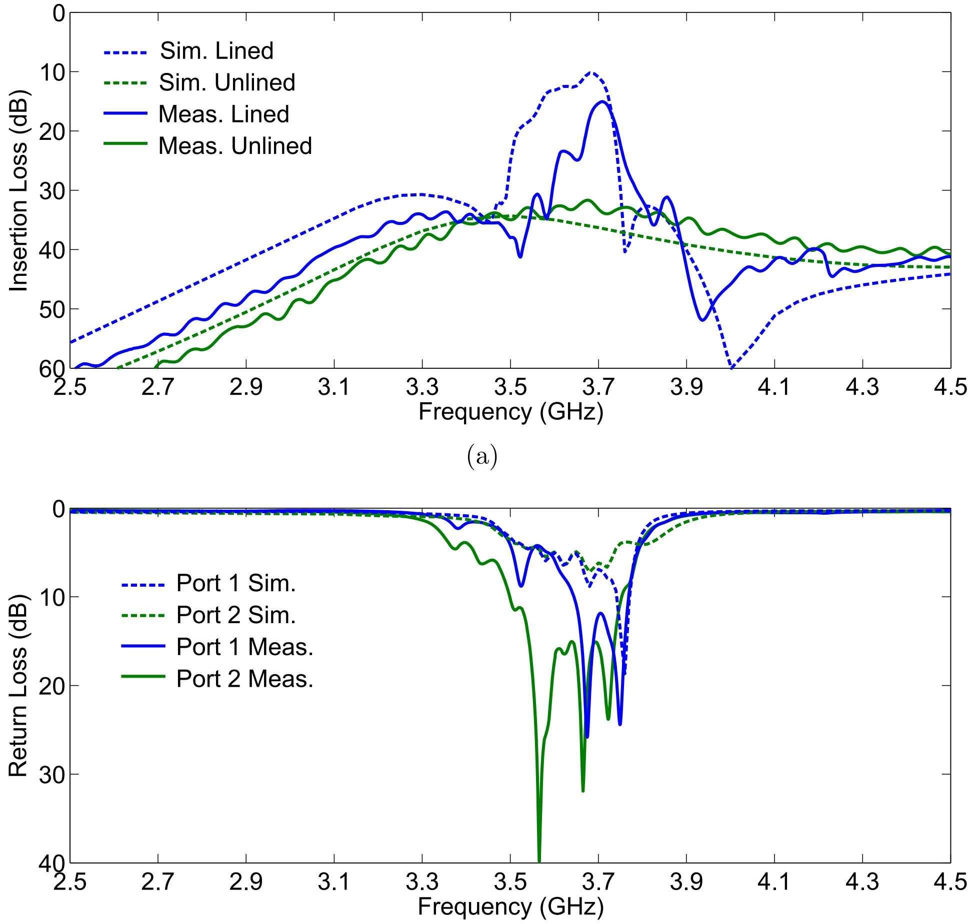

(a)

(b)

Figure 5.17: (a) Insertion loss and (b) return loss as obtained from simulation and measurements for the transmission setup depicted in Figs. 5.12–5.16(a).

This is to be expected from the discussion in Sec. 4.5.1, which highlights that, for the expected tolerances on L_0, g_0, c_g, and p_z, the HE_{11} mode's dispersion remains roughly unchanged. However, the cumulative effect of these imperfections imposed on the multilayered stack will increase insertion loss due to decreased coupling between layers, particularly at lower frequencies in the backward-wave band where the unit cells lose their homogeneity. Furthermore, the inductor's loaded quality factor in the fabricated unit cell may have been lower than approximated in simulations, which increases the insertion loss in the passband while preserving its general profile. Although more accurate simulations would have lowered the discrepancy, the computational intensity to achieve this was not feasible. It is expected that the observed transmission may be improved by reducing the loss in the liner region using either higher-Q inductors or increasing liner thickness to minimize field confinement. Of course, as the liner becomes thicker (i.e., $a \rightarrow 0$), the waveguide becomes homogeneously ENNZ-filled and transmission is expected to become independent of its geometry [88]. It may also be possible to improve the return loss's bandwidth by developing novel feeding structures that are electrically connected to the unit cell, such as in the case of the coaxial pin and SRR in Ref. [133], in which a 10dB return loss fraction bandwidth of 46% was observed. A further discussion of bandwidth and loss can be found in Sec. 6.3.

5.3 Application: Traveling-Wave Magnetic Resonance Imaging

The ability of a thin metamaterial liner to miniaturize a circular waveguide while keeping most of its interior empty could prove useful in magnetic resonance imaging (MRI) technology that employs waveguide concepts. MRI is a powerful, non-invasive, radiological diagnostic tool in which images of the body are formed from the interaction between tissue matter, radio frequency pulses, and a strong static magnetic field . A patient is placed into the interior of a tube surrounded by a superconducting solenoid that produces an strong magnetic field (B_0) down the length of the bore. An electromagnetic resonant coil excites an RF signal in the body which causes a precession of the nuclear magnetization about B_0's axis. The rate of this precession is termed the Larmor frequency (ω_L) and is proportional to B_0. The measured MR signal arises from this precession, by way of a small induced electrical voltage in a receiver coil [134]. In traditional MRI machines, these coils must be placed in close proximity to the patient (i.e., the coil's near-field), which can be achieved in full-body scanners by using cylindrical resonant coils that conform to the MRI bore's geometry [134]. In the recently introduced traveling-wave (TW) magnetic-resonance-imaging (TW-MRI) technique, the bore of an MR scanner is treated as a circular electromagnetic waveguide capable of supporting

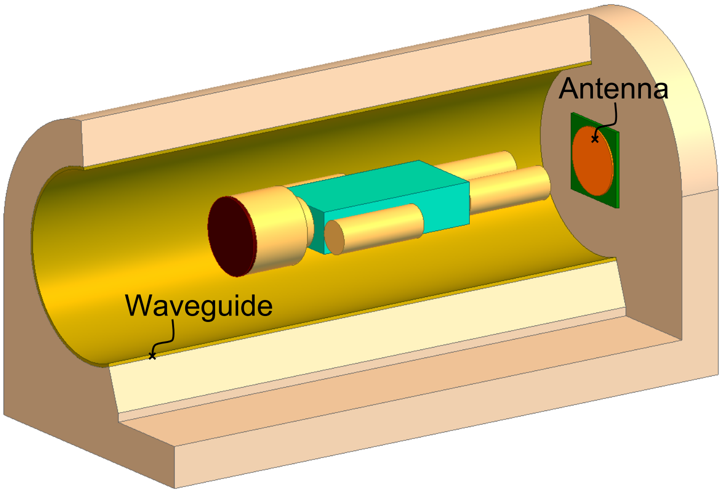

Figure 5.18: A depiction of a typical TW-MRI scanner.

TWs that may be both excited and detected at long range using conventional RF antennas [135]. A typical TW-MRI human-sized scanner is shown in Fig, 5.18. A circular waveguide large enough to accommodate the human body cannot propagate TWs at frequencies below its natural TE_{11} mode cutoff frequency, of several hundreds of megahertz, necessitating that detection and generation of the MR signals (which are centered around ω_L) to be above this cutoff. This requires a sufficiently strong magnet, which is only satisfied by ultra-high field-strength MRI machines (e.g. 7T), and, as a result, existing 1.5T and 3T clinical MR scanners cannot exploit this intriguing new detection paradigm. While imaging at 7T provides a high intrinsic signal-to-noise ratio (SNR) that generally leads to improved image clarity, the reduced wavelength of the RF waves in the human body results in inhomogeneous power absorption and the formation of so-called ‘hot spots’ in the human body, increasing the risk of RF burns [136]. Furthermore, the supporting of standing-wave field distributions in the body decreases the RF field homogeneity, resulting in the creation of dark spots in the MRI image [137]. Achieving TW-MRI at lower frequencies and longer wavelengths would solve these problems, and would significantly reduce the cost associated high-field magnetics and mitigate fears associated with higher B_0. Previous works have sought to reduce the cutoff frequencies by partially filling the bore with high permittivity materials [138] or introducing an additional conductor for coaxial-like propagation [139]; however, these approaches occupy valuable space within the bore and can lead to claustrophobia. Moreover, they do not substantially lower the cutoff frequency of the bore.

A thin metamaterial liner exhibiting ENNZ permittivity applied to the interior of the MR scanner bore would introduce a frequency-reduced HE_{11} mode; thereby enabling TW-based imaging using lower B_0 field strengths without occupying a significant amount of space within the bore. Simply retrofitting current clinical scanners by a comparatively inexpensive metamaterial liner will allow for them to be operated well below their natural cutoff frequencies. Consider a 58cm-diameter (human-sized) MR scanner bore which has a natural cutoff frequency of 303.3MHz. The design equation given by Eq. 3.13 predicts that lining this bore's interior with a 2mm thick metamaterial layer possessing a relative uniaxial permittivity of $\epsilon_{t2} = -0.08$ will introduce a cutoff at 101.8MHz which is well below the Larmor frequency of conventional 3T scanner. We have proposed that this approach may lead to dramatically improved image quality through increased spatial uniformity of the electric and magnetic fields within the bore [30, 140]. The metamaterial liner's rich spectrum of frequency-reduced modes may prove useful for parallel imaging or RF shimming, in which each frequency-reduced mode is a excited by its own probe and represents a single channel. Multichannel transmission permits tailoring the superposition of multiple RF field components, to provide either increased RF field homogeneity or spatially diverse field patterns [141, 142].

Chapter 6

Radiation Characteristics of Miniaturized Metamaterial-Lined Circular OEWG Probe Antennas

In Chapter 5, it was shown that the metamaterial-lined waveguide exhibited substantially improved transmission over a similarly sized (and below-cutoff) hollow circular waveguide in both simulations and experiments. This chapter will investigate the implication of below-cutoff transmission on the radiation characteristics of a metamaterial-lined open-ended waveguide (OEWG) probe antenna. Whereas the miniaturization of OEWG probes may be achieved by homogeneously filling their interior with dielectrics, metamaterials [115], or complex-matching networks [104], we show that the same function can be achieved with a thin metamaterial liner, thereby allowing the interior volume of the probe to interact with the outside environment. Such a probe would be able to sample nearby electromagnetic fields at sub-wavelength spatial resolutions, but access to the interior volume also enables the probe to sense materials such as gases, liquids, or granular solids placed inside the probe, in which the added bonus of miniaturization would minimize the required bulk and losses of such filling materials. This chapter aims to provide theoretical and experimental groundwork for these probing applications by investigating, in detail, the radiation performance of OEWG probe antennas that have been miniaturized by the introduction of thin metamaterial liners.

This study will focus on the metamaterial-lined waveguide's frequency-reduced HE_{11} mode, comparing its far-field characteristics to those of the TE_{11} mode in conventional-sized and below-cutoff OEWG probes through both antenna aperture theory and full-wave transmission simulations using the ideal and practical excitations presented in Chapter 5. Once again, an effective-medium description of the metamaterial liner in the OEWG probe is employed in initial numerical investigations, whose geometrical and material parameters (i.e., b, a, L_1, L_2, $\epsilon_2(\omega)$) remain consistent with the previous studies in Sec. 5.1; hence, the metamaterial-lined waveguide constituting the OEWG probe shares the same dispersion of frequency-reduced modes that was reported in Sec. 3.2.4. Furthermore, the experimental prototype of the metamaterial-lined waveguide whose liner is realized using the printed-circuit implementation presented in Sec. 4.5 is reused here, but with one of the shielded-loop probes and feeding waveguides removed. The similarities between the enclosed waveguides and OEWG probes allow for a number of parallels to be drawn.

6.1 Numerical Investigations of Isotropic, Homogeneous ENNZ-Lined OEWG Probe Antennas

As noted in the previous transmission study, the dispersion of frequency-reduced modes is not greatly altered between isotropic and uniaxial metamaterial liners, particularly when the liner is thin. To aid in the numerical investigation of the metamaterial-lined OEWG probe's radiation features, the liner is assumed for simplicity to be isotropic.

6.1.1 Aperture Theory

Let us consider one end of the infinitely long waveguide to be truncated such that its open aperture is free to radiate into space. The aperture's electric fields ($\bar{E}^{ap} = (E^{ap}_{\rho}, E^{ap}_{\phi}, E^{ap}_{z})$),

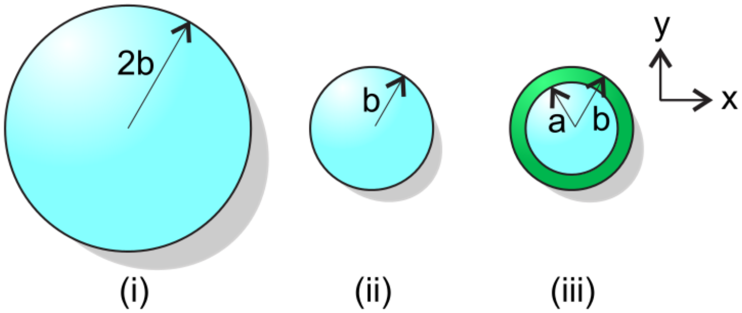

Figure 6.1: The three compared OEWGs, termed (i) 'Standard', (ii) 'Cutoff', and, (iii) 'MTM-Lined'.

which may be obtained from the theoretical field expressions of the metamaterial-lined waveguide in Sec. 3.1, are related to the far-field expressions ($\bar{E}^{ff}$) using the well known Huygen's Field Equivalence Principle (see, for example, Ref. [143]). The aperture is assumed to be mounted on an infinite ground plane, such that the tangential components of ($\bar{E}^{ap}$) can be replaced by equivalent magnetic-current sources. Although the infinite ground plane is not realizable in practice, it allows us to neglect diffraction from the edge of a finite ground plane, which affects the far-field patterns of the aperture particularly when the aperture may be strongly miniaturized. The radiation integral over the aperture's surface can be separated into contributions from the vacuum and liner regions, taking the following form:

$$\overline{E}^{ff} = \iint\limits_{S,Vacuum} \mathcal{L}\left(\bar{E}^{ap}\right) dS + \iint\limits_{S,Liner} \mathcal{L}\left(\bar{E}^{ap}\right) dS. \tag{6.1}$$

The components of the integrand ($\mathcal{L}$), expressed in cylindrical form, can be found in Ref. [143]. Using this approach, the contribution of the liner's fields towards the far-field patterns may be isolated.

Figure 6.1 presents three circular-waveguide geometries that will be compared in the remainder of this section. At this point, we establish some nomenclature: a homogeneously vacuum-filled OEWG of *radius* $2b = 30$mm operating above its TE_{11} mode's natural cutoff frequency of $f_c = 2.928$GHz is termed 'Standard' (i); another of half the radius ($b = 15$mm) operating below its natural cutoff frequency of $f_c = 5.857$GHz is termed 'Cutoff' (ii); and

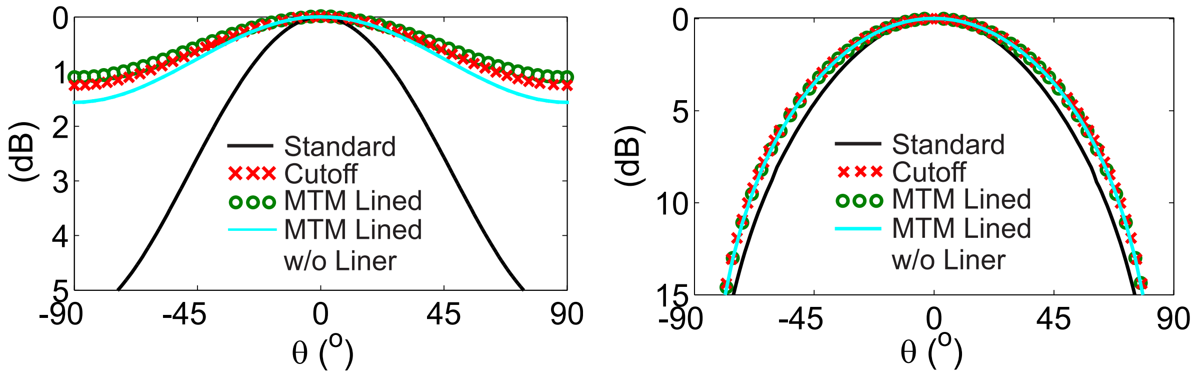

(a) (b)

Figure 6.2: Far-field directivity patterns at $f = 3.381$GHz obtained from Eq. (3.5) for the OEWG's (a) H-plane ($\phi = 0°$) and (b) E-plane ($\phi = 90°$) shown for the 'Standard' OEWG, the 'Cutoff' OEWG , and the 'MTM-Lined' OEWG including and excluding the liner fields.

the metamaterial-lined OEWG, whose dispersion and geometrical parameters ($b = 15$mm, $a = 14$mm) were presented previously, is termed 'MTM-Lined' (iii).

Figure 6.2(a) and Figure 6.2(b) compare, for each of these cases, the normalized H-plane ($x - z$ plane) and E-plane ($y - z$ plane) directivity patterns, respectively, at $f = f_1 = 3.381$GHz. An examination of the directivity patterns of the 'Standard' (solid black curve) and 'Cutoff' (red cross markers) OEWGs show that the reduction of aperture size broadens the OEWG's main beam significantly in the H-plane, but only marginally in the E-plane. This is attributed to an increase in operating wavelength with respect to the aperture's physical size, which leads to less phase variation across the aperture. Since the H-plane contains the greatest field variation, the impact is more pronounced in this plane.

Now, the metamaterial liner is introduced into the 'Cutoff' OEWG, for which the comparison frequency (f_1) is just inside the HE_{11} mode's propagating backward-wave band. The directivity patterns of the 'MTM-Lined' OEWG (green circle markers) are very similar to the 'Cutoff' waveguide, and only differ by a slightly narrower beam width in the H-plane. Since both the 'Cutoff' and 'MTM-Lined' OEWGs have similar negligible electric-field variation in their respective vacuum regions, this difference is attributed to the discontinuous high field strength in the thin liner region. This is affirmed by excluding the fields in the liner regions

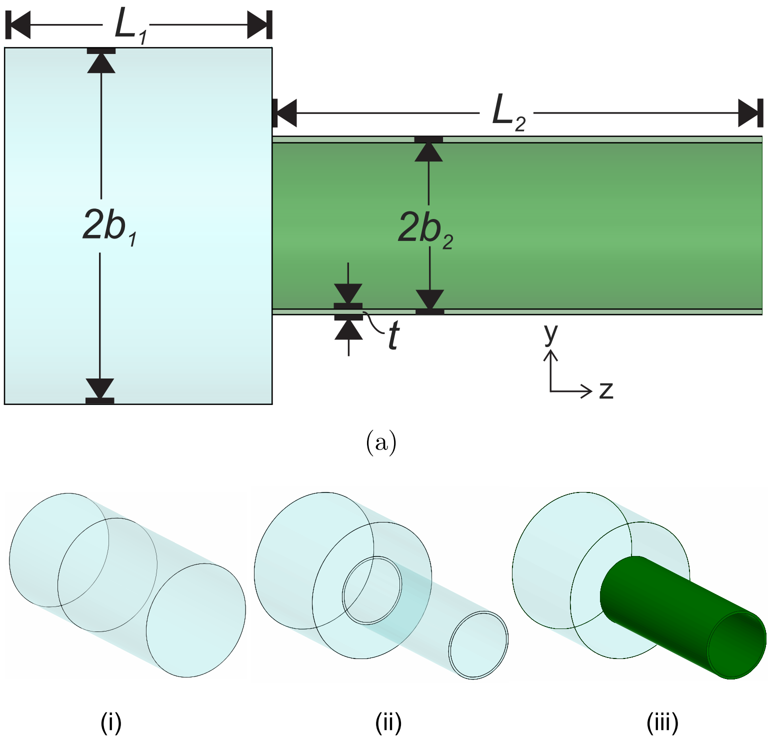

(a)

(b)

Figure 6.3: (a) Generic full-wave simulation model of the OEWG probe used in the comparison of the three cases shown in (b). Case (i) is a large above-cutoff waveguide and termed ‘Standard’. Case (ii) is an above-cutoff waveguide connected to a smaller below-cutoff waveguide and termed ‘Cutoff’. In case (iii), the smaller waveguide contains a metamaterial liner possessing complex dispersive permittivity and is termed ‘MTM-Lined’.

in the integration, such that only the inner vacuum region contributes to the far-fields. In this case (solid teal curve), the patterns are very similar to those of the under-cutoff OEWG, as expected. Therefore, although metamaterial liners do not significantly alter the directivity of the miniaturized OEWG, the next section presents full-wave simulations that show that their impact on gain may be dramatic.

6.1.2 Waveguide Step Transition

In this section, it will be demonstrated that miniaturized waveguides are capable of efficiently radiating power into free space, and their directivity patterns are similar to those of the homogeneously vacuum-filled OEWG. The waveguide-step transition used in Sec. 5.1.1 is

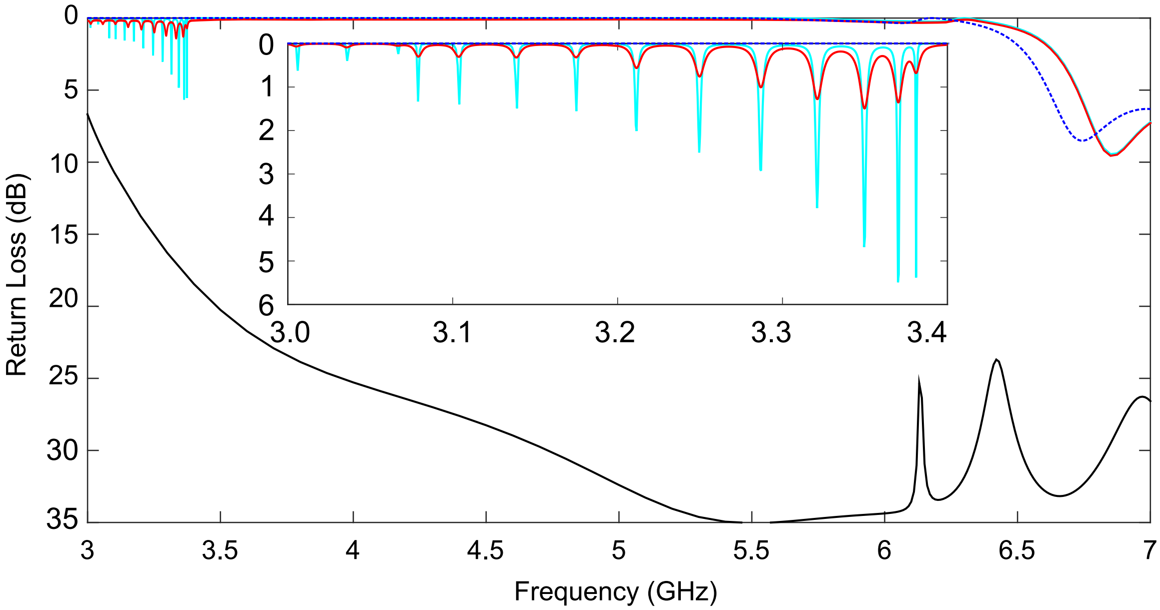

Figure 6.4: The return loss for the 'Standard' (solid black curve), 'Cutoff' (dashed blue curve) 'MTM-Lined Lossless' (solid teal curve) and 'MTM-Lined Lossy' (solid red curve) OEWGs.

reused here to limit this study towards the radiation properties of the 'MTM-Lined' OEWG's HE_{11} mode. HFSS [129] is employed to simulate the generic model shown in Fig. 6.3(a), for the three cases shown in Fig. 6.3(b). In each case, a large vacuum-filled PEC circular waveguide of length $L_1 = 45$mm and radius $b_1 = 30$mm contains a waveport at its closed end that excites the TE_{11} mode for frequencies above its cutoff of 2.928GHz. This, in turn, couples into a connecting waveguide section of length $L_2 = 82.5$mm that is opened at one end, and the whole structure is enclosed in a spherical radiation boundary of radius 76mm.

Now, we reuse the nomenclature used in the previous aperture field study to distinguish the different connecting OEWGs in each case in Fig. 6.3(b). Case (i) contains a homogeneously vacuum-filled OEWG of radius equal to that of the excitation waveguide ($b_2 = 30$mm) operating above its TE_{11} mode's natural cutoff frequency and is termed 'Standard'. Case (ii) contains a homogeneously vacuum-filled OEWG of half the radius ($b_2 = 15$mm) operating below its natural cutoff frequency of $f_c = 5.857$GHz and is termed 'Cutoff'. Case (iii) lines the under-cutoff waveguide of case (ii) with an isotropic ENNZ metamaterial, whose dispersion and geometrical parameters ($b_2 = 15$mm, $t = 1$mm) were presented in Sec. 3.2.4, and is termed ‘MTM-Lined’.

Figure 6.4 presents the return loss of each investigated OEWG probe antenna. As expected, the return loss increases above the cutoff frequencies of the ‘Standard’ (black solid curve) and ‘Cutoff’ (blue dashed curve) cases, in which the former occurs before the shown frequency range. The metamaterial liner is assigned the dispersive permittivity, $\epsilon_2(\omega)$, reported in Sec. 3.2.4 for both lossless (termed ‘MTM-Lined Lossless’ with $\omega_t = 2\pi \times 0\text{MHz}$) and lossy (termed ‘MTM-Lined Lossy’ with $\omega_t = 2\pi \times 5\text{MHz}$) cases. Accordingly, HE_{11} propagation should occur below $f_1 = 3.381\text{GHz}$ for the frequency-reduced backward-wave band and above 5.958GHz in the upper band. Figure 6.4 shows the return loss in the ‘MTM-Lined Lossless’ (teal solid curve) and ‘MTM-Lined Lossy’ (red solid curve) cases. Indeed, the metamaterial liner results in an upper passband, which is described by a return loss profile similar to the ‘Cutoff’ case but shifted to higher frequencies, and introduces a lower passband, which is described by several resonant return-loss peaks. The inset in Fig. 6.4 zooms into the return loss band. Whereas the lossless metamaterial-lined waveguide enclosed between two larger and hollow circular waveguides in Sec. 5.1.1 exhibited nearly 0dB insertion loss and better than 30dB return loss at the transmission peaks, the ‘MTM-Lined Lossless’ OEWG’s return loss does not exceed 6dB across the presented frequency range, leaving only tiny fraction of the feeding waveguide’s incident power to be radiated. This is due, in part, to the reflections that occur at the open aperture of the ‘MTM-Lined’ OEWG. Although the radiation at the aperture presents complex radiation impedance that can selectively improve the return loss, the introduction of loss typically strongly diminishes the matching. Nevertheless, the return loss of the ‘MTM-Lined Lossy’ OEWG is comparable to the return loss observed in Fig. 5.2(b) for the similarly excited lossy metamaterial-lined waveguide, suggesting that the introduction loss dampens the reflections from the open aperture, thereby decreasing the sensitivity of the return loss to aperture’s complex impedance.

As previously shown in Sec. 5.1.1, each of these peaks is akin to a Fabry-Pérot-type resonance through the metamaterial-lined waveguide section. The distribution of resonance

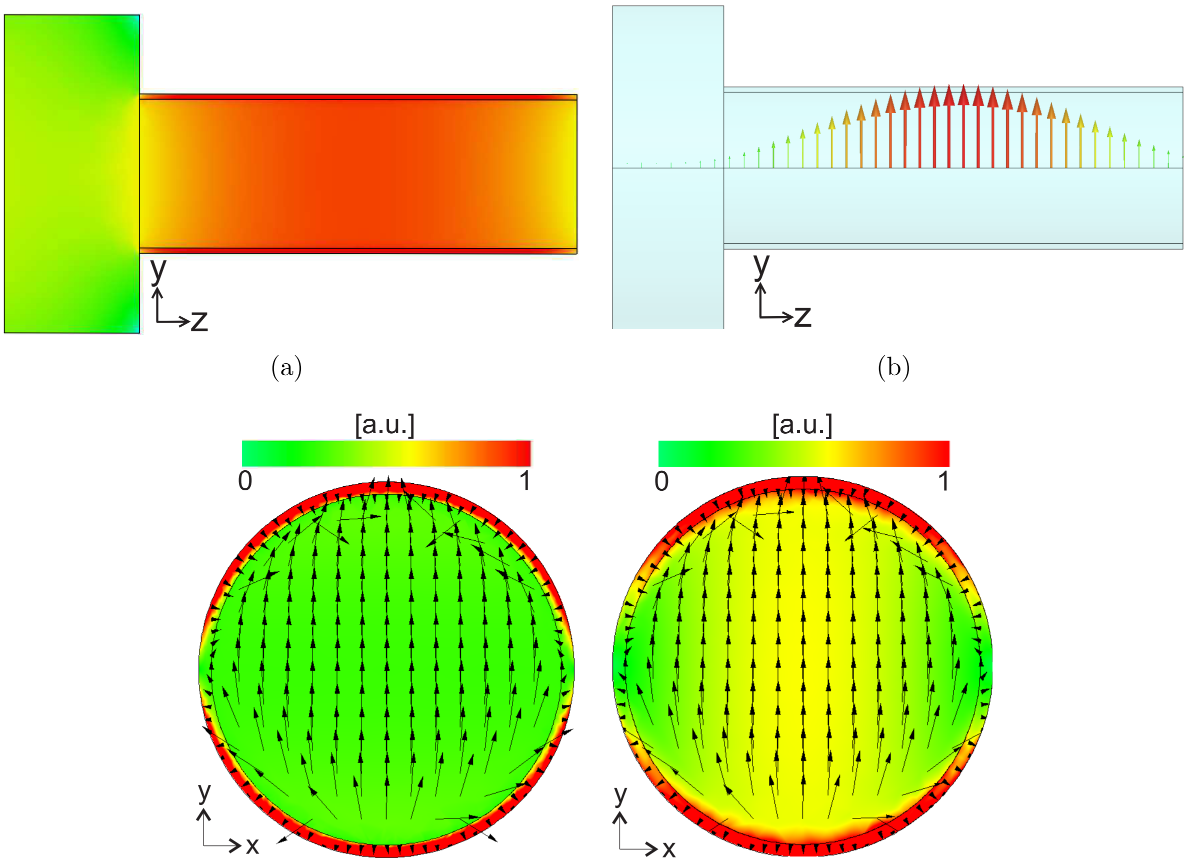

(a) (b) (c) (d)

Figure 6.5: Complex electric field (a) magnitudes and (b) vectors along a longitudinal cut in the E-plane. Electric field vectors along a transverse cut taken at (c) the center of the 'MTM-lined' OEWG and (d) its open aperture. All data presented at $f = 3.381$GHz for the lossless case.

frequencies may be designed by varying either the metamaterial-lined waveguide's length or the liner's permittivity dispersion profile. As such, these resonant frequencies are coincident with those observed in the transmission through the metamaterial-lined waveguide of the same length (L_1) and dispersion $\epsilon_2(\omega)$. Figures 6.5(a) and 6.5(b) present the complex electric-field magnitudes and vectors, respectively, in the E-plane at $f = 3.381$GHz, in which the resonant distribution is evident. The electric fields are purely transverse (ρ- and ϕ-directed) with no longitudinal (z-directed) component, which verifies that an *HE*-type mode, and not the EH_{01} mode, is strongly excited at the waveguide junction. An examination of the fields in the transverse plane at the center of the 'MTM-lined' OEWG (Fig. 6.5(c)) and at its open

	Standard	Cutoff	MTM-Lined	
			Lossless	Lossy
Freq. (GHz)	3.381	3.381	3.381	3.350
Direct. (dB)	7.69	5.96	5.49	5.32
η_{rad} (%)	96	0	75.3	12.9
Gain (dB)	7.51	-71.5	4.26	-3.57
HPBW$_H$(°)	69.0	82.0	77.0	76.4
HPBW$_E$(°)	71.0	74.8	72.6	72.2
F/B (dB)	8.54	5.33	3.83	3.86

Table 6.1: Waveguide-Step Excited Antenna Parameters

aperture (Fig. 6.5(d)) reveals a distinct HE_{11} field pattern, as desired.

Figures 6.6(a)-6.6(b) present the H-plane and E-plane cuts, respectively, of the normalized directivity patterns for each investigated case. In addition, Table I presents relevant antenna parameters such as radiation efficiency (η_{rad}), half-power beamwidth (HPBW), and front-to-back (F/B) ratio. At $f = 3.381$GHz, the 'Standard' (solid black curve) case achieves a 7.69dB directivity, an H-plane HPBW of 69.0°, and a respectable F/B ratio of 8.54dB. Decreasing the outer radius by half in the 'Cutoff' (dashed teal curve) case causes a 1.73dB decrease in directivity and a 13.0° increase in the H-plane HPBW. An increase in the side-lobe and back-lobe levels suggests that substantial currents are also formed on the outer surface of the PEC waveguides. However, as indicated in Table I, the operation of the 'Cutoff' waveguide in the evanescent regime results in truly negligible radiation efficiency and hence, no useful gain.

Now, introducing the lossless metamaterial liner into the 'Cutoff' case and focusing on the radiation pattern at its first resonant peak at $f = 3.381$GHz (solid green curve), the directivity is roughly maintained at 5.49dB. However, the improved return loss at this frequency due to the metamaterial liner causes a dramatic increase in the radiation efficiency (75.3%) and gain (4.26dB). Since the 'MTM-Lined Lossless' and 'Lossy' liners have similar aperture-field profiles, the pattern in the lossy case (red markers) overlaps that of the

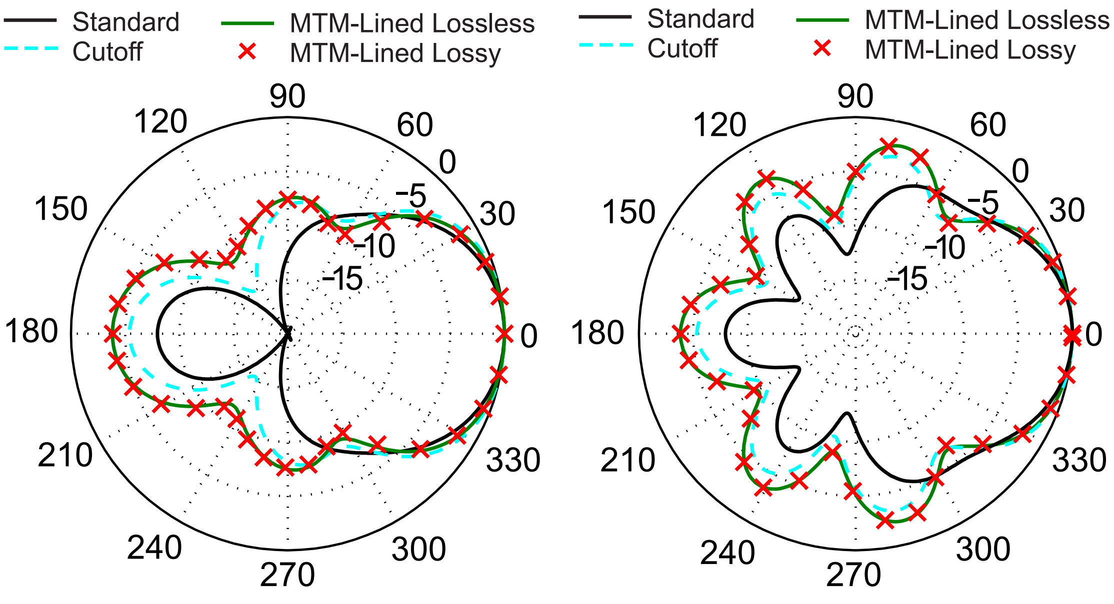

(a) (b)

Figure 6.6: Comparing normalized (a) H-plane and (b) E-plane directivity patterns of the OEWG obtained from simulations of the 'Standard', 'Cutoff', and 'MTM-Lined' (Lossless and Lossy) cases. All data presented at $f = 3.381\text{GHz}$.

lossless case. However, the introduction of loss reduces the relative aperture-field strengths, and for the third resonant peak at $f = 3.350\text{GHz}$, the radiation efficiency is only 12.9% corresponding to a gain of -3.57dB. This is, nevertheless, a useful gain that represents a nearly 70dB improvement over the 'Cutoff' OEWG. Such gain improvements may potentially enable previously impossible sub-wavelength spatial resolution above the noise floor, and/or with increased dynamic range, particularly in continuous-wave applications or those involving narrowband phenomena.

As previously noted, this manner of excitation suffers from poor matching. The next section investigates the balanced-shielded loop as a practical source to more efficiently excite the HE_{11} mode and to mitigate the potential excitation of other modes. This eliminates the need for a larger excitation waveguide and enhances the compactness of the OEWG probe.

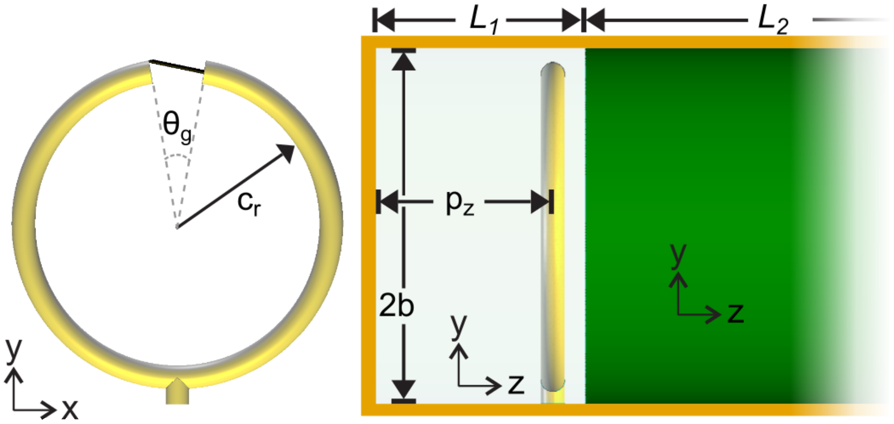

Figure 6.7: Full-wave simulation model of the shielded-loop-excited 'MTM-Lined' OEWG probe.

6.1.3 The Balanced Shielded-Loop Excitation

The balanced-shielded loop excitation was shown in Sec. 5.1.2 to couple efficiently to the lossy metamaterial-lined waveguide's HE_{11} mode without coupling to other frequency-reduced modes. In fact, the shielded-loop excitation strategy benefits from a compact size and exhibited a high degree of matching to the HE_{11} mode in both effective-medium and practical metamaterial-lined waveguides. It will now be used to excite the HE_{11} mode in the metamaterial-lined OEWG probe using the full-wave simulation model presented in Fig. 6.7, whose geometrical and material parameters are kept consistent with $b = 15$mm, $t = 1$mm, $L_2 = 82.5$mm, and $\epsilon_{t2}(\omega)$ as reported in Sec. 3.2.4. In transmission and antenna setups employing the waveguide-step transition in Secs. 5.1.1 and 6.1.2, respectively, similar return-loss profiles were observed across the lossy metamaterial-lined waveguide's HE_{11} mode's backward-wave band. As previously noted, this suggests that the different terminating impedances due, for example, to the larger waveguide or to the open aperture have little effect on the degree of matching at the input, provided the liner is lossy. Accordingly, in this study the optimized shielded-loop excitation's position and placement used in the transmission setup is reused here with $L_1 = 17.8$mm, $p_z = 15.0$mm, and $c_r = 13.5$mm.

Indeed, these optimized parameters provide a significantly improved return loss (> 10dB) at each resonant peak, as shown in Fig. 6.8, while still maintaining a return loss greater than

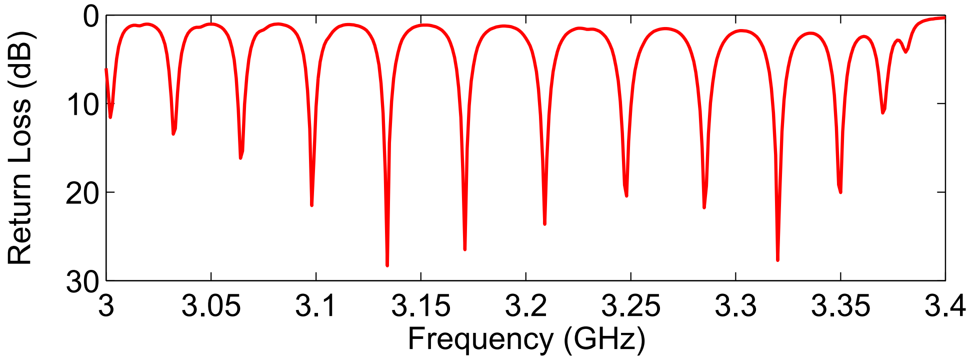

Figure 6.8: The return loss of the shielded-loop-excited 'MTM-Lined' OEWG.

1dB across the band. The frequency range in Fig. 6.8 is limited to clearly observe the highly resonant return loss peaks, and, as will be shown, encompasses the entire bandwidth in which the OEWG exhibits desirable radiation characteristics. Outside the shown frequencies, the 'MTM-Lined' OEWG's return loss profile is similar to the return shown of the waveguide excited metamaterial-lined waveguide shown in Fig. 6.4.

Consider the resonant peak at $f = 3.320$GHz. Figure 6.9(a) shows the electric-field vectors and complex magnitudes at this frequency taken at three locations in the waveguide: at the shielded loop, at the center of the metamaterial-lined region, and at the open aperture. The field patterns confirm that the shielded loop strongly excites the TE_{11} mode, which is coupled to the HE_{11} mode in the metamaterial-lined waveguide. It should be noted that the observable longitudinal (z-directed) electric-field vectors at the open aperture is due the open-boundary condition in this plane.

Shown in Fig. 6.9(b) are the H-plane (red curve) and E-plane (green curve) normalized directivity patterns at $f = 3.320$GHz. The far-field features are similar to the waveport-excited 'MTM-Lined Lossy' case, but with a reduced directivity of 3.43dB and a F/B ratio of 1.38dB. This is expected with the elimination of the larger excitation waveguide, whose front face served as a reflector. Indeed, it has been observed that the directivity of the miniaturized probe may be increased by re-introducing a reflecting plate behind the open aperture. These field and radiation patterns also exhibit a linear polarization purity of greater than 35dB, which is consistent over the entire band. The antenna parameters for the

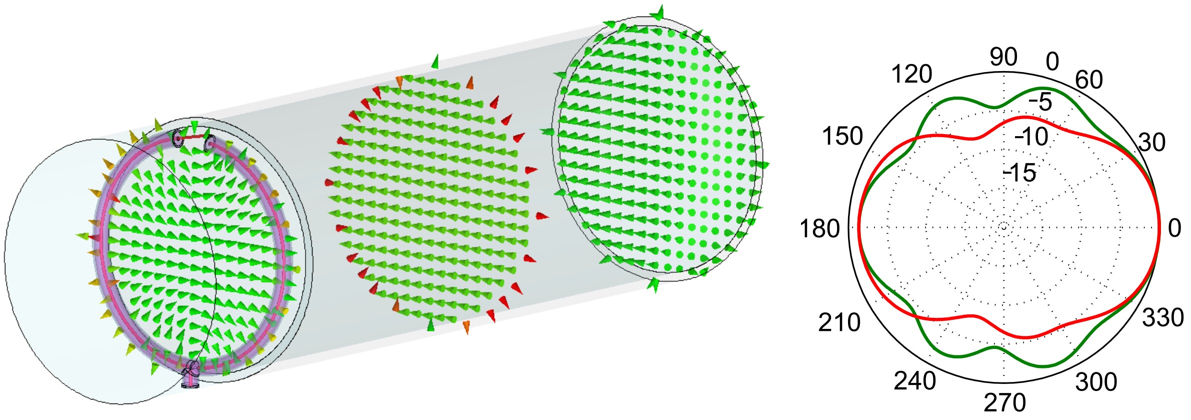

(a) (b)

Figure 6.9: The shielded-loop-excited OEWG's (a) electric-field vectors shown in the planes of the loop, center of the waveguide, and open aperture, and (b) the normalized directivity patterns in the H-plane (red curve) and E-plane (green curve) at $f = 3.320\text{GHz}$.

Direct. (dB)	η_{rad}	Gain (dB)	HPBW$_H$	HPBW$_E$	F/B (dB)
3.43	28.8	-1.94	82.2	168.0	1.38

Table 6.2: Shielded-Loop-Excited Antenna Parameters

shielded-loop-excited case are summarized in Table II.

Figure 6.10 presents the gain and radiation efficiency for the shielded-loop-excited metamaterial-lined OEWG. The following radiation-efficiency definitions are used to aid in discussion: $\eta_{r,i} = P_{rad}/P_{inc}$ (solid red curve) and $\eta_{r,a} = P_{rad}/P_{acc}$ (solid blue curve), in which P_{rad}, P_{acc}, and P_{inc} are the radiated, accepted, and incident powers, respectively, with respect to the coaxial feed. Whereas $\eta_{r,i}$ captures both return loss and insertion loss due to the liner, $\eta_{r,a}$ captures only insertion loss (the IEEE definition of radiation efficiency). Progressing from the HE_{11} cutoff ($f_{11} = 3.381\text{GHz}$) down further into the backward-wave band, $\eta_{r,a}$ ramps up to its maximum value of 29.7% at $f = 3.310\text{GHz}$, after which it experiences a generally linear decrease as frequency reduces. This is consistent with the observed behaviour of HE_{11} mode's attenuation constant (α) in Fig. 3.8(b), which also increases towards lower frequencies. However, given the strongly dispersive nature of the metamaterial-lined OEWG, it is clear that $\eta_{r,i}$ is a more realistic and conservative definition of radiation efficiency. In-

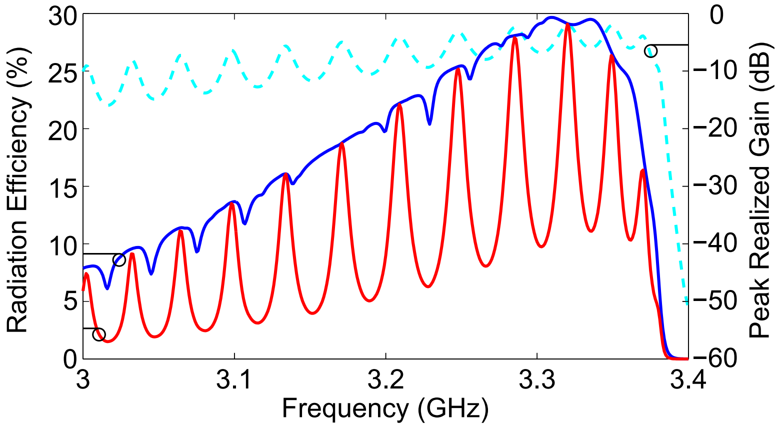

Figure 6.10: Radiation efficiencies for the shielded-loop-excited OEWG, defined by $\eta_{r,i} = P_{rad}/P_{inc}$ (solid red curve) and $\eta_{r,a} = P_{rad}/P_{acc}$ (solid blue curve). The peak realized gain (dashed teal curve) is also shown.

deed, $\eta_{r,i}$ attains local maxima at each of the return-loss peaks shown in Fig. 6.8, where the matching is most substantially improved. At $f = 3.320$GHz the return loss of 27.7dB corresponds to a maximum radiation efficiency of 28.8%. Note that return loss is maximized at $f = 3.134$GHz (28.3dB), but the increased insertion loss at these lower frequencies reduces $\eta_{r,i}$ to 16%. In general, the insertion loss may be alleviated by choosing a shorter metamaterial-lined waveguide length. However, the waveguide length also establishes the distribution of resonant peaks in the band and, at a minimum, must be large enough to allow any practical periodic implementation of the metamaterial liner to satisfy the definition of an effective medium.

The peak realized gain (dashed teal curve) shown in Fig. 6.10 is defined as the maximum directivity of the antenna at broadside, reduced by $\eta_{r,i}$. A maximum value of -1.94dB is achieved at $f = 3.320$GHz. This represents a vast improvement over a similarly sized unlined waveguide excited with the same shielded loop, which had a gain of -76.1dB and for which virtually no power is radiated. In fact, the gain of the metamaterial-lined OEWG is at least 60dB greater than that of the unlined waveguide everywhere over the band. Another meaningful comparison may be drawn to a PEC dipole with a length l equal to the diameter of the 'MTM-Lined' OEWG (i.e., $l = 2b_2 = 30$mm). The directivity and peak realized gain of a 30mm dipole fed by a 50Ω source at $f = 3.320$GHz are confirmed through full-wave simulations to be 2.24dB and −7.69dB, respectively. Therefore, the miniaturized 'MTM-Lined' OEWG offers a nearly four-fold improvement in gain over a similarly sized dipole. Furthermore, it is up to four times smaller than the capacitively loaded evanescent waveguide probe mentioned in Sec. 2.6. The gain of the metamaterial-lined OEWG may be further improved by sacrificing the degree of miniaturization (over 42% in the studied case), which would result in lower insertion loss due to less field confinement in the liner and higher directivity due to larger aperture size.

It was shown that the introduction of a thin ENNZ liner into the OEWG volume results in a frequency-reduced backward-wave passband well below its natural cutoff frequency. Full-wave simulations of the metamaterial-lined OEWG probe in the frequency-reduced region reveal multiple resonant return-loss peaks where the miniaturized antenna exhibits a substantially improved gain over both a similarly sized (and below-cutoff) circular waveguide probe and a reference dipole. The next natural step is to investigate the radiation properties of the printed-circuit implementation of the metamaterial-lined waveguide, and observe if the practical liner's response is similar to that of the isotropic, homogeneous ENNZ liner.

6.2 A Practical Demonstration of Below-Cutoff Radiation in Miniaturized OEWG Probes

This study investigates the radiation characteristics of a prototype metamaterial-lined OEWG probe whose liner is realized using the practical PCB metamaterial liner presented in Sec. 4.5. Figures 6.11(a)-6.11(b) present the full-wave-simulation model and experimental prototypes of the metamaterial-lined OEWG probe, respectively, which consist of a balanced shielded loop ($c_r = 13.5$mm and $\theta_g = 20°$) embedded in a closed vacuum-filled below-cutoff waveguide section ($b = 15$mm, $L_1 = 17.75$mm, and $p_z = 15.0$mm) that is smoothly connected to a metamaterial-lined waveguide which is opened at one end to radiate (into a spherical boundary of radius 85mm, in the case of the simulation model). The PCB metamaterial

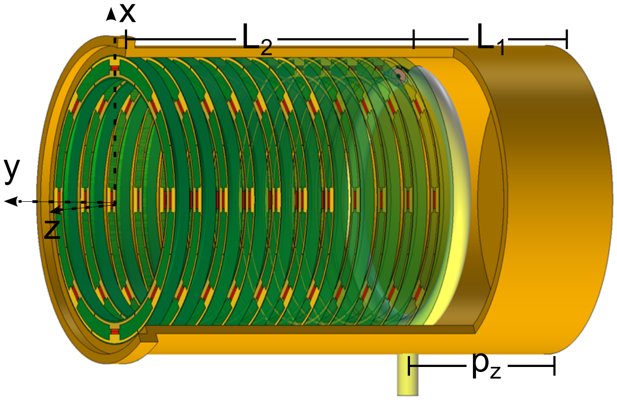

(a)

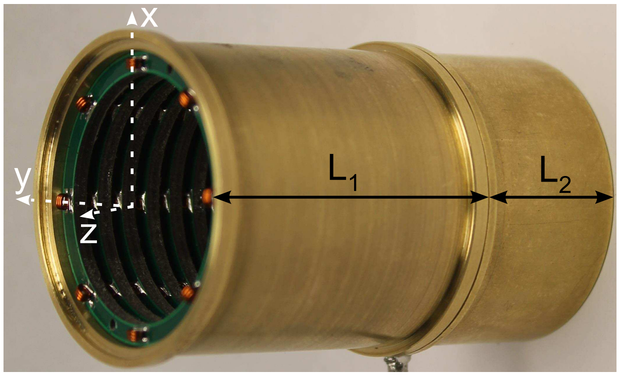

(b)

Figure 6.11: Full-wave simulation model and experimental prototype of the metamaterial-lined OEWG probe excited by a shielded-loop-antenna source, in which the liner is realized using the PCB implementation presented in Sec. 4.5.

presented in Sec. 4.5 is arranged into a stack of 11 layers along the below-cutoff waveguide's length of $L_2 = 32$mm. A Keysight PNA-X N5244A Network Analyzer was used to measure the return-loss response of the experimental prototype.

6.2.1 Return Loss

As mentioned previously, the unloaded vacuum-filled intermediate waveguide is within its natural evanescent region for frequencies below $f = 5.857$ GHz and, as a result, the shielded-loop is poorly matched. Although not shown, the return loss in both simulation and measurements is effectively 0dB below $f = 3.40$GHz. By simply inserting the PCB metamaterial-liner into the open aperture, the return loss will be drastically improved below the frequency-

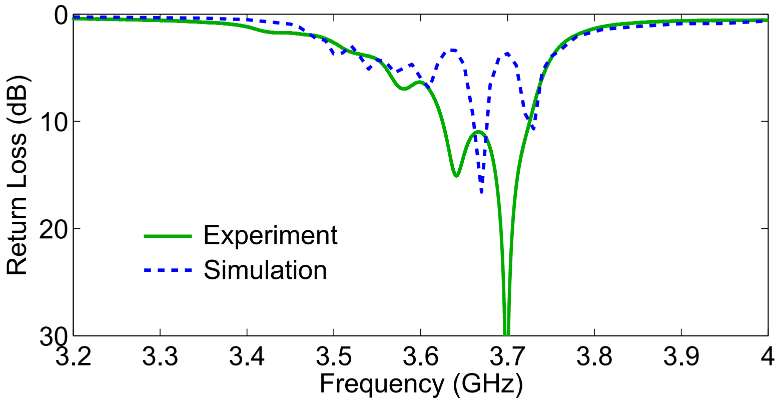

Figure 6.12: Return loss of the simulated and fabricated metamaterial-lined OEWG probe.

reduced HE_{11} mode's cutoff frequency, $f_{11} = 3.685$GHz. Indeed, the simulated (dashed blue curve) and measured (solid green curve) return loss curves in Fig. 5.13(b) exhibit a passband below f_{11} that is characterized by multiple return-loss peaks in which the antenna most optimally accepts the power. The very good agreement between the measurements and simulation is evident. For clarity, the return-loss is shown only up to 30dB; however, the measured return loss achieves a maximum of 57dB at $f = 3.70$GHz, and has a 10dB bandwidth of 100MHz. This represents a significant enhancement over a similarly excited empty waveguide, into which virtually no power would be accepted.

As was observed in the transmission setup (see Sec. 5.2), the simulated and measured return-loss peaks generally don't agree. Once again, this is mostly attributed to the fabrication tolerances imposed on the shielded loop and PCB metamaterial and, to a lesser extent, the numerical accuracy of the simulation, in which the meshing and numerical convergence criteria listed in Sec. 5.2 were employed. Between the transmission and antenna measurements, a new shielded-loop source had to be fabricated and the PCB layers had to be reassembled; altering the orientation and proximity of the source to the nearby metamaterial layers and impacting the return loss greatly.

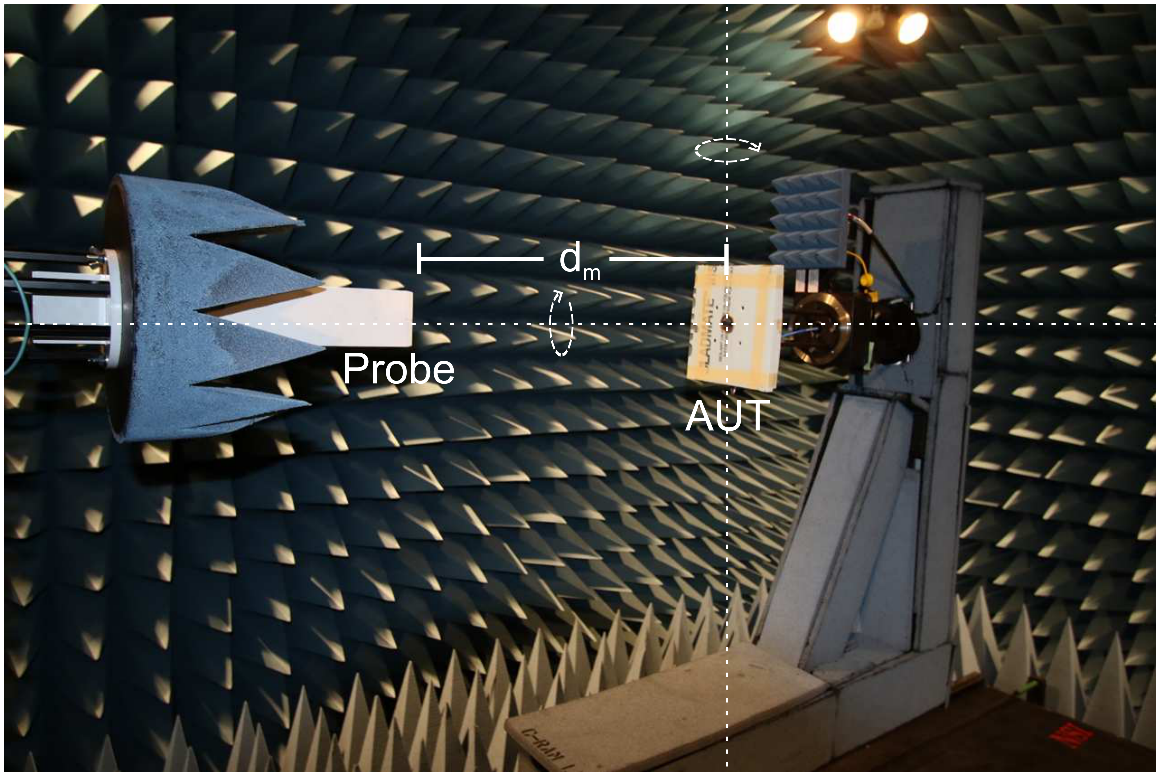

Figure 6.13: The experimental antenna-measurement setup.

6.2.2 Measurement Setup

A Keysight PNA-X N5244A Network Analyzer and a Nearfield Systems Inc. (NSI) antenna-measurement system with an anechoic chamber and automated translation stages were used to measure the prototype metamaterial-lined OEWG probe's radiation pattern. In these measurements, the anechoic chamber acts as a nearfield range and a separate, rectangular 'probe' antenna samples the energy of an antenna under test (AUT) at locations in its near-field; scanning in a path that forms either a planar, cylindrical, or spherical surface. Whereas measurements in a far-field range must occur in the antenna's far-field region (i.e., $d_m > 2D^2/\lambda$, in which d_m is the 'probe' to AUT distance and D is the antenna's largest physical dimension), a nearfield system measures the energy in the antenna's radiating near-field region ($\lambda < d_m < 2D^2/\lambda$) which converts those measurements by a Fourier transform into the far-field result. In this transform, a probe correction is applied to factor out any impact its own radiation pattern may have on the measured far fields.

In this study a NSI-RF-WR284 rectangular-waveguide probe (or simply, ‘probe’) is used to measure the prototype metamaterial-lined OEWG probe (the AUT) using a spherical nearfield scan whose measurement setup is illustrated in Fig. 6.13. In this image, the open apertures of the probe and AUT are facing each other in which the former is mounted on a translational stage that keeps its position fixed during the entire scan but can rotate for different polarization measurements, and the latter is mounted on a translation stage that rotates the AUT around the two axes shown in the image, thereby performing a full spherical scan. To avoid a physical collision between the measuring probe and the AUT’s mount during its rotation, $d_m = 69.85$cm in each spherical measurement. A network analyzer is used to measure the transmitted signal with a 3kHz intermediate-frequency bandwidth, averaging over 5 readings, and 13dBm power output. This ensures an adequate signal-to-noise ratio (SNR) in each measurement.

6.2.3 Radiation Patterns

In an effort to determine if the measurement setup and simulation model are comparable, we first investigate the radiation pattern of the unloaded vacuum-filled circular OEWG probe. In this case, the measured signal has a very small amplitude because the OEWG probe is below cutoff. However, the SNR still exceeds 50dB. Here, the following concise terms are used in describing an antenna’s radiation pattern: co-pol refers to the desired polarization of the AUT that was meant to radiate and whose polarization matches that of the measuring probe, and cross-pol refers to an undesired polarization that is orthogonal to co-pol. In this study, we focus on the linear polarization of the frequency-reduced HE_{11} mode, which should exhibit low cross-pol. Any significant cross-pol would lead to elliptical polarization.

The unloaded OEWG probe’s simulated (blue dashed curve) and measured (green solid curve) co-pol radiation patterns are shown in Figs. 6.14(a)-6.14(b) in its E-plane (y-z) and H-plane (x-z), respectively, at $f = 3.70$GHz, in which each is normalized to the maximum in the co-pol radiation pattern. Due in part to the subwavelength dimensions of the OEWG

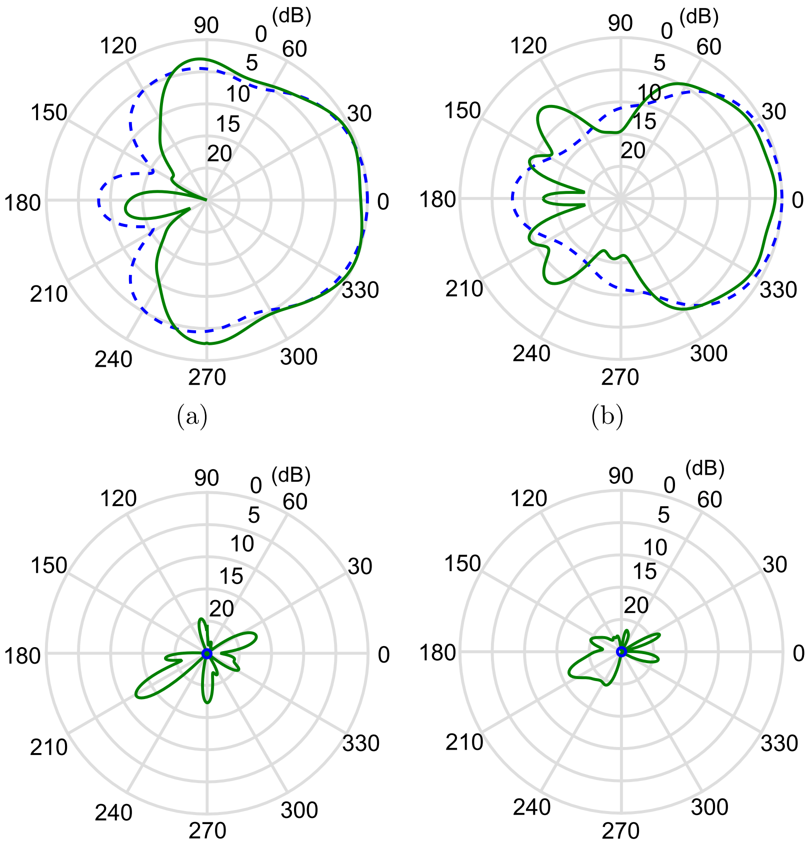

(a) (b)

(c) (d)

Figure 6.14: The shielded-loop-excited unloaded vacuum-filled OEWG's simulated (blue dashed curve) and measured (green solid curve) co-polarization [and cross-polarization] radiation pattern in the (a) [(c)] E-plane and (b) [(d)] H-plane, respectively, at $f = 3.70\text{GHz}$.

probe's aperture, the simulated radiation pattern has a broader main beam and lower front-to-back ratio as compared to a conventional-sized circular OEWG (see Figs. 6.6(a)-6.6(b)). The measured and simulated patterns are in close agreement across the main beam, but differ for large angles away from broadside, which is more pronounced in the H-plane. This is attributed to blockage and multipath diffraction due to the mounting stand located between the measurement probe and the OEWG. Furthermore, it is believed that the shielded loops generate small but still significant unbalanced currents on the feeding coaxial waveguide whose radiated fields will contribute to the measured signal. Figures 6.14(c)-6.14(d) present the cross-pol radiation patterns in the E-plane and H-plane, respectively. While the simulated cross-pol radiation pattern is not shown because it is well below the 25dB scale

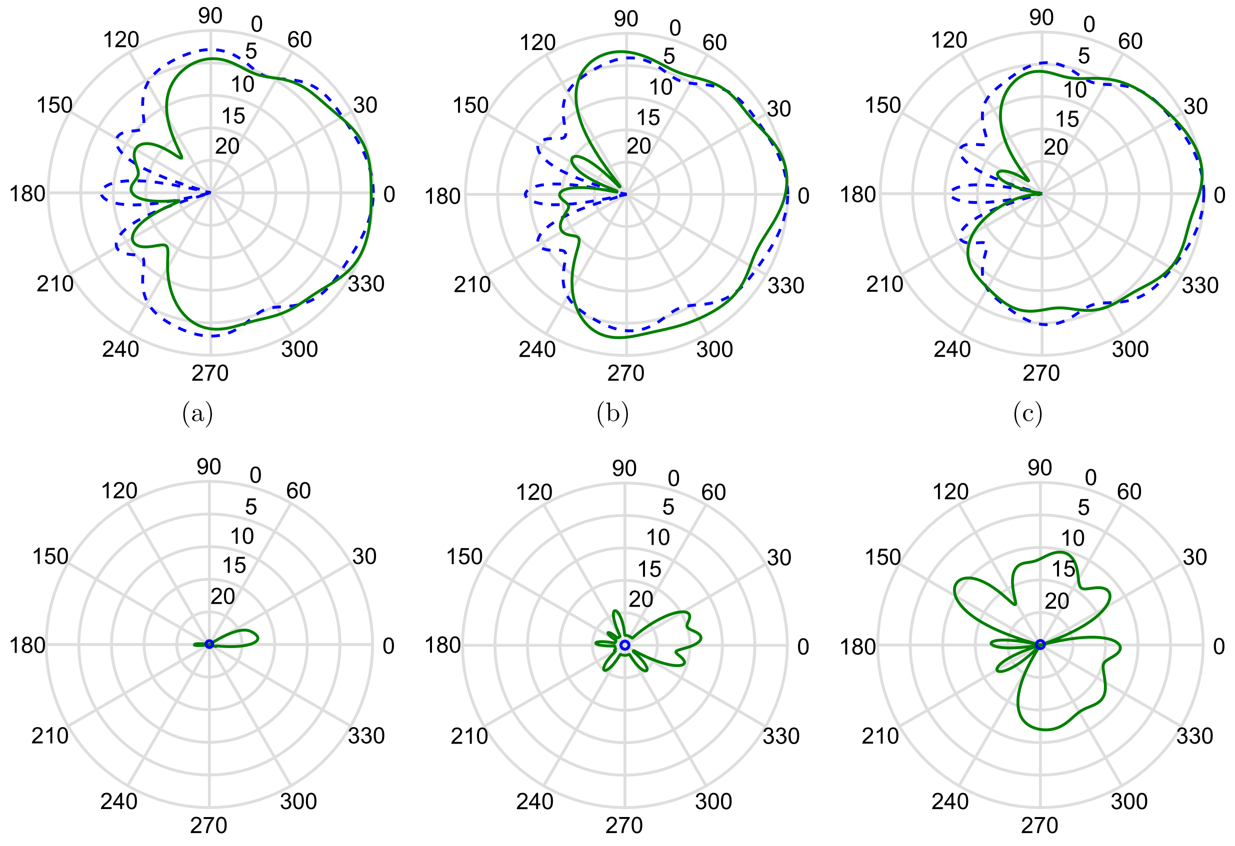

(a) (b) (c)

(d) (e) (f)

Figure 6.15: The shielded-loop-excited metamaterial-lined OEWG's simulated (blue dashed curve) and measured (green solid curve) co-pol [and cross-pol] radiation pattern in the E-plane at (a) [(d)] $f = 3.57\text{GHz}$, (b) [(e)] $f = 3.64\text{GHz}$, and (c) [(f)] $f = 3.70\text{GHz}$.

used, the measured cross-pol is evident here; however, it is at least 20dB lower than co-pol across the main beam.

The metamaterial liner is now introduced into the OEWG probe, which drastically improves the strength of the measured signal and the SNR. The metamaterial-lined OEWG's simulated (dashed blue curve) and measured (solid green curve) co-pol and cross-pol radiation patterns in the E-plane and H-plane are shown in Figs. 6.15(a)–6.15(f) and Figs. 6.16(a)–6.16(f), respectively for the measured resonant return-loss peaks at $f = 3.57\text{GHz}$, $f = 3.64\text{GHz}$, and $f = 3.74\text{GHz}$. At $f = 3.57\text{GHz}$, we observe a radiation pattern that is indicative of the HE_{11} mode being excited and coupled into free-space. Despite the fabrication tolerances of the metamaterial-lined OEWG, the simulated and measured co-pol radiation

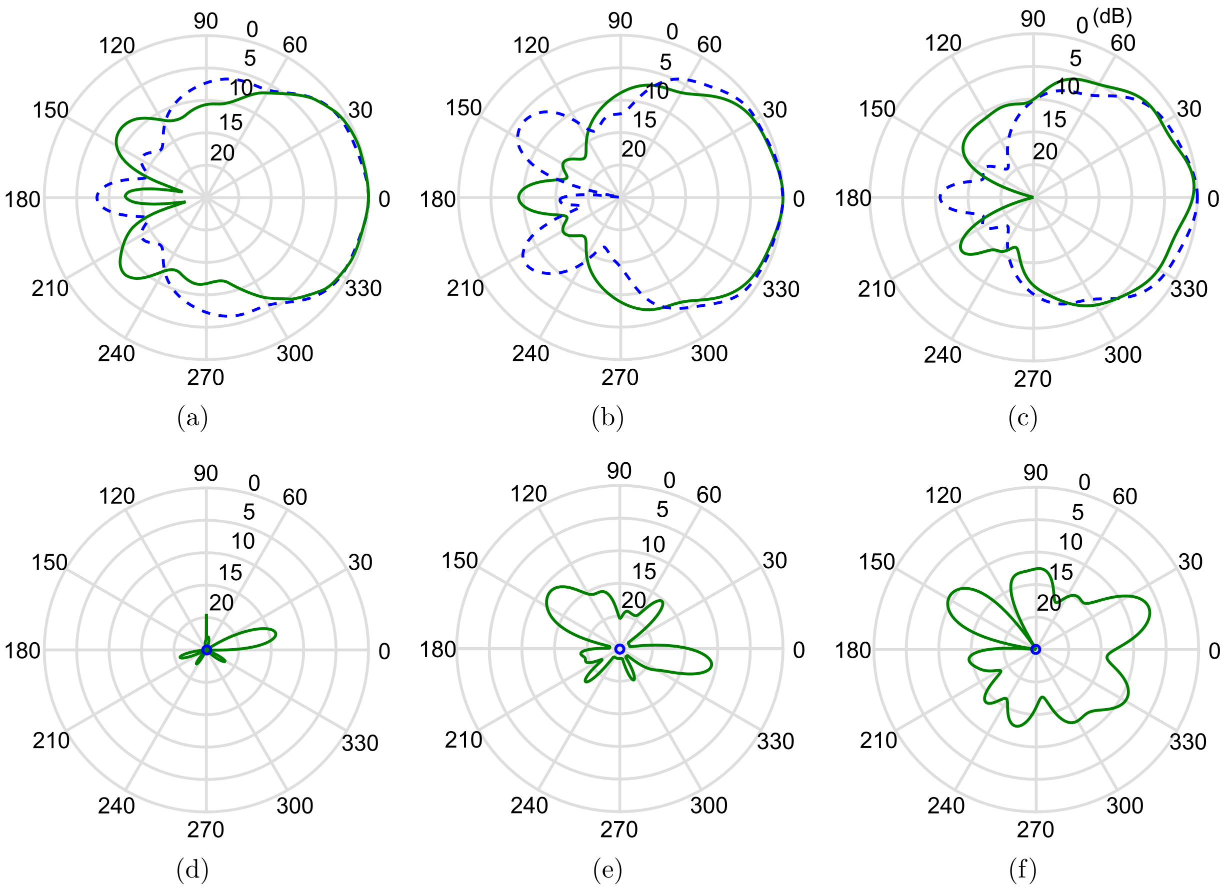

Figure 6.16: The shielded-loop-excited metamaterial-lined OEWG's simulated (blue dashed curve) and measured (green solid curve) co-pol [and cross-pol] radiation pattern in the H-plane at (a) [(d)] $f = 3.57\text{GHz}$, (b) [(e)] $f = 3.64\text{GHz}$, and (c) [(f)] $f = 3.70\text{GHz}$.

patterns are in close agreement across the main beam, in which an observable difference occurs at large angles, particular in the H-plane. Once again, this is attributed to additional diffraction from the antenna mounting stand in measurements and potential unbalanced currents on the feed line. Nevertheless, these results, along with their apparent similarity to the unlined OEWG's radiation patterns, strongly suggest that the metamaterial-lined OEWG is exciting and radiating the desired HE_{11} mode.

Although the metamaterial-lined OEWG probe's simulated cross-pol radiation pattern is once again below the 25dB scale used, the measured cross-pol is more evident. Nevertheless, the cross-pol radiation pattern at $f = 3.57\text{GHz}$ in the E-plane and H-plane shown in Figs. 6.15(a)–6.16(f) is at least 15dB lower than co-pol, indicating a good linear polariza-

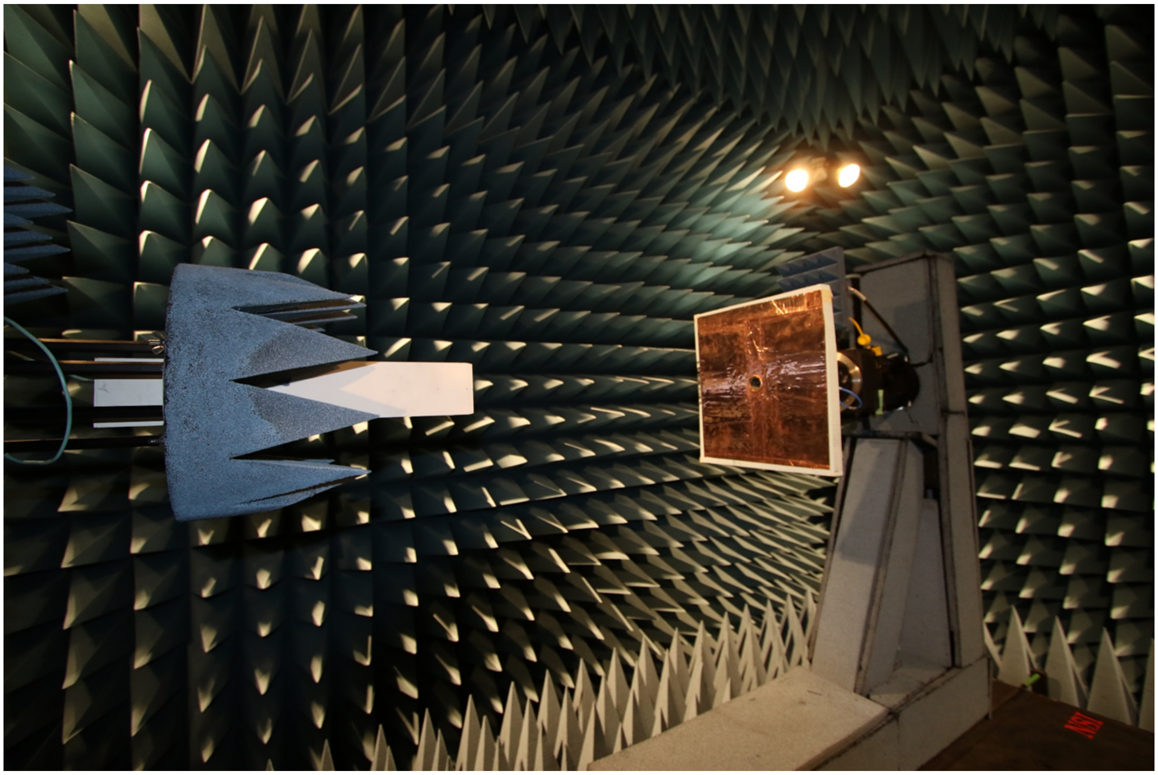

Figure 6.17: The experimental antenna-measurement setup in which the OEWG probe's aperture is mounted on a large copper screen.

tion. As frequency increases, the cross-pol levels begin to increase, in which at $f = 3.70$GHz the cross-pol is only 5dB less than co-pol across the main beam. This suggests a generally elliptical polarization at higher frequencies. The source of this cross-pol will be discussed shortly.

6.2.4 Radiation Patterns Employing a Metallic Screen

The main differences between the simulated and measured radiation patterns may largely be attributed to the AUT's mounting apparatus whose reflections cause so-called multipath propagation. This occurs despite using the thin absorbing material (the blue covering in Fig. 6.13) on most of the mount's metallic surface. To mitigate these undesired reflections, the OEWG's open aperture is placed in a metallic copper screen of dimensions $4\lambda_0 \times 4\lambda_0$ (340mm×340mm) which acts as a reflector that improves the antenna's forward directivity.

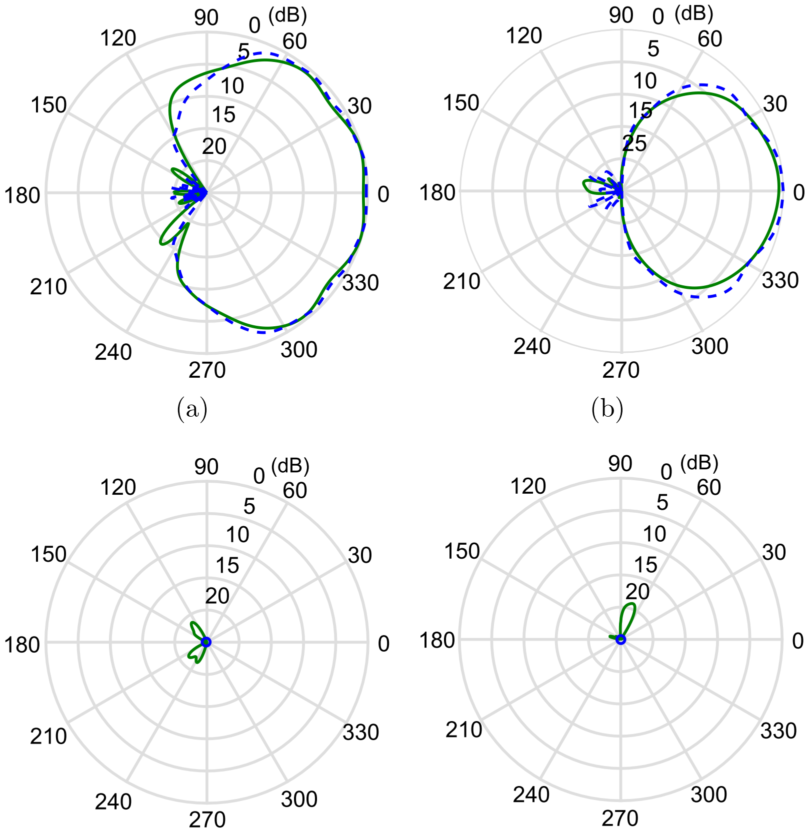

(a) (b) (c) (d)

Figure 6.18: The shielded-loop-excited unloaded vacuum-filled OEWG's simulated (blue dashed curve) and measured (green solid curve) co-polarization [and cross-polarization] radiation pattern in the (a) [(c)] E-plane and (b) [(d)] H-plane, respectively, at $f = 3.70$GHz. Here the OEWG is mounted onto a metallic copper screen.

This metallic screen is included in the simulation model.

The unloaded OEWG probe's simulated (blue dashed curve) and measured (green solid curve) co-pol radiation patterns are shown in Figs. 6.18(a)-6.18(b) in its E-plane and H-plane, respectively, at $f = 3.70$GHz. As desired, the match between simulations and measurements is vastly improved in that the radiation power at large angles behind the AUT is substantially reduced. In fact, the similarity to the numerical far-fields shown in Figs. 6.2(a)–6.2(b) of a below-cutoff aperture cut into an infinite PEC ground plane is quite striking. This includes a broad main-beam with minimal ripple, which drops off sharply near the horizon (i.e., the plane of the aperture). Introducing the metallic screen appears to have reduced the measured

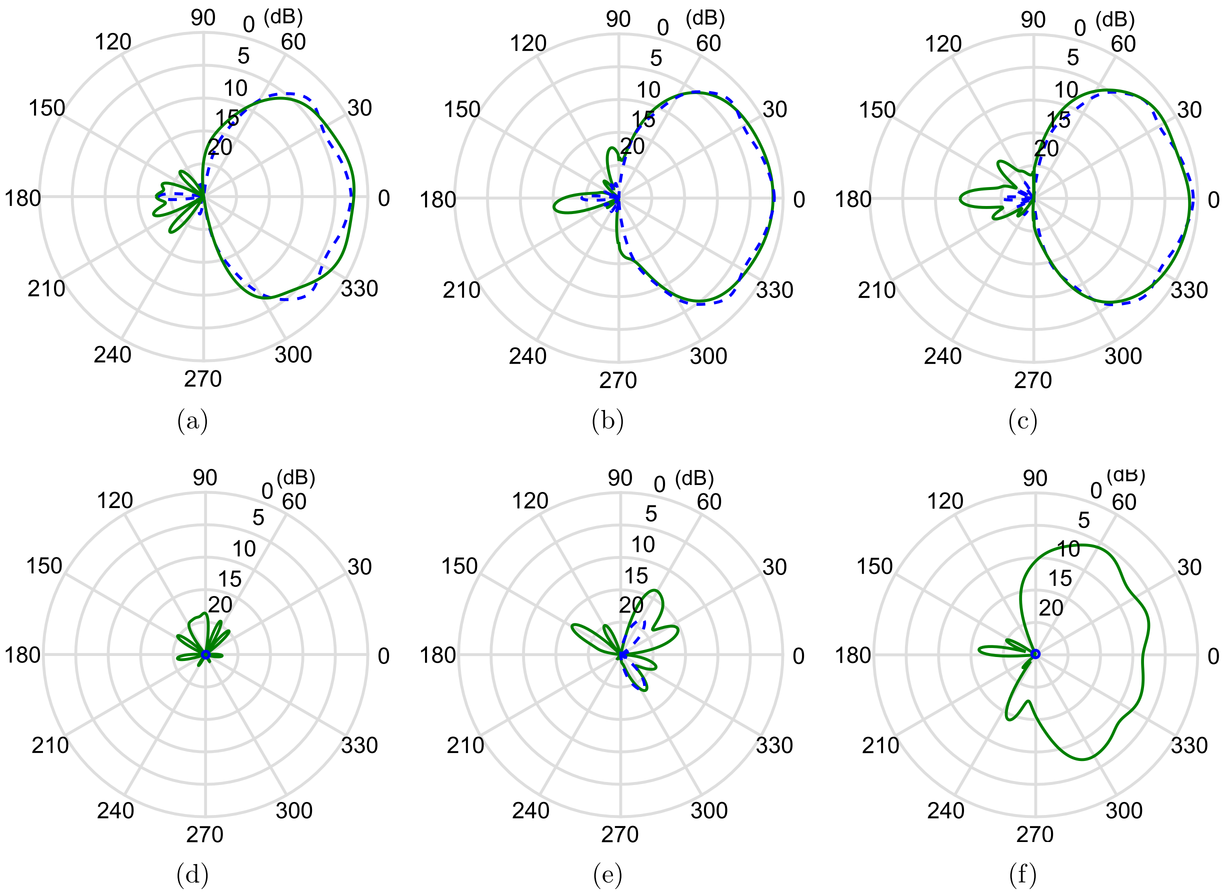

(a) (b) (c) (d) (e) (f)

Figure 6.19: The shielded-loop-excited metamaterial-lined OEWG's simulated (blue dashed curve) and measured (green solid curve) co-pol [and cross-pol] radiation pattern in the E-plane at (a) [(d)] $f = 3.57$GHz, (b) [(e)] $f = 3.64$GHz, and (c) [(f)] $f = 3.70$GHz. Here the OEWG is mounted onto a metallic copper screen.

cross-pol E-plane and H-plane radiation patterns, which is verified in Figs. 6.18(c)–6.18(d), respectively.

Figures 6.19(a)–6.19(f) and Figs. 6.20(a)–6.20(f) presents the metamaterial-lined OEWG's simulated (dashed blue curve) and measured (solid green curve) co-pol and cross-pol radiation patterns in the E-plane and H-plane, respectively at $f = 3.57$GHz, $f = 3.64$GHz, and $f = 3.70$GHz. As expected, the introduction of the metallic screen improves the match between simulation and measurements; however, the metamaterial-lined OEWG generally exhibits a larger back lobe in measurements. Nevertheless, the main beam is reproduced almost perfectly in measurements with a similar HPBW beamwidth and small ripple. Al-

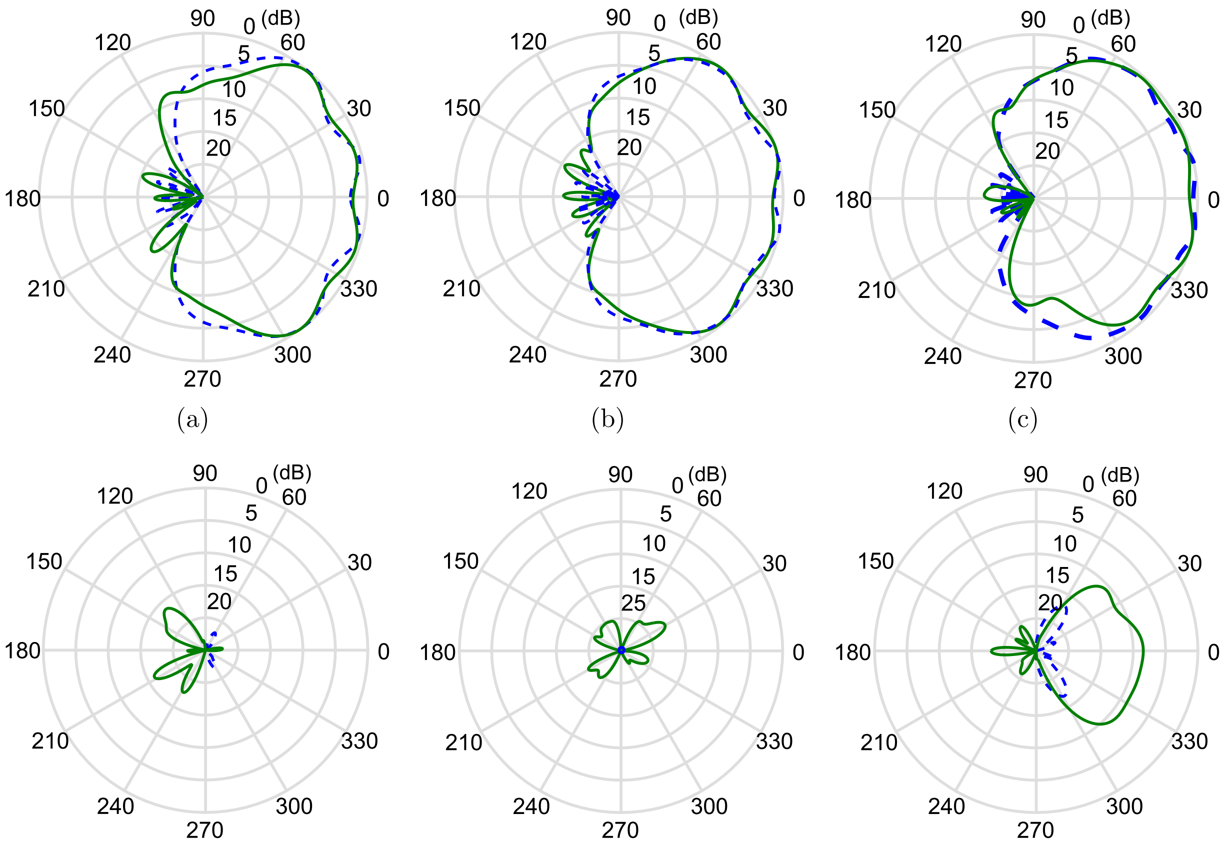

(a) (b) (c)

(d) (e) (f)

Figure 6.20: The shielded-loop-excited metamaterial-lined OEWG's simulated (blue dashed curve) and measured (green solid curve) co-pol [and cross-pol] radiation pattern in the H-plane at (a) [(d)] $f = 3.57$GHz, (b) [(e)] $f = 3.64$GHz, and (c) [(f)] $f = 3.70$GHz. Here the OEWG is mounted onto a metallic copper screen.

though the metallic screen changes the profile of the measured cross-pol radiation pattern, its does not greatly impact the overall level. which increases at high frequencies. Whereas a strong linear polarization is preserved at low frequencies, the cross-pol pattern is only 10dB less than the co-pol pattern over most of the main beam at $f = 3.70$GHz. The HE_{11}-like cross-pol pattern suggests that a HE_{11} mode (polarized orthogonal to the fields generated by the shielded loop) may be weakly excited in the metamaterial-lined OEWG probe. The coupling to the orthogonal HE_{11} mode is most likely due to small azimuthal misalignment between adjacent metamaterial layers and fabrication tolerances in the fabricated prototypes. Nevertheless, these results suggest that linear polarization can be preserved, provided we operate at sufficiently low frequencies in the return-loss band.

6.2.5 Radiation Performance

This study investigates the directivity and gain of the metamaterial-lined OEWG probe. By definition, the directivity is equal to $D = 4\pi U_{max}/P_{rad}$, in which U_{max} is the maximum radiation intensity and P_{rad} is the total power radiated by the antenna. P_{rad} is evaluated numerically by integrating the radiation intensity (U) over the entire 4π steradians in both simulations and measurements. Of course, U is determined from a near-to far-field transform of the fields solved for in the simulation domain and of the fields measured by the probe. Whereas the gain of the simulated OEWG probe is calculated from directivity using $G = \eta_{r,i}D$, in which $\eta_{r,i} = P_{rad}/P_{inc}$, this work employs the so-called gain-comparison method in which the gain of an AUT is found by comparing the resulting far-field level of the AUT to that of a known gain standard substituted under the same conditions. The difference in signal level is the difference in gain between the AUT and the gain standard. This entails two sets of measurements in which 1) an AUT is in receive mode and receives power P_{AUT} from a transmitting probe and 2) the gain standard is in receiving mode and receives power P_H from a transmitting probe. In both measurements, the measuring distance (R), transmitted power (P_o), and gain (G_o) of the transmitting probe is kept the same. In this work, the gain is measured in the AUT's far-field ($R = 1.39$m) using a 15dB standard-gain horn (WR284) whose gain (G_H) is known from simulations. Friis' transmission equation is used to calculate the gain of the AUT (G_{AUT}) as follows:

$$G_{AUT}[dB] + G_o[dB] = 20log_{10}\left(\frac{4\pi R}{\lambda_0}\right) + 10log_{10}\left(\frac{P_{AUT}}{P_o}\right) \tag{6.2a}$$

$$G_H[dB] + G_o[dB] = 20log_{10}\left(\frac{4\pi R}{\lambda_0}\right) + 10log_{10}\left(\frac{P_H}{P_o}\right), \tag{6.2b}$$

which implies

$$G_{AUT}[dB] = G_H[dB] + 10log_{10}\left(\frac{P_{AUT}}{P_H}\right). \tag{6.3}$$

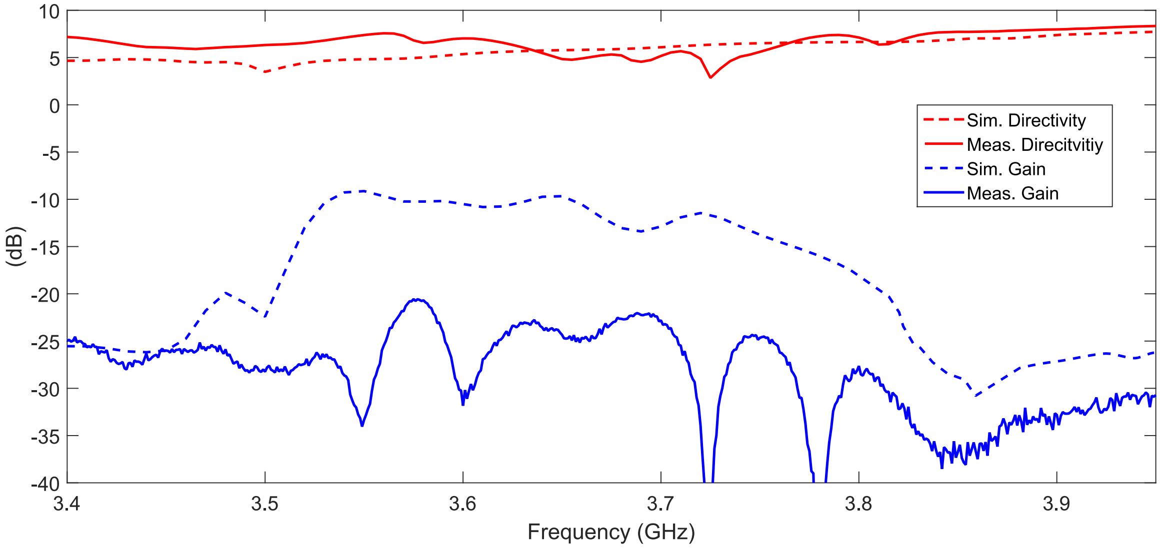

Figure 6.21: The shielded-loop-excited metamaterial-lined OEWG's simulated and measured directivity and gain.

Figure 6.21 presents the simulated (solid curves) and measured (dashed curves) directivity (red curves) and gain (blue curves) for the shielded-loop-excited metamaterial-lined OEWG probe. The simulated and measured directivity are in very good agreement and both appear to generally decrease with frequency. Of course, this is to be expected as the antenna gets electrically smaller. The measured directivity fluctuates between 2.85dB ($f = 3.72$GHz) and 7.57dB ($f = 3.56$GHz), which represents a variation of 3dB with the simulated directivity. Observing the two measured return-loss peaks, the measured [simulated] directivity is 5.98dB [5.67dB] at $f = 3.64$GHz and 6.019dB [5.17dB] at $f = 3.70$GHz. It is expected that the AUT's mounting stand is affecting the measured directivity in the same fashion as the radiation pattern, causing this disagreement with simulations.

The profile of the simulated gain in Fig. 6.21 appears to closely match the simulated return-loss profile in Fig. 6.12, and exhibits a band of improved gain below $f = 3.70$GHz. A maximum value of -9.13dB is achieved at $f = 3.55$GHz. While this gain may appear diminutive when compared to the $3 - 5$dB gain offered by standard OEWG probes, the metamaterial-lined OEWG probe aperture's cross-sectional area is 60% smaller than that of a vacuum-filled circular waveguide operating at cutoff. Therefore, this result represents a significant enhancement over the similarly sized below-cutoff OEWG probe waveguide. Unfortunately, the measured gain doesn't exhibit a clear passband and, on average, is 10dB less than the simulated gain. This is attributed to a number of factors including: diffraction from the mounting stand, accuracy of the standard-gain horn's simulated gain table, and fabrication tolerances of the shielded loop and PCB metamaterial layers. However, it is encouraging to observe a simulated and measured gain with similar overall trends, including an improvement in gain over a small range of frequencies followed by an antiresonance, after which, the gain increases gradually with frequency. This gain may be improved with further refinement of the construction process for the metamaterial-lined OEWG probe and its shielded-loop excitation to reduce fabrication tolerances, using lower-loss inductors and thicker liners to reduce liner loss, and increasing the accuracy of the gain measurement. To address a number of these issues, another prototype shielded-loop antenna, PCB metamaterial liner, and circular waveguide with higher control over fabrication tolerances has been developed and is undergoing experimental validation.

6.3 Bandwidth and Gain Considerations

Although reducing aperture size generally leads to a reduction in bandwidth and gain, it should be noted that this constraint is common to all electrically small antennas. Even the so-called evanescent-mode waveguides [104], which employ dielectric inclusions to restore propagation below cutoff, are operated close to cutoff so as to achieve moderate gains and bandwidth. However, as a result, they offer little to no miniaturization and are therefore unsuitable for applications requiring subwavelength spatial resolutions or unimpeded access to the interior waveguide volume. A meaningful comparison would examine the gains of antennas of a given size. In this work, it is shown that the gain of the miniaturized metamaterial-lined OEWG probe (whose liner is modeled as an isotropic and homogeneous region) is three to four times better than that of a comparably sized dipole antenna operating at the same frequency, where the waveguide is over 42% below its natural cutoff. Although the gain was lower in the prototype PCB-based metamaterial-lined OEWG probe, it may be improved using the previously mentioned techniques and also by using shorter metamaterial-waveguide lengths to mitigate the effects of loss. Furthermore, the introduction of a reflecting plane behind the radiating aperture also improves gain.

In many situations, the benefits of miniaturization outweigh trade-offs in gain and bandwidth – these include near-field imaging that does not significantly perturb the fields to be measured, sub-wavelength spatial resolution measurements with increased dynamic range and/or above the noise floor, improved accuracy in near- to far-field transformations, and increased compactness of antenna arrays. For example, in Ref. [144], the miniaturization of antenna elements in a multi-frequency interlaced waveguide antenna array allowed for an increase in antenna element density.

The multiresonant nature of the return loss best suits the antennas to continuous-wave applications or those involving narrow-band phenomena. For example, narrowband antennas prove useful in high-field traveling-wave magnetic resonance imaging [145] and radio astronomy [146]. Since the locations of the resonant peaks can be designed through varying the waveguide's length or liner's permittivity dispersion, it would be possible to tune to desired discrete operating frequencies. These multiple resonances could enable discrete frequency sampling of dispersive quantities, such as permittivity, over a given bandwidth. Furthermore, applications requiring high selectivity actually benefit from such sharp bandwidths, such as in Ref. [144], to provide frequency isolation between higher-frequency and lower-frequency antenna elements, and in varieties of synthetic aperture radar [147], in which broad-beamwidth, narrowband sources are used to obtain high target resolutions. The inherent filtering capability of metamaterial-lined waveguides could also replace the function of ultranarrow band filters in microwave tomography, which provide isolation between multiple channels of array elements [148], and in radio astronomy, to aid in filtering out terrestrial communications [149]. Higher-density arrays of miniaturized metamaterial-lined OEWGs may be used to meet the gain requirements in these applications.

Chapter 7

A General Class of Metamaterial Circular Waveguides

It has been demonstrated numerous times in this work that the canonical solutions of the wave equation in cylindrically anisotropic media (Eqs. A.17a-A.17b) provide a powerful numerical tool to accurately predict the dispersion features of the metamaterial-lined PEC circular waveguide. Whereas the dispersion and field relations presented in Chapter 3 are uniquely defined for that case, the analysis can be easily translated to various electromagnetic structures that exhibit a similar form of cylindrical symmetry. Consider the general class of circular waveguides that is shown in Fig. 7.1(a) that consists of a three-region system in which, in general, each region may be anisotropic and/or a PEC. The various permutations describe a metamaterial-lined PEC waveguide (Fig. 7.1(b)), a metamaterial-coated PEC rod (Fig. 7.1(c)), and a metamaterial-shell waveguide (Fig. 7.1(d)), in which the metamaterial region is represented using radial lines. Despite the difference in boundary conditions in each case, their similar geometries suggest that we may expect several parallels between their dispersion properties. For instance, a hybrid mode description must be considered in each of three cases due to their generally inhomogeneous nature.

This chapter investigates the impact of introducing into these circular waveguides meta-

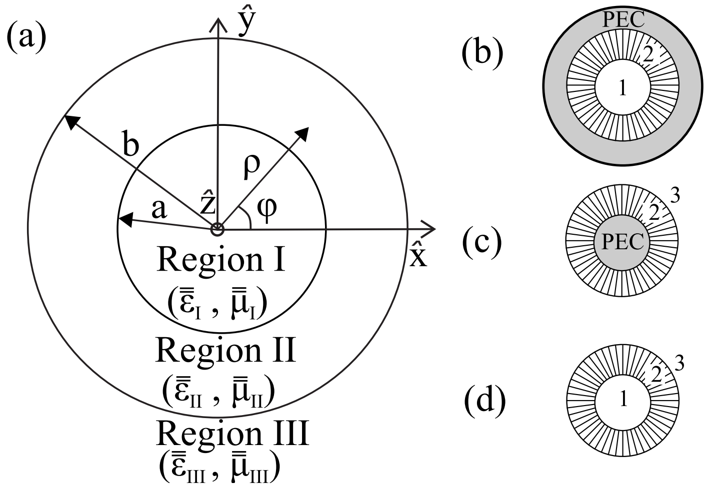

Figure 7.1: (a) Generic three-region waveguide setup, for examination of the following cases: (b) a metamaterial-lined PEC circular waveguide, (c) a metamaterial-coated PEC rod, and (d) a metamaterial-shell waveguide. The metamaterial region is represented using radial lines.

materials with anisotropic permittivities and/or permeabilities that may assume negative, large, and/or near-zero values, which provides new insights into controlling the dispersion of modes, cutoff frequencies, and field patterns. Whereas our previous investigations focused on uniaxial and isotropic metamaterial liners, a fully biaxial description is employed here. The metamaterial-lined PEC circular waveguide and metamaterial-coated rod will be explored for potential applications in particle-beam physics and THz endoscopy, with a focus on useful new dispersion features that may be controlled using anisotropy of the metamaterial as well as the geometrical parameters of the waveguide. To conclude, this study will look at the anisotropic metamaterial-shell waveguide composed of radially oriented NRI-TL layers, which may be used to enhance the radiated power of nearby antennas.

7.1 Theoretical Analysis

In an interest to be concise, the full field and dispersion relations for the metamaterial-coated rod and metamaterial-shell waveguide will not be presented; however, they may be easily derived using the same approach presented in Chapter 3 for the metamaterial-lined

PEC waveguide, and, have been reported previously in the literature [150, 151], albeit for simplified isotropic regions. Nevertheless, it is worth exploring how this analysis would begin by looking at the general field expressions in each region for all three investigated cases.

The general solution for the longitudinal (z) components of the electric and magnetic fields are reproduced below and take the form:

$$E_{zi} = (C_{1,i}J_{\nu_i}(\gamma^{\epsilon}_{\rho i}\rho) + C_{2,i}Y_{\nu_i}(\gamma^{\epsilon}_{\rho i}\rho))cos(n\phi)e^{-\gamma z}, \tag{7.1a}$$

$$H_{zi} = (C_{3,i}J_{\tau_i}(\gamma^{\mu}_{\rho i}\rho) + C_{4,i}Y_{\tau_i}(\gamma^{\mu}_{\rho i}\rho))sin(n\phi)e^{-\gamma z}, \tag{7.1b}$$

in which $C_{1,i}$, $C_{2,i}$, $C_{3,i}$, and $C_{4,i}$ are the region-dependent constants that are derived from applying the appropriate boundary conditions. As mentioned in the analysis of the metamaterial-lined circular waveguide, to avoid a singularity at $\rho = 0$ in Region 1, $C_{2,1} = C_{4,1} = 0$ and Eqs. 7.1a-7.1b reduce to Bessel functions. The linear combination of Bessel and Neumann functions is generally allowed in Region 2, but, can be represented in a simpler form in the metamaterial-lined PEC circular waveguide and metamaterial-coated PEC rod by factoring their respective PEC boundary conditions on the outer interface at $\rho = b$ and the inner interface at $\rho = a$. In these cases, the field expressions in Region 2 take the form:

$$E_{z2} = C'_{1,2}F_{\nu_i}(\gamma^{\epsilon}_{\rho i}\rho)cos(n\phi)e^{-\gamma z}, \tag{7.2a}$$

$$H_{z2} = C'_{2,2}G_{\tau_i}(\gamma^{\mu}_{\rho i}\rho)sin(n\phi)e^{-\gamma z}, \tag{7.2b}$$

with

$$F_{\nu_2}(\gamma^{\epsilon}_{\rho 2}\rho) = Y_{\nu_2}(\gamma^{\epsilon}_{\rho 2}\rho')J_{\nu_2}(\gamma^{\epsilon}_{\rho 2}\rho) - J_{\nu_2}(\gamma^{\epsilon}_{\rho 2}\rho')Y_{\nu_2}(\gamma^{\epsilon}_{\rho 2}\rho), \tag{7.3a}$$

$$G_{\tau_2}(\gamma^{\mu}_{\rho 2}\rho) = Y'_{\tau_2}(\gamma^{\mu}_{\rho 2}\rho')J_{\tau_2}(\gamma^{\mu}_{\rho 2}\rho) - J'_{\tau_2}(\gamma^{\mu}_{\rho 2}\rho')Y_{\tau_2}(\gamma^{\mu}_{\rho 2}\rho). \tag{7.3b}$$

in which $\rho' = b$ in the metamaterial-lined PEC circular waveguide (as previously shown) and $\rho' = a$ in the metamaterial-coated PEC rod. To allow the radiating solution for the metamaterial-coated PEC rod, $C_{2,3} = jC'_{1,3}$ and $C'_{4,3} = jC'_{3,3}$ cause Eqs. 7.1a-7.1b to reduce to Hankel functions of the second kind ($H_{\tau}^{(2)}$). As was done for the metamaterial-lined PEC circular waveguide, deriving the transverse field components using Eqs. 3.8, and applying field-matching at the boundaries between regions, a complete description of the field distributions and full dispersion of modes can be found.

7.2 Metamaterial-lined PEC Waveguide

As particles accelerate to relativistic speeds, they generate Cherenkov radiation (CR) that can be channeled in high-power RF and THz sources, such as the klystron and gyrostron, and can provide a plethora of information on the particles [36]. Acceleration of the particles typically employs a circular waveguide's TM_{01} mode, whose rotationally symmetric electric-field distribution with a significant longitudinal (i.e., z-directed) component can quickly accelerate a particle with minor drift in the transverse direction. However, the phase velocity in a hollow waveguide exceeds the velocity of light and cannot, therefore, be matched to any finite-mass particle. As a result, the phase is said to "roll" over the particles and the net acceleration is zero [152]. To facilitate coupling of the charged particles to a particular waveguide mode, either an isotropic dielectric liner or periodic perturbations, such as irises, are introduced into the waveguide's interior [153, 154]. These perturbations serve to reduce the mode's phase velocity to that of the particles. However, in conventional dielectric- and disc-loaded waveguides, the TM_{01} mode occurs at a higher cutoff than the fundamental TE_{11} mode, and single-mode operation is not possible. While many current systems operate in a multi-mode regime and try to dampen the excitation of unwanted modes to improve beam stability and CR generation, this analysis reveals a new enabling approach based on the use of ENNZ metamaterial liners.

Chapter 3 establishes that the inclusion of thin metamaterial liners into circular waveguides introduces multiple frequency-reduced backward-wave bands that occur in the frequency regime in which the liner exhibits dispersive ENNZ properties. The HE_{11} backward-

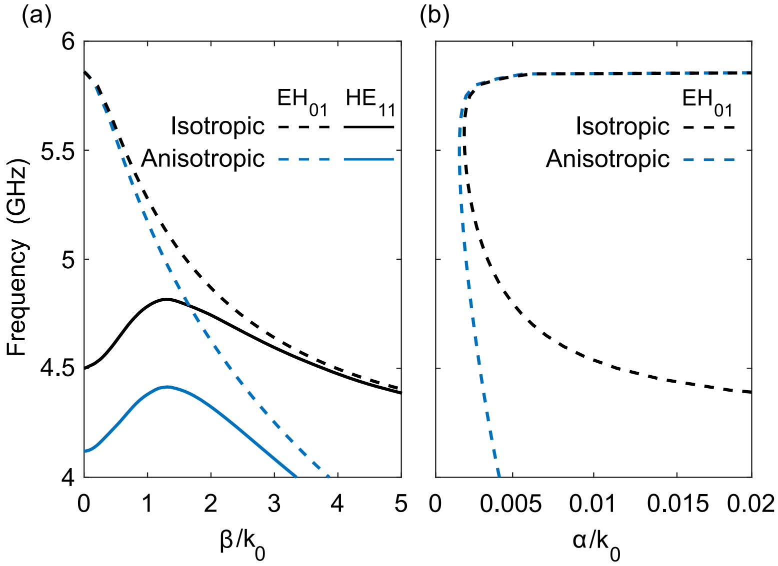

Figure 7.2: (a) The normalized propagation constant (β/k_0) for the frequency-reduced EH_{01} and HE_{11} modes and (b) normalized attenuation constant (α/k_0) for the frequency-reduced EH_{01} mode of a metamaterial-lined circular waveguide ($b = 15$mm) with an inner vacuum region and an outer liner region ($b - a = 3$mm) possessing either isotropic or anisotropic permittivity.

wave band, in particular, occurred over 42% below the waveguide's natural TE_{11} cutoff, and was one of many reduced modes possessing a unique order in frequency not seen with waveguides that are either homogenously or inhomogeneously filled with positive-permittivity dielectrics. Specifically, for negative liner permittivities, the EH_{01} mode possesses the highest cutoff frequency among the frequency reduced modes, followed in decreasing frequency by those of the HE_{n1} modes (i.e., $EH_{01} > HE_{11} > HE_{21}$...). Therefore, the frequency region above the HE_{11}-mode cutoff supports monomodal propagation of the EH_{01} mode, which largely resembles the TM_{01} mode in the inner vacuum region.

In particle-beam studies, it could be useful to extend the EH_{01} monomodal bandwidth. This can be achieved by observing from Eqs. (3.11) that a) the EH_{01} mode's cutoff frequency occurs at $\epsilon_{\rho 2}$'s plasma frequency and is independent of $\epsilon_{\phi 2}$, ϵ_{z2}, and the liner thickness; and b) increasing liner thickness causes a decrease in the HE_{11} mode's cutoff.

Hence, it is worth investigating how imbuing thick metamaterial liners with anisotropy can be beneficially exploited to improve the monomodal EH_{01} bandwidth over similarly thick isotropic liners. To illustrate, Fig. 7.2(a) investigates the dispersion of the frequency-reduced EH_{01} and HE_{11} modes for a representative metamaterial-lined circular waveguide of radius $b = 15$mm with a metamaterial liner of thickness $b - a = 3$mm and an inner vacuum region ($\bar{\bar{\epsilon}}_1 = \bar{\bar{I}}(1, 1, 1)\epsilon_0$). Two cases of liner-permittivity tensors are examined: an isotropic permittivity with $\bar{\bar{\epsilon}}_2 = \bar{\bar{I}}(\epsilon_{\rho 2}, \epsilon_{\rho 2}, \epsilon_{\rho 2})\epsilon_0$, and an anisotropic permittivity with $\bar{\bar{\epsilon}}_2 = \bar{\bar{I}}(\epsilon_{\rho 2}, 6, 1)\epsilon_0$. In all cases, $\epsilon_{\rho 2}$ follows a Drude profile defined by $\epsilon_{\rho 2} = 1 - \omega_{ep}^2/[\omega(\omega - j\omega_t)]$ with a plasma frequency $\omega_{ep} = 2\pi \times 5.86$GHz and damping frequency $\omega_t = 2\pi \times 3$MHz. This plasma frequency was intentionally chosen to be just below the fundamental TE_{11} cutoff of a similarly sized vacuum-filled waveguide, such that operating anywhere below this cutoff frequency implies that the waveguide may be considered miniaturized.

For both isotropic and anisotropic liners, the EH_{01} mode's cutoff frequency occurs at the liner's plasma frequency ($f = 5.86$GHz), below which the band is backward-wave in nature. The steeper dispersion of the anisotropic liner's EH_{01} mode can be attributed exclusively to the change in ϵ_{z2}, which can be theoretically verified from Eq. (3.11c). The strong dependence on ϵ_{z2} is expected from the EH_{01} mode's electric-field distribution, which has a significant z component and no ϕ component. The isotropic liner exhibits an HE_{11}-mode cutoff frequency of $f = 4.50$GHz, which is determined exclusively by $\epsilon_{\rho 2}$. On the other hand, in the anisotropic case, $\epsilon_{\phi 2}$ and ϵ_{z2} provide additional leverage in designing the cutoff and dispersion of the HE_{11} mode, which in this case causes its cutoff to decrease and its dispersion to steepen. As a result, the monomodal EH_{01} bandwidth is increased by 38.5% over the isotropic case (both of which are substantially higher than the monomodal EH_{01} bandwidth of a thinner anisotropic metamaterial liner). In fact, further enhancements have been achieved by increasing $\epsilon_{\phi 2}$ to even more positive values, thereby making the anisotropy more extreme. In the printed-circuit implementation of anisotropic liners, extreme anisotropy may be accomplished by using either inductive or capacitive loading in the ρ and ϕ traces to control, respectively, the effective plasmonic responses of $\epsilon_{\rho 2}$ and $\epsilon_{\phi 2}$.

Figure 7.2(b) presents the EH_{01} mode's normalized attenuation constant for the isotropic

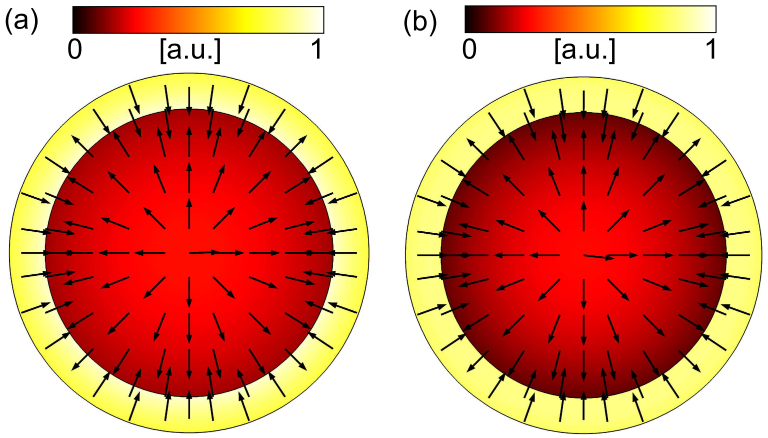

Figure 7.3: The frequency-reduced EH_{01} mode's electric-field magnitudes and vectors for a thick metamaterial liner possessing (a) isotropic and (b) anisotropic permittivity.

and anisotropic liners. Since the damping factor was chosen to accurately model the loss in practical metamaterials, the low level of attenuation suggests the EH_{01} mode could be useful in particle-beam physics [155]. It is evident that the introduction of anisotropy significantly alters both the EH_{01} and HE_{11} modes' dispersions. Nevertheless, the respective electric-field magnitudes and vectors of these modes reveal very similar distributions for the isotropic and anisotropic liners, exhibiting a weak concentration in the inner vacuum region and a discontinuously strong concentration in the liner region. This is illustrated, for example, in Figs. 7.3(a)-7.3(b) for the EH_{01} mode at $f = 5.25$GHz (approximately the center frequency of the EH_{01} monomodal bandwidth).

The viability of metamaterial liners in high-power waveguide applications depends on the power-handling capability of the metamaterial technology itself. Researchers are just beginning to discover the applications, performance, and/or limitations of metamaterials in these environments (see, for example, Refs. [59,156–158]). Nevertheless, in the generation of CR for high-power RF and THz sources, mitigating the propagation of non-EH_{01} modes using anisotropic ENNZ liners would improve beam stability. Furthermore, the miniaturization of the waveguide in this regime may lead to increased yield of the CR, which typically falls off quickly as the distance between the particle beam and the liner medium increases, and also suggests the detection of extremely low-frequency radiation where conventional vacuum-filled waveguides would be cutoff.

7.3 Metamaterial-Coated PEC Rod

The metallic circular PEC rod can be envisioned as the inverse of the hollow metallic waveguide, in which now the metal tightly confines to its surface guided modes (called Sommerfeld modes) that propagate parallel to the rod axis [159]. In recent years, these rods have proven useful in THz-endoscopy measurements, in which the rod acts as a probe to sense small quantities of a material. These applications rely on the circularly symmetric EH_{01} mode, which is capable of efficient propagation and, in this geometry, has no cutoff frequency. This allows for the rod to be tapered to a fine tip resulting in a highly confined mode that enables measurements with subwavelength spatial resolution. In order to achieve greater field confinement, the slow-wave regime of the EH_{01} mode's dispersion is utilized. However, these high values of β may only be achieved near the surface-plasmon resonance. For smooth metal rods, this occurs at $\omega_{ep}/\sqrt{2}$, in which ω_{ep} is the metal's bulk plasma frequency [160]. For most metals, this is typically in the UV range. To compensate at lower frequencies (i.e., sub-THz), the field confinement may be increased by coating the rod with a high-permittivity dielectric or introducing corrugations on the surface [161, 162]. Periodically corrugating the wire with transverse grooves effectively lowers the bulk plasma frequency, hence lowering the surface-plasmon resonance. In the context of planar screens and hollow metallic waveguides, surface corrugations have been shown to be accurately modeled by an anisotropic surface impedance [46] or thin coatings possessing anisotropic permittivity and permeability [163]. These equivalent effective-medium approaches may prove beneficial in engineering a desired dispersion profile for the EH_{01} mode and obtaining high field confinement. Here, we apply this approach by examining the use of a plasmonic coating created from a practical anisotropic metamaterial, such as the printed-circuit implementation, to increase field confinement on these rods in the sub-THz regime.

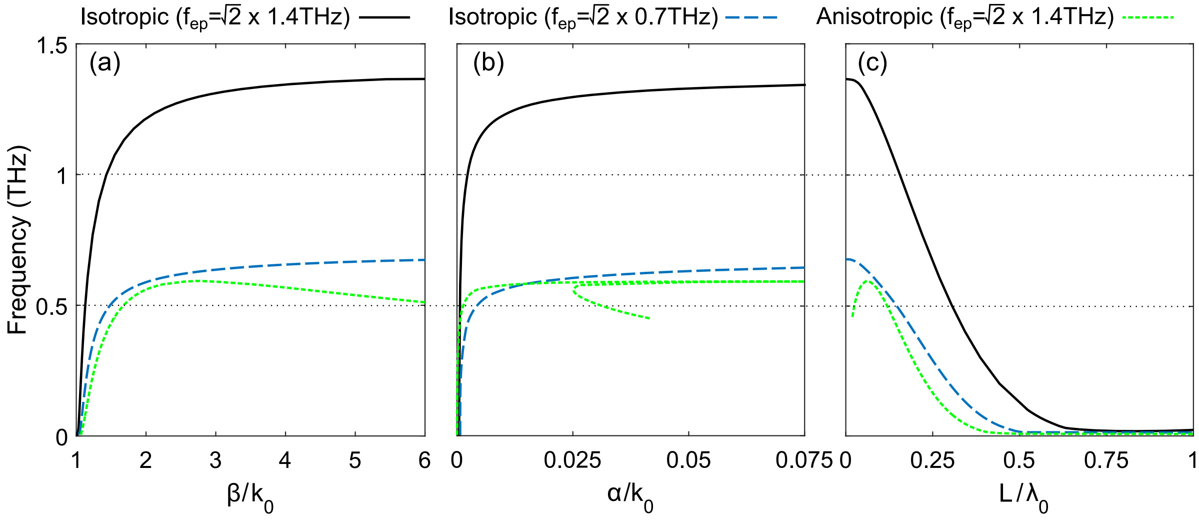

Figure 7.4: The normalized (a) propagation constant (β/k_0), (b) axial attenuation constant (α/k_0), and (c) radial decay length (L/λ_0) of the EH_{01} mode on a metamaterial-coated PEC with a Drude-defined plasmonic coating modeled by an isotropic (solid black and dashed blue curves) and anisotropic (dotted green curve) permittivity.

Consider the metallic rod shown in Fig. 7.1(c), which has an inner PEC region of radius $a = 50\mu$m and an outer metamaterial region of thickness $t = b - a = 50\mu$m that is embedded in a vacuum environment ($\epsilon_3 = \epsilon_0$ and $\mu_3 = \mu_0$). Although not shown, its dispersion relation takes a similar form to Eqs. 3.11. Two categories of the metamaterial coating with dispersive permittivity and a non-magnetic response ($\mu_2 = \mu_0$) are examined: an isotropic coating with $\bar{\bar{\epsilon}}_2 = \bar{\bar{I}}(\epsilon_{\rho 2}, \epsilon_{\rho 2}, \epsilon_{\rho 2})\epsilon_0$ and an anisotropic coating with $\bar{\bar{\epsilon}}_i = \bar{\bar{I}}(\epsilon_{\rho 2}, 1, 1)\epsilon_0$, in which $\epsilon_{\rho 2}$ follows a Drude profile with a fixed damping frequency $\omega_t = 2\pi \times 3$GHz.

Figures 7.4(a)-7.4(c) present the dispersion of the EH_{01} mode's normalized propagation constant, axial attenuation, and radial decay length, respectively, for three different permittivity tensors. When the coating possess an isotropic permittivity with $\omega_{ep} = 2\pi \times \sqrt{2} \times 1.4$THz (solid black curve), the propagation constant's dispersion rapidly diverges from the light line just below the surface-plasmon resonance at $f = 1.40$THz. Due to the liner's thickness and the high field confinement at the metal-air interface, this frequency is nearly the resonance for a homogeneous plasmonic rod of the same permittivity dispersion (i.e., $\omega_{ep}/\sqrt{2} = 1.4$THz). In approaching this resonance, the mode is increasingly bound to the waveguide's surface, which is evident from the decreasing normalized radial decay length in Fig. 7.4(c). Since this results in energy being localized in the lossy coating, the normalized axial attenuation constant α/k_0 increases with β/k_0, as shown in Fig. 7.4(b).

To depress the surface-plasmon resonance to even lower frequencies, the isotropic coating's plasma frequency has to be reduced. However, lowering the plasma frequency using practical metamaterials would require correspondingly stronger reactive loading. For the printed-circuit implementation, these requirements translate to radial inductors with smaller dimensions but larger inductance, which is typically accompanied by increased component loss. This could be modeled by a larger damping factor in the effective-medium model.

An alternative to depressing the surface-plasmon resonance frequency is to employ anisotropy. To illustrate, consider the dotted green curve in Figs. 7.4(a)-7.4(c), which presents the dispersion for the anisotropic coating in which $\epsilon_{\rho 2}$'s plasma frequency is maintained. As a reference case, the dashed blue curve in Figs. 7.4(a)-7.4(c) presents the dispersion for an isotropic liner but with $\omega_{ep} = 2\pi \times \sqrt{2} \times 0.7\text{THz}$. Solely by virtue of the contrast between the dispersive $\epsilon_{\rho 2}$ and the unity value of the remaining tensor elements, it is clear that the surface-plasmon resonance frequency of the anisotropic case is reduced by more than half – a stronger reduction effect than was achieved using an isotropic liner with a reduced plasma frequency. In fact, this difference between the extreme dispersions of the isotropic and anisotropic coatings is largely attributed to the change in ϵ_{z2}, and more extreme cases of anisotropy would lead to further miniaturization. Interestingly, the highest levels of field confinement (i.e., $L_\rho/\lambda_0 \to 0$) and the lowest axial attenuation in the anisotropic case occurs in its backward-wave region. In fact, when $L_\rho/\lambda_0 < 0.037$ the axial attenuation is reduced by up to a factor of 6 in the anisotropic case's backward-wave region with respect to that of the isotropic coatings. Although the anisotropic case's dispersion suggests the mode can propagate at two distinct propagation constants, proper design of the excitation source may enable excitation of only the desired backward-wave component. From this study, it is evident that anisotropy can enable extreme levels of miniaturization through controlling the surface-plasmon resonance. It is true that anisotropy may adversely impact higher-order modes; however, these modes experience generally high attenuation which would, in any event, make them less preferable for the transmission of power.

7.4 Metamaterial Shells To Enhance the Radiation Performance of Antennas

As of this point, the theoretical analysis has been limited to the characteristic solutions of the cylindrical wave equation in a source-free region. While the introduction of an external 'driving' source renders the wave equation mathematically inhomogeneous, analytical solutions of the fields have been formulated for a number of ideal radiating sources, such as the electric-line source (ELS), magnetic-line-source (MLS), and incidence from planar, cylindrical, and propagating propagating waves, in which the fields can be expressed using a weighted sum of planar, cylindrical- or spherical wave harmonics. These techniques have proven useful in designing the radiation properties of isotropic SNG and DNG metamaterial 'shells' to produce resonant configurations that significantly enhance the total radiated power of a nearby antennas [151]. The term 'shell' here refers to the case shown in Fig. 7.1(d), which consists of an hollow metamaterial cylinder that is embedded in free space. The improvement in the antenna's radiated power is attributed to the excitation of resonances in the metamaterial cylinder, which occur when certain conditions relating the cylinder's physical dimensions to its effective-medium properties are satisfied [113]. An ELS oriented in the z-direction (i.e., the metamaterial shell's axis), will strongly couple to the metamaterial shell's *EH* modes due to its dominant E_z. Similarly, an MLS oriented in the z-direction will couple to the shell's *HE* modes, and its fields and dispersion can be readily obtained by duality and are not included here. Whereas a detailed theoretical analysis of an MLS and ELS illuminating isotropic metamaterial shells was presented by Ziolkowski et al, this derivation closely resembles the approach used in Sec. 3.1 for the metamaterial-lined waveguide and is briefly

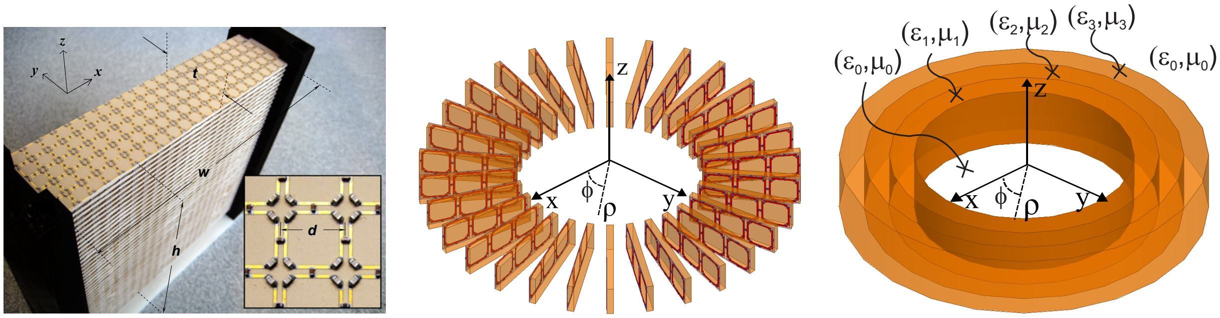

(a) (b) (c)

Figure 7.5: (a) Photograph of fabricated NRI-TL superlens with inset showing lumped loading of the host CPS-TL using discrete surface-mount inductors and capacitors [51]: (b) Cylindrical NRI-TL metamaterial of three-unit-cell thickness; (c) Effective-medium model for the structure shown in (b).

discussed in the upcoming study of an anisotropic metamaterial shell excited by an ELS. Due to the inherent anisotropic material parameters of practical practical metamaterials implementations, it is worth investigating the impact anisotropy has on the shell's resonances and far-field patterns. Our previous analysis suggests that anisotropy may have little effect when certain polarizations and geometrical constraints are satisfied.

This study proposes a practical NRI-TL approach to the design of cylindrical metamaterials, which lends itself to the realization of cylindrical metamaterial shells for improving antenna performance. To this end, the NRI-TL layers used in the free-space superlens [51], shown in Fig. 7.5(a), are arranged in a radial, rather than planar, fashion, resulting in a cylindrical NRI-TL metamaterial exhibiting uniaxially anisotropic and radially inhomogeneous ϵ and μ in the effective-medium limit. Section 7.4.1 presents a physical model for full-wave simulation, as well as a corresponding effective-medium model based on a cylindrical-wave expansion of the fields, which approximates the radial inhomogeneity discretely using concentric homogeneous cylinders of deeply subwavelength thickness, and obtains its uniaxially anisotropic effective-medium properties numerically. Section 7.4.2 compares full-wave simulations of the physical model and the results of the cylindrical-wave expansion for the case of a cylindrical NRI-TL structure of one-unit-cell thickness excited by a displaced ELS. These results exhibit a good mutual agreement and indicate that the practical, anisotropic

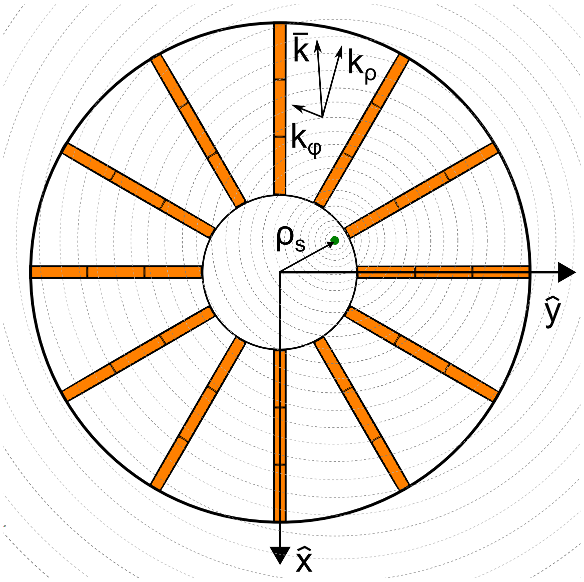

Figure 7.6: A depiction of the cylindrical-wave fronts emanating from an ELS displaced by ρ_s from the cylinder's axis in which the NRI-TL metamaterial shell is superimposed on top. The propagation constant $\bar{k}$ is decomposed into its k_ρ and k_ϕ components.

cylindrical NRI-TL metamaterial exhibits multiple structural resonances and radiated power enhancement analogous to the theoretical observations of Ziolkowski et al for homogeneous, isotropic metamaterial cylinders.

7.4.1 Modeling

The volumetric NRI-TL free-space superlens depicted in Fig. 7.5(a) possesses an effective-medium response that is a function of the host TL parameters, the LC-loading, and also the constant stacking interval, Δh. These design parameters can be found in Ref. [51]. This structure appears isotropic under excitation by a vertical (z-directed) MLS, which produces magnetic fields normal to the NRI-TL unit cells and limits propagation to the 2D isotropic layer planes. Figure 7.5(b) depicts a single-unit-cell cross-section of a cylindrical NRI-TL metamaterial design employing three unit cells in the radial direction. Due to the reorientation of the planar NRI-TL layers, the cylindrical structure is excited by an ELS, which produces z-polarized electric fields. When located on the cylinder axis, the ELS emanates cylindrical waves possessing a radially propagating component (k_ρ) corresponding to

ϕ-polarized magnetic fields alone. These fields are everywhere normal to the constituent NRI-TL unit cells, and the metamaterial appears isotropic to the source. However, as depicted in Fig. 7.6, an ELS displaced from the cylinder axis also produces propagating components in the azimuthal direction (k_ϕ), corresponding to ρ-polarized magnetic fields, which are everywhere tangential to the the NRI-TL unit cells. As a result, the cylindrical NRI-TL structure must, in general, be regarded as anisotropic. Furthermore, the spacing between layers in a cylindrical arrangement varies constantly with radius, rendering the structure radially inhomogeneous. Since the constituent NRI-TL unit cell is electrically very small, radial inhomogeneity over N unit cells may be modeled discretely using N homogeneous, concentric cylindrical regions, as shown for $N = 3$ in Fig. 7.5(c), provided also that the azimuthal spacing, Δh, between adjacent radial layers is electrically very small. This condition may be enforced by choosing a sufficient number of radially arranged layers.

This work examines one such cylindrical region in isolation, whose full-wave and effective-medium models are shown in Fig. 7.7(a) and Fig. 7.7(b), respectively, with an accompanying vertical ELS. The physical structure consists of 12 radially arranged NRI-TL layers, each of thickness one unit cell. The design parameters describing each unit cell are identical to those employed in Ref. [51]. The inner and outer radii, ρ_i and ρ_o, identify the inner and outer boundaries, respectively, of the unit cells. Whereas the effective-medium analogy is strictly valid for propagation in the azimuthal direction, it may appear troublesome to make the same analogy for propagation through a single unit cell in the radial direction. It should be noted that the 2D NRI-TL unit cell is akin to a symmetrically loaded, square split-ring resonator (SRR) possessing a very large area filling factor. As a result, the fields inside a single unit cell are, indeed, homogeneous, and the boundaries of the metamaterial are well defined. Although not presented in this work, effective-medium parameter extractions for slabs of 5-, 3-, and 1-cell thickness yield nearly identical results in the effective-medium limit. The validity of the homogenization over a single-unit-cell thickness shall also be established shortly using a comparison between near fields and radiation patterns produced from full-

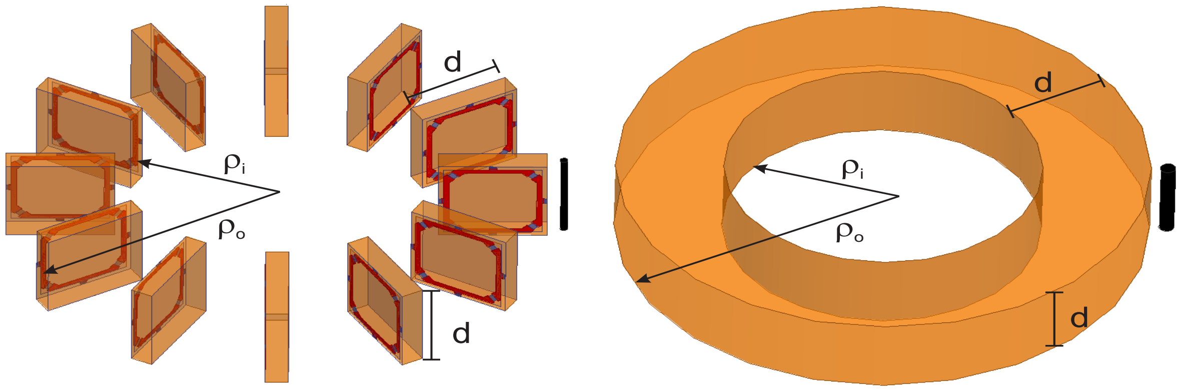

(a) (b)

Figure 7.7: Single-cell NRI-TL structure's (a) full-wave model and (b) effective-medium model with an ELS situated at its outer interface.

wave and effective-medium models.

The homogeneous cylindrical region is described by diagonal effective-medium tensors, $\bar{\bar{\epsilon}}_2(\rho) = \bar{\bar{I}}(\epsilon_{\rho 2}, \epsilon_{\phi 2}, \epsilon_{z2})\epsilon_0$ and $\bar{\bar{\mu}}_2(\rho) = \bar{\bar{I}}(\mu_{\rho 2}, \mu_{\phi 2}, \mu_{z2})\mu_0$. The fields in and around the metamaterial are determined analytically by a cylindrical-wave expansion in each region i. The resulting electric field in region i may be expressed as

$$E_{z,i}(\rho,\phi) = -I_e \frac{\omega\mu_{\phi,i}}{4} \sum_{n=-N_{trun}}^{N_{trun}} \left[C_{m,i} J_m(k_{\rho,i}\,\rho) + C_{m,(i+1)} Y_m(k_{\rho,i}\,\rho) + E_{z,ELS}\right] \cdot \exp jn(\phi - \phi_s) \tag{7.4}$$

where,

$$k_{\rho,i} = \omega\sqrt{\epsilon_{z,i}\,\mu_{\phi,i}}\,, \quad m = n/\sqrt{\mu_{\rho,i}/\mu_{\phi,i}}, \tag{7.5}$$

$E_{z,ELS}$ is nonzero only in the region containing the ELS and N_{trun} is the maximum azimuthal mode number included in the numerical evaluation. The addition theorem is implicated here because the ELS can generally be displaced from the origin ($\rho = 0$). The electric-field generated by the displaced ELS takes the well-known expression:

$$E_{z,ELS} = c_n J_m(k_{\rho,i}\,\rho_s) H_n^{(2)}(k_{\rho,i}\,\rho_s), \tag{7.6}$$

where, c_n is the Neumann number ($c_n = 1$ for $n = 0$ and $c_n = 2$ for $n \neq 0$) [164].

It is interesting to note here the order (m) and argument ($k_{\rho,i}$) of the Bessel functions are in fact the previously defined τ and γ_ρ^ϵ at cutoff ($\gamma = 0$) which were implicated in the EH_{01} mode's dispersion for each investigated class of circular waveguides. The cutoff condition makes sense since we are no longer considered with propagation along the cylinder's axis. Matching the tangential electric and magnetic fields at each interface results in a system of equations that may be inverted to produce the desired field coefficients, $C_{i,m}$. This approach is similar to that employed in Ref. [113], but differs in one important aspect: the anisotropy of the metamaterial leads to tensor elements of opposite sign, resulting in the solutions to Bessel's equation possessing complex orders, m. As a result, several useful simplifications can no longer be made, and the accuracy of numerical evaluation of these solutions is highly sensitive to the degree of anisotropy and must be conducted with very high numerical precision.

Once the field coefficients are obtained it remains only to supply the formulation with the metamaterial's anisotropic effective-medium parameters. These may be obtained from full-wave simulations through a process that will be described in the next section. In addition to providing the near fields, this formulation also provides the directivity pattern of the structure as well as the power ratio (PR), which is defined as the power radiated in the presence of the metamaterial, relative to power radiated in its absence [113]:

$$PR = 10 \cdot \log\left(\frac{P_{rad,\,w/\,metamaterial}}{P_{rad,\,w/o\,metamaterial}}\right) \tag{7.7}$$

7.4.2 Extraction of Anisotropic Effective-Medium Parameters

The effective-medium parameters of a metamaterial may be determined by inversion of the scattering parameters of a thin array of metamaterial unit cells [58]. These are typically obtained using full-wave simulations in which the metamaterial is illuminated by a normally-incident plane wave of fixed linear polarization. To employ these methods in the determination of the tensor parameters of the cylindrical NRI-TL metamaterial, two such simulation

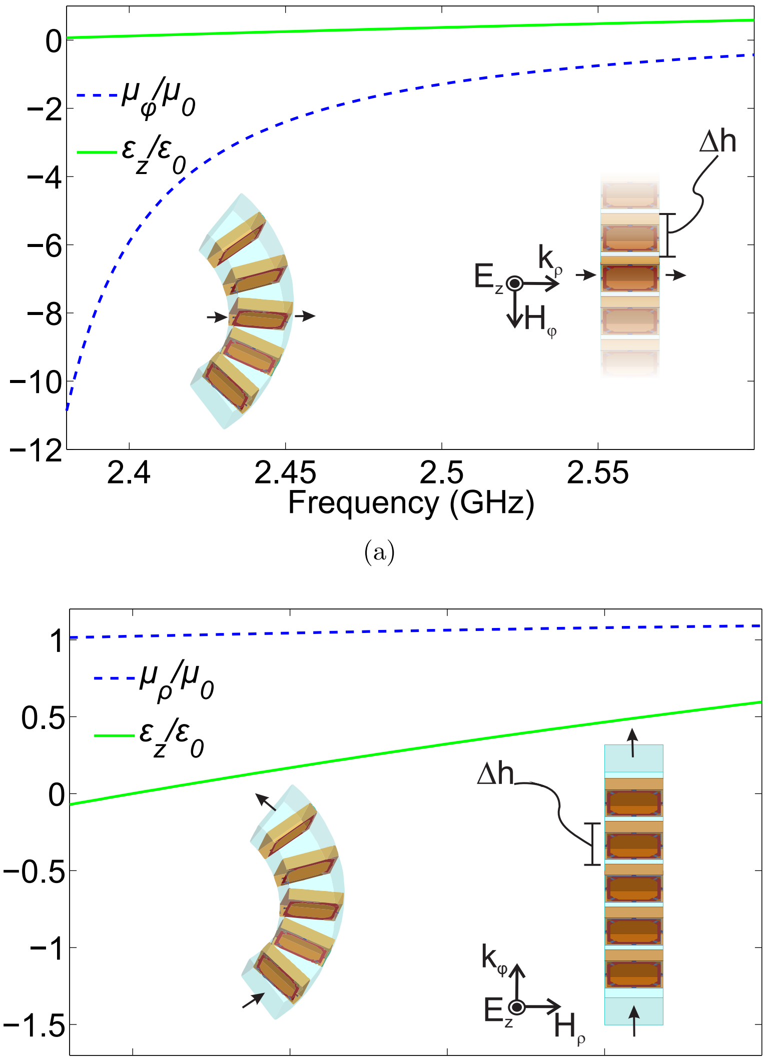

(a)

(b)

Figure 7.8: Relative effective-medium parameters for (a) radial propagation, and (b) azimuthal propagation. Insets show the corresponding extraction models and field polarizations.

models must be developed, corresponding to propagation in the radial and azimuthal directions, and yielding the complex tensor element pairs (ϵ_z, μ_ϕ) and (ϵ_z, μ_ρ), respectively. For this purpose, the radial arrangement of the NRI-TL layers must be approximated by a parallel multilayer arrangement with an equivalent constant layer spacing, Δh, chosen to preserve the mutual coupling between adjacent unit cells. By treating each metamaterial unit cell as a small current loop and accounting for nearest-neighbour interaction only, we have determined the effective separation of parallel layers (the only arrangement for which material parameters may be extracted in HFSS) that results in the same field strength in the central loop as produced by three angled layers. This spacing equates the mutual coupling between unit cells provided they are uniformly excited and possess identical area filling factors.

Azimuthal propagation around a cylindrical structure must be approximated by propagation normally through a finite number of parallel unit cells (five unit cells were employed in this work). Figures 7.8(a) and 7.8(b) present the effective-medium parameters extracted from the two simulation models using HFSS, over a range of frequencies from 2.38GHz to 2.60GHz. As should be expected, μ_ϕ assumes negative values (strong magnetic response for magnetic fields penetrating the NRI-TL unit cells) but μ_ρ remains near the free-space value (weak magnetic response for magnetic fields tangential to the NRI-TL unit-cell plane); furthermore, both propagation directions exhibit the same values of ϵ_z, which remains generally positive and near zero for the range of frequencies and geometrical parameters under consideration.

7.4.3 Comparison of Full-wave Simulations and Effective-Medium Model

Full-wave simulations of the cylindrical NRI-TL structure shown in Fig. 7.7(a) were performed using HFSS. The metamaterial is surrounded by a vacuum region with periodic boundary conditions on the top and bottom surface that render the structure infinite in the axial ($z-$) direction, and a radiation boundary condition a distance of one-quarter wavelength from its outer radius. The ELS is modeled using a PEC cylinder of 0.25mm radius that is also rendered vertically infinite. The effective-medium model of the cylindrical NRI-TL structure is infused with the effective-medium tensors, $\bar{\bar{\epsilon}}$ and $\bar{\bar{\mu}}$, extracted as described in the previous section and excited by an ideal ELS of infinitesimal radius. The fields are

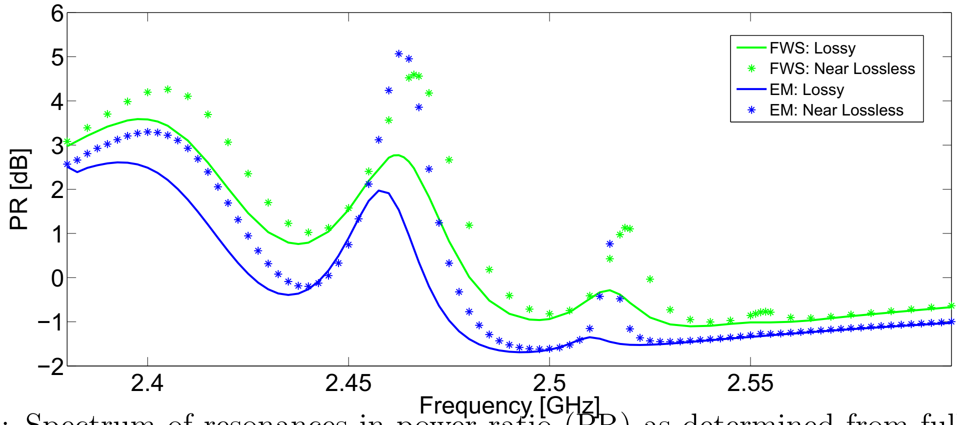

Figure 7.9: Spectrum of resonances in power ratio (PR) as determined from full-wave simulations (FWS) and analytical effective-medium (EM) model in lossy (solid curves) and near-lossless (symbols) cases.

then computed numerically, employing sufficient azimuthal mode numbers to ensure convergence. In both cases, the ELS is supplied with a constant 1-A current and located a distance of 0.5mm from the metamaterial's outer radius, and the fields are obtained under both near-lossless and lossy conditions. Whereas the former includes minimal conductor losses to ensure stronger convergence, the latter additionally incorporates dielectric loss in the host medium, the quality factors of the discrete inductors and capacitors, and surface roughness on the copper TL traces.

Figure 7.9 presents the PR produced by the cylindrical NRI-TL metamaterial structure over a frequency region from 2.38GHz to 2.60GHz. The light green and dark blue curves respectively represent the full-wave simulation results and analytical effective-medium results employing realistic losses, and their near-lossless variations are plotted alongside using discrete markers of the same colour. In the full-wave results (effective-medium results), resonant-like peaks are observed at 2.400GHz (2.395GHz), 2.4625GHz (2.4575GHz), and 2.515GHz (2.510GHz), corresponding respectively to the dipolar, quadrupolar, and sextupolar resonant modes of the cylindrical NRI-TL structure. Whereas the near-lossless structure exhibits PR enhancements anywhere from 1dB to upwards of 5dB, the results for the practical lossy structure are expectedly more modest; nevertheless, they indicate useful enhancements in radiated power of approximately $2 - -3$dB at both the dipolar and quadrupolar reso-

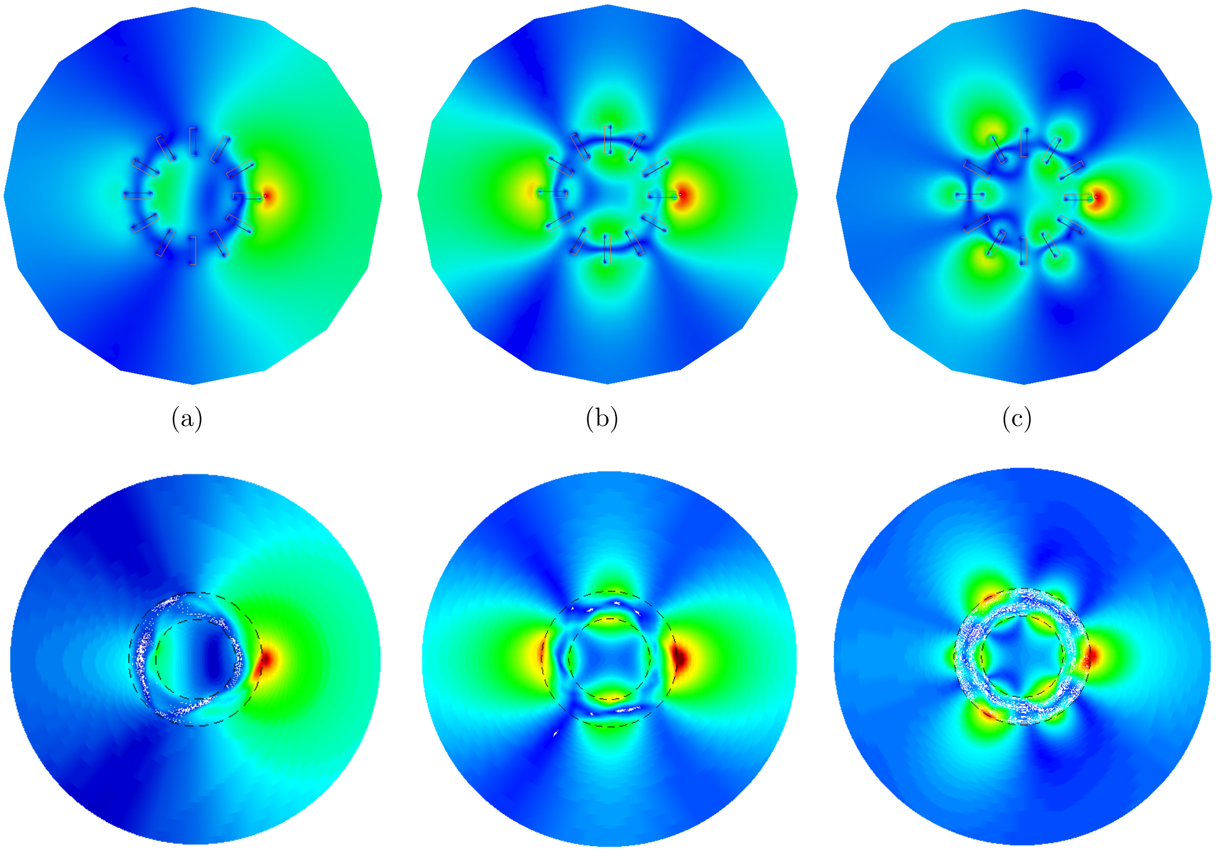
(a) (b) (c)

(d) (e) (f)

Figure 7.10: Complex electric field magnitudes for the dipolar, quadrupolar, and sextupolar resonances obtained from the full-wave model [(a)–(c)], and the effective-medium model [(d)–(f)].

nance frequencies. The values obtained from full-wave simulation and the effective-medium model differ by less than 1dB over the frequency range. As previously noted, the determination of PR in the anisotropic case is highly sensitive to both computational precision of the semi-analytical method, and to a lesser extent, the degree of convergence of the full-wave simulation results. However, it should be noted that the resonance frequencies of the full-wave and analytical results differ by less than 0.2% and the two data share a very similar asymptotic behaviour at high frequencies.

Figures 7.10 present the complex electric field magnitudes for each of the three resonances as revealed by the full-wave simulations [parts (a)–(c)] and the analytical effective-medium model [parts (d)–(f)]. The radiation pattern of each resonance as obtained from simulation

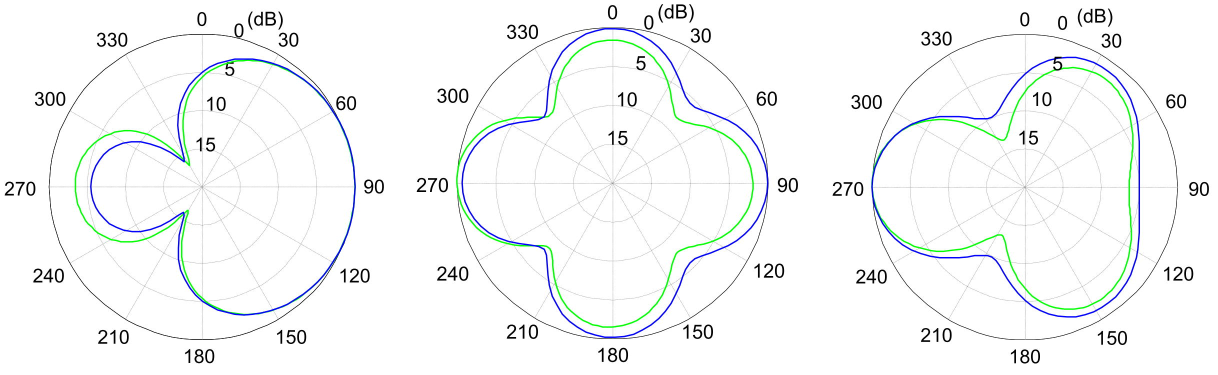

(a)

(b)

(c)

Figure 7.11: Radiation patterns for the (a) dipolar, (b) quadrupolar, and (c) sextupolar resonances obtained from the full-wave model (blue curves), and the effective-medium model (green curves).

(green curve) and the numerical analysis (blue curve) is shown in Fig. 7.11. These results exhibit very good agreement, and therefore establish that the practical, cylindrical NRI-TL metamaterial of thickness as little as one unit cell may, indeed, be accurately modeled as a homogeneous, anisotropic effective-medium and exhibits resonance phenomena that may be exploited to enhance the radiation properties of simple antennas. As a result, the analytical effective-medium model may also be used as a means for rapid synthesis of cylindrical NRI-TL structures with optimized PR response, by properly selecting the TL geometry and lumped-loading values to achieve the desired anisotropic parameters. Moreover, the use of NRI-TL layers consisting of multiple cells, resulting in radial inhomogeneity, may provide an additional degree of freedom in widening the bandwidth of PR enhancement, and may enable the realization of a wide range of antenna patterns.

Chapter 8

Conclusions and Future Work

8.1 Summary

The work described in this thesis has been concerned with the intriguing effects and implications of partially filling circular waveguides with metamaterial liners possessing anisotropic, dispersive, and negative permittivity. The propagation characteristics of a miniaturized PEC circular waveguide containing an anisotropic metamaterial liner have been analyzed theoretically, numerically, and experimentally. A full anisotropic treatment of the liner reveals that a spectrum of frequency-reduced modes is introduced well below its natural cutoff frequency, where the liner's transverse permittivity assumes negative and near-zero values. It was shown how the cutoff frequency of the HE_{n1} modes may be designed using the dimensions and permittivities of the liner and waveguide, while the cutoff frequency of the EH_{01} mode occurs at the liner's plasma frequency. Full-wave simulations of transmission through a lined waveguide section in the backward-wave region reveal multiple resonant transmission peaks corresponding to Fabry-Pérot-type resonant phase conditions over the waveguide's length. Analytical and full-wave-simulation results of the dispersion properties and field profiles exhibit excellent agreement, and validate that metamaterial-lined circular waveguides operating in the frequency-reduced regime offer the potential for miniaturized waveguide components suitable for applications in which the waveguide volume must remain largely empty. A new feeding arrangement employing a shielded-loop source embedded inside the miniaturized waveguide was shown to efficiently excite the HE_{11} mode and avoid the excitation of other modes across the frequency-reduced band while maintaining the waveguide's compactness. It is shown that the introduction of metamaterial liners in traveling-wave MR scanners would enable TW-MRI at lower frequencies by introducing a frequency-reduced passband containing transmission resonances that, although they are narrowband, present sufficient bandwidth for RF detection. This has the significant benefit of enabling TW-MRI in existing clinical scanners, possibly by retrofitting them with low-cost metamaterial liners, where otherwise higher-strength magnets would be required at an additional cost of millions of dollars. A practical PCB-based metamaterial based on inductively loaded metallic traces is shown to yield dispersion and miniaturization properties at RF frequencies that are consistent with those observed for homogeneous, anisotropic metamaterial liners. A first-order homogenization procedure used to model the PCB implementation employs an effective anisotropic permittivity and is shown to accurately match the cutoff frequencies of the lowest-order frequency-reduced modes. Full-wave simulations and experimental results were presented for a waveguide lined with 11 metamaterial layers and excited by two shielded-loop sources. The data are in good agreement, and reveal a frequency-reduced passband demonstrating an enhancement of transmission of up to 19dB as compared to a similarly excited vacuum-filled waveguide, despite the metamaterial-lined waveguide being 60% smaller.

Complementing these studies, it has been shown that the substantial improvement in transmission in a metamaterial-lined waveguide lends itself to the miniaturization of their open-ended variant. Accordingly, this work has presented a rigorous study of the radiation characteristics of metamaterial-lined OEWG probe antennas whose aperture dimensions have been miniaturized. The metamaterial-lined OEWG probe exhibits a frequency reduced HE_{11} backward-wave passband well below its natural cutoff frequency, in which field-equivalence of the open aperture's fields reveal similar directivity and far-field patterns that closely resemble those of the TE_{11} mode in a hollow OEWG probe. Full-wave simulations of the shielded-loop-excited metamaterial-lined OEWG probe in the frequency-reduced region reveal multiple resonant return-loss peaks where the miniaturized antenna exhibits a substantially improved gain over both a similarly sized (and below-cutoff) circular waveguide probe and a reference dipole. A metamaterial-lined OEWG probe antenna implemented using a multilayer printed-circuit approach is designed to operate more than 37% below its natural cutoff frequency. Simulated and experimental return loss, far-field radiation patterns, and directivity are found to be consistent and show a measured operating bandwidth of 100MHz and measured directivity of nearly 6.0dB at the return-loss peaks (a 0.4dB difference as compared to simulated directivity). The introduction of a large metallic-screen (reflector) behind the antenna is shown to improve the match between simulations and measurements and result in higher forward directivity. Although an elliptical polarization is observed in measurements (particularly at higher frequencies), it is suggested that linear polarization can be preserved provided we operate at sufficiently low frequencies in the return-loss band where the measured cross-pol radiation is at least 15dB lower than co-pol. Similar overall trends are observed in both the simulated and measured gain profiles, in which the former reaches a maximum of -9.13dB and the latter is generally is generally 10dB lower. It is suggested the gain may be improved with further refinement of the construction process for the metamaterial-lined OEWG probe and its shielded-loop excitation to reduce fabrication tolerances and loss from the metamaterial liner.

The propagation characteristics of a general class of circular waveguides exhibiting a dispersive and anisotropic permittivity has been theoretically and numerically investigated using a slightly modified version of the theoretical dispersion and field analysis presented for the metamaterial-lined PEC circular waveguide, but which takes into account different boundary conditions and/or external sources. Case studies for a metamaterial-lined PEC circular waveguide and a metamaterial-coated PEC rod detail that anisotropic metamaterial parameters can be exploited to enable unique propagation phenomena not easily obtainable with conventional isotropic materials. This includes widening operational bandwidths of a single mode, enabling higher degrees of miniaturization and high field confinement, and introducing new bands of backward-wave propagation. These may prove useful in the coupling of incident energy to these waveguides, enabling their miniaturization, in Cherenkov radiation experiments, in THz endoscopy measurements, and in a multitude of other applications from RF to optical frequencies. This work concludes by investigating an anisotropic metamaterial shell composed of radially oriented NRI-TL layers to improve the radiation performance of nearby antennas. It is established that cylindrical NRI-TL metamaterials may be described as anisotropic effective media, which support multipole resonances akin to those observed in isotropic media that may be exploited to increase the power radiated by nearby antennas. An analytical determination of near fields, radiation patterns, and power-ratio enhancement based on an anisotropic effective-medium approach exhibits very good agreement with full-wave simulations for a cylindrical NRI-TL metamaterial consisting of 12 radially arranged layers of one-unit-cell thickness.

8.2 Contributions

This section lists refereed journal and conference papers, patents and disclosures, and other academic contributions made during the course of this work.

8.2.1 Journal Papers

[J7] J. G. Pollock, A. K. Iyer, "Experimental Verification of Below-Cutoff Propagation in Miniaturized Circular Waveguides Using Anisotropic ENNZ Metamaterial Liners", *IEEE Trans. Microw. Theory Techn.*, vol. 64 , no. 4, pp. 1297-1305, 2016.

[J6] D. Pratap, S.A. Ramakrishna, J. G. Pollock, and A. K. Iyer, "A class of circular waveguiding structures containing cylindrically anisotropic metamaterials: Applications from radio frequency/microwave to optical frequencies", *Opt. Express*, vol. 119, no. 8, pp. 83103-83113, 2016.

[J5] E. Baladi, J. G. Pollock, A. K. Iyer,"A New Approach for Extraordinary Transmission through an Array of Subwavelength Apertures Using Thin ENNZ Metamaterial Liners", Opt. Express, vol. 23, no. 16, pp. 20356–20365, 2015.

[J4] D. Pratap, S.A. Ramakrishna, J. G. Pollock, and A. K. Iyer, "Anisotropic metamaterial optical fibers", *Opt. Express*, vol. 23, no. 7, pp. 9074-9085, 2015.

[J3] J. G. Pollock, A. K. Iyer, "Miniaturized Circular-Waveguide Probe Antennas Using Metamaterial Liners", *IEEE Trans. Antennas Propag.*, vol. 63, no. 1, pp.428-433, 2015.

[J2] J. G. Pollock and A. K. Iyer, "Below-Cutoff Propagation in Metamaterial-Lined Circular Waveguides", *IEEE Trans. Microw. Theory Techn.*, vol. 61, no. 9, pp. 3169–3178, 2013.

[J1] J. G. Pollock and A. K. Iyer, "Effective-Medium Properties of Cylindrical Transmission-Line Metamaterials", *IEEE Antennas Wireless Propag. Lett.*, vol. 10, pp. 1491–1494, 2011.

8.2.2 Conference Papers

[C11] E. Baladi, J. G. Pollock., and A.K. Iyer., "Enhanced Transmission through Metamaterial-Lined Subwavelength Apertures", *Antennas and Propagation Society International Symposium (APS/URSI)*, Vancouver, Canada, 2015.

[C10] J. G. Pollock, Iyer, A.K., "Radiation Characteristics of Miniaturized Metamaterial-Lined Waveguide Probe Antennas", *Antennas and Propagation Society International Symposium (APS/URSI)*, Vancouver, Canada, 2015.

[C9] E. Baladi, J. G. Pollock., and A.K. Iyer., “A New Approach for Extraordinary Transmission through Subwavelength Apertures Using ENNZ Metamaterials”, *6th International Conference on Metamaterials, Photonic Crystals, and Plasmonics*, New York, USA, 2015.

[C8] Ramakrishna S. A., Pratap D., J. G. Pollock., and Iyer A.K., “Anisotropic Metamaterial optical fibers: Bessel modes with imaginary orders and nanoporous alumina microtubes”, *in 12th International Conference on Fiber Optics and Photonics, OSA Technical Digest*, Kharagpur, India, 2014.

[C7] J. G. Pollock, A. K. Iyer, “Miniaturized circular waveguide probe antennas using ENNZ metamaterial liners”, *Antennas and Propagation Society International Symposium (APS/URSI)*, pp. 338–339, Memphis, USA, 2014.

[C6] J. G. Pollock and A. K. Iyer, “Realization of ϵ-negative-near-zero Metamaterial Liners for Circular Waveguides”, *IEEE Applied Electromagnetics Conference 2013*, Bhubaneswar, India, 2013.

[C5] J. G. Pollock and A. K. Iyer, “Analysis of Propagation in Metamaterial-Lined Circular Waveguides”, *Antennas and Propagation Society International Symposium (APS/URSI)*, Orlando, USA, 2013.

[C4] J. G. Pollock, N. DeZanche, and A. K. Iyer, “Travelling-Wave MRI at Lower B_0 Field Strength Using Metamaterial Liners”, *International Society for Magnetic Resonance in Medicine Annual Meeting ISMRM 2012*, Melbourne, Australia, 2012.

[C3] J. G. Pollock and A. K. Iyer, “A Hybrid Approach for Characterizing Large Anisotropic and Inhomogeneous Metamaterial Structures”,*International Workshop on Finite Elements for Microwave Engineering FEM 2012*, Estes Park, USA, 2012.

[C2] J. G. Pollock and A. K. Iyer, “Cylindrical Free-Space Transmission-Line Metamaterials: A Numerical Study”, *Metamaterials 2011*, Barcelona, Spain, 2011.

[C1] J. G. Pollock and A. K. Iyer, “Multilayer Cylindrical Transmission-Line Metamaterials and their Applications in Imaging and Antenna Beamforming, Experimental and Numerical Validations of Metamaterial Phenomena”, *Antennas and Propagation Society International Symposium (APS/URSI) 2011*, Spokane, USA, 2011.

8.2.3 Patents and Disclosures

[P2] A. K. Iyer, E. Baladi, and J. G. Pollock, “Metamaterial-based aperture arrays enabling engineered transmission and shielding properties”, Utility US Provisional Patent Application #62/194,441 filed July 20, 2015.

[P1] A. K. Iyer, J. G. Pollock, and N. De Zanche, “Metamaterial liners for high-field-strength traveling-wave magnetic resonance imaging”, Utility US Patent Application #13/757,459, filed February 1, 2013.

8.3 Future Considerations

The results presented in this thesis have numerically and experimentally demonstrated that the introduction of a thin-metamaterial liner into the interior of circular waveguides and OEWG probes enables their miniaturization, and, that these structures exhibit improved transmission and radiation characteristics over similarly sized hollow versions. However, further development for the mentioned application in TW-MRI and material and antenna characterization is required. Furthermore, it may be worth further exploring the PCB-based liner in different circular waveguide environments for applications from RF to optical frequencies.

8.3.1 Validation of Metamaterial-lined Waveguides for TW-MRI

In Sec. 5.3, it was shown that coating the interior of human-sized MR-scanner bore with a thin, isotropic metamaterial liner will introduce a HE_{11} cutoff frequency which is well below the Larmor frequency of conventional 3T scanner; thereby enabling TW-based imaging using lower B_0 field strengths without occupying a significant amount of space within the bore. Future research will focus on a practical implementation of these metamaterial-lined based on the PCB-based liners developed in this work but scaled down to operate near 100MHz. Although the liner will be coating the inside of an MR-scanner bore that is roughly 1m in diameter, each metamaterial layer could partitioned into multiple azimuthal sections that can be individually fabricated using standard printed-circuit techniques. Furthermore, implementing the required inductance will be no challenge because there exists a broad range of off-the-shelf low-loss discrete inductors that operate all the way down to MHz frequencies. Dispersion and field analysis performed using electromagnetic simulation software will gauge the metamaterial's impact on detection efficiency, RF energy absorption in tissue, and RF field uniformity. As previously mentioned, the latter is highly desirable in obtaining high-quality MR images Simulations will be complimented by the related theoretical analysis presented in this Ch. 3 that will provide insight into the realistic electromagnetic conditions required to improve MR image quality. This includes studying what level of loss is acceptable in the metamaterial-lined MR bore and techniques to compensate for losses such as by increasing source power, employing more sensitive receivers, or focusing on antenna design for better coupling to the waveguide mode. Nevertheless, it should be pointed out that, even in the presence of losses, through using a source of sufficient excitation strength the magnetic fields inside the vacuum region can be made strong enough to enable traveling-wave imaging. A prototyped metamaterial coating will be retrofitted to an existing clinical whole-body MRI scanner in which experimental imaging will be performed on anatomically correct phantoms. This will allow for a rapid assessment of the metamaterial's value to the imaging system.

8.3.2 Validation of Metamaterial-lined OEWG Probes for Antenna and Material Characterization

As previously noted, miniaturized OEWG probes would be able to sample nearby electromagnetic fields at sub-wavelength spatial resolutions. Achieving this feat using thin metamaterial liners further increases the probe's functionality by retaining access to the probe's interior volume and allowing the probe to sense materials such as gases, liquids, or granular solids placed inside the probe. Future directions of research will focus on experimental validation of these probing applications, which will be based upon the theoretical and experimental groundwork developed in Ch. 6. Before these investigations can proceed, a new prototype metamaterial-lined OEWG probe antenna with improved gain and radiation efficiency will have to undergo experimental validation. This prototype may then be used to experimentally measure the fields produced by a microstrip patch array, in which the probe's decreased aperture size may allow the detection of subwavelength defects that would not be possible with a conventional-sized OEWG probe. This could aid in quickly diagnosing large antenna array systems. In order to gauge the usefulness of the metamaterial-lined OEWG probe in the characterization of materials, a series of simple experiments can be performed, in which different materials are placed in the probe's interior and the return-loss response is measured. The measured return-loss profile will depend on the material's dielectric constant and loss, conductivity, and total quantity. The multiple return-loss peaks would enable discrete frequency sampling of dispersive quantities, such as permittivity, over a given bandwidth. Furthermore, the sharp bandwidths could actually be useful in sensing applications requiring high selectivity. Further sensitivity in measurements could be possible by allowing the material to permeate the metamaterial region, where the field strengths are highest, instead of the inner vacuum region.

8.3.3 Other-Classes of Anisotropic Circular Waveguides

In the study of the metamaterial-coated PEC rod in Sec. 7.3, significant degrees of miniaturization and high field confinement were observed where the liner possesses an anisotropic permittivity with a negative (and dispersive) ϵ_ρ and a large and positive ϵ_ϕ. The printed-circuit metamaterial developed in this work is a natural realization of these anisotropic material parameters. Whereas the homogenization approach in Ch. 4 modeled the thin metamaterial liner using a uniaxial permittivity and permeability, the liner is, in fact, strictly biaxial, which becomes more prevalent as the liner gets thicker. Homogenization of thick biaxial liners will require a more complex circuit model based on multiconductor TL theory, which more rigorously accounts for the presence of the adjacent metamaterial layer, spatial dispersion, and mutual inductance between the isolated conductors. This will allow for the quick design of PCB-based liners that can possess a broad range of anisotropic material parameters, such as those required for the metamaterial-coated rod. The metamaterial-coated PEC rod can be realized by simply stripping a coaxial waveguide's outer conductor and substrate and placing the exposed pin into the interior of the fabricated PCB liner.

The PCB liner could be useful in other classes of circular waveguides. For instance, even without outer or inner PEC boundaries the liner may still have intriguing propagation characteristics. These liners could act similarly to optical fibers, in which the negative-permittivity property may bound a wave to the liner's interior through total internal reflection. Conversely, the PCB liner's inner and outer surface could be coated by a PEC, rendering the liner as a homogeneously filled coaxial waveguide. The exotic and anisotropic material parameters offered by the PCB liner could enable backward-wave, slow-wave, and forward-wave behaviour over a broad range of frequencies. This investigation could also lend insight into analogous investigations of coaxial waveguides operated at optical frequencies that are loaded using radially emanating silver-coated nanopores that exhibit plasmonic-like behaviour [165].

In general, it may be possible to introduce, manipulate, or suppress propagating bands of a subset of modes, or render control over their field configurations, polarizations, and coupling through exploiting anisotropy. This level of control could have a profound impact on the several applications from RF to optical frequencies in which circular waveguiding structures are widely used.

8.3.4 Subwavelength Aperture Screens With Thin Metamaterial Liners

Consider a metamaterial-lined waveguide of finite length L. It was shown in Sec. 5.1.1 that it is possible to tune its spectral response through varying the waveguide's length. However, it hasn't been investigated in this work what occurs when L is allowed to shrink to infinitesimal length. In this case, the waveguide would appear as a circular aperture, and would exhibit a frequency-reduced HE_{11} resonance that is akin the frequency-reduced HE_{11} mode in the metamaterial-lined waveguide. This resonance could enable transmission through subwavelength metamaterial-lined circular apertures on a perfect metallic screen. In fact, extraordinary transmission (ET) at microwave frequencies through an array of subwavelength metamaterial-lined circular apertures has been analyzed numerically and experimentally for apertures measuring one-quarter of a wavelength in diameter [166]. In that work, a practical PCB-based metamaterial liner is shown to yield a fano-type ET profile (i.e., a resonance and antiresonance in close spectral proximity) which is independent of incident angle and array period and instead dependent on the resonance of the individual apertures. Future directions of research include extending these studies to the terahertz and optical regimes by using an ENNZ metamaterial liner technology better suited to these frequency ranges, such as plasmonic metallic spheres on a dielectric substrate. Furthermore, the anisotropy offered by the PCB-based liner could allow for increased control over the aperture's ET profile, potentially allowing for higher degrees of selectivity.

Bibliography

[1] P. J. B. Clarricoats and B. C. Taylor, "Evanescent and propagating modes of dielectric-loaded circular waveguide," *Proc. Inst. Elect. Eng.*, vol. 111, pp. 1951–1956, Dec. 1964.

[2] P. Clarricoats and A. Olver, "Low attenuation in corrugated circular waveguides," *Electronics Letters*, vol. 9, no. 16, pp. 376–377, 1973.

[3] A. Olver, P. Clarricoats, and S. Chong, "Experimental determination of attenuation in corrugated circular waveguides," *Electronics Letters*, vol. 9, no. 18, pp. 424–426, 1973.

[4] S. Hrabar, J. Bartolic, and Z. Sipus, "Waveguide miniaturization using uniaxial negative permeability metamaterial," *IEEE Trans. Antennas Propag.*, vol. 53, no. 1, pp. 110–119, Jan. 2005.

[5] F. Y. Meng, Q. Wu, D. Erni, and L. W. Li, "Controllable metamaterial-loaded waveguides supporting backward and forward waves," *IEEE Trans. Antennas Propag.*, vol. 59, no. 9, pp. 3400–3411, 2011.

[6] C. Anandan, C. Nimisha, B. Jitha, P. Mohanan, and K. Vasudevan, "Transmission properties of microstrip lines loaded with split ring resonators as superstrate," *Microwave and optical technology letters*, vol. 48, no. 11, pp. 2280–2282, 2006.

[7] Y. Huang, W. Lu, and S. Sridhar, "Nanowire waveguide made from extremely anisotropic metamaterials," *Physical Review A*, vol. 77, no. 6, p. 063836, 2008.

[8] V. A. Podolskiy and E. E. Narimanov, "Strongly anisotropic waveguide as a nonmagnetic left-handed system," *Physical Review B*, vol. 71, no. 20, p. 201101, 2005.

[9] Q. Zhang, T. Jiang, and Y. Feng, "Slow-light propagation in a cylindrical dielectric waveguide with metamaterial cladding," *Journal of Physics D: Applied Physics*, vol. 44, no. 47, p. 475103, 2011.

[10] W. T. Lu, S. Savo, B. D. F. Casse, and S. Sridhar, "Slow microwave waveguide made of negative permeability metamaterials," *Microwave and Optical Technology Letters*, vol. 51, no. 11, pp. 2705–2709, 2009.

[11] O. Ozgun and M. Kuzuoglu, "Utilization of anisotropic metamaterial layers in waveguide miniaturization and transitions," *Microwave and Wireless Components Letters, IEEE*, vol. 17, no. 11, pp. 754–756, 2007.

[12] E. Lier, D. H. Werner, C. P. Scarborough, Q. Wu, and J. A. Bossard, “An octave-bandwidth negligible-loss radiofrequency metamaterial,” *Nature materials*, vol. 10, no. 3, pp. 216–222, 2011.

[13] D. Ramaccia, F. Scattone, F. Bilotti, and A. Toscano, “Broadband compact horn antennas by using eps-enz metamaterial lens,” *IEEE Trans. Antennas Propag.*, vol. 61, no. 6, pp. 2929–2937, June 2013.

[14] R. Ziolkowski and A. Erentok, “At and below the chu limit: passive and active broad bandwidth metamaterial-based electrically small antennas,” *IET Microwaves, Antennas & Propagation*, vol. 1, no. 1, pp. 116–128, 2007.

[15] Z. Duan, B. I. Wu, S. Xi, H. Chen, and M. Chen, “Research progress in reversed cherenkov radiation in double-negative metamaterials,” *Progress in Electromagnetic Research, PIER*, vol. 90, pp. 75–87, 2009.

[16] Z. Duan, Y. Wang, X. Mao, W.-X. Wang, and M. Chen, “Experimental demonstration of double-negative metamaterials partially filled in a circular waveguide,” *Progress In Electromagnetics Research*, vol. 121, pp. 215–224, 2011.

[17] T. C. K. Rao, “Propagation characteristics of a circular waveguide coated inside with a metamaterial,” *International Journal of Electronics*, vol. 94, no. 10, pp. 935–942, 2007.

[18] G. F. Brand, “Dispersion relations for cylindrical waveguides with metamaterial linings,” *International Journal of Electronics*, vol. 96, no. 1, pp. 99–107, 2009.

[19] B. Ghosh and A. B. Kakade, “Guided modes in a metamaterial-filled circular waveguide,” *Electromagnetics*, vol. 32, no. 8, pp. 465–480, 2012.

[20] M. A. Baqir, A. A. Syed, and Q. A. Naqvi, “Electromagnetic fields in a circular waveguide containing chiral nihility metamaterial,” *Progress In Electromagnetics Research M*, vol. 16, pp. 85–93, 2011.

[21] J. B. Pendry, A. J. Holden, W. J. Stewart, and I. Youngs, “Extremely low frequency plasmons in metallic mesostructures,” *Physical review letters*, vol. 76, no. 25, p. 4773, 1996.

[22] R. A. Shelby, D. R. Smith, and S. Schultz, “Experimental verification of a negative index of refraction,” *science*, vol. 292, no. 5514, pp. 77–79, 2001.

[23] A. A. Houck, J. B. Brock, and I. L. Chuang, “Experimental observations of a left-handed material that obeys snells law,” *Physical Review Letters*, vol. 90, no. 13, p. 137401, 2003.

[24] A. K. Iyer and G. V. Eleftheriades, “Volumetric layered transmission-line metamaterial exhibiting a negative refractive index,” *JOSA B*, vol. 23, no. 3, pp. 553–570, 2006.

[25] A. Sanada, C. Caloz, and T. Itoh, “Characteristics of the composite right/left-handed transmission lines,” *Microwave and Wireless Components Letters, IEEE*, vol. 14, no. 2, pp. 68–70, 2004.

[26] A. Alù, M. G. Silveirinha, and N. Engheta, “Transmission-line analysis of ϵ-near-zero–filled narrow channels,” *Phys. Rev. E*, vol. 78, p. 016604, Jul. 23 2008.

[27] A. Penirschke and R. Jakoby, “Microwave mass flow detector for particulate solids based on spatial filtering velocimetry,” *IEEE Trans. Microw. Theory Techn.*, vol. 56, no. 12, pp. 3193–3199, 2008.

[28] P. Ratanadecho, K. Aoki, and M. Akahori, “A numerical and experimental investigation of the modeling of microwave heating for liquid layers using a rectangular wave guide (effects of natural convection and dielectric properties),” *Appl. Math. Modelling*, vol. 26, no. 3, pp. 449–472, 2002.

[29] Y.-Z. Yin, “The cyclotron autoresonance maser with a large-orbit electron ring in a dielectric-loaded waveguide,” *Int. J. Infrared and Millimeter Waves*, vol. 14, no. 8, pp. 1587–1600, 1993.

[30] J. G. Pollock, N. De Zanche, and A. K. Iyer, “Travelling wave MRI at lower B_0 field strengths using metamaterial liners,” *Proc. International Society for Magnetic Resonance in Medicine*, vol. 20, p. 2792, 2012.

[31] L. R. F.R.S., “Xviii. on the passage of electric waves through tubes, or the vibrations of dielectric cylinders,” *Philosophical Magazine Series 5*, vol. 43, no. 261, pp. 125–132, 1897. [Online]. Available: http://dx.doi.org/10.1080/14786449708620969

[32] K. S. Packard, “The origin of waveguides: A case of multiple rediscovery,” *IEEE Trans. Microw. Theory Techn.*, vol. 32, no. 9, pp. 961–969, 1984.

[33] L. Brown, *Technical and Military Imperatives: A Radar History of World War 2.* CRC Press, 1999, ch. Chapter 4: New Ideas, pp. 145–158.

[34] T. Satoh, “Dielectric-loaded horn antenna,” *Antennas and Propagation, IEEE Transactions on*, vol. 20, no. 2, pp. 199–201, 1972.

[35] R. J. Meredith, *Engineers’ Handbook of Industrial Microwave Heating.* IET, 1998, no. 25.

[36] A. Cook, R. Tikhoplav, S. Y. Tochitsky, G. Travish, O. Williams, and J. Rosenzweig, “Observation of narrow-band terahertz coherent cherenkov radiation from a cylindrical dielectric-lined waveguide,” *Physical review letters*, vol. 103, no. 9, p. 095003, 2009.

[37] K. W. Whites, “Electromagnetic wave propagation through circular waveguides containing radially inhomogeneous lossy media,” Master’s thesis, University of Illinois, Urbana-Champaign, Aug. 1988, Available through Defense Technical Information Center (DTIC) Online, http://www.dtic.mil/dtic/tr/fulltext/u2/a213062.pdf [Accessed March 18, 2016].

[38] P. Chorney, "Power and energy relations in bidirectional waveguides," Tech. Rep. 396, Research Lab. of Electronics, MIT. Cambridge, MA, Sept. 1961.

[39] R. Islam and G. V. Eleftheriades, "On the independence of the excitation of complex modes in isotropic structures," *IEEE Trans. Antennas Propag.*, vol. 58, no. 5, pp. 1567–1578, 2010.

[40] G. N. Tsandoulas, "Bandwidth enhancement in dielectric-lined circular waveguides," *IEEE Trans. Microw. Theory Tech*, vol. 21, no. 10, pp. 651–654, Oct. 1973.

[41] R.-C. Chou and S.-W. Lee, "Modal attenuation in multilayered coated waveguides," *IEEE Trans. Microw. Theory Techn.*, vol. 36, no. 7, pp. 1167–1176, 1988.

[42] C. Jing, W. Liu, W. Gai, J. Power, and T. Wong, "Mode analysis of a multilayered dielectric-loaded accelerating structure," *Nuclear Instruments and Methods in Physics Research Section A: Accelerators, Spectrometers, Detectors and Associated Equipment*, vol. 539, no. 3, pp. 445–454, 2005.

[43] J. Y. Choe and H. S. Uhm, "Theory of gyrotron amplifiers in disc or helix-loaded waveguides," *International Journal of Electronics Theoretical and Experimental*, vol. 53, no. 6, pp. 729–741, 1982.

[44] V. Kesari and J. P. Keshari, "Analysis of a circular waveguide loaded with dielectric and metal discs," *Progress In Electromagnetics Research*, vol. 111, pp. 253–269, 2011.

[45] P. Potter, *A new horn antenna with suppressed sidelobes and equal bandwidths.* Jet Propulsion Laboratory, California Institute of Technology, 1963.

[46] P.-S. Kildal, "Artificially soft and hard surfaces in electromagnetics," *Antennas and Propagation, IEEE Transactions on*, vol. 38, no. 10, pp. 1537–1544, 1990.

[47] N. Raveu, B. Byrne, L. Claudepierre, and N. Capet, "Modal theory for waveguides with anisotropic surface impedance boundaries," *IEEE Transactions on Microwave Theory and Techniques*, vol. 64, no. 4, pp. 1153–1162, 2016.

[48] I. A. Eshrah, A. A. Kishk, A. B. Yakovlev, and A. W. Glisson, "Rectangular waveguide with dielectric-filled corrugations supporting backward waves," *Microwave Theory and Techniques, IEEE Transactions on*, vol. 53, no. 11, pp. 3298–3304, 2005.

[49] N. Engheta and R. W. Ziolkowski, *Metamaterials: physics and engineering explorations.* Wiley. com, 2006.

[50] D. Schurig, J. Mock, B. Justice, S. Cummer, J. Pendry, A. Starr, and D. Smith, "Metamaterial electromagnetic cloak at microwave frequencies," *Science*, vol. 314, no. 5801, pp. 977–980, 2006.

[51] A. K. Iyer and G. V. Eleftheriades, "Free-space imaging beyond the diffraction limit using a Veselago-Pendry transmission-line metamaterial superlens," *IEEE Trans. Antennas Propag.*, vol. 57, no. 6, pp. 1720–1727, 2009.

[52] A. Alù and N. Engheta, “Pairing an epsilon-negative slab with a mu-negative slab: resonance, tunneling and transparency,” *IEEE Trans. Antennas Propag.*, vol. 51, no. 10, pp. 2558–2571, 2003.

[53] R. W. Ziolkowski, “Metamaterial-based antennas: Research and developments,” *IEICE transactions on electronics*, vol. 89, no. 9, pp. 1267–1275, 2006.

[54] M. Navarro-Cia, M. Beruete, I. Campillo, and M. Ayza, “Beamforming by left-handed extraordinary transmission metamaterial bi- and plano-concave lens at millimeter-waves,” *IEEE Trans. Antennas Propag.*, vol. 59, no. 6, pp. 2141–2151, June 2011.

[55] J. Zhu and G. V. Eleftheriades, “A compact transmission-line metamaterial antenna with extended bandwidth,” *Antennas and Wireless Propagation Letters, IEEE*, vol. 8, pp. 295–298, 2009.

[56] G. V. Eleftheriades and K. G. Balmain, *Negative-Refraction Metamaterials: Fundamental Principles and Applications.* Wiley-IEEE Press, 2005.

[57] D. R. Smith and J. B. Pendry, “Homogenization of metamaterials by field averaging,” *JOSA B*, vol. 23, no. 3, pp. 391–403, 2006.

[58] D. R. Smith, S. Schultz, P. Markoš, and C. M. Soukoulis, “Determination of effective permittivity and permeability of metamaterials from reflection and transmission coefficients,” *Physical Review B*, vol. 65, no. 19, p. 195104, 2002.

[59] A. Erentok, R. W. Ziolkowski, J. Nielsen, R. Greegor, C. Parazzoli, M. Tanielian, S. A. Cummer, B.-I. Popa, T. Hand, D. Vier *et al.*, “Lumped element-based, highly sub-wavelength, negative index metamaterials at uhf frequencies,” *Journal of Applied Physics*, vol. 104, no. 3, p. 034901, 2008.

[60] D. R. Smith, D. Vier, N. Kroll, and S. Schultz, “Direct calculation of permeability and permittivity for a left-handed metamaterial,” *Applied Physics Letters*, vol. 77, no. 14, pp. 2246–2248, 2000.

[61] J.-M. Lerat, N. Malléjac, and O. Acher, “Determination of the effective parameters of a metamaterial by field summation method,” *Journal of applied physics*, vol. 100, no. 8, p. 084908, 2006.

[62] A. Pors, I. Tsukerman, and S. I. Bozhevolnyi, “Effective constitutive parameters of plasmonic metamaterials: homogenization by dual field interpolation,” *Physical Review E*, vol. 84, no. 1, p. 016609, 2011.

[63] I. Tsukerman, “Nonlocal homogenization of metamaterials by dual interpolation of fields,” *JOSA B*, vol. 28, no. 12, pp. 2956–2965, 2011.

[64] G. Lubkowski, R. Schuhmann, and T. Weiland, “Extraction of effective metamaterial parameters by parameter fitting of dispersive models,” *Microwave and Optical Technology Letters*, vol. 49, no. 2, pp. 285–288, 2007.

[65] R. A. Shore and A. D. Yaghjian, "Traveling waves on two-and three-dimensional periodic arrays of lossless scatterers," *Radio Science*, vol. 42, no. 6, 2007.

[66] S. Obrien and J. Pendry, "Magnetic activity at infrared frequencies in structured metallic photonic crystals," *Journal of Physics: Condensed Matter*, vol. 14, no. 25, p. 6383, 2002.

[67] P. Markoš and C. M. Soukoulis, "Transmission properties and effective electromagnetic parameters of double negative metamaterials," *Optics express*, vol. 11, no. 7, pp. 649–661, 2003.

[68] X. Chen, T. M. Grzegorczyk, B.-I. Wu, J. Pacheco Jr, and J. A. Kong, "Robust method to retrieve the constitutive effective parameters of metamaterials," *Physical Review E*, vol. 70, no. 1, p. 016608, 2004.

[69] G. V. Eleftheriades, "Analysis of bandwidth and loss in negative-refractive-index transmission-line (NRI–TL) media using coupled resonators," *Microwave and Wireless Components Letters, IEEE*, vol. 17, no. 6, pp. 412–414, 2007.

[70] A. Ishimaru, S.-W. Lee, Y. Kuga, and V. Jandhyala, "Generalized constitutive relations for metamaterials based on the quasi-static lorentz theory," *IEEE Trans. Antennas Propag.*, vol. 51, no. 10, pp. 2550–2557, 2003.

[71] J. B. Pendry, A. J. Holden, D. Robbins, and W. Stewart, "Magnetism from conductors and enhanced nonlinear phenomena," *IEEE Trans. Microw. Theory Techn.*, vol. 47, no. 11, pp. 2075–2084, 1999.

[72] D. Liu, C. Li, F. Zhou, T. Zhang, H. Zhang, X. Li, G. Duan, W. Cai, and Y. Li, "Rapid synthesis of monodisperse au nanospheres through a laser irradiation-induced shape conversion, self-assembly and their electromagnetic coupling sers enhancement," *Scientific reports*, vol. 5, 2015.

[73] W. Rotman, "Plasma simulation by artificial dielectrics and parallel-plate media," *Antennas and Propagation, IRE Transactions on*, vol. 10, no. 1, pp. 82–95, 1962.

[74] D. Wu, N. Fang, C. Sun, X. Zhang, W. J. Padilla, D. N. Basov, D. R. Smith, and S. Schultz, "Terahertz plasmonic high pass filter," *Applied Physics Letters*, vol. 83, no. 1, pp. 201–203, 2003.

[75] T.-J. Yen, W. Padilla, N. Fang, D. Vier, D. Smith, J. Pendry, D. Basov, and X. Zhang, "Terahertz magnetic response from artificial materials," *Science*, vol. 303, no. 5663, pp. 1494–1496, 2004.

[76] J. Zhou, T. Koschny, M. Kafesaki, E. Economou, J. Pendry, and C. Soukoulis, "Saturation of the magnetic response of split-ring resonators at optical frequencies," *Physical review letters*, vol. 95, no. 22, p. 223902, 2005.

[77] N. Liu, H. Guo, L. Fu, S. Kaiser, H. Schweizer, and H. Giessen, "Three-dimensional photonic metamaterials at optical frequencies," *Nature materials*, vol. 7, no. 1, pp. 31–37, 2008.

[78] A. Alù and N. Engheta, "Polarizabilities and effective parameters for collections of spherical nanoparticles formed by pairs of concentric double-negative, single-negative, and/ or double-positive metamaterial layers," *Journal of Applied Physics*, vol. 97, no. 9, p. 094310, 2005.

[79] C. L. Holloway, E. F. Kuester, J. Baker-Jarvis, and P. Kabos, "A double negative (dng) composite medium composed of magnetodielectric spherical particles embedded in a matrix," *IEEE Trans. Antennas Propag.*, vol. 51, no. 10, pp. 2596–2603, 2003.

[80] C. Pfeiffer and A. Grbic, "Metamaterial huygens surfaces: tailoring wave fronts with reflectionless sheets," *Physical review letters*, vol. 110, no. 19, p. 197401, 2013.

[81] G. V. Eleftheriades, A. K. Iyer, and P. C. Kremer, "Planar negative refractive index media using periodically lc loaded transmission lines," *IEEE Trans. Microw. Theory Techn.*, vol. 50, no. 12, pp. 2702–2712, 2002.

[82] N. Engheta, "An idea for thin subwavelength cavity resonators using metamaterials with negative permittivity and permeability," *Antennas and Wireless Propagation Letters, IEEE*, vol. 1, pp. 10–13, 2002.

[83] A. Alù and N. Engheta, "Mode excitation by a line source in a parallel-plate waveguide filled with a pair of parallel double-negative and double-positive slabs," in *Antennas and Propagation Society International Symposium, 2003. IEEE*, vol. 3. IEEE, 2003, pp. 359–362.

[84] I. Nefedov and S. Tretyakov, "Waveguide containing a backward-wave slab," *Radio Science*, vol. 38, no. 6, 2003.

[85] A. Alù and N. Engheta, "Guided modes in a waveguide filled with a pair of single-negative (SNG), double-negative (DNG), and/or double-positive (DPS) layers," *IEEE Trans. Microw. Theory Tech*, vol. 52, no. 1, pp. 199–210, 2004.

[86] R. Marques, J. Martel, F. Mesa, and F. Medina, "Left-handed-media simulation and transmission of em waves in subwavelength split-ring-resonator-loaded metallic waveguides," *Physical Review Letters*, vol. 89, no. 18, p. 183901, 2002.

[87] B. Edwards, A. Alù, M. E. Young, M. Silveirinha, and N. Engheta, "Experimental verification of epsilon-near-zero metamaterial coupling and energy squeezing using a microwave waveguide," *Physical Review Letters*, vol. 100, no. 3, p. 033903, 2008.

[88] M. G. Silveirinha and N. Engheta, "Tunneling of electromagnetic energy through subwavelength channels and bends using ϵ-near-zero materials," *Phys. Rev. Lett.*, vol. 97, p. 157403, 2006.

[89] A. Alù and N. Engheta, "Coaxial-to-waveguide matching with ϵ-near-zero ultranarrow channels and bends," *IEEE Trans. Antennas Propag.*, vol. 58, no. 2, pp. 328–339, 2010.

[90] M. Silveirinha and N. Engheta, "Tunneling of electromagnetic energy through subwavelength channels and bends using ε-near-zero materials," *Phys. Rev. Lett.*, vol. 97, no. 15, p. 157403, 2006.

[91] R. Liu, Q. Cheng, T. Hand, J. J. Mock, T. J. Cui, S. A. Cummer, and D. R. Smith, "Experimental demonstration of electromagnetic tunneling through an epsilon-near-zero metamaterial at microwave frequencies," *Phys. Rev. Lett.*, vol. 100, no. 2, p. 23903, 2008.

[92] R. Maas, J. Parsons, N. Engheta, and A. Polman, "Experimental realization of an epsilon-near-zero metamaterial at visible wavelengths," *Nature Photonics*, vol. 7, no. 11, pp. 907–912, 2013.

[93] A. Alu and N. Engheta, "Dielectric sensing in ϵ-near-zero narrow waveguide channels," *Physical Review B*, vol. 78, no. 4, p. 045102, 2008.

[94] O. Siddiqui and O. M. Ramahi, "A novel dielectric detection system based on wire-loaded waveguides," *Microwave and Wireless Components Letters, IEEE*, vol. 21, no. 2, pp. 113–115, Feb 2011.

[95] H. A. Wheeler, "Fundamental limitations of small antennas," *Proceedings of the IRE*, vol. 35, no. 12, pp. 1479–1484, 1947.

[96] L. J. Chu, "Physical limitations of omni-directional antennas," *Journal of applied physics*, vol. 19, no. 12, pp. 1163–1175, 1948.

[97] R. F. Harrington, "Effect of antenna size on gain, bandwidth, and efficiency," *Journal of Research of the National Bureau of Standards*, vol. 64, no. 1, pp. 1–12, 1960.

[98] M. C. Decreton and M. Ramachandraiah, "Nondestructive measurement of complex permittivity for dielectric slabs (short papers)," *IEEE Trans. Microw. Theory Techn.*, vol. 23, no. 12, pp. 1077–1080, 1975.

[99] C. Huber, H. Abiri, S. I. Ganchev, and R. Zoughi, "Modeling of surface hairline-crack detection in metals under coatings using an open-ended rectangular waveguide," *IEEE Trans. Microw. Theory Techn.*, vol. 45, no. 11, pp. 2049–2057, 1997.

[100] A. H. Barrett and P. C. Myers, "Basic principles and applications of microwave thermography," pp. 41–46, 1986.

[101] A. Yaghjian, "An overview of near-field antenna measurements," *IEEE Trans. Antennas Propag.*, vol. 34, no. 1, pp. 30–45, 1986.

[102] T. Tice and J. Richmond, "Probes for microwave near-field measurements," *Microwave Theory and Techniques, IRE Transactions on*, vol. 3, no. 3, pp. 32–34, 1955.

[103] J. E. Hansen, *Spherical near-field antenna measurements.* London:Peter Pegrinus, 1988, vol. 26.

[104] P. Ludlow, V. Fusco, G. Goussetis, and D. E. Zelenchuk, "Applying band-pass filter techniques to the design of small-aperture evanescent-mode waveguide antennas," *IEEE Trans. Antennas Propag.*, vol. 61, no. 1, pp. 134–142, 2013.

[105] M. Kehn and P. S. Kildal, "Miniaturized rectangular hard waveguides for use in multifrequency phased arrays," *IEEE Trans. Antennas Propag.*, vol. 53, no. 1, pp. 100–109, Jan 2005.

[106] G. V. Eleftheriades and M. A. Antoniades, *Modern Antenna Handbook.* John Wiley and Sons, Inc., 2007, ch. Antenna Applications of Negative-Refractive-Index Transmission-Line (NRI-TL) Metamaterials, pp. 675–736.

[107] S. Lim, C. Caloz, and T. Itoh, "Metamaterial-based electronically controlled transmission-line structure as a novel leaky-wave antenna with tunable radiation angle and beamwidth," *IEEE Trans. Microw. Theory Techn.*, vol. 52, no. 12, pp. 2678–2690, 2004.

[108] E. Lier, D. H. Werner, C. P. Scarborough, Q. Wu, and J. A. Bossard, "An octave-bandwidth negligible-loss radiofrequency metamaterial," *Nature materials*, vol. 10, no. 3, pp. 216–222, 2011.

[109] Q. Wu, P. Pan, F.-Y. Meng, L.-W. Li, and J. Wu, "A novel flat lens horn antenna designed based on zero refraction principle of metamaterials," *Applied Physics A*, vol. 87, no. 2, pp. 151–156, 2007.

[110] D. Ramaccia, F. Scattone, F. Bilotti, and A. Toscano, "Broadband compact horn antennas by using eps-enz metamaterial lens," *IEEE Trans. Antennas Propag.*, vol. 61, no. 6, pp. 2929–2937, 2013.

[111] K. Buell, H. Mosallaei, and K. Sarabandi, "Metamaterial insulator enabled superdirective array," pp. 1074–1085, April 2007.

[112] J. Zhu and G. Eleftheriades, "Dual-band metamaterial-inspired small monopole antenna for wifi applications," *Electronics Letters*, vol. 45, no. 22, p. 1, 2009.

[113] S. Arslanagic, R. W. Ziolkowski, and O. Breinbjerg, "Analytical and numerical investigation of the radiation and scattering from concentric metamaterial cylinders excited by an electric line source," *Radio Science*, vol. 42, no. 6, p. RS6S15, 2007.

[114] K. Buell, H. Mosallaei, and K. Sarabandi, "A substrate for small patch antennas providing tunable miniaturization factors," *IEEE Trans. Microw. Theory Techn.*, vol. 54, no. 1, pp. 135–146, 2006.

[115] S. Hrabar and G. Jankovic, "Basic radiation properties of waveguides filled with uniaxial single-negative metamaterials," *Microwave and optical technology letters*, vol. 48, no. 12, pp. 2587–2591, 2006.

[116] Y.-R. Ju, S.-S. Oh, W.-K. Park, and H.-D. Park, “Open-ended waveguide antenna using a single split-ring resonator,” *ETRI Journal*, vol. 33, no. 2, pp. 291–294, 2011.

[117] J. B. Pendry, “Negative refraction makes a perfect lens,” *Physical review letters*, vol. 85, no. 18, p. 3966, 2000.

[118] J. G. Pollock and A. K. Iyer, “Effective-medium properties of cylindrical transmission-line metamaterials,” *Antennas and Wireless Propagation Letters, IEEE*, vol. 10, pp. 1491–1494, 2011.

[119] P. J. B. Clarricoats and R. A. Waldron, “Non-periodic slow-wave and backward-wave structures,” *International Journal of Electronics*, vol. 8, no. 6, pp. 455–458, 1960.

[120] L. Novotny and C. Hafner, “Light propagation in a cylindrical waveguide with a complex, metallic, dielectric function,” *Phys. Rev. E*, vol. 50, no. 5, p. 4094, 1994.

[121] J. G. Pollock and A. K. Iyer, “Experimental verification of below-cutoff propagation in miniaturized circular waveguides using anisotropic ennz metamaterial liners,” *IEEE Trans. Microw. Theory Techn.*, submitted March 20, 2015. Currently Under Review.

[122] P. A. Belov, C. R. Simovski, and S. A. Tretyakov, “Two-dimensional electromagnetic crystals formed by reactively loaded wires.” *Physical review. E, Statistical, nonlinear, and soft matter physics*, vol. 66, no. 3 Pt 2B, p. 036610, Sep 2002.

[123] M. G. Silveirinha and C. A. Fernandes, “Homogenization of 3-d-connected and non-connected wire metamaterials,” *IEEE Trans. Microw. Theory Techn.*, vol. 53, no. 4, pp. 1418–1430, 2005.

[124] M. G. Silveirinha, C. A. Fernandes, and J. R. Costa, “Additional boundary condition for a wire medium connected to a metallic surface,” *New J. Phys.*, vol. 10, no. 5, p. 053011, 2008.

[125] A. Demetriadou and J. Pendry, “Taming spatial dispersion in wire metamaterial,” *J. Phys: Condensed Matter*, vol. 20, no. 29, p. 295222, 2008.

[126] G. V. Eleftheriades, A. K. Iyer, and P. C. Kremer, “Planar negative refractive index media using periodically L-C loaded transmission lines,” *IEEE Trans. Microw. Theory Techn.*, vol. 50, no. 12, pp. 2702–2712, 2002.

[127] G. V. Eleftheriades, O. Siddiqui, and A. K. Iyer, “Transmission line models for negative refractive index media and associated implementations without excess resonators,” *IEEE Microw. Compon. Lett.*, vol. 13, no. 2, pp. 51–53, 2003.

[128] Coilcraft, “Air core inductors, 0806SQ6N0 datasheet,” Mar. 2015.

[129] HFSS. ver. 13, ANSYS Corporation, Canonsburg, PA, 2011. [Online]. Available: http://www.ansoft.com/products/hf/hfss

[130] P. J. B. Clarricoats and A. B. Birtles, “Circular waveguide backward-wave experiments,” *International Journal of Electronics*, vol. 15, no. 4, pp. 325–330, 1963.

[131] N. Marcuvitz, *Waveguide Handbook.* IET, 1951.

[132] H. Whiteside and R. W. P. King, "The loop antenna as a probe," *IEEE Trans. Antennas Propag.*, vol. 12, no. 3, pp. 291–297, 1964.

[133] Q. Tang, F.-Y. Meng, Q. Wu, and J.-C. Lee, "A balanced composite backward and forward compact waveguide based on resonant metamaterials," *J. Appl. Phys.*, vol. 109, no. 7, p. 07A319, 2011.

[134] J. Mispelter, "Homogeneous resonators," in *NMR Probeheads for Biophysical and Biomedical Experiments, 2nd ed.*

[135] D. O. Brunner, N. De Zanche, J. Fröhlich, J. Paska, and K. P. Pruessmann, "Travelling-wave nuclear magnetic resonance," *Nature*, vol. 457, no. 7232, pp. 994–998, 2009.

[136] S. Wolf, D. Diehl, M. Gebhardt, J. Mallow, and O. Speck, "Sar simulations for high-field mri: How much detail, effort, and accuracy is needed?" *Magnetic Resonance in Medicine*, vol. 69, no. 4, pp. 1157–1168, 2013.

[137] A. Kangarlu, B. A. Baertlein, R. Lee, T. Ibrahim, L. Yang, A. M. Abduljalil, and P.-M. L. Robitaille, "Dielectric resonance phenomena in ultra high field mri," *Journal of computer assisted tomography*, vol. 23, no. 6, pp. 821–831, 1999.

[138] C. van den Berg, H. Kroeze, B. van de Bank, B. van den Bergen, P. Luijten, J. Lagendijk, and D. Klomp, "Optimizing traveling wave rf excitation for in vivo use," in *Proceedings of the 17th Annual Meeting of ISMRM, Honolulu, Hawaii, USA*, 2009, p. 2944.

[139] A. Andreychenko, H. Kroeze, D. W. Klomp, J. J. Lagendijk, P. R. Luijten, and C. A. van den Berg, "Coaxial waveguide for travelling wave mri at ultrahigh fields," *Magnetic Resonance in Medicine*, 2012.

[140] A. K. Iyer, P. J. G., and N. DeZanche, "Metamaterial liners for traveling wave magnetic resonance imaging," Feb 2012, utility US Provisional Patent Application 61/594,608.

[141] D. O. Brunner, J. Paška, J. Froehlich, and K. P. Pruessmann, "Traveling-wave rf shimming and parallel mri," *Magnetic resonance in medicine*, vol. 66, no. 1, pp. 290–300, 2011.

[142] B. Zhang, D. K. Sodickson, R. Lattanzi, Q. Duan, B. Stoeckel, and G. C. Wiggins, "Whole body traveling wave magnetic resonance imaging at high field strength: homogeneity, efficiency, and energy deposition as compared with traditional excitation mechanisms," *Magnetic resonance in medicine*, vol. 67, no. 4, pp. 1183–1193, 2012.

[143] C. A. Balanis, *Antenna Theory: Analysis and Design Ver. 3.* John Wiley & Sons, 2012.

[144] M. N. M. Kehn and P.-S. Kildal, "Miniaturized rectangular hard waveguides for use in multifrequency phased arrays," *IEEE Trans. Antennas Propag.*, vol. 53, no. 1, pp. 100–109, 2005.

[145] B. Zhang, G. Wiggins, Q. Duan, and D. Sodickson, "Design of a patch antenna for creating traveling waves at 7 tesla," in *Proceedings of International Society for Magnetic Resonance in Medicine*, vol. 7, no. 4746, 2009.

[146] S. Joardar and A. Bhattacharya, "Simultaneous resolving of frequency separated narrow band terrestrial radio sources by multi antenna spectrum monitoring systems assisting radio astronomy," *Journal of Electromagnetic Waves and Applications*, vol. 20, no. 9, pp. 1195–1209, 2006.

[147] L. Wang and B. Yazici, "Ground moving target imaging using ultranarrowband continuous wave synthetic aperture radar," *Geoscience and Remote Sensing, IEEE Transactions on*, vol. 51, no. 9, pp. 4893–4910, 2013.

[148] M. C. Wicks, B. Himed, L. J. E. Bracken, H. Bascom, and J. Clancy, "Ultra narrow band adaptive tomographic radar," in *Computational Advances in Multi-Sensor Adaptive Processing, 2005 1st IEEE International Workshop on.* IEEE, 2005, pp. 36–39.

[149] J. Zhou, M. J. Lancaster, F. Huang, N. Roddis, and D. Glynn, "Hts narrow band filters at uhf band for radio astronomy applications," *Applied Superconductivity, IEEE Transactions on*, vol. 15, no. 2, pp. 1004–1007, 2005.

[150] K. Naishadham and L. B. Felsen, "Dispersion of waves guided along a cylindrical substrate-superstrate layered medium," *IEEE Trans. Antennas Propag.*, vol. 41, no. 3, pp. 304–313, 1993.

[151] R. W. Ziolkowski and A. D. Kipple, "Application of double negative materials to increase the power radiated by electrically small antennas," *IEEE Trans. Antennas Propag.*, vol. 51, no. 10, pp. 2626–2640, 2003.

[152] H. Wiedemann, *Particle Accelerator Physics*, ser. Graduate Texts in Physics. Springer International Publishing, 2015.

[153] G. T. Flesher and G. I. Cohn, "Dielectric loading for waveguide linear accelerators," *American Institute of Electrical Engineers, Transactions of the*, vol. 70, no. 1, pp. 887–893, 1951.

[154] J. Lawson, *The Physics of Charged-particle Beams*, ser. International series of monographs on physics. Clarendon Press, 1988. [Online]. Available: https://books.google.ca/books?id=j87vAAAAMAAJ

[155] A. Altmark, A. Kanareykin, and I. Sheinman, "Tunable wakefield dielectric-filled accelerating structure," *Technical physics*, vol. 50, no. 1, pp. 87–95, 2005.

[156] R. Seviour, "Towards photonic crystal and metamaterial high-power microwave applications," in *High Power RF Technologies, 2009. IET. Conference on.* IET, 2009, pp. 1–5.

[157] N. Behdad, M. Al-Joumayly, and M. Li, “High-power microwave metamaterials for phased-array, anti-hpm, and pulse shaping applications,” *Bulletin of the American Physical Society*, vol. 55, 2010.

[158] D. Shiffler, R. Seviour, E. Luchinskaya, E. Stranford, W. Tang, and D. French, “Study of split-ring resonators as a metamaterial for high-power microwave power transmission and the role of defects,” *Plasma Science, IEEE Transactions on*, vol. 41, no. 6, pp. 1679–1685, 2013.

[159] G. Goubau, “Surface waves and their application to transmission lines,” *Journal of Applied Physics*, vol. 21, no. 11, pp. 1119–1128, 1950.

[160] K. Wang and D. M. Mittleman, “Metal wires for terahertz wave guiding,” *Nature*, vol. 432, no. 7015, pp. 376–379, 2004.

[161] A. J. L. Adam, “Review of near-field terahertz measurement methods and their applications,” *Journal of Infrared, Millimeter, and Terahertz Waves*, vol. 32, no. 8-9, pp. 976–1019, 2011.

[162] C. R. Williams, S. R. Andrews, S. Maier, A. Fernández-Domínguez, L. Martín-Moreno, and F. García-Vidal, “Highly confined guiding of terahertz surface plasmon polaritons on structured metal surfaces,” *Nature Photonics*, vol. 2, no. 3, pp. 175–179, 2008.

[163] A. Pors, E. Moreno, L. Martin-Moreno, J. B. Pendry, and F. J. Garcia-Vidal, “Localized spoof plasmons arise while texturing closed surfaces,” *Phys. Rev. Lett.*, vol. 108, p. 223905, May 2012. [Online]. Available: http://link.aps.org/doi/10.1103/PhysRevLett.108.223905

[164] B. TI CA, “Advanced engineering electromagnetics,” 1989.

[165] D. Pratap, S. A. Ramakrishna, J. G. Pollock, and A. K. Iyer, “Anisotropic metamaterial optical fibers,” *Opt. Exp.*, vol. 23, no. 7, pp. 9074–9085, Apr 2015.

[166] E. Baladi, J. G. Pollock, and A. K. Iyer, “New approach for extraordinary transmission through an array of subwavelength apertures using thin ennz metamaterial liners,” *Optics express*, vol. 23, no. 16, pp. 20 356–20 365, 2015.

[167] M. D. Deshpande and B. N. Das, “Input impedance of coaxial line to circular waveguide feed,” *IEEE Trans. Microw. Theory Techn.*, vol. 25, no. 11, pp. 954–957, 1977.

[168] H. Whiteside and R. W. P. King, “The loop antenna for transmission and reflection,” *in Antenna Theory: part I, R. E. Collin and F. J. Zucker.*

[169] E. M. Thomas, J. D. Heebl, C. Pfeiffer, and A. Grbic, “A power link study of wireless non-radiative power transfer systems using resonant shielded loops,” *Circuits and Systems I: Regular Papers, IEEE Transactions on*, vol. 59, no. 9, pp. 2125–2136, 2012.

[170] A. Stensgaard, “Optimized design of the shielded-loop resonator,” *Journal of Magnetic Resonance, Series A*, vol. 122, no. 2, pp. 120–125, 1996.

[171] A. K. Iyer, “Free-space metamaterial superlenses using transmission-line techniques,” Ph.D. dissertation, University of Toronto, 2009.

[172] H. Pocklington, “Electrical oscillations in wire,” *Comb. Phil. Soc. Proc*, pp. 324–332, 1897.

[173] R. W. P. King and G. S. Smith, *Antennas in matter: Fundamentals, theory, and applications.* Cambridge: The M.I.T. Press, 1981, pp. 527–605.

[174] R. W. P. King, *R. E. Collin and F. J. Zucker (eds.), Antenna Theory, part 1.* New York: McGraw-Hill, 1969, ch. The Loop Antenna for Transmission and Reception, pp. 527–605.

Appendix A

Transverse Decomposition of Maxwell's Equations for Cylindrically Anisotropic Media

This section will present a transverse decomposition of Maxwell's equations for cylindrically anisotropic media. Maxwell's equations in vector notation takes the form:

$$\overline{\nabla} \times \overline{E} = -j\omega\overline{\overline{\mu}}\,\overline{H}, \tag{A.1a}$$

$$\overline{\nabla} \times \overline{H} = j\omega\overline{\overline{\epsilon}}\,\overline{E}, \tag{A.1b}$$

$$\overline{\nabla} \cdot \overline{D} = 0, \tag{A.1c}$$

$$\overline{\nabla} \cdot \overline{B} = 0. \tag{A.1d}$$

The electric- and magnetic- field vectors, permittivity and permeability, and Laplacian operator can be decomposed into its transverse (T) and longitudinal (z) components and expressed as $\overline{E} = \overline{E}_T + \overline{E}_z$, $\overline{H} = \overline{H}_t + \overline{H}_z$, $\overline{\overline{\epsilon}} = \overline{\overline{\epsilon}}_T + \epsilon_z\hat{z}$ and $\overline{\overline{\mu}} = \overline{\overline{\mu}}_T + \mu_z\hat{z}$, and $\overline{\nabla} =$

$\overline{\nabla}_T + \frac{d}{dz}\hat{z} = \overline{\nabla}_T - \gamma\hat{z}$. Suppressing the time-harmonic nature of the fields (e^{jwt}), the electric- and magnetic- field components of a wave propagating in the z-direction can be represented by the general form $\overline{E}(T,z) = \overline{E}(T)e^{-\gamma z}$ and $\overline{H}(T,z) = \overline{H}(T)e^{-\gamma z}$, in which $\gamma = \alpha + j\beta$. Then Eqs. A.1a-A.1d become:

$$\left(\overline{\nabla}_T - \gamma\hat{z}\right) \times \left(\overline{E}_T + \hat{z}E_z\right) = -j\omega\overline{\overline{\mu}}\,\left(\overline{H}_T + \hat{z}H_z\right), \tag{A.2a}$$

$$\left(\overline{\nabla}_T - \gamma\hat{z}\right) \times \left(\overline{H}_T + \hat{z}H_z\right) = j\omega\overline{\overline{\epsilon}}\,\left(\overline{E}_T + \hat{z}E_z\right), \tag{A.2b}$$

$$\left(\overline{\nabla}_T - \gamma\hat{z}\right) \cdot \left(\overline{\overline{\epsilon}}_T\overline{E}_T + \epsilon_z E_z\hat{z}\right) = 0, \tag{A.2c}$$

$$\left(\overline{\nabla}_T - \gamma\hat{z}\right) \cdot \left(\overline{\overline{\mu}}_T\overline{H}_T + \mu_z H_z\hat{z}\right) = 0. \tag{A.2d}$$

Expanding Eqs. A.2a-A.2d gives:

$$\overline{\nabla}_T E_z \times \hat{z} - \gamma\hat{z} \times \overline{E}_T = -j\omega\overline{\overline{\mu}}_T\,\overline{H}_t, \tag{A.3a}$$

$$\overline{\nabla}_T H_z \times \hat{z} - \gamma\hat{z} \times \overline{H}_T = j\omega\overline{\overline{\epsilon}}_T\,\overline{E}_t, \tag{A.3b}$$

$$\overline{\nabla}_T \times \overline{E}_T + j\omega\mu_z H_z\hat{z} = 0, \tag{A.3c}$$

$$\overline{\nabla}_T \times \overline{H}_T - j\omega\epsilon_z E_z\hat{z} = 0, \tag{A.3d}$$

$$\overline{\nabla}_T \cdot \overline{\overline{\epsilon}}_T\overline{E}_T - \epsilon_z\gamma E_z = 0, \tag{A.3e}$$

$$\overline{\nabla}_T \cdot \overline{\overline{\mu}}_T\overline{H}_T - \mu_z\gamma H_z = 0. \tag{A.3f}$$

Multiplying Eq. A.3b by $(\times\hat{z})$ and expanding the cross product gives:

$$\hat{z} \times \left(\overline{\nabla}_T H_z \times \hat{z}\right) - \gamma\hat{z} \times \left(\hat{z} \times \overline{H}_T\right) = \hat{z} \times j\omega\overline{\overline{\epsilon}}_T\,\overline{E}_T, \tag{A.4a}$$

which gives,

$$\overline{\nabla}_T H_z + \gamma \overline{H}_T = \hat{z} \times \left(j\omega \overline{\overline{\epsilon}}_T \overline{E}_T \right). \tag{A.4b}$$

Use Eq. A.3a and Eq. A.4b, and mathematically isolate $\hat{z} \times \overline{E}_T$ and $\overline{H}_T$ to get:

$$\hat{z} \times \overline{E}_T = \frac{j\omega \overline{\overline{\mu}}_T}{\gamma} \overline{H}_T + \frac{\overline{\nabla}_T E_z \times \hat{z}}{\gamma}, \tag{A.5a}$$

$$\overline{H}_T = \frac{\hat{z} \times \left(j\omega \overline{\overline{\epsilon}}_T \overline{E}_T \right)}{\gamma} - \frac{\overline{\nabla}_T E_z \times \hat{z}}{\gamma}. \tag{A.5b}$$

Substitute Eq.A.5b into Eq. A.5a to get:

$$\overline{E}_T = \frac{-\gamma}{\overline{\overline{\gamma}}_c} \left[\overline{\nabla}_T E_z - \frac{j\omega}{\gamma} \hat{z} \times \overline{\overline{\mu}}_T \overline{\nabla}_T H_z \right]. \tag{A.6}$$

Similarly, substitute Eq. A.6 into Eq. A.5b to get

$$\overline{H}_T = \frac{-\gamma}{\overline{\overline{\gamma}}_c} \left[\overline{\nabla}_T H_z + \frac{j\omega}{\gamma} \hat{z} \times \overline{\overline{\epsilon}}_t \overline{\nabla}_T E_z \right]. \tag{A.7}$$

In a cylindrical coordinate system (ρ, ϕ, z), $\overline{\nabla}_T = \hat{\rho}\frac{\partial}{\partial \rho} + \hat{\phi}\frac{1}{\rho}\frac{\partial}{\partial \phi}$, $\overline{E}_T = E_\rho \hat{\rho} + E_\phi \hat{\phi}$, $\overline{H}_T = H_\rho \hat{\rho} + H_\phi \hat{\phi}$, and $\overline{\overline{\gamma}}_c$ takes the form:

$$\overline{\overline{\gamma}}_c = \begin{bmatrix} \gamma^2_{c,\rho,\phi} & 0 \\ 0 & \gamma^2_{c,\phi,\rho} \end{bmatrix} = \begin{bmatrix} \gamma^2 + \omega^2 \epsilon_\rho \mu_\phi & 0 \\ 0 & \gamma^2 + \omega^2 \epsilon_\phi \mu_\rho \end{bmatrix}. \tag{A.8}$$

Equations A.6-A.7 can be expressed in component form as:

$$E_\rho = \frac{-\gamma}{\gamma^2_{c,\rho,\phi}} \left[\frac{\partial E_z}{\partial \rho} + \frac{j\omega \mu_\phi}{\gamma \rho} \frac{\partial H_z}{\partial \phi} \right], \tag{A.9a}$$

$$E_\phi = \frac{-\gamma}{\gamma^2_{c,\phi,\rho}} \left[\frac{1}{\rho} \frac{\partial E_z}{\partial \phi} - \frac{j\omega \mu_\rho}{\gamma} \frac{\partial H_z}{\partial \rho} \right], \tag{A.9b}$$

$$H_\rho = \frac{-\gamma}{\gamma^2_{c,\phi,\rho}} \left[\frac{\partial H_z}{\partial \rho} - \frac{j\omega \epsilon_\phi}{\gamma \rho} \frac{\partial E_z}{\partial \phi} \right], \tag{A.9c}$$

$$H_\phi = \frac{-\gamma}{\gamma^2_{c,\rho,\phi}} \left[\frac{1}{\rho} \frac{\partial H_z}{\partial \phi} + \frac{j\omega \epsilon_\rho}{\gamma} \frac{\partial E_z}{\partial \rho} \right]. \tag{A.9d}$$

Provided the longitudinal (z) component of the electric and magnetic fields are known, the expressions for the remaining transverse field components may be calculated using Eqs. A.9a-A.9d.

A.1 Wave Equation for Cylindrically Anisotropic Medium

This section will derive the general form of the longitudinal (z) electric- and magnetic-fields from the wave equation. Whereas this analysis follows the standard approach often used to derive the wave equation, it is worth going into detail this derivation in the case of cylindrical anisotropy which increases the complexity of the solution.

Substituting Eqs. A.9a-A.9b into Eq. A.3c gives:

$$\frac{\gamma}{\rho}\frac{\partial^2 E_z}{\partial\rho\partial\phi}\left(\frac{1}{\gamma^2_{c,\rho,\phi}}-\frac{1}{\gamma^2_{c,\phi,\rho}}\right)+j\omega\left(\frac{\mu_\rho}{\rho\gamma^2_{c,\phi,\rho}}\frac{\partial}{\partial\rho}\left(\rho\frac{\partial H_z}{\partial\rho}\right)+\frac{\mu_\phi}{\rho^2\gamma^2_{c,\rho,\phi}}\frac{\partial^2 H_z}{\partial\phi^2}\right)+j\omega\mu_z H_z=0. \quad \text{(A.10)}$$

Substituting Eqs. A.9c-A.9d into Eq. A.3f gives:

$$\frac{j\omega}{\rho}\frac{\partial^2 E_z}{\partial\phi\partial\rho}\left(\frac{\epsilon_\phi\mu_\rho}{\gamma^2_{c,\phi,\rho}}-\frac{\epsilon_\rho\mu_\phi}{\gamma^2_{c,\rho,\phi}}\right)-\gamma\left(\frac{\mu_\rho}{\rho\gamma^2_{c,\phi,\rho}}\frac{\partial}{\partial\rho}\left(\rho\frac{\partial H_z}{\partial\rho}\right)+\frac{\mu_\phi}{\rho^2\gamma^2_{c,\rho,\phi}}\frac{\partial^2 H_z}{\partial\phi^2}\right)-\gamma\mu_z H_z=0. \quad \text{(A.11)}$$

Substituting Eqs. A.9c-A.9d into Eq. A.3d gives:

$$\frac{\gamma}{\rho}\frac{\partial^2 H_z}{\partial\phi\partial\rho}\left(\frac{1}{\gamma^2_{c,\phi,\rho}}-\frac{1}{\gamma^2_{c,\rho,\phi}}\right)-j\omega\left(\frac{\epsilon_\rho}{\rho\gamma^2_{c,\rho,\phi}}\frac{\partial}{\partial\rho}\left(\rho\frac{\partial E_z}{\partial\rho}\right)+\frac{\epsilon_\phi}{\rho^2\gamma^2_{c,\phi,\rho}}\frac{\partial^2 E_z}{\partial\phi^2}\right)-j\omega\epsilon_z E_z=0. \quad \text{(A.12)}$$

Substituting Eqs. A.9a-A.9b into Eq. A.3e gives:

$$\frac{-j\omega}{\rho}\frac{\partial^2 H_z}{\partial\rho\partial\phi}\left(\frac{\epsilon_\rho\mu_\phi}{\gamma^2_{c,\rho,\phi}}-\frac{\epsilon_\phi\mu_\rho}{\gamma^2_{c,\phi,\rho}}\right)-\gamma\left(\frac{\epsilon_\rho}{\rho\gamma^2_{c,\rho,\phi}}\frac{\partial}{\partial\rho}\left(\rho\frac{\partial E_z}{\partial\rho}\right)+\frac{\epsilon_\phi}{\rho^2\gamma^2_{c,\phi,\rho}}\frac{\partial^2 E_z}{\partial\phi^2}\right)-\gamma\epsilon_z E_z=0. \quad \text{(A.13)}$$

It is useful to define the intermediate variables:

$$\chi=\left(\frac{1}{\gamma^2_{c,\rho,\phi}}-\frac{1}{\gamma^2_{c,\phi,\rho}}\right) \text{ and } \chi_{\epsilon,\mu}=\left(\frac{\epsilon_\phi\mu_\rho}{\gamma^2_{c,\rho,\phi}}-\frac{\epsilon_\rho\mu_\phi}{\gamma^2_{c,\phi,\rho}}\right). \quad \text{(A.14)}$$

Using Eq. A.14 and substituting Eq. A.10 into Eq. A.11 gives:

$$\frac{\mu_\rho}{\rho}\frac{\partial}{\partial\rho}\left(\rho\frac{\partial H_z}{\partial\rho}\right)\frac{1}{\gamma^2_{c,\phi,\rho}}\left(\frac{\omega^2\chi_{\epsilon,\mu}}{\chi}-\gamma^2\right)+\frac{\mu_\phi}{\rho^2}\frac{\partial^2 H_z}{\partial\phi^2}\frac{1}{\gamma^2_{c,\rho,\phi}}\left(\frac{\omega^2\chi_{\epsilon,\mu}}{\chi}-\gamma^2\right)+\mu_z H_z\left(\frac{\omega^2\chi_{\epsilon,\mu}}{\chi}-\gamma^2\right)=0. \tag{A.15}$$

Using Eq. A.14 and substituting Eq. A.12 into Eq. A.13 gives:

$$\frac{\epsilon_\rho}{\rho}\frac{\partial}{\partial\rho}\left(\rho\frac{\partial E_z}{\partial\rho}\right)\frac{1}{\gamma^2_{c,\rho,\phi}}\left(\frac{\omega^2\chi_{\epsilon,\mu}}{\chi}-\gamma^2\right)+\frac{\epsilon_\phi}{\rho^2}\frac{\partial^2 E_z}{\partial\phi^2}\frac{1}{\gamma^2_{c,\phi,\rho}}\left(\frac{\omega^2\chi_{\epsilon,\mu}}{\chi}-\gamma^2\right)+\epsilon_z E_z\left(\frac{\omega^2\chi_{\epsilon,\mu}}{\chi}-\gamma^2\right)=0. \tag{A.16}$$

Equations A.15 and A.16 can be reduced down to:

$$\frac{\mu_\rho}{\rho}\frac{\partial}{\partial\rho}\left(\rho\frac{\partial H_z}{\partial\rho}\right)\frac{1}{\gamma^2_{c,\phi,\rho}}+\frac{\mu_\phi}{\rho^2}\frac{\partial^2 H_z}{\partial\phi^2}\frac{1}{\gamma^2_{c,\rho,\phi}}+\mu_z H_z=0, \tag{A.17a}$$

$$\frac{\epsilon_\rho}{\rho}\frac{\partial}{\partial\rho}\left(\rho\frac{\partial E_z}{\partial\rho}\right)\frac{1}{\gamma^2_{c,\rho,\phi}}+\frac{\epsilon_\phi}{\rho^2}\frac{\partial^2 E_z}{\partial\phi^2}\frac{1}{\gamma^2_{c,\phi,\rho}}+\epsilon_z E_z=0. \tag{A.17b}$$

Equations A.17a-A.17b are the wave equations for the longitudinal component of the electric and magnetic field in cylindrically anisotropic media.

To find the general form of the solutions of Eq. A.17a, it may be rearranged to take the following form:

$$\frac{1}{\rho}\frac{\partial}{\partial\rho}\left(\rho\frac{\partial H_z}{\partial\rho}\right)+\frac{\mu_\phi}{\mu_\rho}\frac{\gamma^2_{c,\phi,\rho}}{\gamma^2_{c,\rho,\phi}}\frac{1}{\rho^2}\frac{\partial^2 H_z}{\partial\phi^2}+\frac{\mu_z}{\mu_\rho}\gamma^2_{c,\phi,\rho}H_z=0. \tag{A.18}$$

Now we employ the separation of variables and let $H_z(\rho,\phi)=R(\rho)\Phi(\phi)$. Substituting this into Eq.A.18 and multiplying through by $\frac{\rho^2}{R\Phi}$ gives:

$$\rho\frac{\partial}{\partial\rho}\left(\rho\frac{\partial R}{\partial\rho}\right)\frac{1}{R}+\frac{\mu_\phi}{\mu_\rho}\frac{\gamma^2_{c,\phi,\rho}}{\gamma^2_{c,\rho,\phi}}\frac{\partial^2\Phi}{\partial\phi^2}\frac{1}{\Phi}+\frac{\mu_z}{\mu_\rho}\gamma^2_{c,\phi,\rho}\rho^2=0. \tag{A.19}$$

Since the 1^{st} and 3^{rd} terms are independent of ϕ, then the 2^{nd} term must take the form:

$$\frac{\partial^2\Phi}{\partial\phi^2}\frac{1}{\Phi}=-n^2. \tag{A.20}$$

The solution to Eq. A.20 is:

$$\Phi(\phi) = a_1 e^{jn\phi} + a_2 e^{-jn\phi}, \tag{A.21}$$

in which n must be an integer to satisfy the periodic boundary conditions (i.e. $\Phi(0) = \Phi(2\pi)$). Substituting Φ into Eq. A.19 allows it to be reduced to:

$$\rho \frac{\partial}{\partial \rho}\left(\rho \frac{\partial R}{\partial \rho}\right)\frac{1}{R} - \frac{\mu_\phi}{\mu_\rho}\frac{\gamma_{c,\phi,\rho}^2}{\gamma_{c,\rho,\phi}^2} n^2 + \frac{\mu_z}{\mu_\rho}\gamma_{c,\phi,\rho}^2 \rho^2 = 0. \tag{A.22}$$

It should be noted here that Eq. A.22 reduces to the well-known cylindrical-wave equation for the isotropic case. A similar approach to solve this slightly more complex differential equation is now presented. To ease the analysis let $\tau^2 = \frac{\mu_\phi}{\mu_\rho}\frac{\gamma_{c,\phi,\rho}^2}{\gamma_{c,\rho,\phi}^2} n^2$ and $\gamma_\rho^{\mu 2} = \gamma_{c,\phi,\rho}^2 \frac{\mu_z}{\mu_\rho}$. After multiplying Eq. A.22 through by R, it can be expressed as:

$$\rho^2 \frac{d^2 R}{d\rho^2} + \rho \frac{dR}{d\rho} + \left(\gamma_\rho^{\mu 2}\rho^2 - \tau^2\right) R = 0. \tag{A.23}$$

This is Bessel's differential equation, whose solutions are well documented and take the form:

$$R(\rho) = a_3 J_\tau(\gamma_\rho^\mu \rho) + a_4 Y_\tau(\gamma_\rho^\mu \rho) \text{ therefore,} \tag{A.24a}$$

$$H_z(\rho, \phi, z) = \left(a_3 J_\tau(\gamma_\rho^\mu \rho) + a_4 Y_\tau(\gamma_\rho^\mu \rho)\right)\left(a_1 e^{jn\phi} + a_2 e^{-jn\phi}\right) e^{-\gamma z}. \tag{A.24b}$$

The two linearly independent solutions in Eq. A.24b are Bessel (J_τ) and Neumann (Y_τ) functions of order τ. A similar approach can be used with Eq. A.17b and it can be shown that the general solution of E_z takes the form:

$$E_z(\rho, \phi, z) = \left(b_3 J_\nu(\gamma_\rho^\epsilon \rho) + b_4 Y_\nu(\gamma_\rho^\epsilon \rho)\right)\left(b_1 e^{jn\phi} + b_2 e^{-jn\phi}\right) e^{-\gamma z}, \tag{A.25}$$

in which, $\nu^2 = \frac{\epsilon_\phi}{\epsilon_\rho}\frac{\gamma_{c,\rho,\phi}^2}{\gamma_{c,\phi,\rho}^2} n^2$ and $\gamma_\rho^{\epsilon 2} = \gamma_{c,\rho,\phi}^2 \frac{\epsilon_z}{\epsilon_\rho}$. Although the linear combination of exponentials in Eqs. A.24b and A.25 appears to implicate two independent solutions to fully describe the angular variation of the field expressions, the azimuthal periodicity in the cylindrical coordinate system ensures these solutions can in fact be mathematically related to one another. Therefore, for $n \neq 0$, these two azimuthal solutions describe two orthogonal but degenerate modes, in which each may be described by a simple $cos(n\phi)$ or $sin(n\phi)$ through proper choice of the coordinate system's azimuthal alignment.

Appendix B

The EH_{01} Mode in the Metamaterial-Lined Circular Waveguide: A Field Comparison

This appendix aims to illustrate the initial premise of the homogenization procedure: that the fields of the EH_{01} mode in the practical metamaterial-lined waveguide are similar to the EH_{01} mode in the inner vacuum region but can be described by an azimuthally oriented TL mode in the outer liner region that can then be related to an extracted ϵ_{t2} and μ_{z2}.

B.1 Effective-Medium Metamaterial-Lined Waveguide

In a homogeneously vacuum-filled circular waveguide, the TM_{01} mode is generally described by E_ρ, E_z, and H_ϕ, and no E_ρ at cutoff. However, when lined using a thin, near-zero-permittivity dielectric, an E_ρ component at cutoff is generally allowed, and the boundary condition on the normal electric fields at the vacuum-liner interface insists that the E_ρ component in the liner region is much more intense than in the vacuum region. Figures B.1(a) and B.1(b) shows the ρ, ϕ and z components of the electric- and magnetic-field magnitudes of the effective-medium metamaterial-lined waveguide's EH_{01} mode whose geometrical

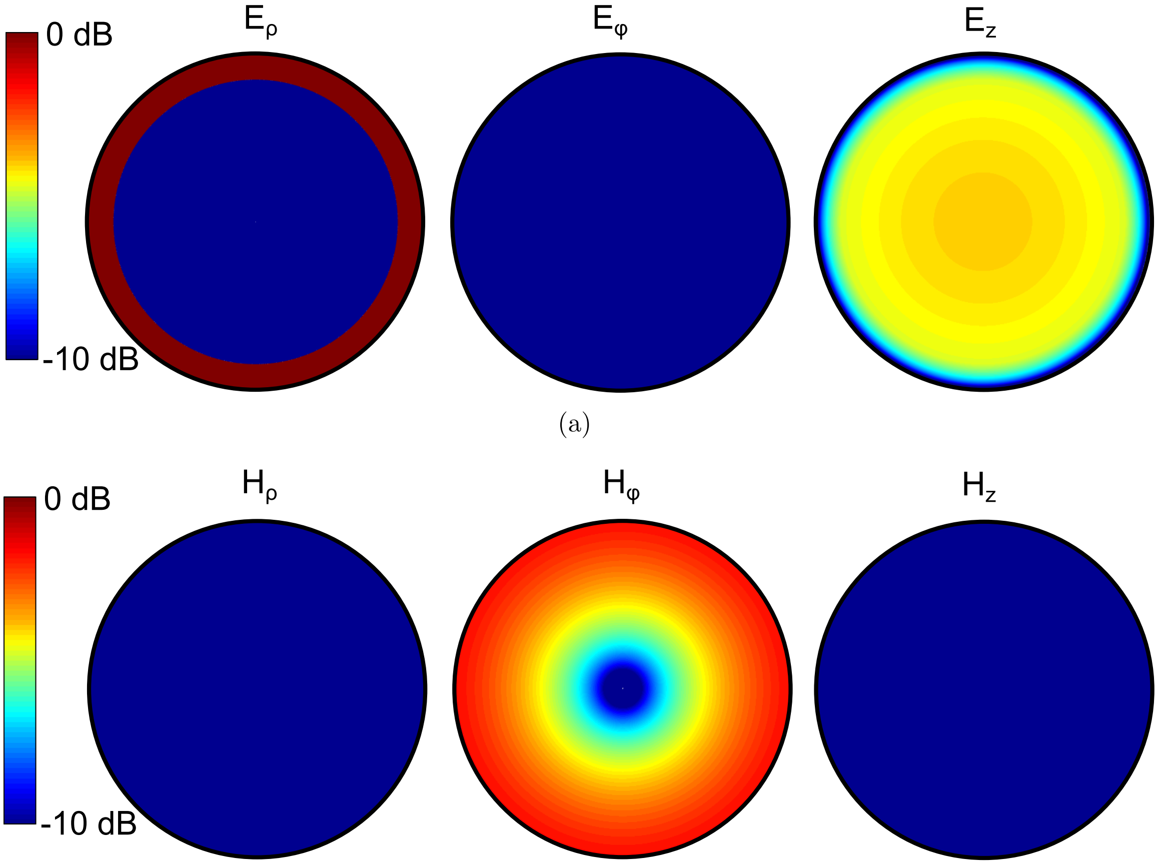

(a)

(b)

Figure B.1: Complex (a) electric and (b) magnetic- field magnitude plots of the homogenized effective-medium metamaterial-lined circular waveguide's EH_{01} mode at cutoff. More details can be found in Sec. 4.4.

and material parameters were presented in Sec. 4.4. The electric [magnetic] field plots are normalized to the same electric- [magnetic-] field magnitudes and presented on a dB scale. Indeed, the E_ρ, E_z, and H_ϕ components are dominant, in which E_ρ in the liner region is of greater magnitude than E_z in liner and vacuum regions. Take note that E_ρ [and H_ϕ] radially increase [and decrease] and is strongest [weakest] on the waveguide's axis.

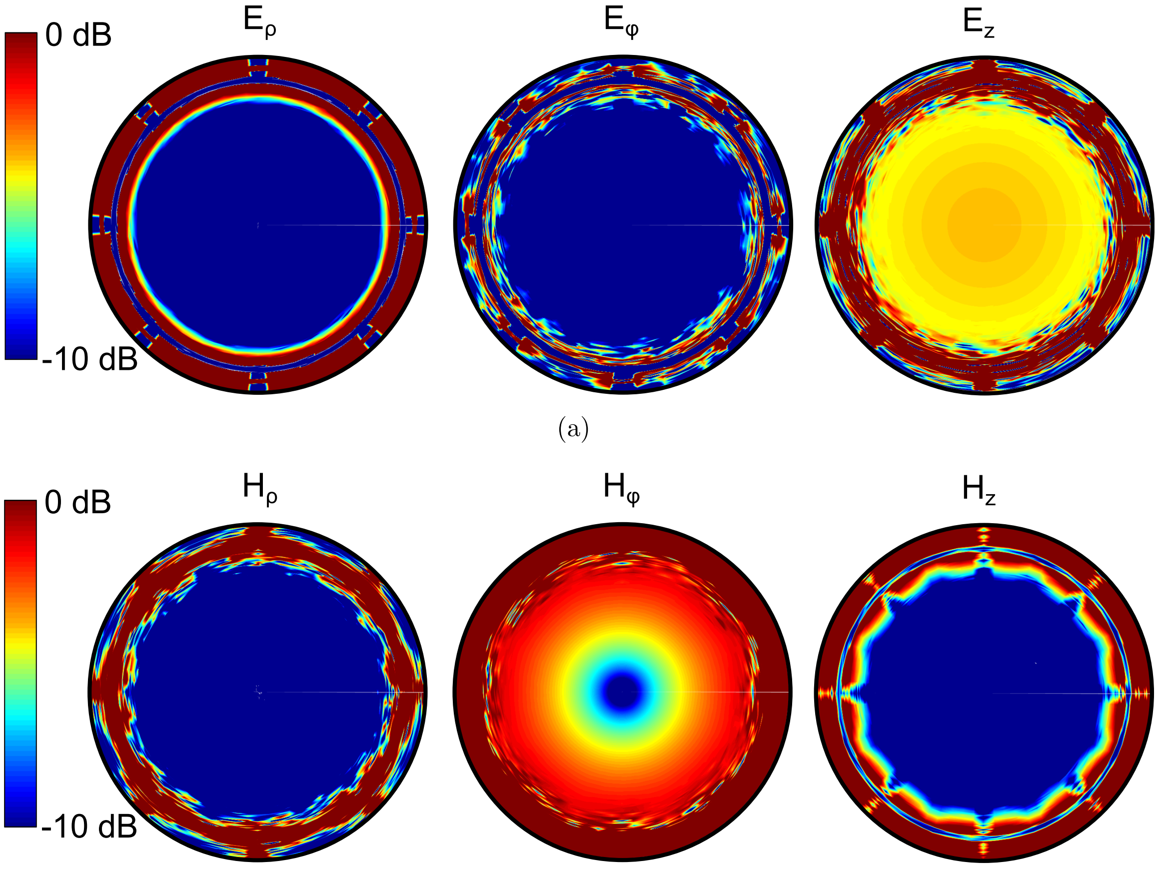

(a)

(b)

Figure B.2: Complex (a) electric- and (b) magnetic-field magnitude plots of the PCB metamaterial-lined circular waveguide's EH_{01} mode at cutoff. More details can be found in Sec. 4.4.

B.2 PCB Implementation of the Metamaterial-Lined Waveguide

Figures B.2(a) and B.2(b) respectively present the ρ, ϕ, and z components of the electric and magnetic field magnitudes of the practical metamaterial-lined waveguide's EH_{01} mode at cutoff. The electric and magnetic field plots are normalized to the same electric- and magnetic- field magnitudes and presented on a dB scale. The practical metamaterial-lined waveguide's geometrical parameters and electrical loading were presented in Sec. 4.4, and was employed in the homogenization scheme to characterize the liner's anisotropic effective-medium parameters.

The chosen normalization value saturates the fields in the liner region, in order to more clearly illustrate their variation in the inner vacuum region. This reveals that, in the inner vacuum region, the major field components are indeed E_z and H_ϕ, which observe the characteristic radial field variation of the EH_{01} mode, and match the EH_{01} field polarizations in the effective-medium metamaterial-lined waveguide. Although the conventional EH_{01} mode does not support an H_z component, the practical metamaterial liner's azimuthal metallic traces are current-carrying and therefore introduce a significant H_z field component in the vicinity of the interface. Even though periodic perturbations are apparent (i.e., a significant E_z component that is normal to the metallic trace's surface), in general $E_\rho >> E_z$ in the liner region. Therefore, although the vacuum fields largely resemble the conventional EH_{01} mode, the practical metamaterial-lined waveguides exhibit a field structure in the liner region that is quite distinct from the conventional EH_{01} mode. It is these E_ρ and H_z components that we relate to a transmission-line (TL) mode to homogenize the liner. It should be noted that the field components E_ϕ, E_z, H_ρ, and H_ϕ are present in the liner region but are of much weaker magnitude than E_ρ and H_z. This is not clearly evident with the chosen dB scale.

Appendix C

Coaxial Pin Excitation

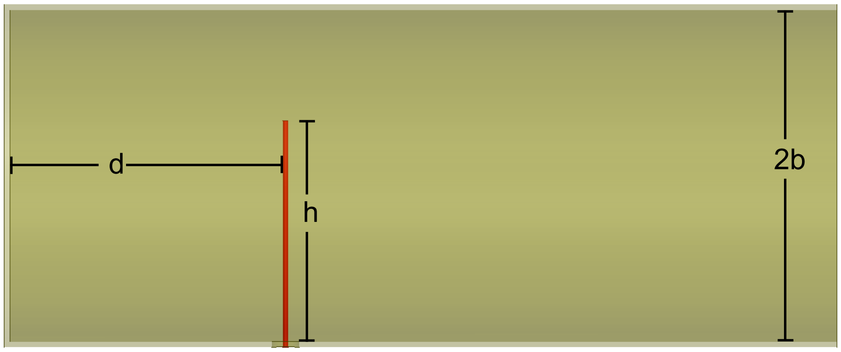

Figure C.1: A cylindrical pin feeding a hollow circular waveguide.

Fig. C.1 presents a hollow circular waveguide of radius b loaded by a cylindrical pin of height h at a distance d from a PEC back wall. By ensuring $h < \lambda_g/4$ and $d \approx \lambda_g/4$, in which λ_g is the wavelength in the waveguide, this feeding arrangement has been shown to efficiently excite the waveguide's TE_{11} mode [131, 167]. This coaxial to waveguide transition is referred to as a side-launch type, whereas a pin extending out the PEC back wall is referred to as end-launch type and strongly excites the waveguide's TM_{01} mode.

Figures C.2(a)-C.2(b) present the electric-field vectors of the hollow circular waveguide's TE_{11} mode and those generated by the pin excitation, respectively. The electric current on the pin supports a significant ρ-directed electric field along the pin's axis which couples to the circular waveguide system to set up an electric field distribution similar to the TE_{11}

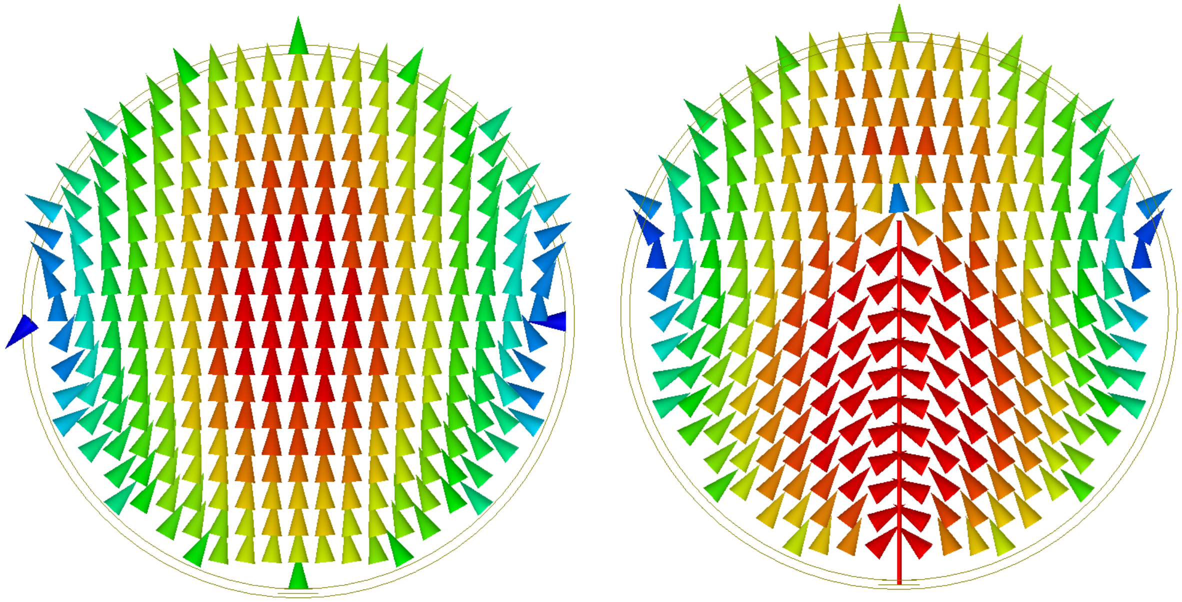

(a) (b)

Figure C.2: The electric-field vectors of (a) a hollow circular waveguide's TE_{11} mode and (b) those generated by a cylindrical pin feeding the waveguide.

mode. However, the field profiles differ very close to the pin, where the electric-field vectors must be normal to the pin's surface. This is partially why the pin excitation weakly excites the TM_{01} mode above its cutoff frequency, which limits the pin's TE_{11} monomodal bandwidth to 12.4%. If the pin was designed to excite the metamaterial-lined waveguide's frequency-reduced HE_{11} mode, there is a strong potential to couple into the full-spectrum of frequency-reduced modes, particularly the co-propagating EH_{01} mode. For instance, preliminary simulations of pin excitations located in or very close to the lined waveguide section revealed that other-order modes such as the EH_{01} and HE_{21} are strongly excited below their respective cutoff frequencies, resulting in unexpected transmission characteristics.

Appendix D

Balanced Shielded-Loop Antenna

The balanced shielded-loop antenna is widely used as highly sensitive magnetic near-field probe because of its ability to detect low magnitude magnetic fields by shielding the signal line from an external electric field [51]. When the antenna is in receive mode, any currents induced by an impinging electric field are balanced by exploiting structural symmetry in the design of the antenna's loop and feed and, as a result, the magnetic field is responsible for generating a signal [132, 168]. Furthermore, this ensures there are no unbalanced currents on the feed line which would generate an electric-dipole-like radiation pattern when the antenna is operated in transmit mode. Whereas these probing applications rely upon the ideal magnetic-loop radiation pattern offered by electrically small balanced shielded loops to provide subwavelength sampling of the magnetic field, resonant versions have proven useful in the wireless transmission of power [169] and in MRI systems [170].

D.1 Basic Principles of Operation

Consider the coaxial shielded loop shown in Fig. D.1, which consists of a coaxial waveguide formed into a loop that is electrically connected at its base, opposite to which the outer conductor is stripped over a small gap. The inner (signal) conductor is connected to the outer conductor across this gap. A complete description of the balancing effect of this

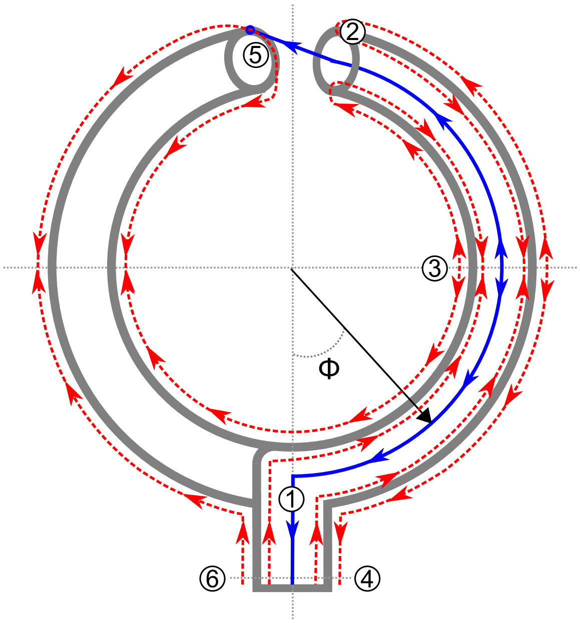

Figure D.1: The currents on the inner and outer conductors of a coaxial shielded-loop antenna of resonance size that is in transmit mode.

topology is provided in Ref. [171] for the infinitesimal shielded-loop antenna with a uniform-current distribution along the loop. When the loop's radius becomes larger, a constant-current assumption in the shielded-loop antenna is no longer valid and the current is better represented by a Fourier series [172–174]:

$$I(\Phi) = I_0 + \sum_{n=N}^{0} I_n cos(n\Phi). \tag{D.1}$$

Here Φ is measured from the feed point, and I_0 and I_n for $n > 0$ is the current's dc and harmonic amplitudes, respectively. When the electrical size of the loop is resonant (i.e. $C/\lambda = n$), the n^{th} term dominates in the current's Fourier series (Eq. D.1) [174]. For instance, consider the shielded-loop antenna in Fig. D.1 that is operated in transmit mode and is driven by a current I_1 (see ①) from the feeding coaxial waveguide. Near the first resonance ($n = 1$), the current on the signal line is approximately $I(\Phi) \approx I_1 cos(\Phi)$, and has its maxima at the feed and gap locations and its minima halfway between. Since the inner conductor is shielded, it will not contribute directly to the antenna's radiation. Instead, this current will induce an oppositely directed current on the inner surface of the outer conductor, which will wrap around the outside of the coaxial waveguide (see ②), setup the cosine current distribution on the outer surface of the outer conductor, and will either continue around the loop (see ③) or exit down the coaxial feed (see ④). Similarly, the inner conductor's current crosses the small gap and smoothly transitions to the outer surface of the outer conductor (see ⑤)), which will setup a reinforcing cosine current distribution on the loop's outer surface, and, due to the shielded loop's resonant size and this particular cosine distribution, will draw a current up from the coaxial feed (see ⑥). The reader should note that despite the loop's resonant size, the currents on the feed line's outer conductor (see ⑥−−④) are in fact balanced, which is a feature shared with electrically small versions, and therefore do not contribute to the antenna's radiation. In fact, it is the unbalanced currents on the loop's outer surface which radiate, and the particular form of the antenna's radiation pattern is a strong function of the current distribution. This signifies that the outer coaxial conductor serves as both the shield and antenna in the balanced-shielded-loop topology. Of course, this condition is contingent on the current obtaining its maxima at the feed and gap locations, which is only valid for resonant and electrically small loops.

D.2 Simulation of the Resonant Balanced Shielded-Loop Antenna

This study will investigate a shielded-loop antenna of resonant size using full-wave simulations. Figure D.2(a) presents the current vectors at $f = 3.4$GHz on the outer surface of a balanced shielded loop of radius $c_r = 13.5$mm and gap $\theta_g = 20°$. It is clear that the loop supports a standing-wave current with a full-wavelength resonance at this frequency, taking its maxima at the gap and feed location and its minima halfway in-between. This is consistent with the previous theoretical analysis. The virtually negligible current magnitudes on the feed line confirms that, despite being of resonant size, this particular shielded loop

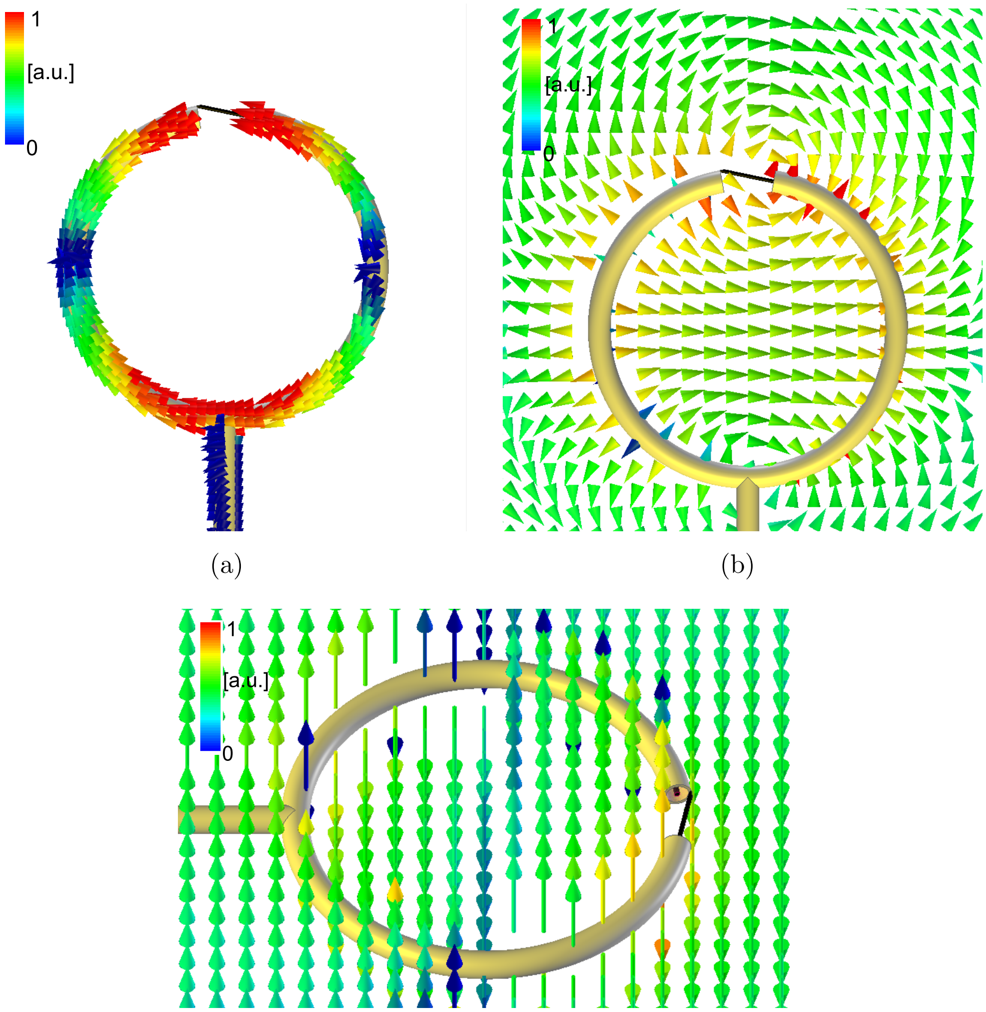

(a) (b)

(c)

Figure D.2: (a) The surface currents supported on a resonant shielded-loop antenna and the (b) electric and (c) magnetic fields generated in its vicinity.

topology ensures the current is balanced.

Considering the antenna in transmit mode, these outer currents will generate electric and magnetic fields, which are shown in the loop's plane in Figs. D.2(b)–D.2(c). Interestingly, the electric and magnetic fields in the loop's interior exhibit a field profile that is similar to the TE_{11} mode in a hollow circular waveguide at cutoff. This includes an electric field with no E_z component and a magnetic field with only a strong H_z component. It is worth noting that the electric field reverses direction transversing from the interior to the exterior of the loop.

D.3 Balanced Shielded Loop In a Circular Waveguide

While the above discussion suggests that the balanced shielded loop would be useful to excite the TE_{11} mode above its natural cutoff in a hollow circular waveguide, there are some clear drawbacks. First, the loop must support the full-wavelength current resonance, which restricts its size. For instance, to use the balanced shielded loop to excite TE_{11} mode above its cutoff would require a waveguide of radius $b = 26$mm. However, the loop would only occupy a small portion (in this case roughly half) of the waveguide's cross-sectional area. The extreme mismatch between the fields generated exterior to the loop and the fields of the TE_{11} mode would lead to reduced coupling. Compensating by increasing the loop's size would only serve to increase the phase variation of the loop's current, causing the field profiles to become non-TE_{11} like.

Another solution is to decrease the size of the waveguide but somehow still operate above cutoff. As discussed in Chapter 3, this can be achieved using a metamaterial liner possessing an ENNZ permittivity. In fact, the reversal of the electric-field vectors exterior to the loop would mimic the action of the ENNZ liners. By appropriately sizing the loop's radius to coincide with the radius of the metamaterial-lined waveguide's interior vacuum region, the fields produced would strongly resemble those of the HE_{11} mode.